




2017

INITIAL MICROSEISMIC RECORDINGS AT THE ONSET OF UNCONVENTIONAL HYDROCARBON DEVELOPMENT IN THE ROME TROUGH, EASTERN KENTUCKY

Andrew Holcomb

University of Kentucky, asholc2@g.uky.edu

Author ORCID Identifier:

 <https://orcid.org/0000-0002-3184-747X>

Digital Object Identifier: <https://doi.org/10.13023/ETD.2017.316>

[Right click to open a feedback form in a new tab to let us know how this document benefits you.](#)

Recommended Citation

Holcomb, Andrew, "INITIAL MICROSEISMIC RECORDINGS AT THE ONSET OF UNCONVENTIONAL HYDROCARBON DEVELOPMENT IN THE ROME TROUGH, EASTERN KENTUCKY" (2017). *Theses and Dissertations--Earth and Environmental Sciences*. 51.

https://uknowledge.uky.edu/ees_etds/51

This Master's Thesis is brought to you for free and open access by the Earth and Environmental Sciences at UKnowledge. It has been accepted for inclusion in Theses and Dissertations--Earth and Environmental Sciences by an authorized administrator of UKnowledge. For more information, please contact UKnowledge@lsv.uky.edu.

STUDENT AGREEMENT:

I represent that my thesis or dissertation and abstract are my original work. Proper attribution has been given to all outside sources. I understand that I am solely responsible for obtaining any needed copyright permissions. I have obtained needed written permission statement(s) from the owner(s) of each third-party copyrighted matter to be included in my work, allowing electronic distribution (if such use is not permitted by the fair use doctrine) which will be submitted to UKnowledge as Additional File.

I hereby grant to The University of Kentucky and its agents the irrevocable, non-exclusive, and royalty-free license to archive and make accessible my work in whole or in part in all forms of media, now or hereafter known. I agree that the document mentioned above may be made available immediately for worldwide access unless an embargo applies.

I retain all other ownership rights to the copyright of my work. I also retain the right to use in future works (such as articles or books) all or part of my work. I understand that I am free to register the copyright to my work.

REVIEW, APPROVAL AND ACCEPTANCE

The document mentioned above has been reviewed and accepted by the student's advisor, on behalf of the advisory committee, and by the Director of Graduate Studies (DGS), on behalf of the program; we verify that this is the final, approved version of the student's thesis including all changes required by the advisory committee. The undersigned agree to abide by the statements above.

Andrew Holcomb, Student

Dr. Edward W. Woolery, Major Professor

Dr. Edward W. Woolery, Director of Graduate Studies

INITIAL MICROSEISMIC RECORDINGS AT THE ONSET OF
UNCONVENTIONAL HYDROCARBON DEVELOPMENT IN THE ROME
TROUGH, EASTERN KENTUCKY

THESIS

A thesis submitted in partial fulfillment of the
Requirements for the degree of Master of Science in the
College of Arts and Sciences
At the University of Kentucky

By

Andrew Holcomb

Lexington, Kentucky

Co-Directors: Dr. Edward W. Woolery, Professor of Geophysics
and Dr. Zhenming Wang, Professor of Geophysics

Lexington, Kentucky

Copyright © Andrew Scott Holcomb 2017

ABSTRACT OF THESIS

INITIAL MICROSEISMIC RECORDINGS AT THE ONSET OF UNCONVENTIONAL HYDROCARBON DEVELOPMENT IN THE ROME TROUGH, EASTERN KENTUCKY

The Cambrian Rogersville Shale is a part of a hydrocarbon system in the Rome Trough of eastern Kentucky and West Virginia that can only be produced unconventionally. In Kentucky, the Rogersville Shale ranges in depth from ~1,800 to ~3,700 m below the surface with the crystalline basement ~1,000 m lower than the formation's base. Baseline Rome Trough microseismicity data were collected, focusing on wastewater injection wells and recently completed and planned unconventional hydrocarbon test wells in the Rogersville Shale, using thirteen broadband seismic stations installed between June, 2015 and June, 2016 and existing University of Kentucky and central and eastern United States network stations. In addition, the network's minimum detection threshold, the magnitude at which the theoretical signal exceeds the noise by a factor of 3 between 1 and 20 Hz for at least 4 stations, was estimated for the project area. Thirty-eight local and regional events were located and magnitudes were calculated for each event. No events were proximal to operating disposal or hydrocarbon test wells, nor did any occur in the eastern Kentucky's Rome Trough. The minimum detection threshold varies between 0.4 and 0.7 Mw from 0000-1100 UTC and 0.6 to 0.9 Mw from 1100-2300 UTC.

KEYWORDS: induced seismicity, detection threshold, Rome Trough, EKMMP, microseismicity

Andrew Holcomb

07/27/2017

INITIAL MICROSEISMIC RECORDINGS AT THE ONSET OF
UNCONVENTIONAL HYDROCARBON DEVELOPMENT IN THE ROME
TROUGH, EASTERN KENTUCKY

By

Andrew Scott Holcomb

Edward W. Woolery

Co-Director of Thesis

Zhenming Wang

Co-Director of Thesis

Edward W. Woolery

Director of Graduate Studies

07/27/2017

ACKNOWLEDGEMENTS

A well-deserved expression of gratitude belongs to the following champions of life: Mama and Pa Holcomb, Brother Ben, Luke Duke and the Luke Duke familiars, Edward Woolery, Zhenming Wang, John Hickman, Seth Carpenter, all of the employees of the fine establishment that is the Kentucky Geological Survey, all of the employees of the fine establishment that is the Tolly-Ho Restaurant, Ron Underwood, and all of the fine students and the fine staff of the fine establishment that is the University of Kentucky Earth and Environmental Sciences Department.

TABLE OF CONTENTS

ACKNOWLEDGEMENTS	III
LIST OF TABLES	VI
LIST OF FIGURES	VII
Chapter 1 Introduction	1
Chapter 2 Geology	4
2.1 Geologic Setting of the Rome Trough	4
2.2 Geologic History of the Rome Trough.....	5
2.3 Formations of Interest	7
Chapter 3 Induced Seismicity	18
3.1 Mechanisms of Induced Seismicity.....	18
3.2 Historical Induced Seismicity	19
3.2.1 Rocky Mountain Arsenal	19
3.3 Recent Cases of Induced Seismicity Related to Oil and Gas Activities	20
3.3.1 Induced Seismicity Caused by Wastewater Injection Related to Oil and Gas-	21
3.3.1.1 Raton Basin, Northern New Mexico/Southern Colorado.....	21
3.3.1.2 Guy-Greenbrier, Central Arkansas.....	21
3.3.1.3 Youngstown, Ohio.....	22
3.3.1.4 Oklahoma	22
3.3.2 Induced Seismicity Related to Hydraulic Fracturing of Unconventional Oil and Gas Shale Resources	23
3.3.2.1 Alberta, Canada	23
3.3.2.2 Poland Township, Ohio.....	23
Chapter 4 Methodology	33
4.1 - Microseismic Monitoring Network.....	33
4.1.1 Station Locations	33
4.1.2 Station Installation and Instrumentation	34
4.1.3 Network Event Triggering	37
4.1.4 Seismic Event Location	38
4.1.5 Seismic Event Categorization	39
4.2 Detection Threshold Modeling.....	40
4.2.1 Site Noise	41

4.2.2 Synthetic Source Modeling.....	43
4.2.3 Minimum Detection Threshold.....	48
4.3 Magnitude Calculations.....	51
4.3.1 Duration Magnitude	51
4.3.2 Local Magnitude	52
4.3.3 Moment Magnitude.....	53
Chapter 5 Results and Discussion.....	66
5.1 Minimum Network Detection Threshold	66
5.2 Earthquake Catalog and Associated Discussion	70
5.3 Magnitude.....	70
Chapter 6 Conclusions and Future Research	83
Appendix A: Well location Information.....	86
Appendix B - Moment Magnitude Calculations.....	88
Appendix D: Local Magnitude Calculations	137
Appendix E: MATLAB Code for Methodology Analysis.....	146
Appendix F: All stations Used for the EKMMP.....	215
REFERENCES	218
VITA.....	224

LIST OF TABLES

Table 1- EKMMP Seismic Station Information. Temporary stations installed for the project and existing stations are shown.	54
Table 2 - Relative Bandwidth Factors (RBW) for typical octave bandpass filters.....	55
Table 3 - Local and Regional Seismicity Detected by the EKMMP.	72
Table 4 - Local events (<100 km) detected by the EKMMP.....	73
Table 5- Boatwright spectral magnitude calculation values for Event 16.....	74
Table 6- Boatwright spectral magnitude calculation values for Event 19.....	74
Table 7- Brune spectral magnitude calculation values for Event 16.....	75
Table 8- Brune spectral magnitude calculation values for Event 19.....	75

LIST OF FIGURES

Figure 1 – Project Study Area Overview	3
Figure 2 - Southeast margin of Laurentia with basement faults in red.....	9
Figure 3 - Major structural features in and around the Rome Trough of eastern Kentucky and western West Virginia.....	10
Figure 4 – Earthquakes near Kentucky since January 1 st , 1974 according to the Center for Earthquake Research and Information.....	11
Figure 5 – Maximum horizontal stress orientations for the central and eastern United States.....	12
Figure 6 – Generalized Rome Trough Cross-Section.....	13
Figure 7 – Structure contour map of the top of the Rogersville Shale to sea level	14
Figure 8- Isopach map of the base of the Rogersville Shale to the crystalline basement.	15
Figure 9- Isopach map of the top of the Rogersville Shale to the crystalline basement...	16
Figure 10- Rogersville Shale Depth to crystalline basement relative to sea level.....	17
Figure 11– Two situations in relation to oil and gas injection activity that can cause induced seismicity.....	25
Figure 12 - Diagram a shows the shearing of a split block as an idealized concept of seismic slip. Diagram b is a graphical representation of the Coulomb criterion	26
Figure 13 – Illustration of the vertical, σ_v , and horizontal, σ_h , stresses acting on a fault at inclination, β	26
Figure 14 Histograms showing the relationship of contaminated waste injected and earthquake frequency related to the Rocky Mountain Arsenal injection wells	27
Figure 15 - Earthquakes $M \geq 3$ in the central and eastern United States since 1973.....	28
Figure 16 – Generalized geologic cross-section of the Guy-Greenbrier earthquake sequence in central Arkansas	29
Figure 17– A generalized cross-section including injection wells in Oklahoma.....	30
Figure 18 – Map of located earthquakes in Poland Township, Ohio.....	31
Figure 19 – (a) East-west and (b) north-south cross sections with located seismicity shaded by time.	32
Figure 20 - Idealized seismic station posthole installation	56
Figure 21 - An idealized vault-style installation.....	57
Figure 22 - Example of event location using EK32 from the EK MMP network.	58
Figure 23 Seismic waveform of a blast at the broadband seismometer, EK22.	59
Figure 24 – One hour of continuous vertical component data taken from station EK12	60
Figure 25 – A PSD estimate of 15 minutes of continuous waveform data.....	60
Figure 26 – Vertical component ground displacement waveform of an earthquake	61
Figure 27 - A Fast Fourier Transform of one second of 0.8 Hz high-pass filtered, ground displacement data starting at the onset of S-wave of the earthquake.	62
Figure 28 - Hamburg Earth Model.....	63
Figure 29 - Boatwright (1980) Model of best fit with observed data.....	64

Figure 30 – A schematic of a focal mechanism for a vertical strike-slip fault	65
Figure 31 - Idealized radiation pattern of an a) S-wave and a b) P-wave.....	65
Figure 32 – Daytime (1100-2300 UTC) minimum detection threshold map.	76
Figure 33 – Nighttime (0000-1100 UTC) minimum detection threshold map.....	77
Figure 34 – Daytime (1100-2300 UTC) minimum detection threshold map with features of interest highlighted by black ellipses.....	78
Figure 35 – Frequency response of PKKY, a short-period seismometer	79
Figure 36 – A PQLX Noise plot of the short-period seismometer, PKKY	79
Figure 37 – Frequency response of EK22, a broadband seismometer.....	80
Figure 38 – A PQLX noise plot of the broadband seismometer, EK22	80
Figure 39 – Minimum detection threshold map for the nighttime hours (0000-1100 UTC) with features of interest highlighted by black ellipses.....	81
Figure 40 – Map of all earthquakes detected by the EKMMP network	82

Chapter 1 Introduction

Seismicity induced from anthropogenic sources has been documented since at least the 1920s, but it has not become a significant societal concern until the oil and gas shale boom of recent years (Pratt, 1926). As has been observed in Oklahoma and multiple other locations worldwide, it is possible for massive wastewater injection, and in a few cases, hydraulic fracturing, to trigger earthquakes, called induced seismicity (Keranen et al., 2014). Within the context of this thesis, an induced seismic event is defined as a seismic event resulting from an activity that has caused a change in the stress field surrounding a fault. A seismic event can only be categorized as induced by wastewater disposal or hydraulic fracturing if it spatially correlates with the area of influence of an injection well, constitutes a change in background seismicity, and temporally correlates with wastewater injection parameters such as well injection rates and pressures (Davis, 1993). If there is not a thorough understanding of a region's geology and seismological history in areas of wastewater injection and hydraulic fracturing, then an event is not able to be proven as induced seismicity.

The Cambrian Rogersville Shale is part of a petroleum system in the fault-bounded Rome Trough of eastern Kentucky and West Virginia that is currently being produced with high-volume hydraulic fracturing. The purpose of this regional study is to determine baseline microseismicity in the Rome Trough of eastern Kentucky, and monitor the new wells at the onset of oil and gas production. Thirteen broadband seismic stations were deployed with installations between June, 2015 and June, 2016 with a configuration that focused on recently completed and planned oil and gas test wells in the Rogersville Shale and clusters of wastewater injection wells. The purpose of the

configuration focus was to be able to detect an event that is lower in magnitude in these areas than other, less dense, areas of the network. These thirteen stations, in addition to existing University of Kentucky (KY Network), Central and Eastern United States Network (CEUSN) (N4 network), and EarthScope Transportable Array (TA Network) seismic stations, are contributing to a multi-year Kentucky Geological Survey (KGS) project called the Eastern Kentucky Microseismic Monitoring Project (EKMMP) (Figure 1). This thesis research presents the EKMMP's network observations and detection threshold for the period of June, 2015 through July 2016.

The research has three objectives: 1) To characterize the geology in the project area; 2) To determine the background rates of natural earthquakes; and 3) To determine the theoretical network detection threshold.

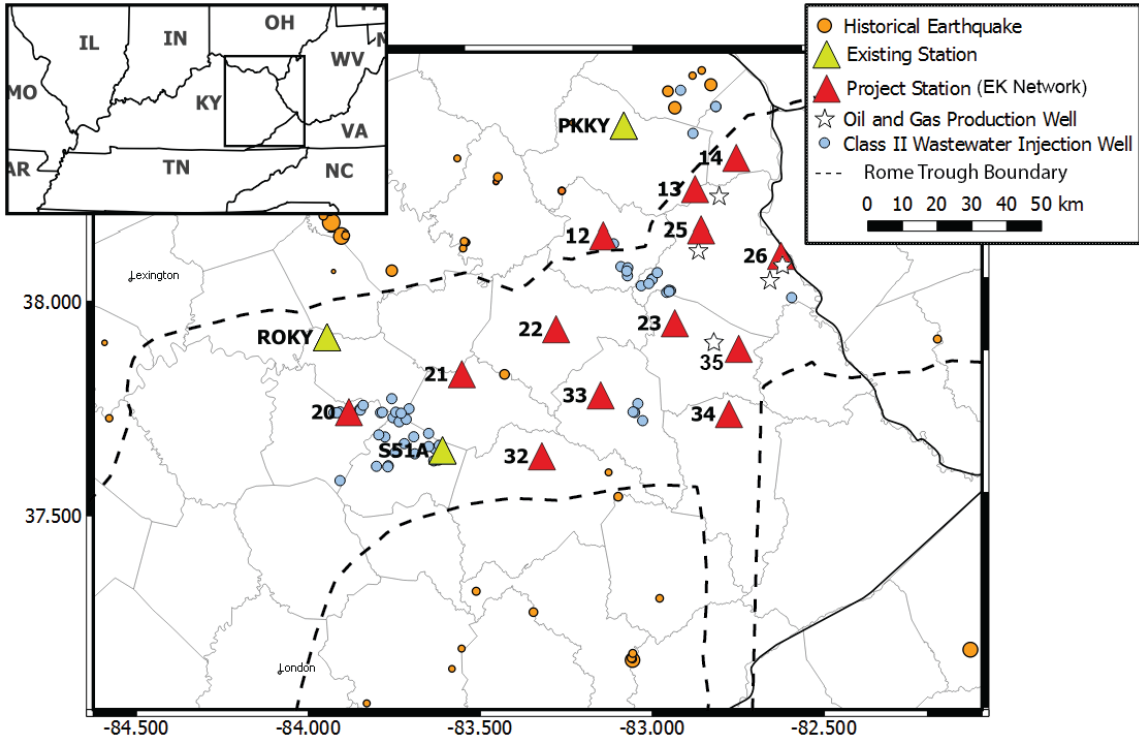


Figure 1 - Oil and gas test wells are in the Rogersville Shale (~3,660 m deep; white stars) in the northeastern part of the project area. The Class II wastewater injection wells, (blue circles), are injected in many different formations ranging between 200 and 1,340 m deep (Appendix A).

Chapter 2 Geology

2.1 Geologic Setting of the Rome Trough

The study area (Figure 1) is located in a stable continental region of the central Appalachian foreland basin of North America. It is underlain by a series of continental grabens that are collectively part of a more extensive interior failed rift system associated with the breakup of the supercontinent Rodinia during the Early and Middle Cambrian (Gao et al., 2000). The Rome Trough, a northeast-trending graben, is part of a larger Cambrian extensional failed rift system extending from eastern Kentucky northeastward across West Virginia and Pennsylvania into southern New York. It has also been associated with the similar-age Rough Creek Graben and Reelfoot Rift farther west in western Kentucky and Tennessee, eastern Missouri, Arkansas, and northwestern Mississippi (Harris, 1996) (Figure 2). As a result of the crustal extension of the interior rift system, a thick sequence of lower Paleozoic sedimentary rocks is present in several grabens along the Appalachian foreland basin in eastern North America (Hickman, 2011).

In eastern Kentucky, the Rome Trough is bounded on the west by the Lexington Fault System, on the north by the Kentucky River Fault System (a major basement fault system that has also been mapped at the surface), and on the south by the Rockcastle River Fault System (White, 2001) (Figure 3). Although the Rome Trough does not coincide with a known zone of seismicity, it is adjacent to the Eastern Tennessee Seismic Zone to the south, and is regionally proximal (~500 km) to the New Madrid Seismic Zone in the west, and the Wabash Valley and South Central Illinois Seismic Zones to the northwest

(Figure 4). The maximum horizontal regional stress is compressive and oriented predominantly SW-NE, and nearly E-W in some locations (Figure 5) (Zoback, 1989).

2.2 Geologic History of the Rome Trough

Major horizontal extension within the Rome Trough occurred at the end of the Precambrian and is associated with the active rifting of the breakup of the supercontinent Rodinia. Volcanism within the Blue Ridge Rift between Laurentia and Amazonia evolved into the Mid-Iapetan Ridge to the east of the trough and by the early part of the Early Cambrian, the southeastern rifted edge of Laurentia had developed into a passive margin (Sloss, 1988).

In the early to middle Cambrian the average sea level rose and flooded the graben leading to the deposition of thick, arkosic synrift siliciclastic successions known as the Rome formation. By the Middle Cambrian the sea level had risen and the entire region was covered in a shallow sea. The Middle-Late Cambrian saw the deposition of the Conasauga Group consisting of low-energy siltstones and shales with episodic carbonate deposits indicative of a slowly subsiding basin margin (Hickman, 2011). The Rogersville Shale is one of six formations recognized within the Conasauga Group and the only one that shows evidence of greater than 1% total organic content (Harris, 2015). The tectonic subsidence of the Rome Trough ended during the Late Cambrian and sedimentation had filled the graben with sediment to the point that no topographic relief remained across the structure (Hickman, 2011).

From the Late Cambrian to the Early Ordovician a regional carbonate platform deposition, known as the Knox Group, replaced the clastic/episodic carbonate deposition

seen in the Conasauga Group. The Knox Group, which is composed predominantly of carbonate (dolomitic) with minor amounts of mature, quartz-rich sandstone, overlies the synrift strata of the entire graben system. A short and intense regression followed this deposition leading to subaerial exposure and erosion of Lower Ordovician dolomites and limestones producing the widespread Knox Unconformity (Hickman, 2011).

In the early part of the Middle Ordovician rising sea levels led to deposition of a transgressive succession consisting of near-shore sandstone followed by argillaceous limestones and dolomites, and later by a broad carbonate bank facies of Black River Formation and the High Bridge Group. The Taconic Orogeny began taking place east of the Rome Trough in the Late Ordovician which supplied sufficient clastic detritus to the warm, shallow seas of the midcontinent leading to the deposition of many carbonate platform to carbonate shale facies including the High Bridge Group, the Lexington Limestone, the Kope formation, the Garrard Siltstone, the Ashlock Formation, and the Drakes Formation (Hickman, 2011).

The Early Silurian through the Middle Devonian saw a warm water, shallow marine environment with deposits of limestone and dolostone with minor amounts of sandstone and shale as seen in the Brassfield Dolomite. In the Middle Devonian the sea levels rose and deeper water environments returned. From the Middle Devonian to the Early Mississippian organic-rich deposits of pro-deltaic black shales formed on the midcontinent in the form of Ohio shale in the Rome Trough region. This is coeval with the formation of the Appalachian Basin and the subsequent formation of the Cincinnati Arch. During this time an estimated 150 m of Devonian through Ordovician was removed

from the Cincinnati Arch exposing Late Ordovician formations in the Inner Bluegrass region on the northwest boundary of the Rome Trough. Uplift from the arches adjacent to subsiding basin areas led to extensive depositional thickening of Devonian black shales in the Appalachian Basin (Hickman, 2011).

In the Middle to Late Mississippian the sea level dropped and led to the deposition of progressively shallower water sediments across the region. Prograding deltaic siltstones of the Borden and Fort Payne Formations were deposited after the Ohio Shale. In the Middle Mississippian the water depth decreased and limestones began to be deposited. Alternating units of sandstones and limestones were deposited throughout the Late Mississippian as the seas became shallower (Hickman, 2011). A general overview of the stratigraphy can be seen in the cross-section in Figure 6.

2.3 Formations of Interest

A formation with potential to produce oil and natural gas within the Rome Trough is the Rogersville Shale of the Middle to Upper Cambrian Conasauga Group. Four samples from the Rogersville shale showed Total Organic content (TOC) values ranging from 1.20% to 4.40% and indicated a formation thickness of approximately 35 m (Ryder, 2003).

Induced seismicity has occurred in other locations (i.e., Oklahoma) due to the interaction of either hydraulic fracturing fluid or wastewater with the underlying Precambrian basement. Figures 7 through 10 (personal communication, Hickman, 2017) assist in giving a thorough understanding of the Rogersville shale depth, thickness and distance to the Precambrian basement. Figure 7 shows the depth to the top of the

Rogersville shale from sea level. Figures 8 and 9 show the thickness of the Rogersville shale by showing the distance from the top of the Rogersville shale to the Precambrian basement and the distance from the bottom of the Rogersville Shale to the Precambrian basement. Figure 10 shows that the Precambrian basement ranges from ~3.5 to 4.5 km deep, and contains faults that show basement offset.

Many formations within the Rome Trough are being used for the disposal of wastewater associated with the production of oil and gas injected by Class II wastewater injection wells (Appendix A) (Class II wastewater injection wells, as defined by the Environmental Protection Agency's Underground Injection Control program, are those wells that inject brines and other fluids associated with oil and gas production and hydrocarbons for storage). These wells are shallow compared to the Precambrian basement in eastern Kentucky and have total depths that are at least 1500 m above the Rogersville Shale in all locations of injection. Because of these large separations, the wastewater associated with these wells is highly unlikely to interact with the Precambrian basement and is less likely to cause induced seismicity. The depth, location, injection formation age, and current status (active/inactive) of each well is listed in Appendix A. Class II wastewater injection formations within the study area include: Rose Run Sandstone (Upper Part Knox), Beekmantown Dolomite (Early Ordovician – Knox Group), Weir Sandstone (Mississippian), Corniferous Dolomite, Lockport Dolomite (Early to Late Silurian), and the Berea Sandstone (Early Mississippian).

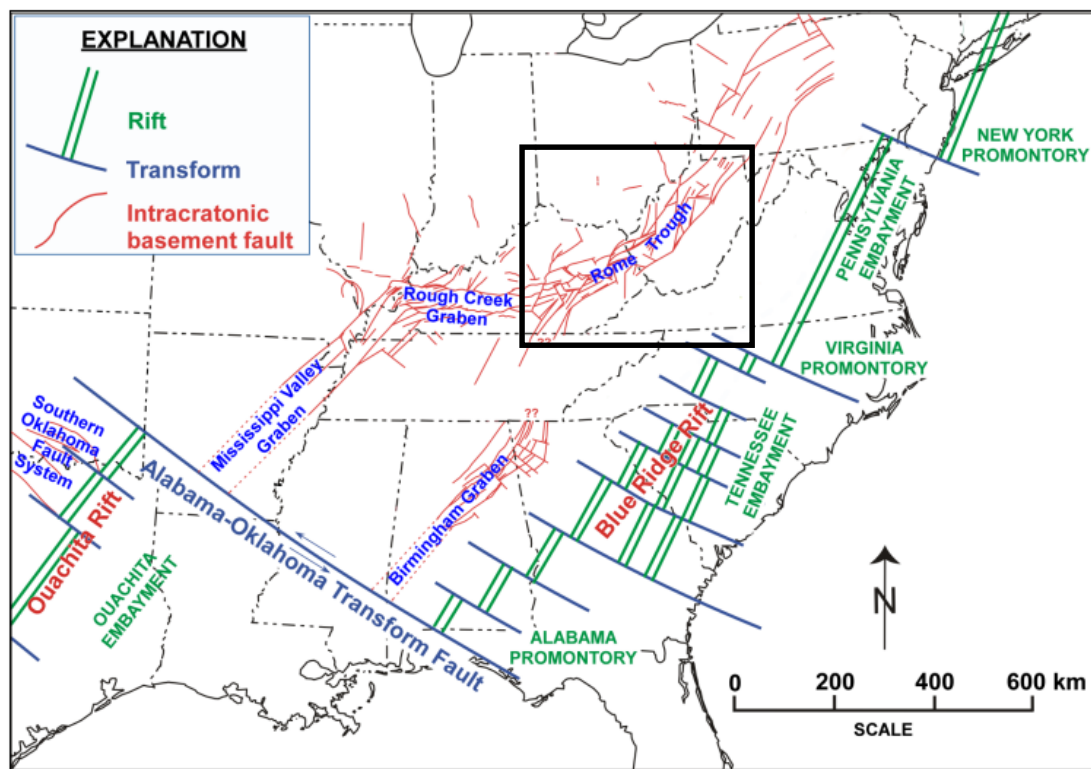


Figure 2 - Southeast margin of Laurentia with basement faults in red. Rome Trough faults are from Patchen, 2006. Cambrian rifted margin from Thomas, 1991. Outline of Figure 3 in black. (Modified from Hickman, 2011)

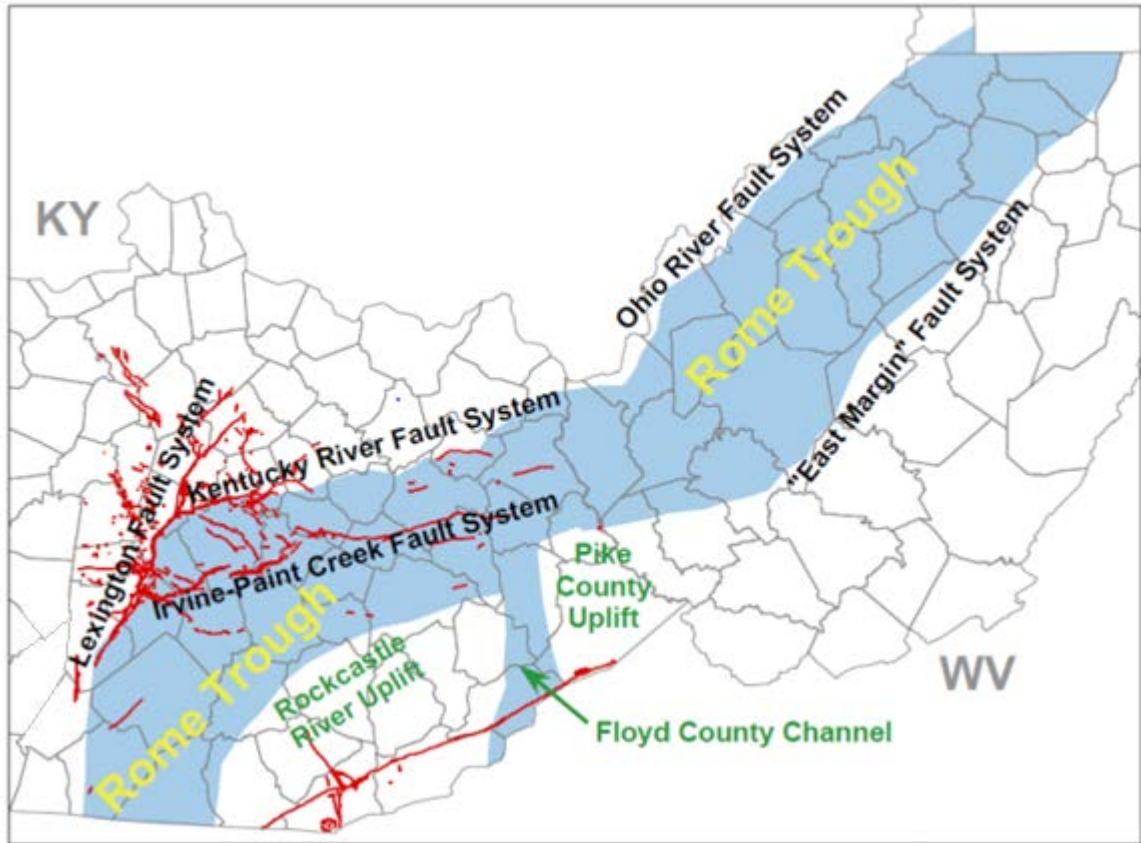


Figure 3 - Major structural features in and around the Rome Trough (graben area highlighted in blue) of eastern Kentucky and western West Virginia (Harris, 2004).

Mapped surface faults shown in red. (The Pine Mountain thrust fault and faults within the Middlesboro impact structure in southeasternmost Kentucky are not basement-rooted and postdate the rift system.) (Hickman, 2011).

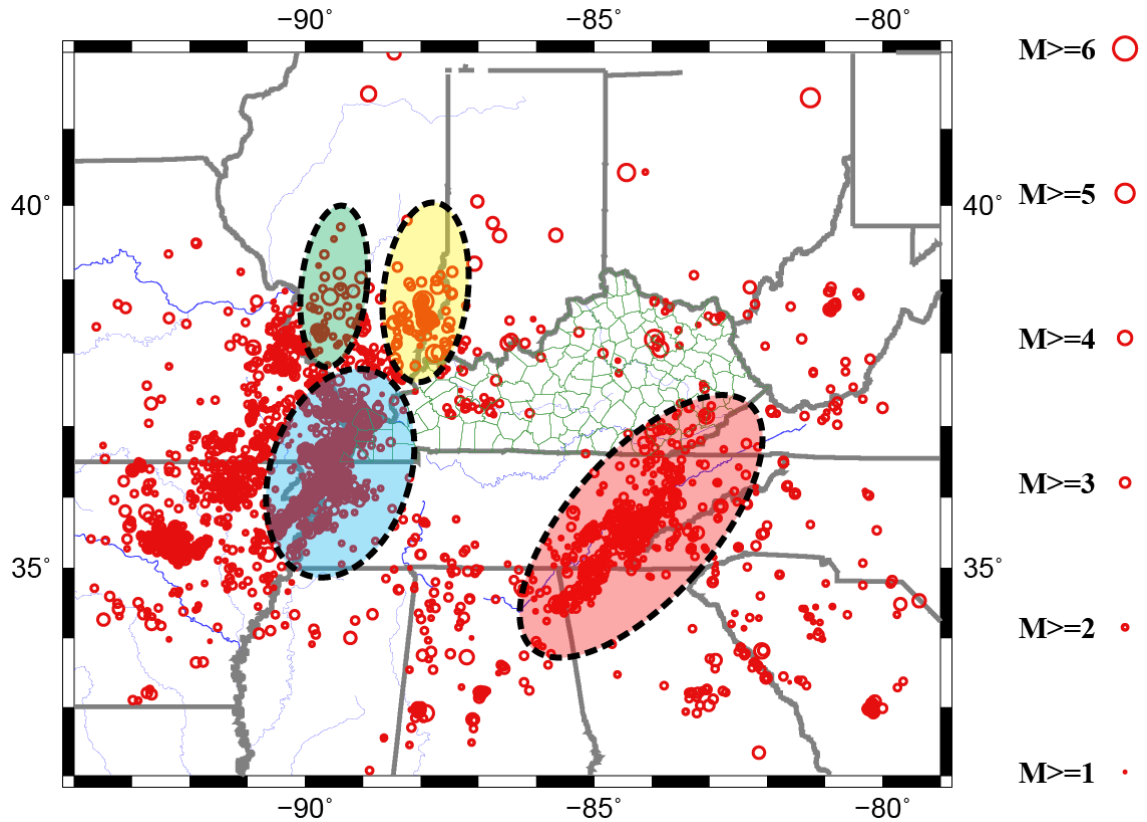


Figure 4 – Earthquakes near Kentucky since January 1st, 1974 according to the Center for Earthquake Research and Information. Seismic Zones indicated by ellipses. Green ellipse – South Central Illinois Seismic Zone. Yellow ellipse – Wabash Valley Seismic Zone. Blue ellipse – New Madrid Seismic Zone. Red ellipse – Eastern Tennessee Seismic Zone.

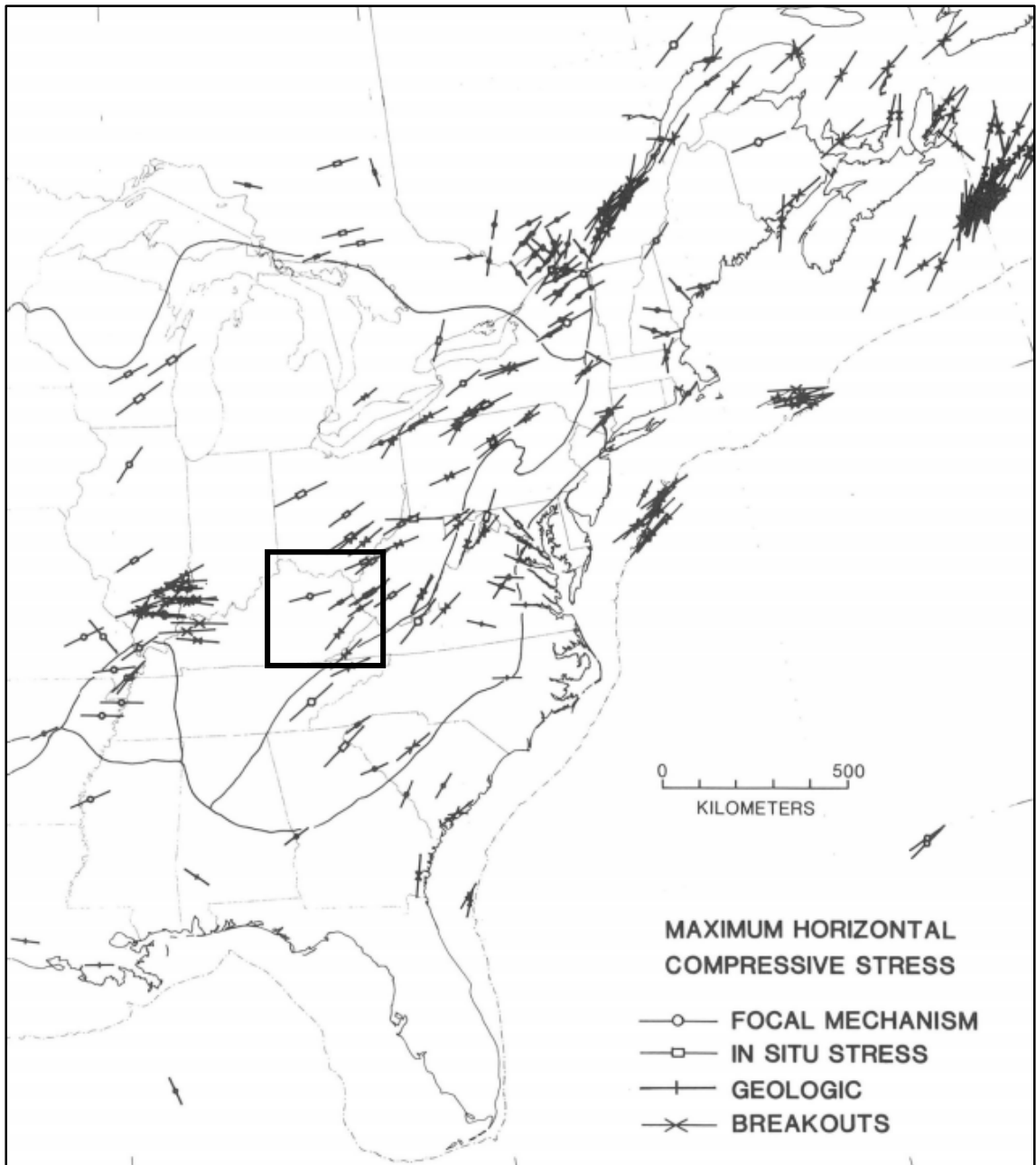


Figure 5 – Maximum horizontal stress orientations for the central and eastern United States. The offshore dot-dash line is the 200 m bathymetric contour, approximating the shelf-slope break. Black rectangle marks the study area for the EKMP (Modified from Zoback, 1989).

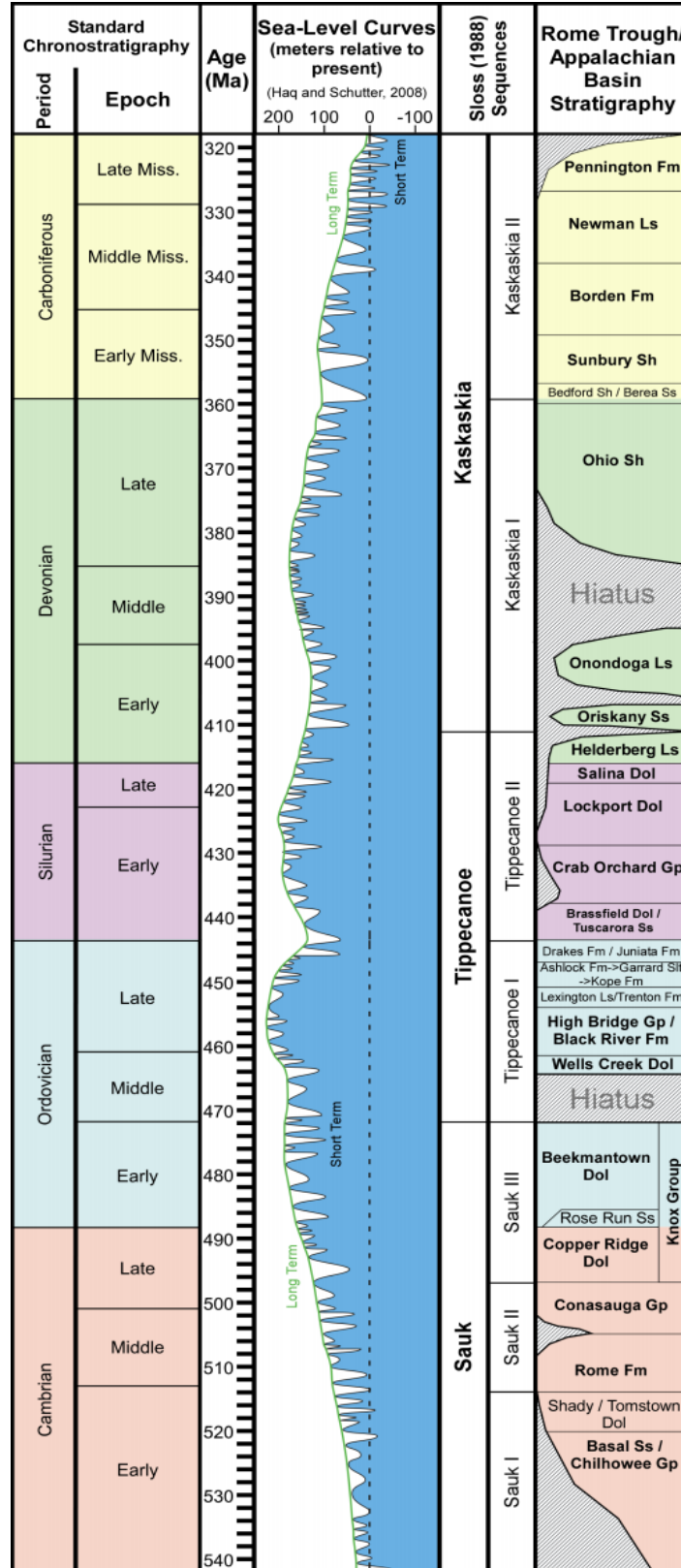


Figure 6 – Generalized Rome Trough Cross-Section (Modified from Hickman, 2011)

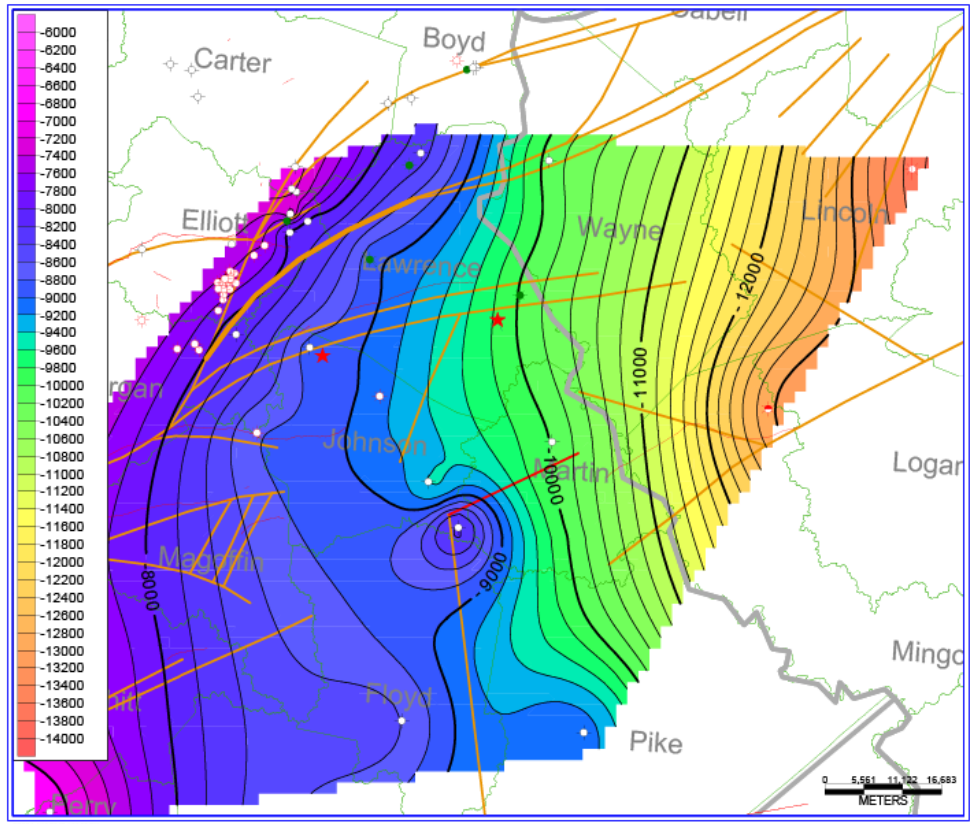


Figure 7 – Structure contour map of the top of the Rogersville Shale to sea level. Structure contours are in feet (1 ft = 0.3048 m). Red stars are areas of known horizontal hydraulic fracturing wells. Basement faults outlined. (Personal communication, John Hickman, Kentucky Geological Survey, 2016)

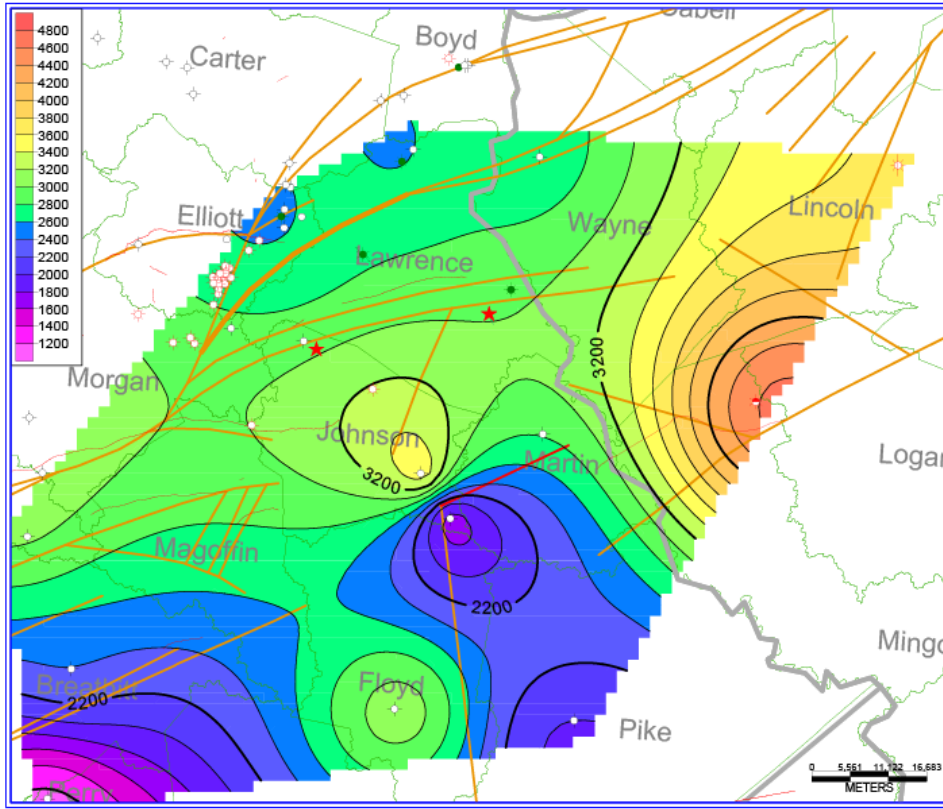


Figure 8- Isopach map of the base of the Rogersville Shale to the top of the Precambrian Basement. Structure contours are in feet (1 ft = 0.3048 m). Red stars are areas of known horizontal hydraulic fracturing wells. Basement faults outlined. (Personal communication, John Hickman, Kentucky Geological Survey, 2016)

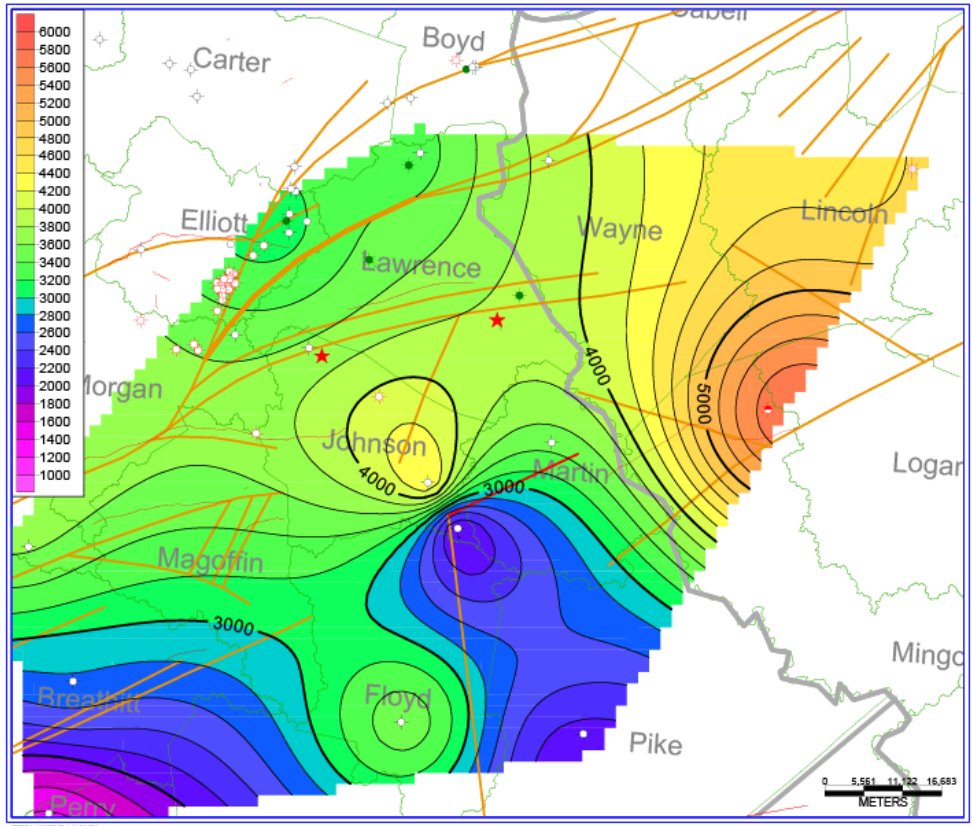


Figure 9- Isopach map of the top of the Rogersville Shale to the Precambrian Basement. Structure contours are in feet (1 ft = 0.3048 m). Red stars are areas of known horizontal hydraulic fracturing wells. Basement faults outlined. (Personal communication, John Hickman, Kentucky Geological Survey, 2016)

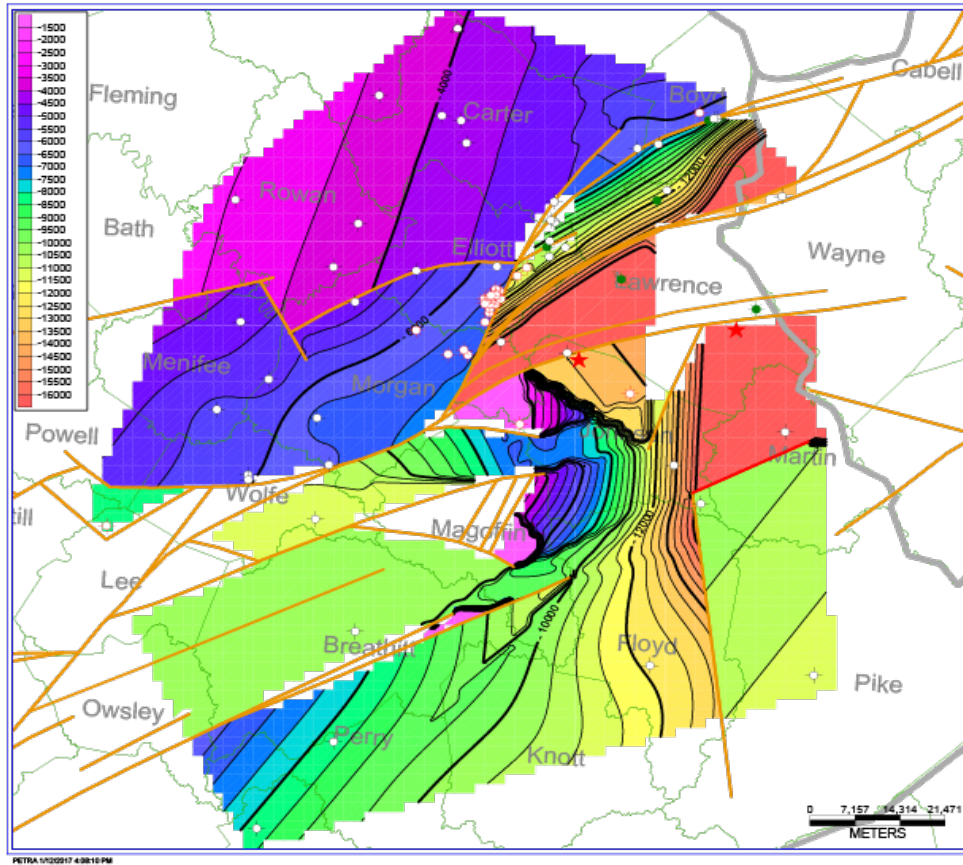


Figure 10- Depth to Precambrian basement relative to sea level. Structure contours are in feet (1 ft = 0.3048 m). Red stars are areas of known horizontal hydraulic fracturing wells. Basement faults outlined in orange. (Personal communication, John Hickman, Kentucky Geological Survey, 2016)

Chapter 3 Induced Seismicity

3.1 Mechanisms of Induced Seismicity

Fluid injection, fluid withdrawal and hydraulic fracturing itself are all sources known to induce seismicity in relation to energy technologies. Fluid injection can induce earthquakes in four different ways: 1) the injection of fluids raises pore-fluid pressure within a fault, 2) fluid injected adds mass to the injection formation 3) the injection of fluid that is colder than the rock into which it is being injected causes thermo-elastic deformation, and 4) the injection of fluids fills and compresses fluids within pore spaces causing deformation (poro-elastic effects) (Rubinstein et al., 2015). The first two ways are the most pertinent in terms of induced seismicity in relation to oil and gas activity associated with hydraulic fracturing production wells and Class II wastewater injection wells (National Research Council, 2013). Figure 11 shows these two possibilities as they directly relate to injection induced seismicity. Notice that neither possibility "lubricates" the fault as is a common misconception in relation to induced seismicity.

The most important aspects of these processes needed to properly assess the seismicity potential in relation to extraction technologies are the presence and orientation of existing faults, the state of stress of the Earth's crust, and the rates, volumes, and timing of injection or withdrawal. (National Research Council, 2013). All of these factors are directly related to the Coulomb failure criterion's two critical terms, friction and effective stress. Within Figure 12, a normal force (F_n) and a shear force (F_s) are both acting on a joint or fault surface, A , with fluid infiltrating at pressure, p . Normal stress is defined as

$$\sigma = \frac{F_n}{A} \quad (3.1)$$

and the shear stress by

$$\tau = \frac{F_s}{A} \quad (3.2)$$

Seismic slip will occur along the surface when the shear stress, τ , is greater than or equal to the frictional strength $\mu(\sigma - \rho)$, where $(\sigma - \rho)$ is the effective stress and μ is the coefficient of friction.

$$\tau > \mu(\sigma - \rho) \quad (3.3)$$

If the shear stress acting on a fault overcomes the fault's resistance to movement due to friction it will slip and create a seismic event. Figure 13 shows how normal and shear stresses relate to vertical stress (σ_v), horizontal stress (σ_n), and fault inclination (β). When wastewater is injected into a formation overlying a fault, the vertical stress on the fault has the potential to increase depending on the orientation of the underlying fault. If vertical stress increases then a larger shear stress will be placed on the underlying fault which will lead to seismic slip if the above condition is met.

3.2 Historical Induced Seismicity

3.2.1 Rocky Mountain Arsenal

The earliest case of documented induced seismicity related to fluid injection occurred at the Rocky Mountain Arsenal liquid waste disposal ~10 km northeast of downtown Denver, Colorado. Between April 1962 and August 1967 over 1,500 earthquakes were recorded, some of which exceeded moment magnitude, M_w , 4. The

Rocky Mountain Arsenal was used for the manufacture and disposal of chemical weapons from 1945 through 1985. A well drilled in 1961 to a depth of 3.67 km, and extending into the underlying Precambrian basement was directly related to seismicity in the area. According to the National Research Council (2013), fluid injection occurred from March 1962 through September 1963 at an average rate of 685 m³/day and again, from August 1964 to April 1965, at a gravity flow rate of 250 m³/day. Pressure injection resumed in April 1965 at a rate of 560 m³/day.

The U.S. Geological Survey and other university researchers found a relationship between injection volumes and earthquake frequency with many earthquake locations being within 3.1 km of the Arsenal injection well (Evans, 1966) (Figure 14). Depths of the earthquakes were shown to be in the Precambrian basement between 3.7 and 7 km, and having a general northwest-to-southeast orientation that followed a system of natural vertical fractures in the local Precambrian rocks (Evans, 1966). The largest earthquakes related to the injection were the April 1967 (Mw 4.5), August 1967 (Mw 4.8), and November 1967 (Mw 4.5) events, all of which occurred after injection had ceased at the well. Although the cause of the earthquakes was initially attributed to the lubrication of the fault systems within the basement, further analysis suggested that the increase in pressure of the existing fluid in the formation through high-pressure injection lowered the frictional resistance along the existing fault system allowing seismic slip to occur (National Research Council, 2013).

3.3 Recent Cases of Induced Seismicity Related to Oil and Gas Activities

The central and eastern United States has seen a dramatic increase in the number of earthquakes above M 3.0 since 2009 (Figure 15). Much of the seismicity has been

attributed to oil and gas activities including wastewater injection and hydraulic fracturing, both of which are taking place in the Rome Trough. It is important to understand the geological and seismological context for each case of induced seismicity as each has its own particular set of circumstances that led to seismic slip. A few examples that have been published in scientific journals are summarized below.

3.3.1 Induced Seismicity Caused by Wastewater Injection Related to Oil and Gas-

3.3.1.1 Raton Basin, Northern New Mexico/Southern Colorado

The August 23, 2011 M 5.3 earthquake event is the second largest earthquake for which there is clear evidence that the earthquake sequence was induced by fluid injection. This sequence began on August 21 and included an M 4.6 earthquake on August 22, was followed by the aforementioned mainshock six hours later on August 23. The largest aftershock was an M 4.0 that occurred on August 23. The hypocenter locations aligned with a steeply dipping tabular structure that is similar to the structure produced from locations of earlier earthquake sequence hypocenters (i.e., a 2001 earthquake swarm and a 2005 earthquake swarm). The majority of the seismicity of the August-September 2011 earthquake sequence lies within 5 km of active disposal wells and ranged between 2 and 8 km depth. (Rubinstein, 2014)

3.3.1.2 Guy-Greenbrier, Central Arkansas

Three Class II wastewater disposal wells, associated with gas development from the Fayetteville Shale, were spatiotemporally correlated with a swarm of earthquakes ($M \leq 4.7$) starting in September 2010 with all but 2 percent of the earthquakes occurring within a 6 km radius. A moratorium area of approximately 3000 km² was approved for any new or additional Class II wastewater disposal wells on January 26, 2011. The area is

located between the towns of Guy and Greenbrier with one well in close proximity to a known Precambrian fault system, called the Guy-Greenbrier Fault (Figure 16) (Horton, 2012).

3.3.1.3 Youngstown, Ohio

Over 167 small earthquakes (M 0.0-3.9) were detected between January 2011 and February 2012 near Youngstown, Ohio (Kim, 2013). All earthquakes were proximal to a fluid injection well that was drilled to a total depth of 2802 m into Paleozoic sedimentary rock composed of carbonates, evaporates, shale, sandstone and siltstone. These approximately 2.7 km thick strata overlie the Precambrian basement. Twelve regional events with $M_w \geq 1.8$ that occurred between March 17, 2011 and January 13, 2012, including the largest M 3.9 event, had hypocenters located within the Precambrian basement. Volumes and pressures were lowered at associated wastewater injection wells and the level of seismicity dropped directly with the reductions.

3.3.1.4 Oklahoma

Moderate earthquakes (M5+) in Oklahoma were rare before the onset of the oil and gas shale boom with documented events occurring only in 1882 and 1952 (Yeck, 2017). Since November 2011, four M5+ earthquakes have occurred including the 2011 Mw 5.7 Prague (Keranen et al., 2014), 2016 Mw 5.1 Fairview (Yeck, 2017), Mw 5.8 Pawnee, and Mw 5.0 Cushing earthquakes. The September 3, 2016 earthquake (Mw 5.8) is the largest earthquake ever instrumentally recorded in the state of Oklahoma. United States mid-continental seismicity has increased from ~1 to 7 $M \geq 3.0$ per year to 75 to 190 per year between 2011 and 2013 and > 650 earthquakes per year in 2014 (Weingarten, 2015). 48 injection wells were shut down in response to the Pawnee, Oklahoma

earthquake. Currently, the number the earthquakes in the region has decreased while the energy release per earthquake has increased, resulting in earthquakes that are larger in magnitude and fewer in frequency. The Arbuckle Group, the formation that receives a large majority of Oklahoma's wastewater from oil and gas operations, directly overlies the Precambrian basement (Figure 17). This has resulted in frequent interaction between wastewater injected in the Arbuckle and the faulted Precambrian basement.

3.3.2 Induced Seismicity Related to Hydraulic Fracturing of Unconventional Oil and Gas Shale Resources

3.3.2.1 Alberta, Canada

On June 13, 2015, an Mw 3.9 earthquake was located at a depth of 3-4 km within the Duvernay Shale formation near the interface of the shale and Precambrian basement (Wang, 2016). This earthquake was located within 2 km of 5 different wells that were fracturing within the area and was the third moderate earthquake ($M > 3.5$) in the area in 2015. All events were suspected to be associated with hydraulic fracturing as this is a historically seismically quiescent area with no $M_L > 3.5$ recorded in the area prior to 2015. This is potentially the largest recorded case of induced seismicity due to hydraulic fracturing.

3.3.2.2 Poland Township, Ohio

77 earthquakes with magnitudes between $M_L \sim 1$ up to 3 occurred in Poland Township, Mahoning County, Ohio that were closely related spatially and temporally to active hydraulic fracturing operations (Figure 18). All events occurred from 4 to 12 March 2014, and the rate decayed once the Ohio Department of Natural Resources issued a shutdown of hydraulic fracturing at a nearby well on 10 March. Earthquakes occurred

during six stimulation stages along two horizontal well legs that were located ~0.8 km away, with hypocenters migrating ~600 m to define a vertically oriented plane of seismicity close to the top of the Precambrian basement (Figure 19). The focal mechanism, orientation, and depth of hypocenters were similar to those of the 2011 Youngstown earthquake sequence that occurred 18 km to the northwest and was correlated with wastewater injection instead of hydraulic fracturing (Skoumal, 2015).

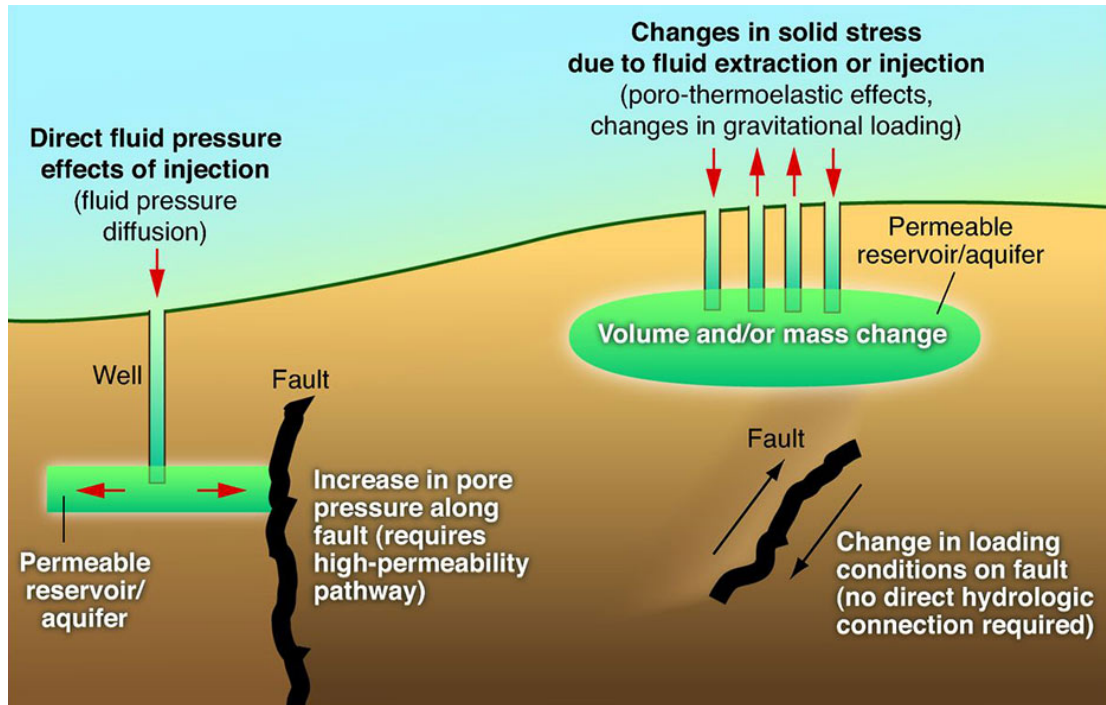


Figure 11– Two situations in relation to oil and gas injection activity that can cause induced seismicity. On the left, the pore pressure along a fault increases due to its direct connection to a permeable reservoir/aquifer. This increase in pore pressure decreases the effective stress being applied on the fault which allows for the frictional strength to be overcome and for slip to occur. On the right, a mass change changes the vertical and horizontal stresses acting on the surrounding rock and a deeper fault that allow for the frictional strength to be overcome by the frictional strength on the fault. (from Ellsworth, 2013)

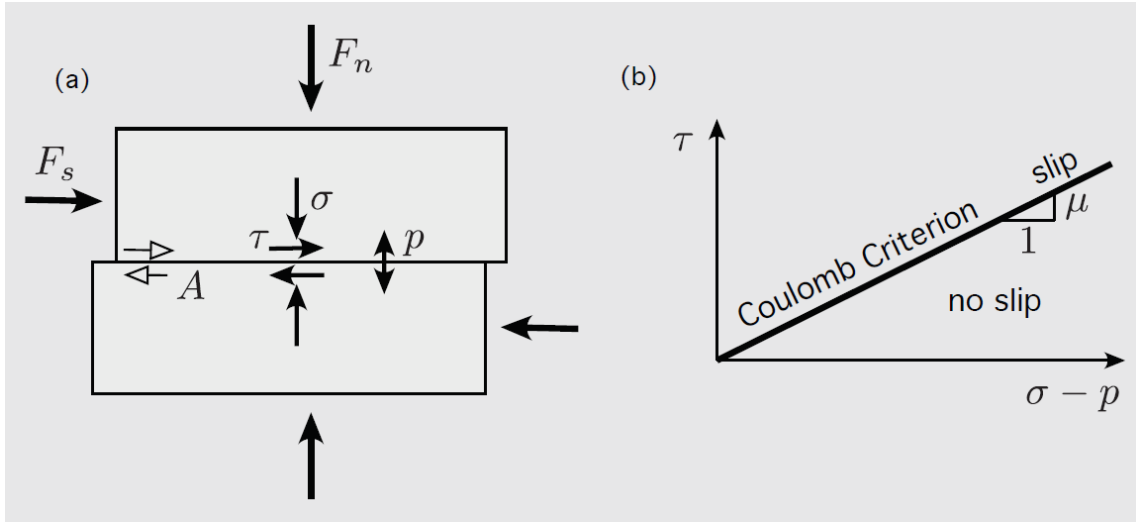


Figure 12 - Diagram a) shows the shearing of a split block as an idealized concept of seismic slip. F_s = Shear Force, F_n = Normal Force, A = the interface area of a joint, τ = Shear Stress = F_s/A , σ = Normal Stress = F_n/A , and p = pressure which is defined by a fluid that infiltrates into a joint at depth. Seismic slip will occur along a joint when the shear stress τ is equal to the frictional strength $\mu(\sigma - p)$, where $(\sigma - p)$ is the effective stress and μ is the coefficient of friction. (Diagram b) is a graphical representation of the Coulomb criterion. If the frictional strength is such that it lies below the Coulomb criterion then there is no slip. (from National Research Council, 2013)

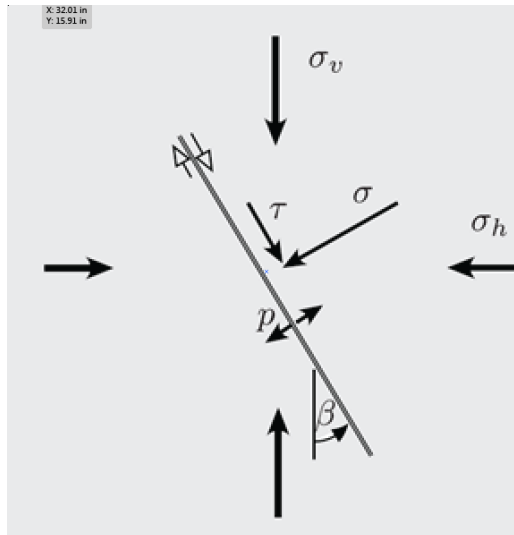


Figure 13 – Illustration of the vertical, σ_v , and horizontal, σ_h , stresses acting on a fault at inclination, β . (from National Research Council, 2013)

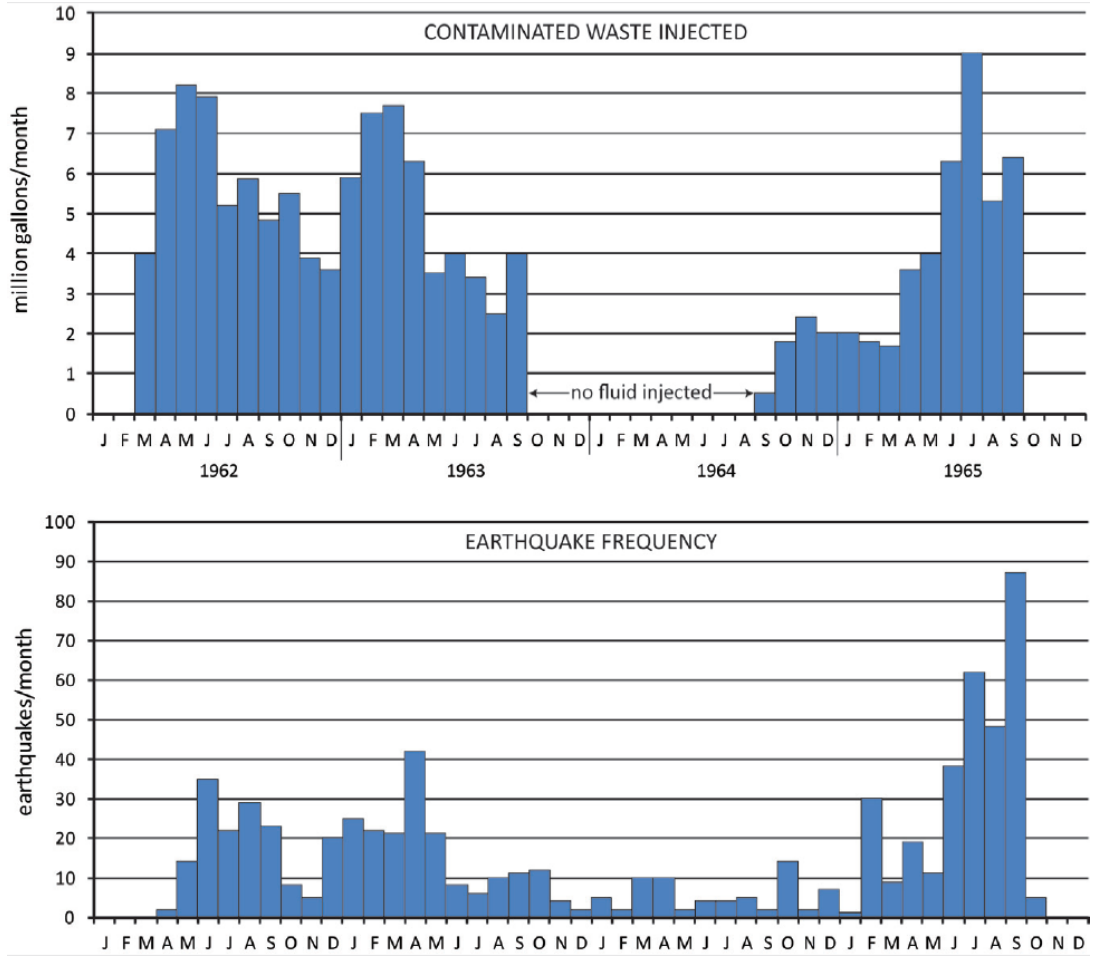


Figure 14 Histograms showing the relationship of contaminated waste injected and earthquake frequency related to the Rocky Mountain Arsenal injection wells. (from National Research Council, 2013)

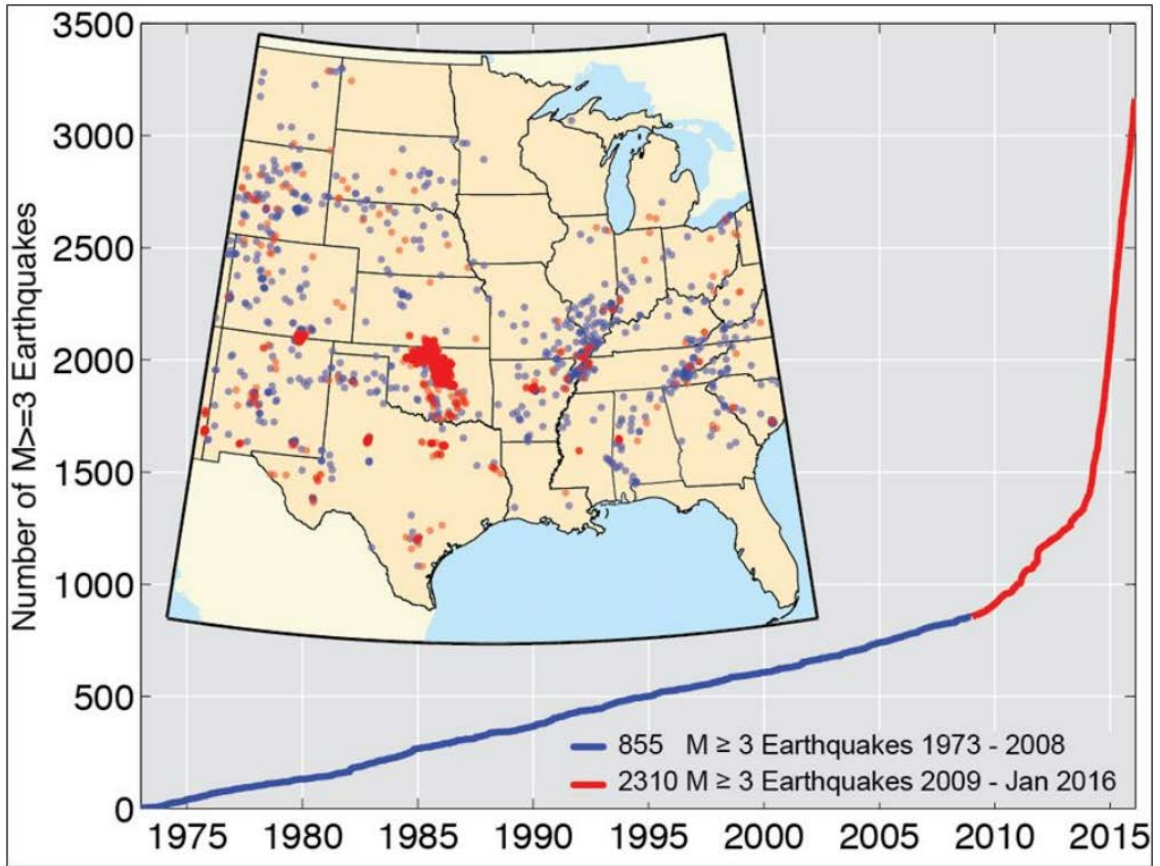


Figure 15 – Earthquakes $M \geq 3$ in the central and eastern United States since 1973.
 (USGS, Earthquake Hazards Program, <http://earthquake.usgs.gov/research/induced>)

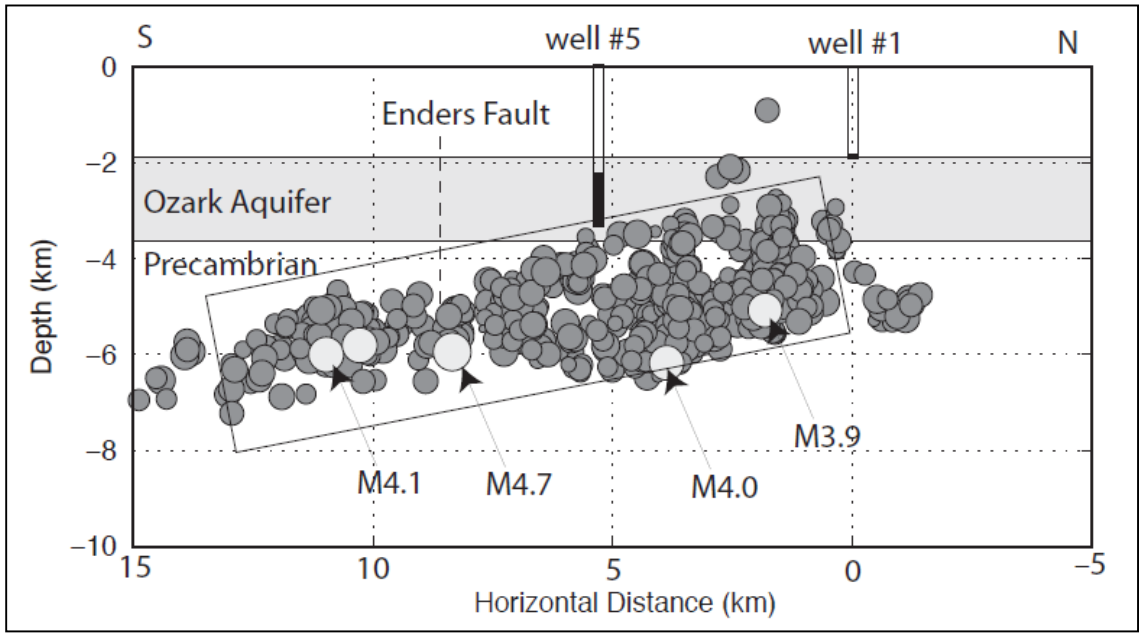


Figure 16 – Generalized geologic cross-section of the Guy-Greenbrier earthquake sequence in central Arkansas. (from Horton, 2012)

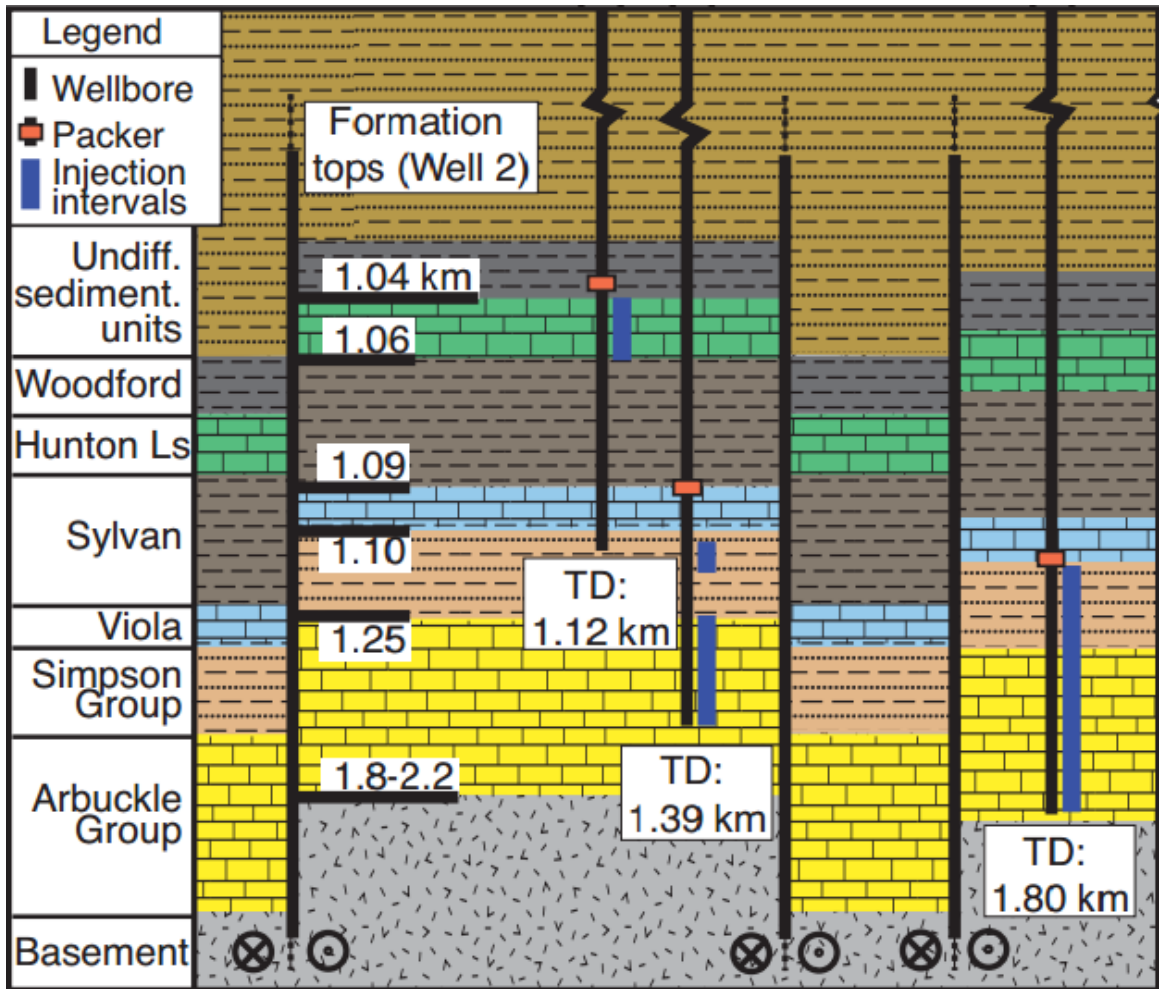


Figure 17– A generalized cross-section including injection wells in Oklahoma (from Keranen, 2013).

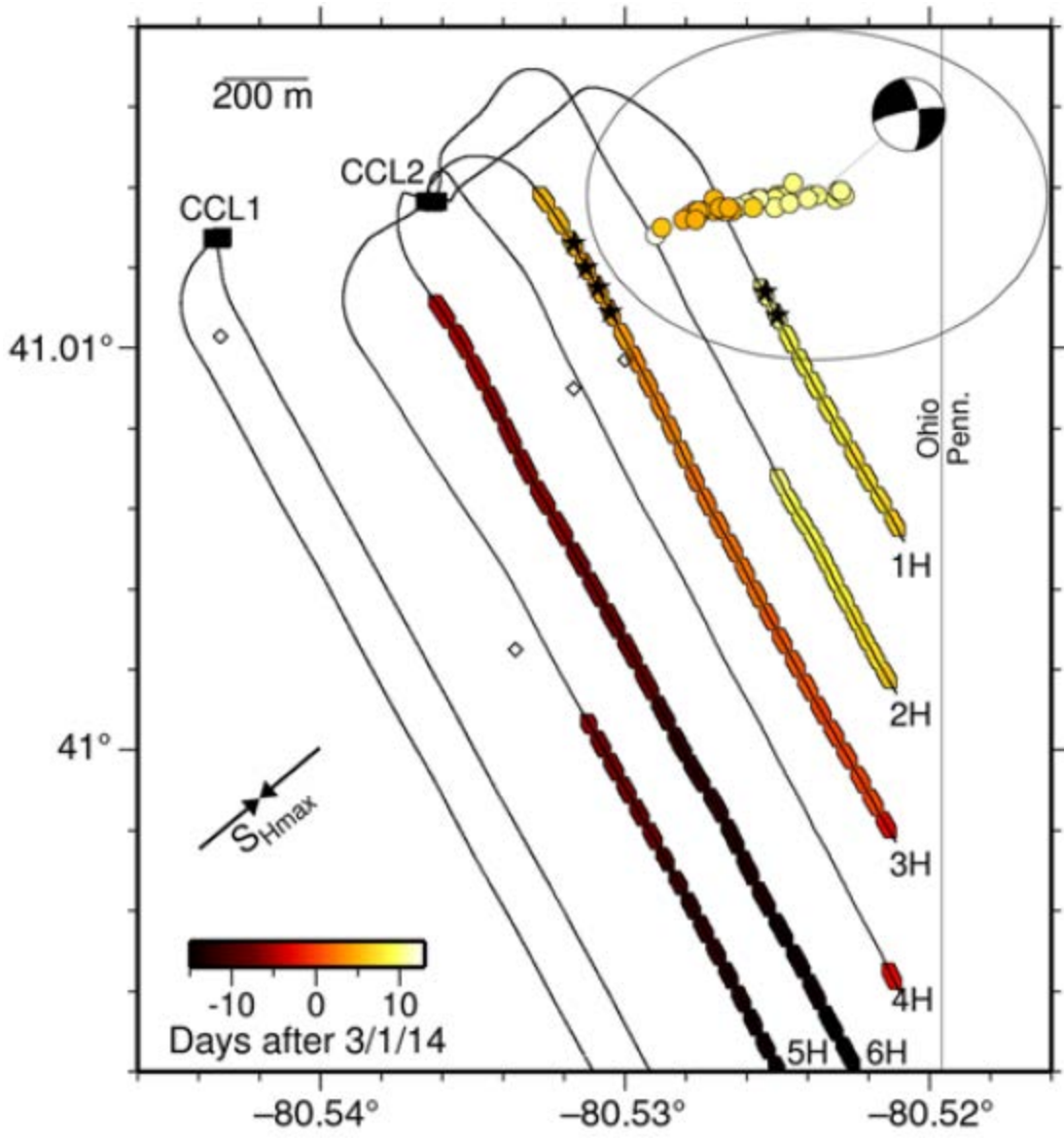


Figure 18 – Map of located earthquakes in Poland Township, Ohio. Lowest relative location uncertainties shaded according to time with stimulation stages shaded according to same time scale. Curved lines indicate horizontal drilling paths. Stars indicate stages correlating with times of seismicity, and focal mechanism is from the 10 March 2014 06:26 M_L 3 event. Diamonds are the reported Ohio Department of Natural Resources/Lamont Doherty Earth Observatory/National Earthquake Information Center locations of the largest earthquakes in this sequence (from Skoumal, 2015).

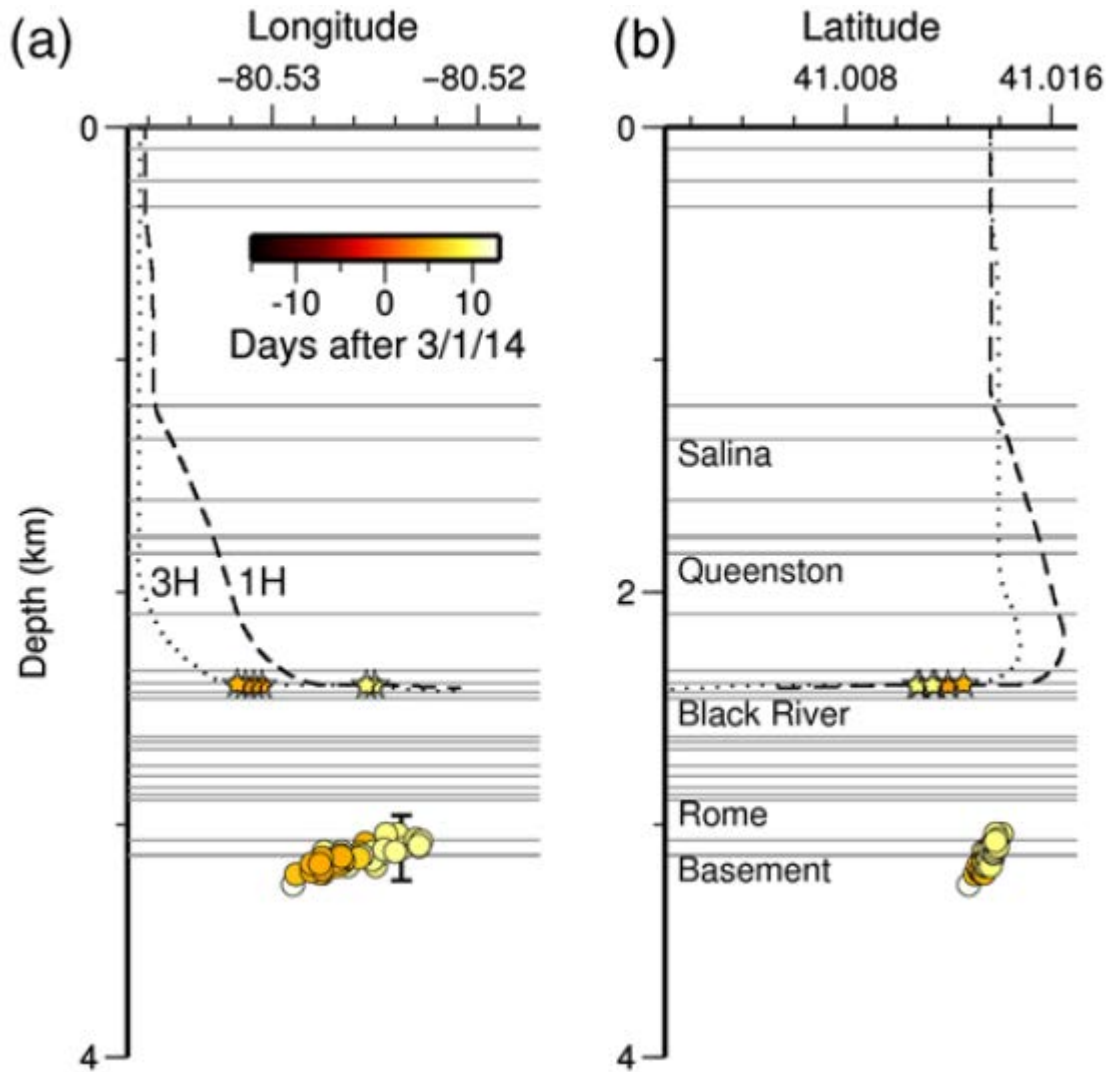


Figure 19 – (a) East-west and (b) north-south cross sections with located seismicity shaded by time. The vertical error bar through this event is based on bootstrap estimation of depth uncertainties indicating the events most likely occurred near the Precambrian basement contact. Horizontal gray lines mark key strata. The dashed and dotted black lines were the paths of wells 1H and 3H, respectively, targeting the Point Pleasant formation (from Skoumal, 2015).

Chapter 4 Methodology

The issue of potential induced seismicity in the Rome Trough is being addressed from a seismological perspective by determining the background rates of natural earthquakes in the region. A network of thirteen broadband seismometers was installed and one year of seismic data was collected within and surrounding the Rome Trough. Using this data, a database of events was created, event magnitudes were calculated, and the theoretical minimum magnitude that the network was able to detect was calculated within the study area.

4.1 - Microseismic Monitoring Network

The Eastern Kentucky Microseismic Monitoring Project (EK MMP) features thirteen broadband seismic stations installed from June, 2015 through June, 2016 in eastern Kentucky within or near the Rome Trough. In addition, multiple existing seismic stations from the Central and Eastern United States Network and the Kentucky Seismic and Strong-Motion Network are contributing data to the project. The study area consists of two separate Class II wastewater injection fields with a total of 26 active and 8 inactive wastewater injection wells, and variability in injection depth, formation and volume (Appendix A). There were five oil and gas production wells that were also active during the time of the study.

4.1.1 Station Locations

Locations for each station within the network were chosen with the goal of providing broad, uniform coverage of the project area while concentrating coverage on areas of ongoing or expected oil and gas activity. The high network density around these areas was intended to provide increased sensitivity to detect lower magnitude seismic

events. For particular stations, the following location-based criteria were also considered at each station site:

1. Landowner permission for access and installation on property
2. Must have clear view of the southern sky for proper functionality of solar panels
3. Installation not exposed to influences of trees and other tall structures that may cause a long-period noise
4. Cellular network coverage for real-time data transmission
5. Avoid areas that are known to contain large animals (cow pastures, etc.) that may cause instrument damage
6. Avoid areas that are known to have poor water drainage
7. Avoid areas that have line-of-sight from major highways to avoid vandalism

An average station spacing of approximately 25 km was achieved throughout the targeted area of injection wells. Specific details associated with the station location, instrument, digitizer, installation type and installation date are provided in Table 1.

4.1.2 Station Installation and Instrumentation

The first four installations were Nanometrics Trillium Compact Posthole seismometers, followed by three Nanometrics Meridian seismometers. Both sensor types have flat velocity responses between 120 seconds and 100 Hz with sample rates of 200 samples per second. The Trillium Compact Posthole sensors were used with a Nanometrics Centaur data logger and for local storage of the data. The Meridian sensor unit contains this data logger and seismometer within the same housing. Data were

wirelessly telemetered via cellular modems to the Kentucky Geological Survey for analysis. Two solar panels at ~20 Volts per panel are used to keep two batteries charged that, should the solar panels fail, are able to power the entire system for approximately one month.

Posthole installation of the broadband seismometers involved excavating a cylindrical hole, approximately 15 cm in diameter, to (Figure 20) depths between ~90 and 180 cm. Station bedrock types varied from medium-grained sandstone to fine-grained gray shales surrounded by soils that ranged from sandy loam to silty clay to clay. A 15.24 cm (6 inch) diameter PVC pipe was then emplaced in concrete that has been poured on to bedrock at the bottom of the hole for sensor protection. Sensor orientation was completed downhole using a rod that set directly into a groove oriented N-S on the top of sensor. Leveling was completed by gently pushing the downhole sensor with the rod and checking that the mass voltages of the sensor were within specification. Sand was used as the base on which the seismometer sits, in addition to being used to backfill the hole to approximately 30-60 centimeters from the surface. Seismometers were buried approximately 3 to 10 m from the site of the mounting pole to avoid any long period frequencies that may be induced by wind pushing on the pole. The mounting pole supported the two solar panels and a housing which contained two batteries, the Centaur Data Logger (Trillium Compact Posthole only), cellular modem, solar power regulator and circuit breakers.

The last six stations have Nanometrics Trillium 40 broadband seismometers and were deployed using a vault-style installation (Figure 21). They have flat velocity

responses between 40 seconds and 50 Hz, and sample at a rate of 100 samples per second. Taurus digitizers were placed inside the vault on a shelf just above the sensor. Vault construction began in the lab prior to deployment with a ~0.75m long x 0.30m wide plastic corrugated drainage pipe being sealed at the base with a rubber membrane. The vault was equipped with a conduit for the necessary cables exiting the vault and to the mounting pole that housed the batteries, the cellular modem, the solar power regulator and the circuit breakers for the system. On-site installation began with ground excavation deep and wide enough (~0.7m x 0.6m) to hold the vault. Grout was placed in base of the hole. The vault was placed into the grout, vertically and horizontally leveled, and left to set. A thin layer of grout was also placed at the bottom of the inside of the vault and leveled.

The tripod deployment cradle was then placed within the vault on top of the hardened grout to hold the unit off of the vault bottom for easier leveling. The seismometer was placed in a heavy duty garbage bag and oriented in the N-S direction in accordance with the north direction labeled on the Trillium 40 unit. The sensor was then leveled using the gently pushing on the seismometer until the onboard leveling bubble was near its center, and the mass voltage recordings from the Taurus data logger and digitizing unit were within accepted range. After sensor leveling and orientation were completed, the unit was wrapped in the garbage bag and sealed with tape to keep the sensor dry. Silica sand was poured around the bag to a level above the sensor, and a shelf was set within the vault on three equally spaced elbow brackets above the sand. The Taurus Data Logger was placed on the shelf and surrounded by fiberglass insulation.

Finally, the vault was fit with a precisely cut piece of Styrofoam to fit within the top part of the vault. This was covered with a rubber membrane, a layer of flashspun high-density polyethylene fibers (Tyvek housewrap), and a concrete paver. These layers were covered with surrounding soil to provide additional insulation.

All stations excavated ~15 cm deep surface trenches around the installation to divert rainwater from the vaults. All vault-style installations (Table 1) had fencing installed around the mounting pole and the sensor for protection. Deep posthole installations (Table 1) had fencing installed around the mounting pole only.

4.1.3 Network Event Triggering

The EKMMP data is collected in real-time through the Earthworm software suite (Johnson, 1995). Events were analyzed if a “trigger” file was created by exceeding a short-term average (STA) amplitude to long-term average (LTA) amplitude ratio within the carlstatrig module in Earthworm. For the vertical component of each station within the EKMMP network, a STA of the recorded trace amplitude is calculated over a time window of 1 second. A weighted average of the previous 20 STAs (not including the STA that is being used in the STA/LTA ratio) is then taken to get the LTA of the trace. An absolute value of the difference between the trace and the LTA averaged over one second is referred to as the short-term rectified average (STAR). The long-term rectified average (LTAR) is a weighted average of previous STARS. These four variables are used in the following triggering algorithm:

$$eta = STAR - Ratio * LTAR - |STA - LTA| - Quiet \quad (4.1)$$

The ‘Ratio’ term is a configurable parameter that, if decreased, creates more, and longer, trigger files. This also affects noisy stations more than quiet ones. The ‘Quiet’ term is a configurable parameter that also creates more and longer triggers but it affects all stations equally. The ‘eta’ parameter is calculated once a second for every station independently and when ‘eta’ is above zero for 4 or more stations within 20 seconds, a file referred to as a ‘trigger’ file is created within the EKMMP database and is then reviewed manually by an analyst.

4.1.4 Seismic Event Location

The hypocenter of an event was determined for this study using a prepackaged routine within the SeisAn earthquake analysis software package (Havskov, 1999). This program is based on, first, making an initial guess at an earthquake’s unknown hypocenter and origin time, (x_0, y_0, z_0, t_0) . For events near or within a network this is done by using a location near the station with the first arrival time and using that as t_0 . Calculated arrival times at station i , t_i^{arr} from the trial location are given as

$$t_i^{arr} = t_i^{arr}(x_0, y_0, z_0, x_i, y_i, z_i) + t_0 \quad (4.2)$$

An assumption is made that the residuals are due to the error in the trial solution and the corrections needed to make them zero are Δx , Δy , Δz , and Δt . Corrections in travel times are made by approximating the travel time function using the first term of a Taylor Series written. The residual can be written as

$$r_i = \frac{\partial t_i^{tra}}{\partial x_i} \Delta x + \frac{\partial t_i^{tra}}{\partial y_i} \Delta y + \frac{\partial t_i^{tra}}{\partial z_i} \Delta z + \Delta t \quad (4.3)$$

In matrix form,

$$\mathbf{r} = \mathbf{G}\mathbf{x} \quad (4.4)$$

where \mathbf{r} is the residual vector, \mathbf{G} is the matrix of partial derivatives (with 1 in the last column corresponding to the source time correction term) and \mathbf{x} is the unknown correction vector in location and origin time. Then a set of linear equations with 4 unknowns (corrections to hypocenter and origin time) is solved with one equation for each observed phase time. The best solution to equation 4.4 can be obtained with standard least squares techniques, and the original trial solution is corrected with the results of equation 4.4 and the new solution is used as a trial solution for the next iteration. This iteration process continues until a minimum residual r is reached. This inversion method was first invented and applied by Geiger (1910) and is called the Geiger method of earthquake location.

4.1.5 Seismic Event Categorization

Manual analysis of a set of waveforms triggered by an event consists of, first, registering each trigger file into a category of seismic event within the SeisAn earthquake analysis program. These categories include:

D – Distant or teleseismic seismic event (>~2000 km away from network)

R – Regional seismic event – (~100-2000km away from network)

L – Local Seismic event – (<100 km from any station used for network triggering algorithm)

LP – Local Probable Blast Event – An event with a source that is most likely an anthropogenic explosion. This is labeled as “Probable” because it is not officially verified with any local blasting records.

LQ – Local Questionable Event – May be a blast or a natural seismic event. Event needs to be verified with blasting records and more in-depth waveform analysis to be more accurately labeled.

The events are categorized by visual inspection of the waveforms based upon the following criteria:

Surface Wave Behavior –The surface wave behavior from sources that reside near the surface exhibit a long-period, nearly sinusoidal motion that is uncharacteristic of small magnitude seismicity created by natural or triggered events that are deeper than ~5-10 km (Figure 22). This behavior can be observed on all three components of a seismometer during a shallow blasting event.

P-Wave Arrival Amplitude and Distinct Phases – Because of the source mechanism of seismic sources related to mine blasting, the compressive strength of the source is often very small in relation to the shear strength and ground motion. A seismogram shows this as having a P-wave amplitude that is emergent, rather than the impulsive nature of a P-wave arrival from a naturally occurring event (Figure 23).

4.2 Detection Threshold Modeling

A minimum detection threshold model was created for areas of wastewater oil and gas wells within the Rome Trough as another measure of baseline microseismicity for the

area. The approach used to find the minimum detection threshold for the network is a combination of three elements: 1) measurement of site noise at each station, 2) creation of synthetic source spectra that are calibrated by real earthquake data, and 3) estimation of the minimum detection threshold for the study area using signal to noise ratios.

4.2.1 Site Noise

The site noise measurements are estimated by the median values of a power spectral density (PSD) probability density functions (PDF) (McNamara, 2004). This is done using the IRIS-PASSCAL Quick Look Extended (PQLX) program. This program uses all data within a continuous waveform for its noise measurements. The data for January of 2016 were acquired for all stations within the EKMMP seismic network (except for station EK34 in Prestonsburg, KY), as well as three other surrounding stations from the Kentucky seismic and strong-motion network and the central and eastern United States seismic network. EK34 was not active until June 6, 2016 and, thus, did not have data for the month of January. Instead, data from July 2016 were used for this station's noise measurements as it was the first full active month of data collection for this station.

The following is an explanation of the processing steps of the PQLX program developed by McNamara and Buland (2004). The continuous data for each station were then parsed into one-hour time series segments (Figure 24), overlapping by 50%, lasting the duration of the month of January 2016 to reduce variance in the PSD estimate (Cooley, 1965). To further reduce variance, each of these one-hour time series segments is divided into 13 segments of 15 minutes each, and overlapped by 75%. Then, the value for the number of samples taken per time series segment is truncated to the next lowest power of two to improve the Fast Fourier Transform (FFT) speed ratio. Subsequently, the

data are transformed to a zero mean value to remove any long period trends. To suppress side lobe leakage in the FFT, a 10% cosine taper is applied to the ends of each truncated and detrended time series segment (McNamara, 2004). The ratio of the total power in the raw FFT to the total power in the smoothed filter is 1.142857 and is used to correct absolute power in the final spectrum (Bendat, 1971).

Estimating the PSD for stationary random seismic data is often done using the direct Fourier transform (Cooley, 1965) which computes a finite-range Fourier transform of the original data given by:

$$Y(f, T_r) = \int_0^{T_r} y(t) e^{-i2\pi ft} dt \quad (4.5)$$

Where T_r = length of time series segment, 819.2 s

f = frequency

The Fourier components, Y_k , for discrete frequency values, f_k , are defined as:

$$Y_k = \frac{Y(f_k, T_r)}{\Delta t} \quad (4.6)$$

Where Δt = sample interval (0.01s or 0.005 s depending on the station (4.1.2)) and N = number of samples in each time-series segment. Using the Fourier components as defined above the total power spectral density estimate is defined as:

$$P_k = \frac{2\Delta t}{N} |Y_k|^2 \quad (4.7)$$

The PSD is then corrected by the factor of 1.142857 to account for the 10% cosine taper applied earlier, and mentioned previously. The seismometer instrument response is removed by dividing the PSD estimate by the instrument's transfer function and converting the PSD to units of decibels(dB) with respect to acceleration $(m/s^2)^2/Hz$ for

direct comparison to the new low and high noise models (NLNM and NHHM) (Peterson, 1993). This process is repeated for each of the 13 separate overlapping segments within the one-hour record and a final PSD estimate is calculated as the average of the 13 segment PSDs.

In order to adequately sample the PSDs, PDFs are calculated by taking full octave averages of a PSD over 1/8 octave intervals (Figure 25). The power is averaged between a short period, T_s , and long period, $T_l=2*T_s$, with a center period, T_c , such that $T_c = \sqrt{T_s*T_l}$ is the geometric mean period between the octave interval. T_s is then incremented by 1/8 of an octave to compute the average power for the next period bin. This process is repeated for every one-hour PSD estimate resulting in smoothed PSDs for each station component. Powers are then accumulated in 1 dB bins to produce frequency distribution plots for each period. The PDF for a given center period, T_c , can be estimated as:

$$P(T_c) = \frac{N_{PT_c}}{N_{T_c}} \quad (4.8)$$

Where N_{PT_c} is the number of spectral estimates that fall into a 1 dB power bin, P , with a range between -200 and -80 dB, and a center period, T_c . N_{T_c} is the total number of spectral estimates over all powers with a center period, T_c . Finally, a probability of occurrence of a given power at a particular period is plotted to yield a PSD PDF noise plot (McNamara, 2004).

4.2.2 Synthetic Source Modeling

Earthquake source models were obtained by fitting a synthetic displacement spectrum to a one second window around the onset of the S-wave arrival of local earthquakes recorded by the EKMMP network. Data were high-pass filtered above 0.8

Hz and instrument frequency response was removed to get data in units of ground displacement in nanometers (Figure 26). A fast Fourier transform was then applied to the 1 second window around the S-wave onset (Figure 27).

The displacement spectral amplitude, $A(f)$, after removal of the instrument response is given by (Ottemöller, 2003)

$$A(f) = S(f) * D(f) * G(R) \quad (4.9)$$

Where $S(f)$ is the source term, $D(f)$ is the diminution function, $G(R)$ is the geometrical spreading, and R is the hypocentral distance. The model used in this study to fit the source term spectra of the S-wave is given by

$$S(f) = \frac{M_0 * C}{4\pi\rho V_s^3} * \left[1 + \left(\frac{f}{f_c} \right)^{\gamma n} \right]^{\frac{1}{\gamma}} \quad (4.10)$$

Where M_0 is the seismic moment (in N-m) as defined by (Kanamori, 1977)

$$M_0 = 10^{\frac{3}{2}(M_w + 6.06)} \quad (4.11)$$

and M_w is the moment magnitude. Following Boore (1983), C is a constant given by

$$C = R_{\theta\phi} * FS * PRTITN \quad (4.12)$$

Where $R_{\theta\phi}$ is the rms displacement radiation pattern (0.55), FS is the free-surface amplification (2), and $PRTITN$ is the reduction factor that accounts for the partitioning of energy into two horizontal components (taken as $1/\sqrt{2}$) (Boore, 1983). The density of the rock at the source, ρ , is in (kg/m^3) and the S-wave velocity at the source, V_s , is in (m/s). Both ρ and V_s are determined from the Hamburg earth model (Herrmann, 1997)

(Figure 28) based on the focal depth used in the model. Frequency, f , is given in Hz and is incremented as an independent variable. Corner frequency, f_c , is given by

$$f_c = \frac{k * V_s}{R_o} \quad (4.13)$$

Where the value of k is 0.21, a constant that is directly related to rupture velocity (Madariaga, 1976). The fault radius, R_o , is given in meters and assumes a circular rupture model (Eshelby, 1957)

$$R_o = \sqrt[3]{\frac{7}{16} * \frac{M_o}{\sigma^3}} \quad (4.14)$$

Where σ is the stress drop, or the magnitude of the stress released by an earthquake, given in Pascals. Stress drop is allowed to vary to find the best fit between the source model and the observed event spectra.

Within the source term, $S(f)$ (Equation 4.10), n is the high-frequency fall-off rate (on a log-log plot) and γ is a constant related to spectral shape. Two variations of this spectral shape were tested: $n=2$ and $\gamma=1$ (Brune, 1970), and $n=2$ and $\gamma=2$ (Boatwright, 1980), the latter produces a sharper corner frequency and a higher spectral fall-off rate.

The diminution function, $D(f)$, is given by

$$D(f) = e^{\left[\frac{-\pi * T * f}{Q(f)}\right]} \quad (4.15)$$

Where T is the travel time (in seconds) determined using the Hamburg Model (Herrmann, 1997). $Q(f)$, according to (Aki K., 1980), is the frequency-dependent quality factor given by

$$Q(f) = Q_0 f^\alpha \quad (4.16)$$

Where, $Q_0 = 525$ and $\alpha = 0.45$ for eastern North America (Atkinson, 2014).

The geometrical spreading term, $G(R)$, for S-waves is given by (Herrmann, 1983)

$$G(R) = \begin{cases} R^{-1}, & \text{for } R \leq 100 \text{ km} \\ (100 * R)^{-\frac{1}{2}}, & \text{for } R \geq 100 \text{ km} \end{cases} \quad (4.17)$$

For unit congruency between all variables within the displacement spectrum, $A(f)$, convert this value to displacement in terms of meters.

For this study, it is necessary to model the amount of energy that would be felt solely on the vertical component of the seismometer because it activates the triggering algorithm. To accurately model the energy of a wave that can propagate towards the seismometer in any direction, the incidence angle of the incoming source S-wave must be taken into account. The incidence angle, i , of a ray emerging at a distance x can be found from dT/dx , the slope of the travel time curve evaluated at x , when the velocity, V_s , is known

$$\sin i = \frac{V_s dT}{dx} \quad (4.18)$$

The ray parameter, P , is constant along the path of this ray and is determined by the slope of the hyperbolic travel-time curve at a certain distance x .

$$P = \frac{dT}{dx} = \frac{\sin i}{V_s} \quad (4.19)$$

Because the slope decreases with increasing velocity, travel time curves with lower slopes indicate higher velocities. The incidence angle of the wave at the surface can be

solved using a known surface velocity from the Hamburg model (Herrmann, 1997) of 2,850 m/s:

$$P = \frac{\sin i}{v_{surface}} \quad (4.20)$$

yielding

$$i = \sin^{-1}(V_{surface} * P) \quad (4.21)$$

This term recognizes all the S-wave energy will not be delivered onto the vertical component, providing a more accurate vertical component source model as can be seen in the final used equation for the source model.

$$A(f) = \left(\frac{1}{\sin(i)}\right) * S(f) * D(f) * G(R) \quad (4.22)$$

The misfit between multiple source spectrum models was minimized with moment magnitude (Mw) and stress drop (σ) as free parameters as Mw is directly proportional to a spectrum's low-frequency plateau and σ to the corner frequency. The lowest root mean square residuals between the source displacement models and an event's high-pass filtered, ground motion displacement spectrum yielded a model of best fit (Figure 29). Although this is the model of best fit method used in this study, the root mean square residual model of best fit may not be the most accurate representation of the S-wave arrival. This misfit minimization was repeated using the Brune (1970) and Boatwright (1980) models for the closest five stations to two different events detected by the EKMMP (Appendix B). A median value of all of the stress drops and moment magnitude calculations was used for subsequent analysis.

4.2.3 Minimum Detection Threshold

The minimum detection threshold, of the EKMMP network is defined as the minimum magnitude at which the network triggering algorithm is activated. The signal of the calculated displacement source model must exceed the median background noise, calculated in PQLX, by a factor set by a network seismologist between 1 and 20 Hz for at least four stations for this activation to occur. For this study, a signal-to-noise ratio of 3 was used as an estimate at which our network triggering algorithm is activated. The signal-to-noise ratio is calculated for signal and noise spectra in units of velocity amplitude per Hz. Because both spectra are given in other units, many conversions must take place before the ratio can be calculated accurately.

The displacement spectrum model signal is calculated in meters per Hz and is converted to velocity amplitude per Hz as follows:

Displacement Amplitude Spectrum (m/Hz)

$$V(\omega) = i\omega D(\omega)$$

$$V(\omega) = i2\pi f D(\omega) \quad (4.23)$$

The noise measurement for PQLX is in dB with respect to acceleration squared per Hz. PQLX units were first converted to power spectral density, P_a , of acceleration relative to the metric unit $1(m/s^2)^2/Hz$. The following conversion yields the power spectral density, P_v , of velocity relative to the metric unit $1 (m/s)^2/Hz$:

$$P_a[dB] = 10 \log_{10}[P_a/1(m/s^2)^2 /Hz] \quad (4.24)$$

$$P_v[dB] = P_a[dB] + 20 \log_{10}(T/2\pi) \quad (4.25)$$

Where $T = (1/f)$ in seconds. Converting from $P_v[\text{dB}]$ to P_v

$$P_v = 10^{(0.1 * P_v[\text{dB}])} \quad (4.26)$$

gives a velocity power spectral density in units of $\text{Velocity}^2/\text{Hz}$.

Converting a power spectrum to a quantity that can be compared with an amplitude spectrum is approximated by the product of the “amplitude spectral density” and the bandwidth of a wavelet (Aki K. R., 1980). Defining the “amplitude spectral density” must be done by integrating over a bandwidth to obtain the mean square amplitude. The square root of this power is the root mean square (RMS) or effective amplitude (Bormann, 2013),

$$a_{RMS} = \sqrt{[2P_v * (f_u - f_l)]} \quad (4.27)$$

With f_u and f_l being the upper and lower corner frequencies of the band-passed signal.

Stationary signals must be characterized by their PSD, and specifying seismic noise by its RMS amplitude is meaningless without definition of the bandwidth (Bormann, 2013).

Rather than changing the upper and lower corner frequencies over which the PSD is taken for each measurement, each f_o is multiplied by a fixed fraction that represents the width of the passband of the signal. This fixed fraction is referred to as the constant relative bandwidth factor (RBW). When taken over n octaves it is defined by the following relationship

$$RBW = 2^{n/2} - 2^{-n/2} \quad (4.28)$$

Table 2 lists typical octave filters and their associated constant relative bandwidth factors.

As PQLX data were filtered over 1 octave RBW becomes

$$RBW = 0.707 * f_o = \frac{1}{\sqrt{2}} * f_o \quad (4.29)$$

This frequency, now represented properly with the passband over which it was filtered, is used within the root mean square effective amplitude formula as

$$a_{RMS} = \sqrt{2P_v * RBW} \quad (4.30)$$

The instantaneous amplitude of random noise within a Gaussian amplitude distribution has a 95% probability of lying within a range of $\pm 2a_{RMS}$ (Bormann, 2013). In this case, the absolute peak amplitudes of the narrowband filtered signal envelopes should follow a Rayleigh distribution. Within an ideal Rayleigh distribution the theoretical average peak amplitudes (APA) are $1.253a_{RMS}$ (Bormann, 2013). This yields the following average peak amplitude

$$APA = 1.253 * a_{RMS} = \sqrt{\frac{\pi}{2}} * a_{RMS} \quad (4.31)$$

A final conversion factor is:

$$V(\omega) = \sqrt{\frac{\pi}{2}} * a_{RMS} \quad (4.32)$$

$$V(\omega) = \sqrt{\frac{\pi}{2}} * \sqrt{2P_v * RBW} \quad (4.33)$$

$$V(\omega) = \sqrt{\frac{\pi}{2}} * \sqrt{2P_v * \frac{1}{\sqrt{2}} * f_o} \quad (4.34)$$

The conversion places both values in a velocity spectrum (in units of (m/s)/Hz) for calculating the signal-to-noise ratio

$$SNR = \frac{V(\omega)_{Theoretical\ Source\ spectrum}}{V(\omega)_{PQLX\ Noise}} = \frac{V(\omega)_{Signal}}{V(\omega)_{Noise}} \quad (4.35)$$

The displacement source model minimum magnitude that exceeds a SNR of three for at least four stations within the passband of 1 to 20 Hz is the minimum detection threshold and defines the minimum detectable magnitude at a particular location for this study. Values of minimum detection threshold were calculated every five km in an equally spaced grid within the project area to yield detection threshold maps for the hours 0000-1100 UTC (Nighttime) and 1100-2300 UTC (Daytime).

4.3 Magnitude Calculations

Duration magnitude, M_D , local magnitude, M_L , and moment magnitude, M_w , scales were calculated to determine the size of the events detected by the network. Not every scale was able to be calculated for every event due to poor station coverage and lack of data. Only duration magnitudes were calculated for all events.

4.3.1 Duration Magnitude

Duration magnitude, M_D , is calculated using the time from the onset of the P-wave to the time at which the waveform amplitude diminishes to amplitude levels near the background noise. Duration magnitudes were estimated for all located events using the relationship applied from the southeastern United States Seismic Network Bulletin (Chapman, 2002) using the following form to calculate the magnitudes seen in Tables 2 and 3 in the Results/Discussion section.

$$M_D = -3.45 + 2.85 \log_{10}(coda) \quad (4.36)$$

Where *coda* is the duration of an event waveform in seconds. Because some stations are affected by high amounts of site noise there is a bias in the coda's ending time value for each station. This station noise may cause the coda length to decrease, and will affect the duration magnitude calculations. The mean of all stations' duration magnitudes is what is listed as the event duration magnitude.

4.3.2 Local Magnitude

Events were assigned a local magnitude based on the (Richter, 1935) method

$$M_L = \log(A) - \log(A_0) + S \quad (4.37)$$

where A is zero-to-peak amplitude (in mm) of the horizontal component on a standard Wood-Anderson(WA) seismometer, $-\log(A_0)$ is the distance-correction function that reflects the overall attenuation attributes in the region of interest, and S is the station correction defined relative to a reference site condition. Within this study, $-\log(A_0)$ is defined such that 10 mm of amplitude on a WA instrument located at a reference site at 17 km away from an event yields a magnitude 3 event. Additionally, this scale was not calibrated for site correction implying a factor of zero for S. The distance-correction function, as calculated by Bockholt (2015) for the Eastern Tennessee Seismic Zone, used for this study was

$$-\log_{10}(A_0) = 0.538 \log_{10}(r/17) - 0.0002516(r - 17) + 2.0 \quad (4.38)$$

where A_0 is the maximum horizontal trace amplitude measured in millimeters and r is the hypocentral distance measured in kilometers.

For a local magnitude calculation to reliably estimate the magnitude, there must be proper station coverage within, at least, one full quadrant of the event's focal mechanism to properly sample the radiation pattern. This concept is illustrated by examining the idealized body wave radiation pattern of a vertical strike-slip fault (Figure 30) where C = compressional motion and T = tensional motion. An idealized radiation pattern for the vertical strike-slip fault is shown in Figure 31. If there are enough stations to adequately sample a quadrant of a focal mechanism then the median value of all of the amplitudes measured within the quadrant will serve as an accurate local magnitude measurement.

4.3.3 Moment Magnitude

The moment magnitude, M_w , is directly related to the seismic moment, M_0 (Nm). M_0 is directly proportional to the low-frequency plateau of the Fourier transform of a one second window around the S-Wave arrival of an earthquake and is estimated by minimizing the best fit between observed and synthetic spectral amplitudes. The M_w is determined using a best fit method as discussed in the synthetic source modeling section (4.2.3).

Table 1- EK MMP Seismic Station Information. Temporary stations installed for the project and existing stations are shown.

Station Name	Latitude (Decimal Degrees)	Longitude (Decimal Degrees)	Instrument	Digitizer	Installation Type	Installation Date
EK12	38.12870	-83.1042	Trillium 40	Taurus	Vault	9/30/2015
EK13	38.23010	-82.8286	Trillium 40	Taurus	Vault	10/19/2015
EK14	38.29963	-82.7037	Trillium Compact Posthole	Centaur	Posthole	6/3/2015
EK20	37.73320	-83.8661	Trillium 40	Taurus	Vault	11/6/2015
EK21	37.81595	-83.5315	Meridian Compact Posthole	N/A	Posthole	9/2/2015
EK22	37.91525	-83.2507	Meridian Compact Posthole	N/A	Posthole	8/25/2015
EK23	37.92127	-82.9004	Trillium 40	Taurus	Vault	9/29/2015
EK25	38.13583	-82.8145	Trillium Compact Posthole	Centaur	Direct Burial	6/10/2015
EK26	38.07035	-82.5810	Trillium Compact Posthole	Centaur	Posthole	6/4/2015
EK32	37.61982	-83.3024	Meridian Compact Posthole	N/A	Posthole	9/2/2015
EK33	37.75818	-83.1249	Trillium 40	Taurus	Vault	11/4/2015
EK34	37.70558	-82.7495	Trillium 40	Taurus	Vault	6/9/2015
EK35	37.85687	-82.7147	Trillium Compact Posthole	Centaur	Direct Burial	6/6/2016
S51A	37.63920	-83.5935	Part of adopted Transportable Array (TA) from Earthscope Project. Three-component, broadband seismometer			
PKKY	38.383	-83.034	Stations from the Kentucky Seismic and Strong-Motion Network (KSSMN). Vertical component only. Short period seismometers.			
ROKY	37.909	-83.926				

Table 2 - Relative Bandwidth Factors (RBW) for typical octave bandpass filters

Octaves	RBW
1	$0.707 \cdot f_o$
2/3	$0.466 \cdot f_o$
1/2	$0.348 \cdot f_o$
1/3	$0.232 \cdot f_o$

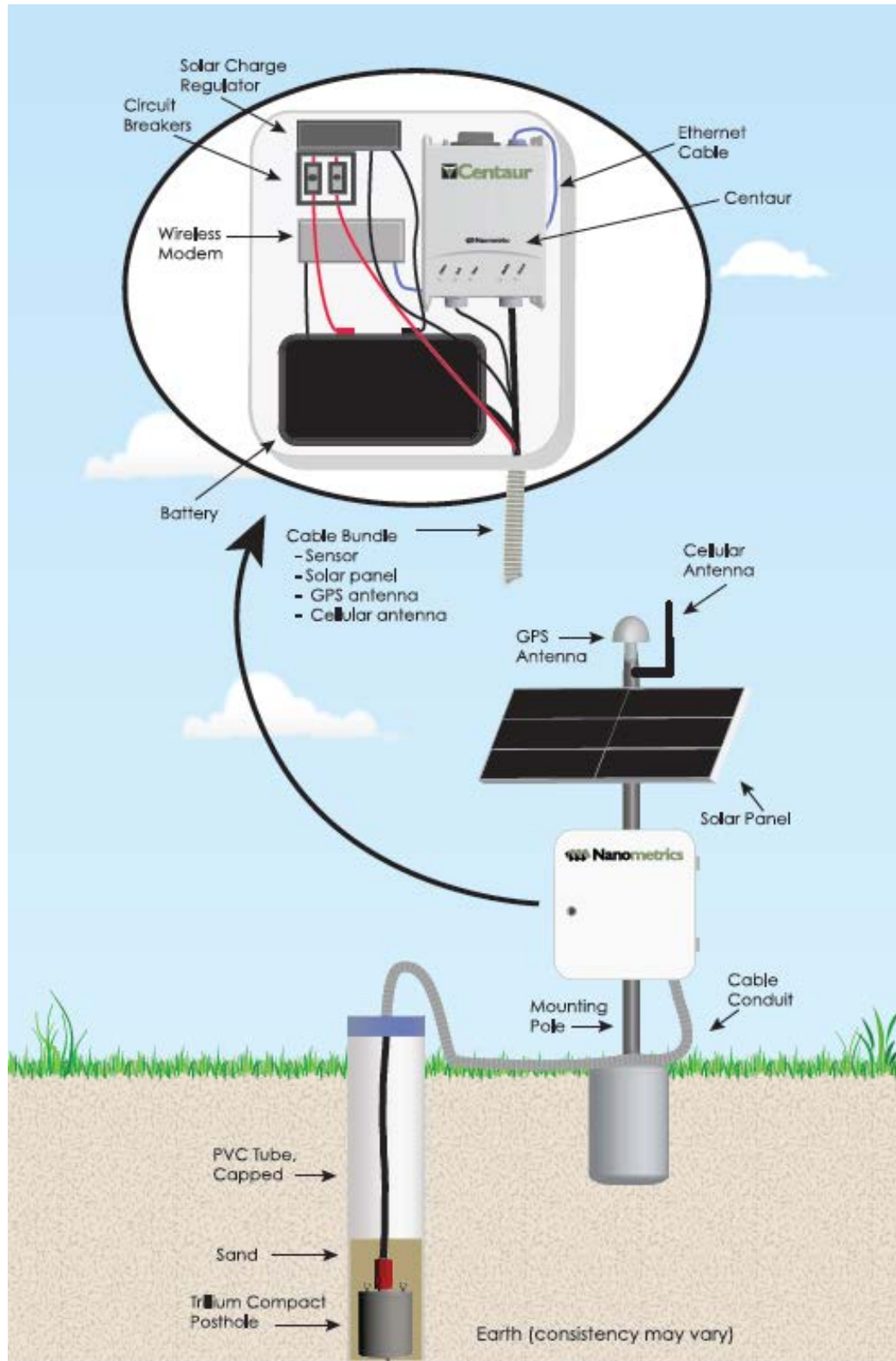


Figure 20 - Idealized seismic station posthole installation (from Nanometrics, Inc., 2017)

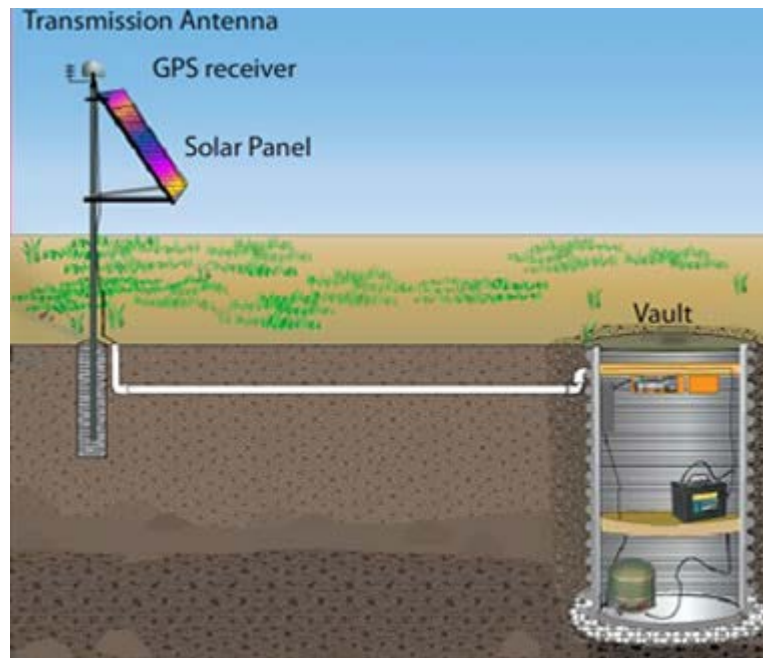


Figure 21 - An idealized vault-style installation. Batteries and cellular modem were kept in an equipment box that was either attached to the mounting pole or in a waterproof case on the ground near the solar panel. (from IRIS, 2017)

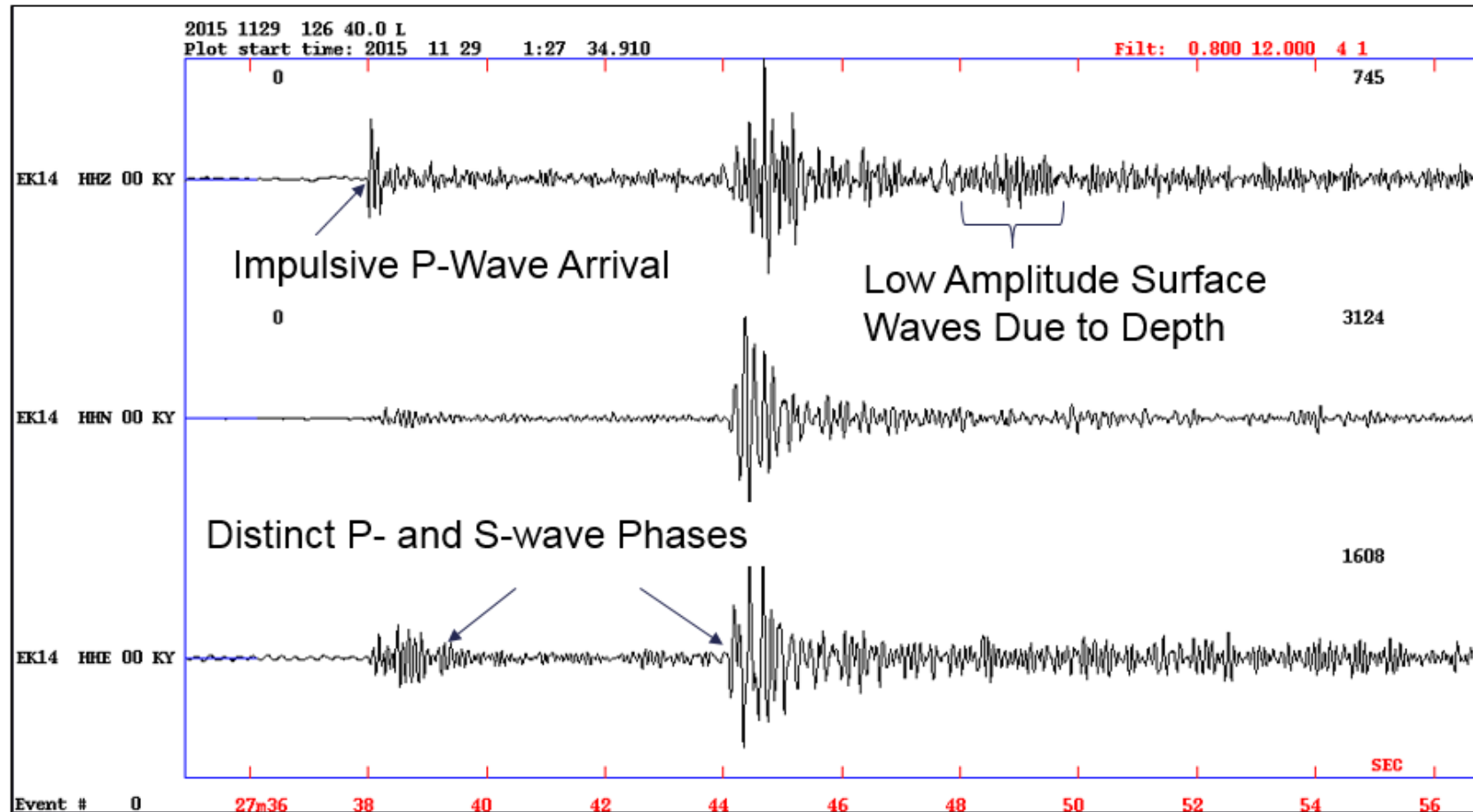


Figure 22 - Example of event location using EK32 from the EKMMP network. An impulsive P-wave arrival is marked on the Vertical component (HHZ) and the emergent S-wave arrival is marked on the East component (HHE). Signals are filtered by a band-pass filter from 0.8-12 Hz.

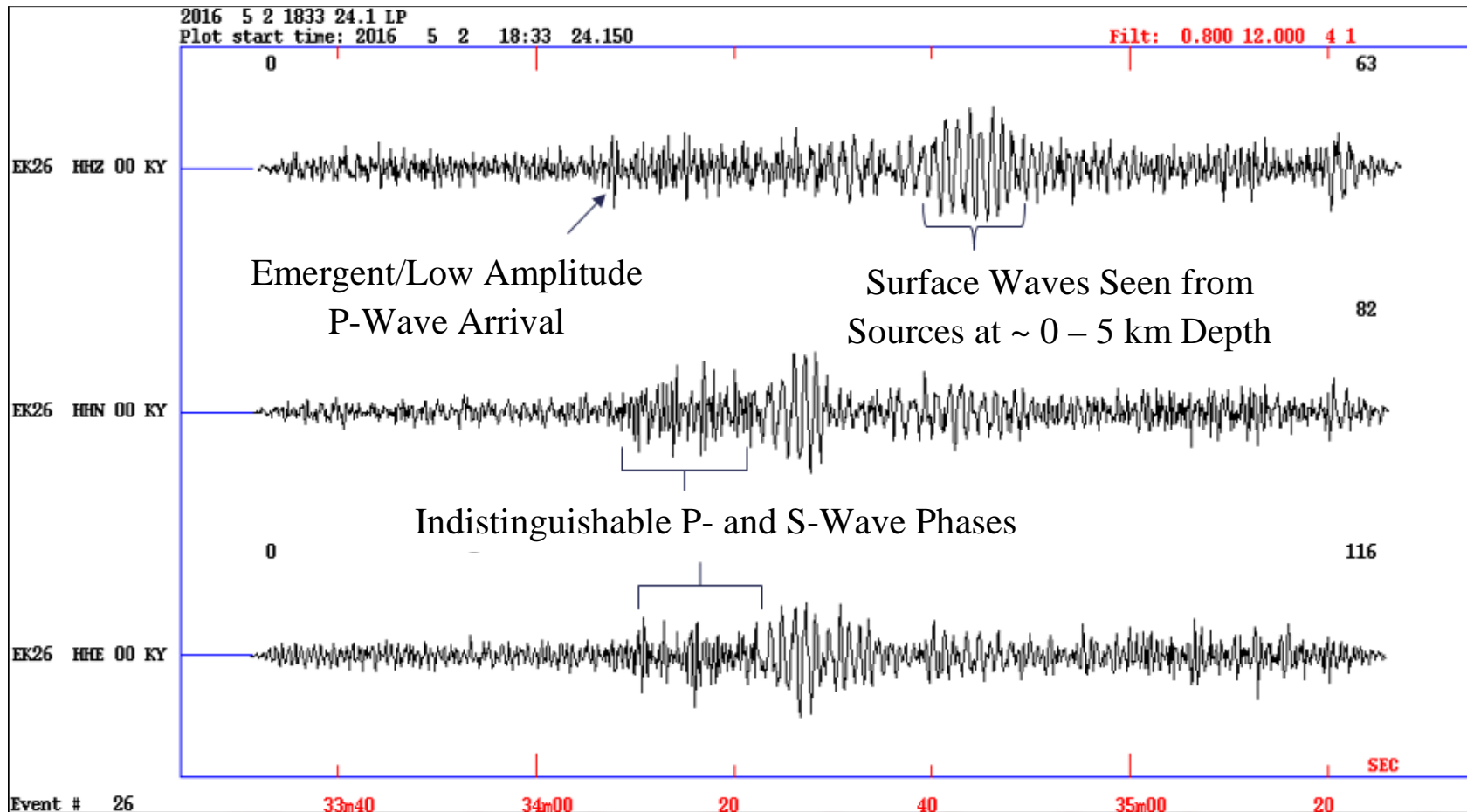


Figure 23 Seismic waveform of a blast at the broadband seismometer, EK22. The vertical (HHZ) and horizontal (HHN, HHE) components are shown. Because of the nature of the waveform of a blast, the P-wave arrival can hardly be seen at around 35 seconds on the vertical channel. The surface waves, the long-period waves seen in the latter part of the wavetrain on all three channels, are much larger than surface waves seen from a deep earthquake.

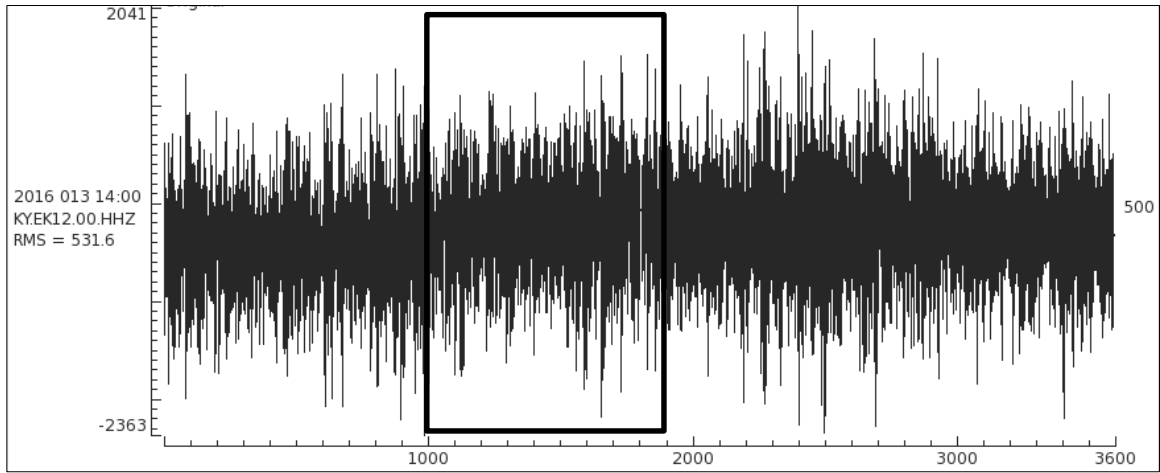


Figure 24 – One hour of continuous data taken from the vertical component of the EK12 station. The black rectangle shows a data window used for a PDF PSD calculated over 15 minutes as in Figure 25.

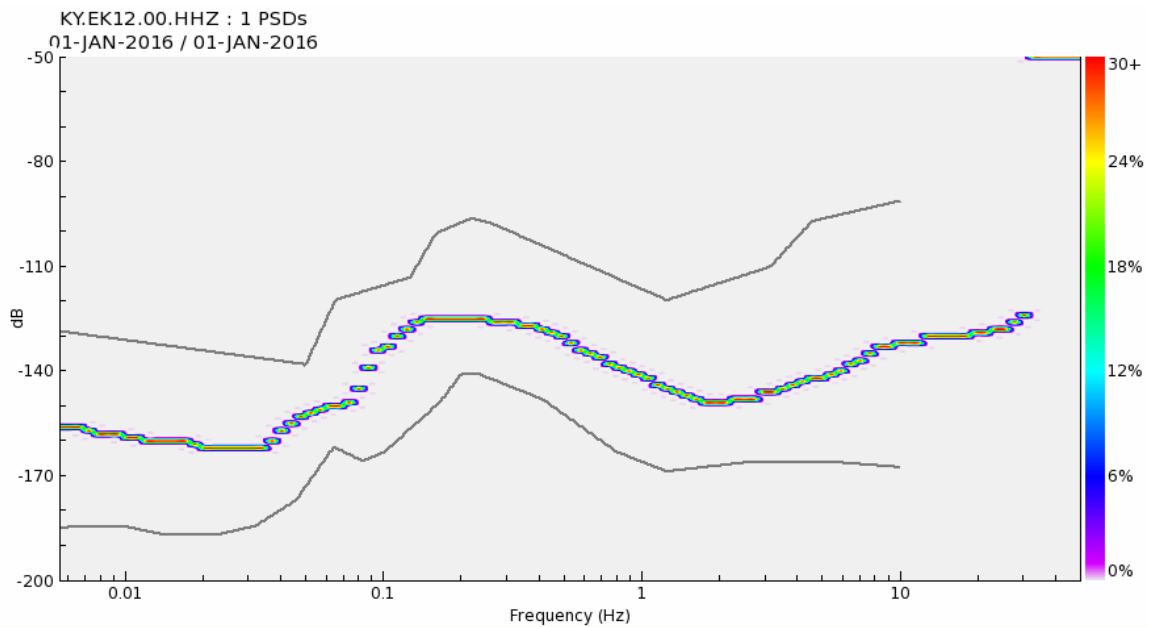


Figure 25 – A PSD estimate of 15 minutes of continuous waveform data.

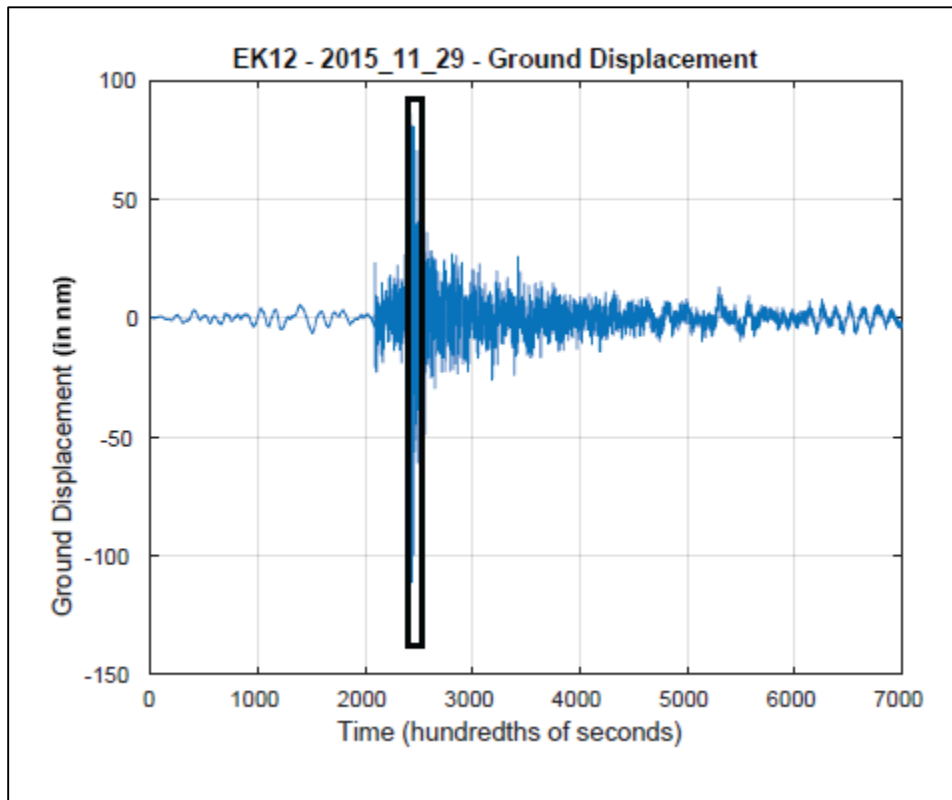


Figure 26 – Vertical component ground displacement waveform of an earthquake. The black rectangle delineates the 1 second of data around the S-wave arrival

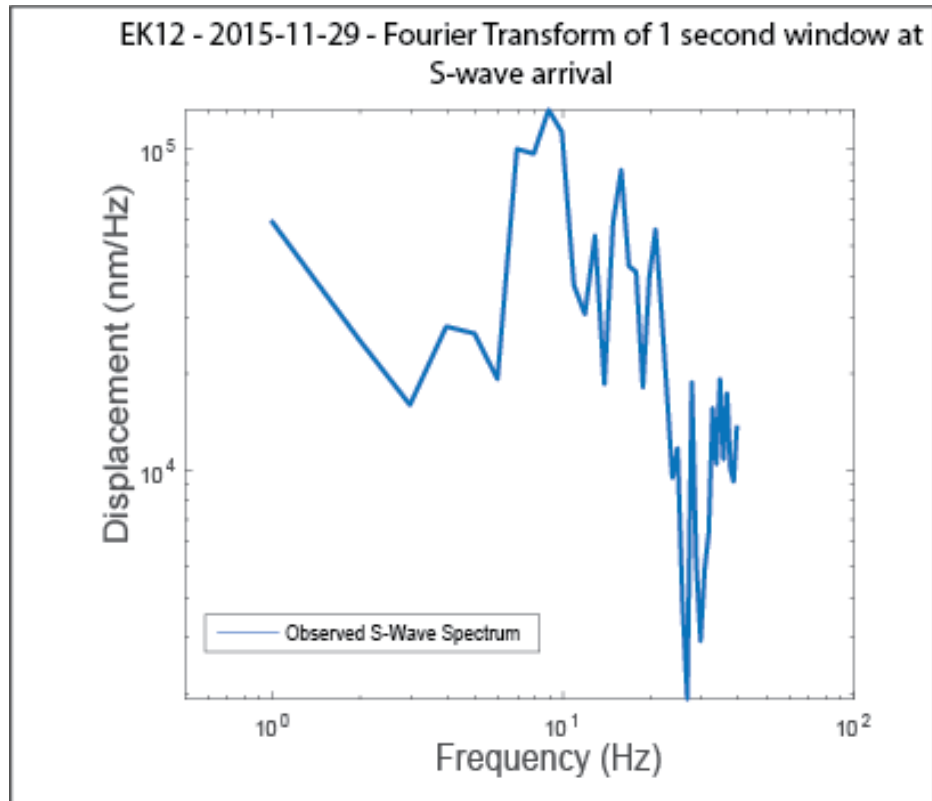


Figure 27 - A Fast Fourier Transform of one second of 0.8 Hz high-pass filtered, ground displacement data starting at the onset of S-wave of the earthquake.

Hamburg Model [Hermann-Ammon (1997)]

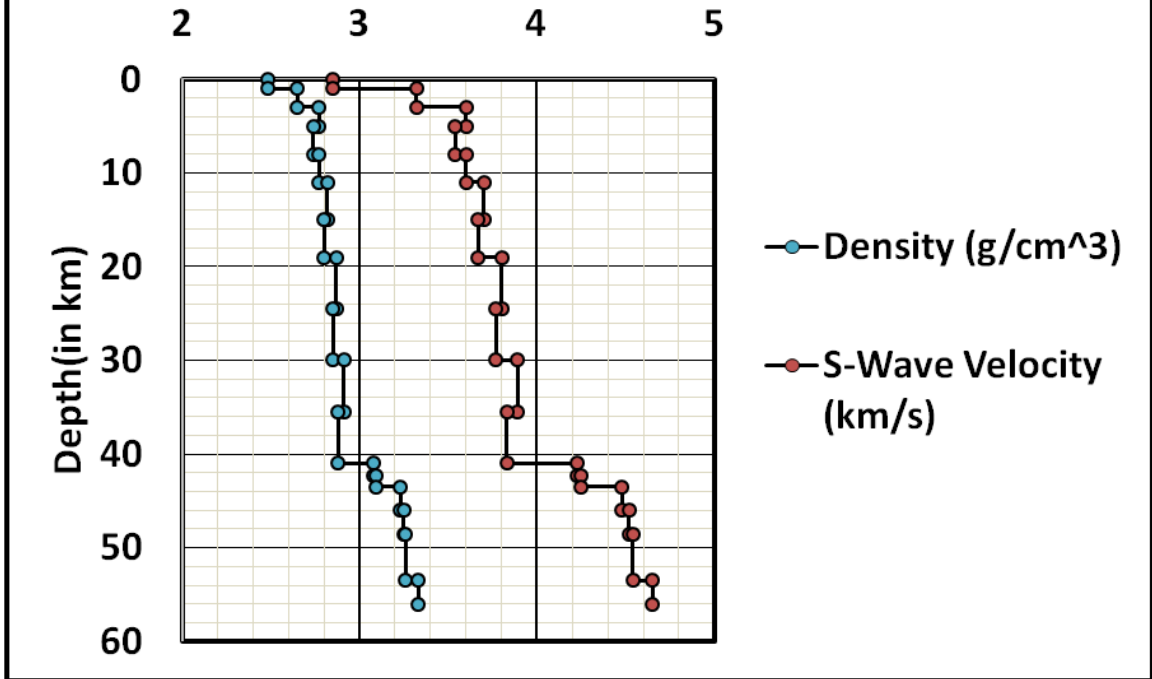


Figure 28 - Hamburg Velocity-Density Model (Herrmann, 1997)

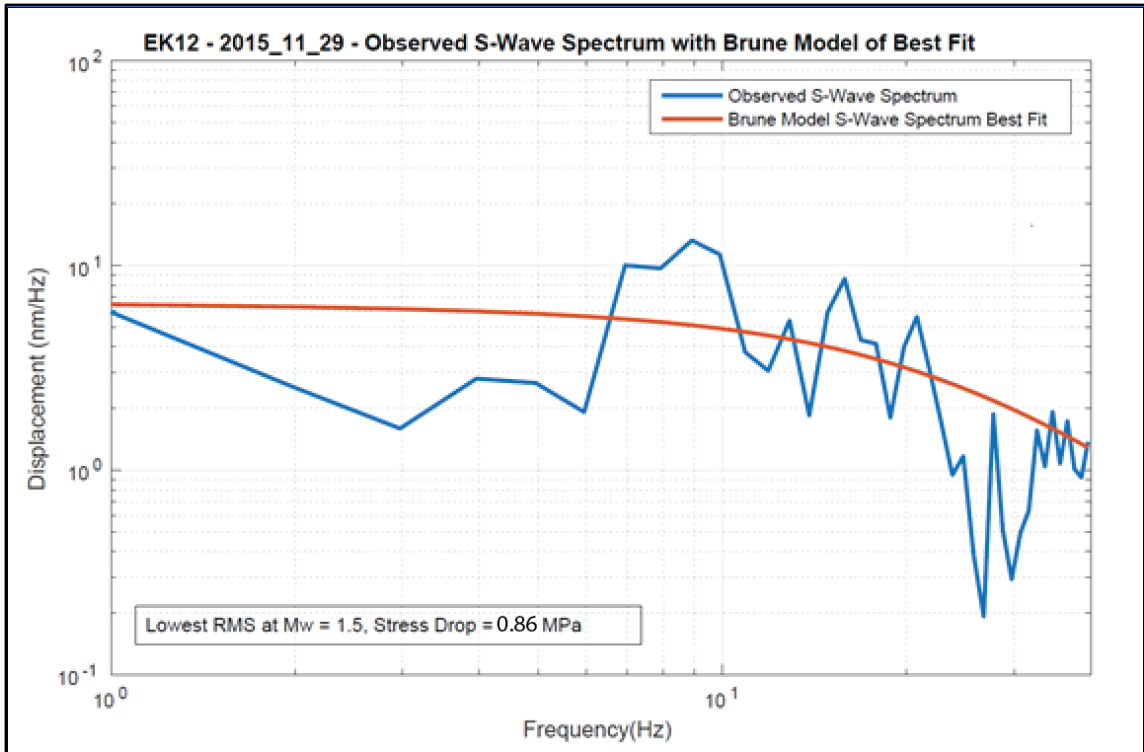


Figure 29 - Displacement spectrum using Boatwright (1980) high-spectrum fall-off constants overlain on top of 1 second of data around S-wave onset of earthquake.

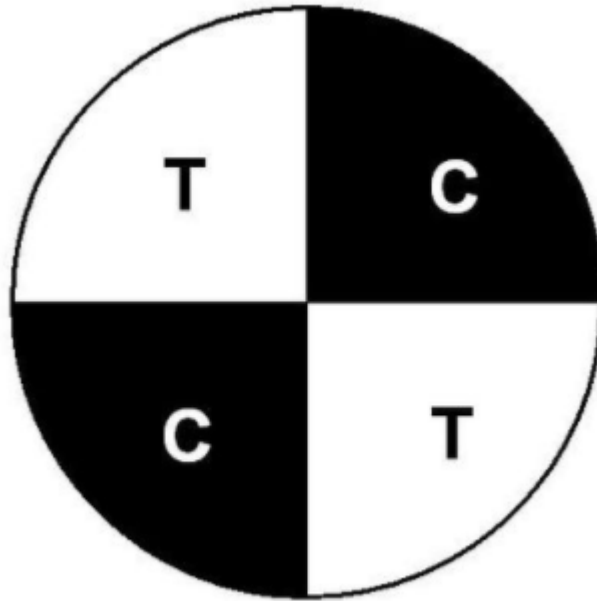


Figure 30 – A schematic of a focal mechanism for a vertical strike-slip fault. C = Compressional motion, T = Tensional motion

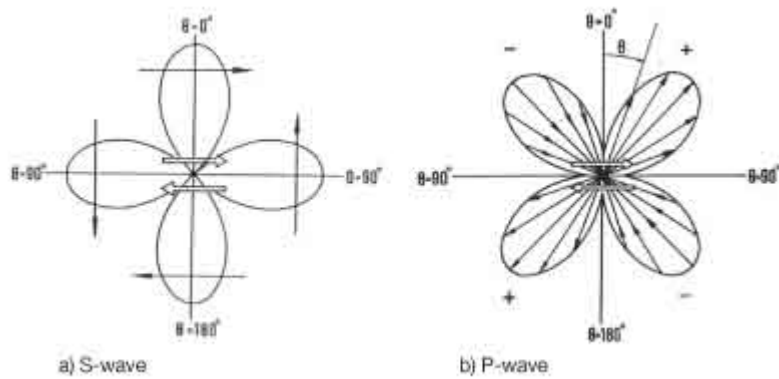


Figure 31 - Idealized radiation pattern of an a) S-wave and a b) P-wave. After (Aki K. R., 1980)

Chapter 5 Results and Discussion

5.1 Minimum Network Detection Threshold

A method of determining the EKMMP network's minimum detection threshold was estimated for daytime hours (0000-1100 UTC) and nighttime hours (1100-2300 UTC). The maps resulting from this analysis estimate the minimum magnitude at which a "trigger" file is created for manual analysis. These data are presented in the form of daytime and nighttime contour maps overlain on a map of active deep oil and gas wells, local (<25 km) earthquakes recorded between June 2015 and July 2016, Class II wastewater injection wells, seismic stations and the boundaries of Rome Trough (Figures 32 and 33). With few exceptions, the maps show the effectiveness of the network's seismic station locations in providing the smallest minimum detectable magnitude around areas of active wastewater injection and production wells. While the contours for both maps generally mimic the network layout and density, both contain regions that deviate from the expected minimum detectable magnitude.

The daytime detection threshold map (Figure 32) shows five crescent-shaped areas capable of detecting a Mw 0.7; however, the majority of the network area has a detectable threshold between Mw 0.8 and 0.9. Figure 34 highlights three features of the daytime contour map that deviate from the expected minimum detectable magnitude contours. The northernmost ellipse surrounds the station PKKY. The Mw 0.9 contours do not resolve this station as well as other stations along the outer edges, such as those in the western part of the network. This is likely due to high site noise during these hours, and the nature of the short-period seismometer's detection capability at this station. The frequency response and PSD PDF site noise measurements for station PKKY are shown

in Figures 35 and 36, respectively. This station is relatively less sensitive to frequencies outside of the 1-10 Hz bandwidth (i.e., it has corner frequencies at 1 and 10 Hz), thus is not as effective in lowering the minimum detectable magnitude as a broadband seismometer under similar conditions. For comparison, the instrument frequency response for the relatively low-noise broadband station, EK22, and its site noise for the nighttime hours in January are shown in Figures 37 and 38, respectively. The median noise measurements between 1 and 20 Hz are the most important differences, because these median noise measurements were used for the detection threshold signal-to-noise ratios.

The easternmost ellipse is an area around EK26 with a higher detection threshold relative to other stations within the network. This is a broadband sensor marked by high ambient noise, -115 dB between ~6 and 13 Hz, which is within the bandwidth of wave frequencies produced by local earthquakes (i.e., 1-20 Hz). Analogously, EK14, a station that also has high noise levels relative to the rest of the network, has an average noise level of -130 dB within the same bandwidth (Appendix C).

The southernmost ellipse, surrounding station EK34, is also marked by high ambient noise issues. EK34's noise measurements were taken in July during its first full month of recording since installation on June 6, 2016. EK34 has a noise measurement of approximately -110 dB between 10 and 20 Hz. Although the EK34 site has high noise levels in this bandwidth range, it is consistently noisy exhibiting little to no diurnal variation (~3 - 5 dB increase from daytime to nighttime) compared to an average of 10 to 20 dB increase for most stations in the network. Because the triggering mechanism is based on a four station location, it is necessary consider all of the nearby station noise

measurements. Analysis of the four closest stations shows that EK33 has the largest diurnal variation with an increase of ~15 dB from nighttime to daytime. This effectively creates a three station detection in this area at lower magnitudes, which will not initiate an event within the algorithm. The nighttime map shows a significantly different contour set in this area because of the changes in noise at EK33. The large changes in noise are most likely due to the proximity of this station to the construction of a four lane highway taking place ~4 km SSE of the station.

The nighttime minimum detection threshold map shows a small crescent-shaped area having a minimum detectable magnitude of Mw 0.4, with the remaining network area able to detect between Mw 0.5 and 0.6 (Figure 33). This area lies outside of the areas of concentration that were intended to have the lowest detectable magnitude. Figure 39 highlights four features of the nighttime contour map that deviate from the hypothesized minimum detectable map contours.

The northernmost ellipse surrounds station PKKY which does not have as much effect on the detection threshold as other stations. Because PKKY is a short-period seismometer, the aforementioned detection capability issues that exist in the daytime, also exist at night.

The northeasternmost ellipse surrounds an area of high station density that deviates from a expected area of lowest detectable minimum magnitude for the network. During the daytime this ellipse surrounds an area representing a detection threshold that is the lowest in the network (Mw 0.6), but at night it is a Mw 0.6 when the lowest detectable magnitude for the network is a Mw 0.4. The difference is due to the sources of

noise at stations EK14 and EK26 that exhibit little to no diurnal variation. The noise that is within the passband of interest does not change between night and day as does most cultural noise. These constant sources of noise could also be responsible for a smaller than expected change in the minimum detectable magnitude between day and night relative to other areas of the map.

The southeasternmost ellipse surrounding EK34 highlights an area that is highly affected by cultural noise differences between the day and night hours. In the daytime, the detection threshold is hardly affected by the presence of EK34, but at night the detection threshold is significantly altered due to its presence. As discussed earlier, because a four station triggering algorithm is used for the detection threshold, it is necessary to consider the noise of the four closest stations to this area and how their noise varies diurnally. The noise levels at EK34, EK23, and EK35 do not exhibit significant diurnal variations (~3-5 dB), but the noise at EK33 is drastically lower (~15 dB). The large changes in noise at EK33 are, thus, responsible for the low magnitudes that are capable of being detected in the area surrounding EK34.

The westernmost ellipse surrounds a small crescent-shaped area that marks the minimum detectable magnitude of Mw 0.4 for the EKMMP network. This area is surrounded by stations EK21, EK22, EK32, and EK33. Station EK32 has minimal changes of ~3-5 dB between day and night, while EK21 and EK22 have changes varying between 5 and 9 dB. The significant variability between EK21 and EK22 along with the large (~15 dB) changes observed at EK33 explain the low magnitude detection capability in this area.

5.2 Earthquake Catalog and Associated Discussion

Thirty-eight local and regional earthquakes were detected by the EKMMP network (Table 3, Figure 40) between June 2015 and July 2016. Twelve of these events were located within 100 km of the network and were categorized as local earthquakes. Sixteen earthquakes were not reported by the American National Seismic System used by the United States Geological Survey. Of the sixteen events not reported by the USGS, six were local (<100km from the EKMMP network) and ten were regional (>100km). No local events can be attributed to anthropogenic activity related to oil and gas operations. Furthermore, no events occurred within the Rome Trough of eastern Kentucky. Four earthquakes (1.9-2.5 M_D) were detected ~17 km WSW of Cadiz, OH, three of which were not reported by the USGS. This earthquake cluster has been spatially correlated to nearby oil and gas operations but has not been temporally related to any oil and gas operations. As such, it has only been noted as an area of interest for further research.

5.3 Magnitude

Duration magnitudes have been calculated for all 38 events detected by the EKMMP. Local magnitudes were calculated for all local events and are listed in Table 4 along with their respective median absolute deviations, and moment and duration magnitudes. All amplitude measurements used for local magnitude calculations can be found in Appendix D. Because no events were detected within the Rome Trough, the network was unable to fully surround any events rendering it unlikely to obtain adequate station coverage to be absolutely certain of proper amplitude sampling of an event's radiation pattern. Focal mechanisms for local events have yet to be determined and, thus, the station coverage needed to obtain an accurate local magnitude (i.e., sampling of at

least one full quadrant of an event's radiation pattern) for most events is uncertain. The three events closest to the network (Events 16, 19, and 29 (Table 3)) have station coverage between $\sim 90^\circ$ and 180° of the surface area southeast of the event. This may be adequate to sample at least one radiation pattern quadrant depending on the actual focal mechanism of the event.

Tables 5 through 8 list Brune (1970) and Boatwright (1980) spectral models that were used to minimize misfit to determine moment magnitudes. Because the Boatwright models have a lower residual value, they are listed as the moment magnitude in Table 4.

Table 3 - Local and Regional Seismicity Detected by the EKMMP. Events not reported by the USGS ANSS Network highlighted in yellow. M_D is Duration Magnitude.

Event	Date(mm/dd/yyyy)	Time(UTC)	Lat. (°N)	Lon. (°E)	Depth (km)	M_D
1	6/11/2015	4:40	38.742	-80.771	15	2.3
2	6/15/2015	14:28	36.511	-83.936	21.2	2.2
3	6/16/2015	4:37	37.108	-80.863	1.4	2.6
4	6/27/2015	7:16	38.634	-82.917	3.5	1.3
5	7/3/2015	5:20	36.867	-83.729	22.5	1.3
6	7/10/2015	6:09	38.981	-81.93	29.5	1.5
7	7/21/2015	3:10	36.462	-83.748	11.7	2.8
8	7/27/2015	7:37	36.039	-83.675	20.7	1.6
9	8/20/2015	2:45	37.999	-84.836	34.6	2.8
10	9/10/2015	23:27	40.211	-81.184	5.6	1.9
11	9/12/2015	4:12	40.225	-81.183	6.1	2
12	9/30/2015	3:34	40.214	-81.169	3.8	2.5
13	10/1/2015	7:25	40.206	-81.167	1.4	2.1
14	10/6/2015	2:52	38.28	-85.272	2	3.1
15	10/18/2015	7:24	38.725	-82.555	0.1	1.6
16	11/29/2015	1:27	38.235	-83.223	21.8	2.1
17	12/13/2015	00:41	38.674	-83.99	4.8	1.7
18	12/13/2015	10:38	36.692	-83.744	3.1	2.6
19	12/22/2015	15:20	38.26	-83.417	0.83	1.6
20	1/4/2016	11:15	36.491	-84.015	23.1	2.8
21	2/2/2016	8:09	38.335	-84.392	34	1.3
22	2/20/2016	9:24	36.188	-83.332	0	2.5
23	2/24/2016	3:30	38.535	-83.84	4.8	1.8
24	2/25/2016	11:37	37.648	-80.323	9.76	2.3
25	3/1/2016	2:38	35.981	-82.365	7.7	2.5
26	3/8/2016	14:25	38.911	-82.443	18.4	2
27	4/19/2016	8:35	35.597	-84.431	9	2.4
28	4/25/2016	14:43	35.753	-82.572	4.3	2.5
29	4/26/2015	19:24	38.123	-83.51	3.48	2.1
30	5/8/2016	9:09	36.115	-83.779	15	3
31	5/8/2016	11:04	36.118	-83.777	10	2.4
32	5/8/2016	11:26	36.119	-83.775	20	2.3
33	5/8/2016	23:17	39.029	-81.43	25	2.2
34	5/15/2016	16:48	38.445	-80.859	0	2.1
35	5/18/2016	15:10	39.403	-81.396	4.9	2.7
36	5/20/2016	14:11	36.298	-83.72	21.5	2.1
37	5/27/2016	6:04	38.789	-82.426	12.3	1.2
38	7/6/2016	9:00	37.196	-81.855	4.1	

Table 4 - Local events (<100 km) detected by the EKMMP. Events highlighted in yellow are not reported by the USGS. M_L MAD is an abbreviation for Median Absolute Deviation of the local magnitude calculations

Local (<100 km) Events Detected by the EKMMP								
Date (mm/dd/yyyy)	Origin Time(UTC)	Latitude (Decimal Degrees)	Longitude (Decimal Degrees)	Depth(km)	M _D	M _L	M _L MAD	M _w
6/27/2015	7:16:25	38.634	-82.917	3.5	1.3	1.2	0.16	
7/3/2015	5:20:53	36.867	-83.729	22.5	1.3	2.3	0.12	
8/20/2015	2:45:41	37.999	-84.836	34.6	2.8	1.2	0.25	
10/18/2015	7:24:11	38.725	-82.555	0.1	1.6	1.9	0.12	
11/29/2015	1:27:30	38.235	-83.223	21.8	2.1	1.1	0.15	1.5
12/13/2015	0:41:18	38.674	-83.990	4.8	1.7	1.9	0.10	
12/22/2015	15:20:33	38.260	-83.417	0.8	1.6	1.3	0.21	1.3
2/2/2016	8:09:03	38.335	-84.392	34.0	1.3	1.6	0.19	
2/24/2016	3:30:05	38.535	-83.840	4.8	1.8	1.8	0.19	
3/8/2016	14:25:29	38.911	-82.443	18.4	2.0	1.8	0.11	
4/26/2016	19:24:04	38.123	-83.510	3.5	2.1	1.1	0.18	
5/27/2016	6:04:18	38.789	-82.426	12.3	1.2		0.06	

Table 5- Boatwright model spectral magnitude calculation values for Event 16 (Labeled in Table 3).

Station Name	Residual(nm/Hz)	Mw	Stress Drop (Pascals)	Seismic Moment (Nm)	Fault Radius (m)	Corner Frequency (Hz)
EK12	2.56	1.5	8.60E+05	2.19E+11	48.10	15.72
EK13	0.57	1.3	1.70E+05	1.10E+11	65.59	11.53
EK23	0.50	1.5	4.60E+04	2.19E+11	127.67	5.92
EK22	0.36	1.2	1.36E+06	7.76E+10	29.23	25.86
EK25	0.38	1.6	2.10E+05	3.09E+11	86.35	8.76
Median	0.50	1.5	2.10E+05	2.19E+11	65.59	11.53

74

Table 6- Boatwright Spectral magnitude calculation values for Event 19 (Labeled in Table 3).

Station Name	Residual(nm/Hz)	Mw	Stress Drop (Pascals)	Seismic Moment (Nm)	Fault Radius (m)	Corner Frequency (Hz)
EK12	3.40	1.4	9.99E+05	1.55E+11	40.78	18.54
EK22	0.62	1.3	9.31E+04	1.10E+11	80.17	9.43
EK13	0.38	1.2	1.04E+05	7.76E+10	68.84	10.98
EK21	0.39	1.2	4.02E+05	7.76E+10	43.87	17.23
EK25	0.34	1.5	1.51E+04	2.19E+11	185.07	4.08
Median	0.39	1.3	1.04E+05	1.10E+11	68.84	10.98

Table 7- Brune spectral magnitude calculation values for Event 16 (Labeled in Table 3)

Station Name	Residual(nm/Hz)	Mw	Stress Drop (Pascals)	Energy Release (N-m)	Fault Radius (m)	Corner Frequency (Hz)
EK12	2.67	1.5	2.34E+06	2.19E+11	34.46	21.94
EK13	0.59	1.3	4.60E+05	1.10E+11	47.07	16.06
EK23	0.52	1.5	1.20E+05	2.19E+11	92.74	8.15
EK22	0.38	1.2	3.50E+06	7.76E+10	21.33	35.44
EK25	0.36	1.6	4.50E+05	3.09E+11	66.98	11.29
Median	0.52	1.5	4.60E+05	2.19E+11	47.07	16.06

75

Table 8- Brune spectral magnitude calculation values for Event 19 (Labeled in Table 3)

Station Name	Residual(nm/Hz)	Mw	Stress Drop (Pascals)	Energy Release (N-m)	Fault Radius (m)	Corner Frequency (Hz)
EK12	3.48	1.5	1.47E+06	2.19E+11	40.23	18.79
EK22	0.58	1.3	2.70E+05	1.10E+11	56.22	13.45
EK13	0.35	1.3	1.00E+05	1.10E+11	78.28	9.66
EK21	0.40	1.2	9.00E+05	7.76E+10	33.54	22.54
EK25	0.34	1.5	2.10E+04	2.19E+11	165.80	4.56
Median	0.40	1.3	2.70E+05	1.10E+11	56.22	13.45

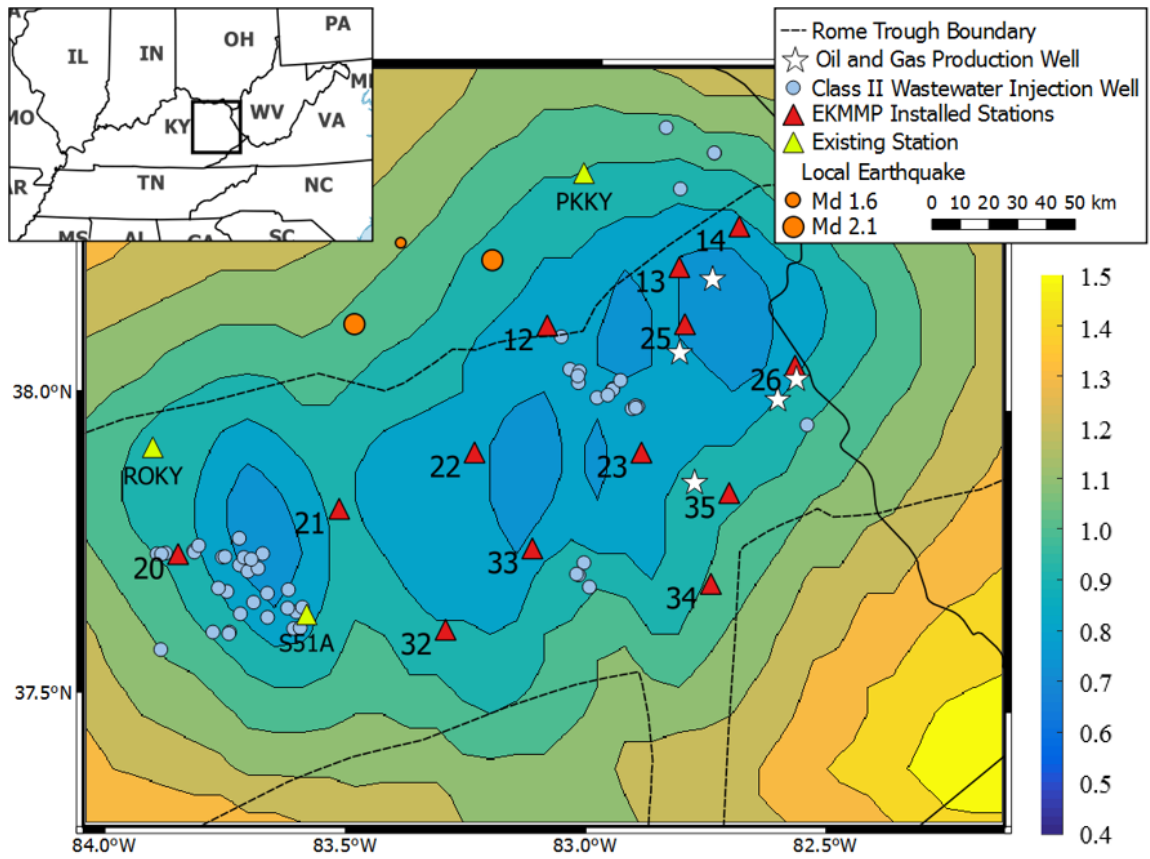


Figure 32 – Daytime (1100-2300 UTC) minimum detection threshold map. The lowest contours seen are Mw 0.7.

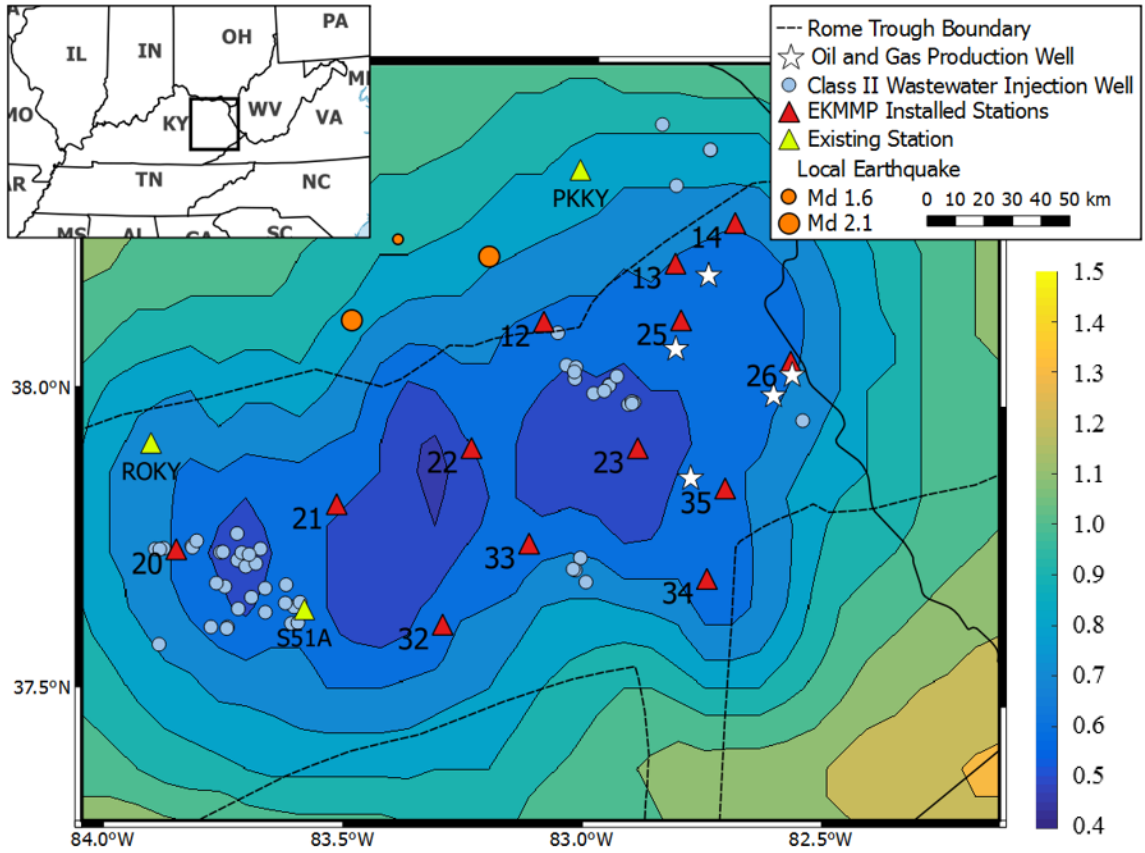


Figure 283 – Nighttime (0000-1100 UTC) minimum detection threshold map. The lowest contours seen are Mw 0.4.

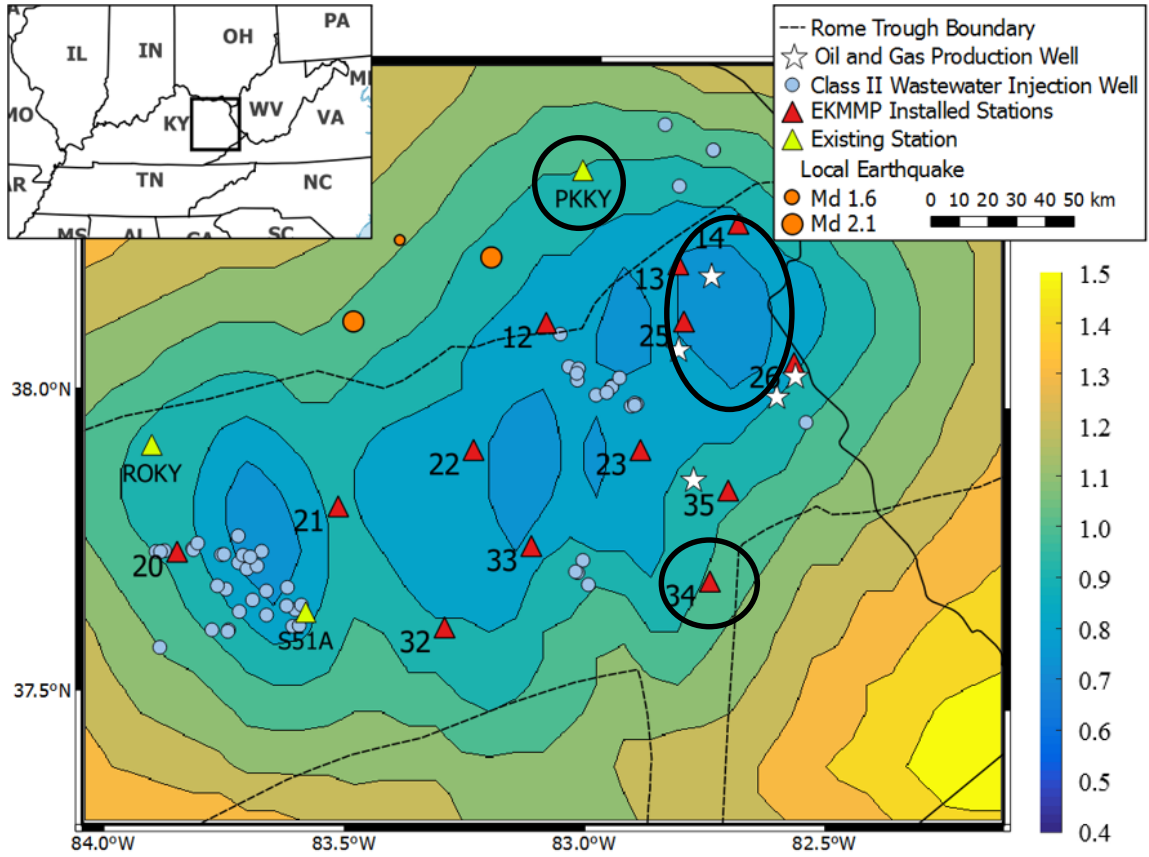


Figure 294 – Daytime (1100-2300 UTC) minimum detection threshold map with features of interest highlighted for purposes of discussion by black ellipses

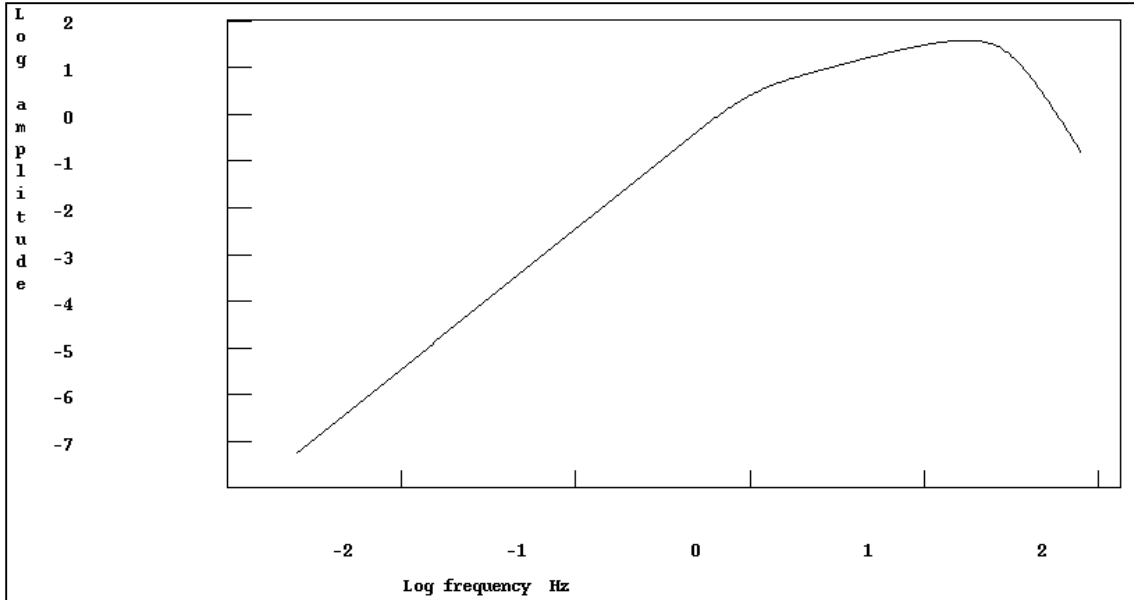


Figure 305 – Frequency response of PKKY, a short-period seismometer. Note the logarithmic axes which show the flat frequency response between 1 second and 10 Hz as a linearly sloped line.

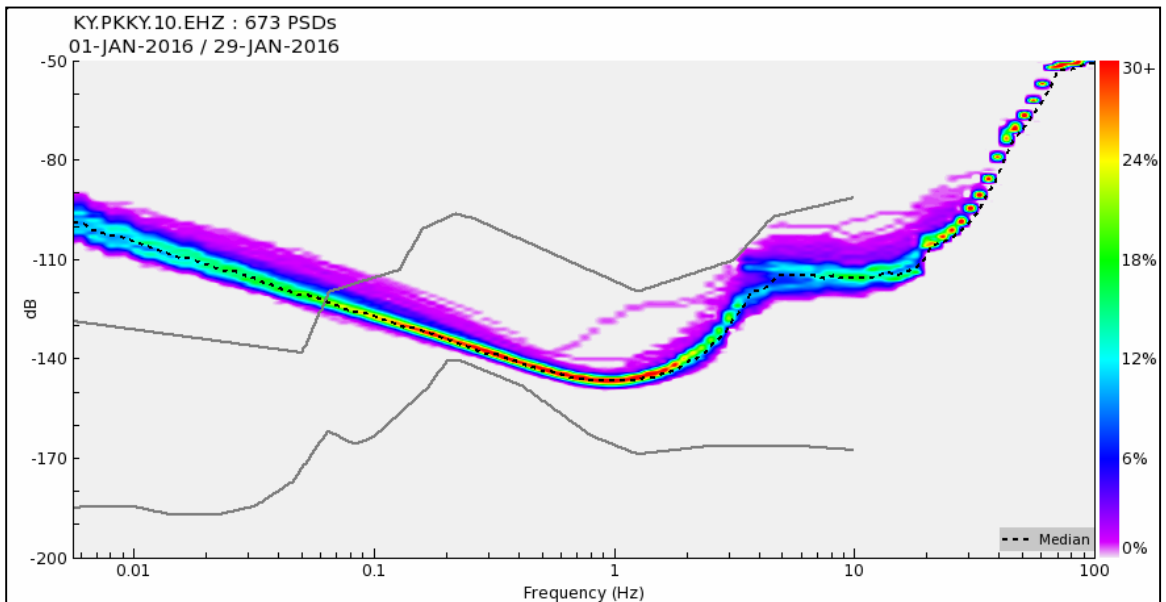


Figure 316 – A PQLX Noise plot of the short-period seismometer, PKKY

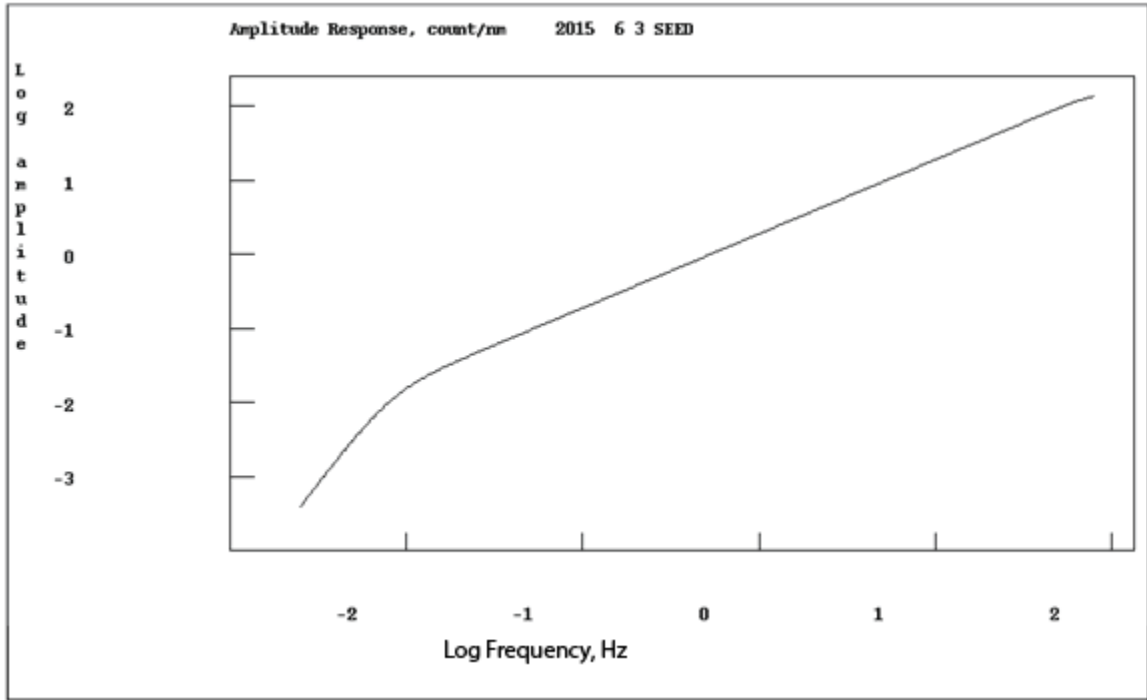


Figure 327 – Frequency response of EK22, a broadband seismometer. Note the logarithmic axes which show the flat frequency response between 100 seconds and 100 Hz as linearly sloped line.

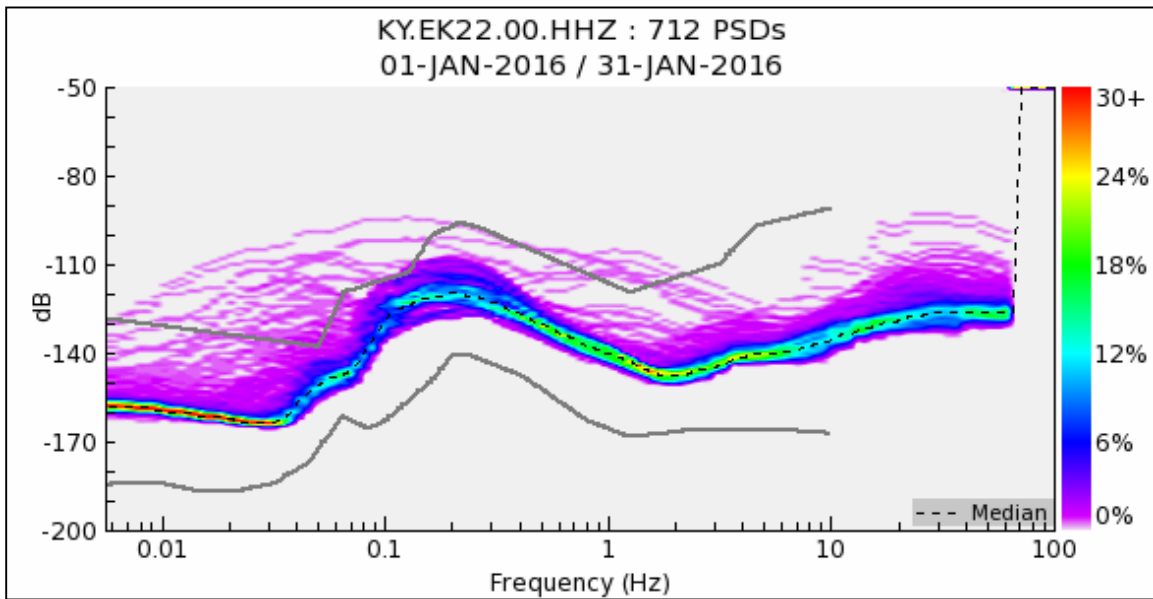


Figure 338 – A PQLX noise plot of the broadband seismometer, EK22

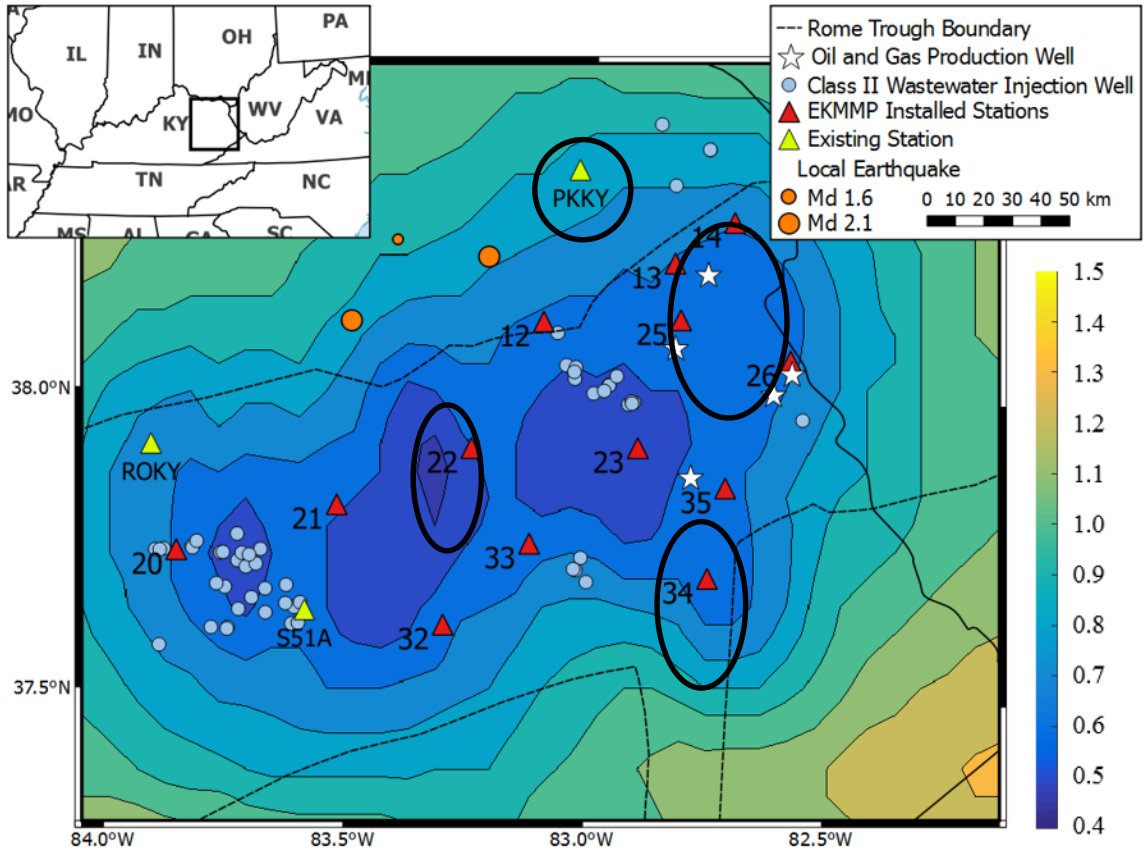


Figure 349 – Minimum detection threshold map for the nighttime hours (0000-1100 UTC) with features of interest highlighted by black ellipses.

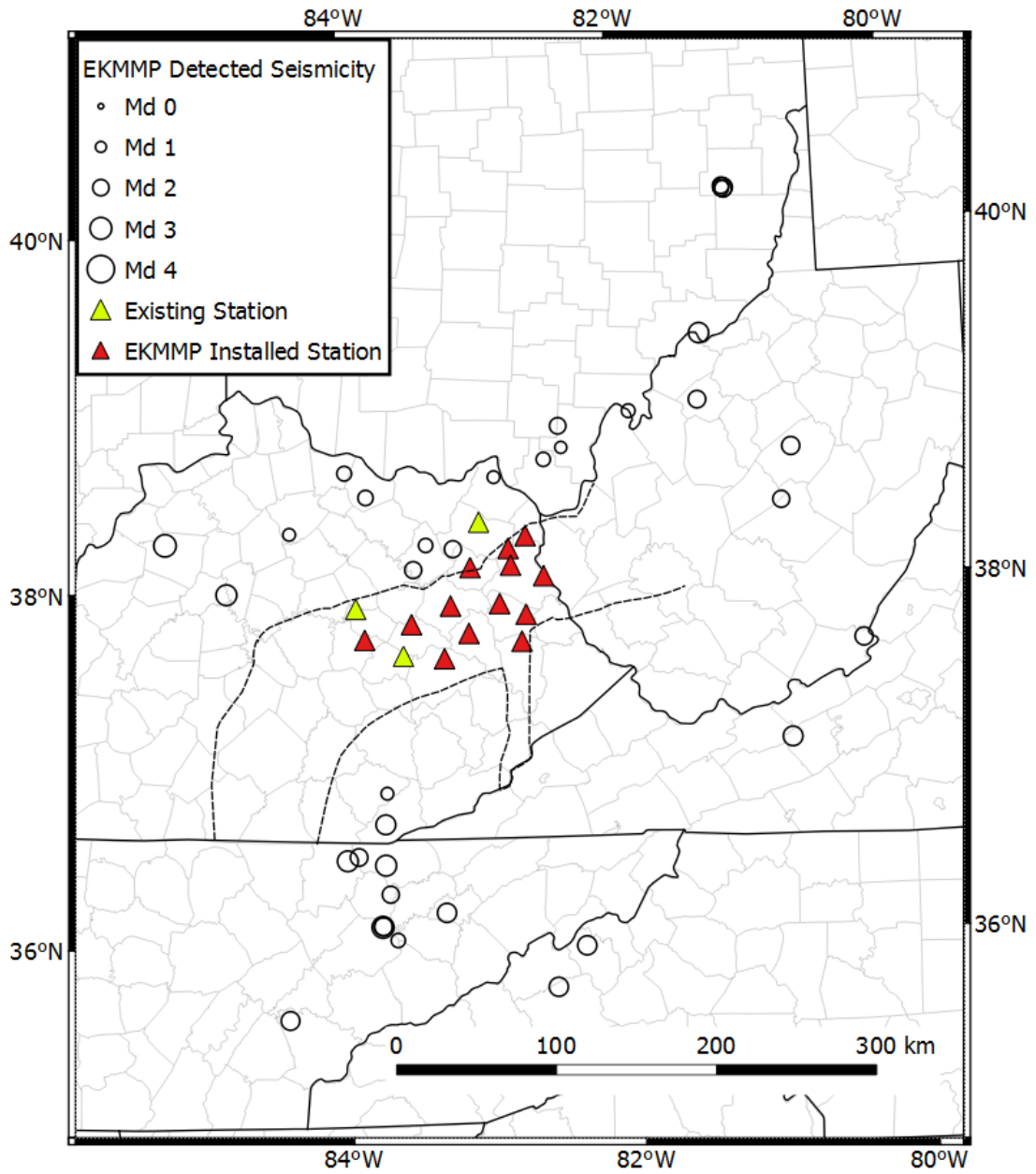


Figure 40 – Map of all local and regional earthquakes detected by the EKMMP network

Chapter 6 Conclusions and Future Research

The main objective for this work was to determine the baseline microseismicity for the Rome Trough at the onset of the development of the Cambrian Rogersville shale which can only be produced using high-volume hydraulic fracturing. This objective was achieved by installing thirteen broadband seismic stations with the highest station density being in areas of Class II wastewater injection wells and active oil and gas production wells. A catalogue of 38 local and regional earthquakes was created from June 2015 to July 2016 with duration magnitudes ranging from M_d 1.2 to 3.1. Further, no earthquakes being proximal to any operating oil and gas or disposal wells. To evaluate the observed microseismicity, the minimum detectable magnitude of the network was estimated for the project area. The minimum detectable magnitude was found to vary spatiotemporally between 0.4 and 0.7 M_w for the nighttime (0000-1100 UTC) and 0.6 to 0.9 M_w for the daytime (1100-2300 UTC).

Although a method was developed in the area that effectively describes the baseline microseismicity, it could be improved using other approaches and/or criteria. Two primary source models were used as the base source models for this project (Brune, 1970) (Boatwright, 1980). As discussed in the methodologies section, the Boatwright(1980) model produces a sharper corner frequency and a faster spectral fall-off rate by changing the constant, γ , to 2. This model also produced lower residuals and was used to create the detection threshold maps. Testing models with other constants could prove to have lower residuals than either of the models used for this paper which would produce a more accurate detection threshold map.

Some stations are known to have high noise within certain passbands that significantly affects an area's detection threshold. Individual site noise characterization studies would yield a more thorough understanding of each site's detection threshold, and collected data would be useful for future installations. Site noise characterization could begin with the creation of a minimum detection threshold map for a 1 station detection (rather than 4) along with spectrograms showing changes in site noise throughout a 24-hour period. Geographic noise distribution plots at different frequencies within the band of interest (1-20 Hz) could also be applied to determine where noise issues are present within the study area.

The detection threshold maps show the EKMMP network minimum detection threshold when each station is running and collecting data with no data transmission latency, and with all stations fully operational for two different ranges of time within the same month. This is an idealized situation because the network rarely ran with all seismometers functioning at 100% efficiency. Many stations would stop collecting data because of flooding or hardware breakdown. Although repairs were made as soon as possible, there are packets of dropped time that may have a significant influence on background measurements. A detection threshold map that shows how data change from month to month due to late installation dates, station outages, and varying noise due to cultural activity would give a more accurate idea of the Rome Trough's minimum detection threshold and background seismicity.

Because focal mechanisms were not calculated for each event, accurate focal mechanism quadrant coverage is not able to be proven. This led to inaccurate local magnitude measurements for a large majority of the events. Focal mechanisms can be

found using surrounding stations and more existing stations surrounding the EK MMP could then be used to calculate more accurate local magnitudes. Station corrections and a network-specific distance-correction attenuation function, both necessary for proper calibration of a local magnitude scale, were also not calculated as could be done for the most accurate local magnitude determination.

Appendix A: Well location Information

Table A. 1 – Wastewater injection wells within the Rome Trough during the time of study

COUNTY	Injection Formation	Top (ft)	Bottom (ft)	Well Latitude	Well Longitude	Formation Age	Status
ELLIOT	WEIR SD	997	1000	38.035	-83.036	Mississippian	Active
ELLIOTT	WEIR SS	770	778	38.0571	-83.055	Mississippian	Inactive
ELLIOTT	WEIR SS	904	958	38.0538	-83.035	Mississippian	Active
ELLIOTT	WEIR SD	746	850	38.1093	-83.074	Mississippian	Active
ELLIOTT	WEIR SD	747	824	38.0466	-83.037	Mississippian	Active
LAWRENCE	WEIR SD	850	932	38.0108	-82.997	Mississippian	Active
LAWRENCE	WEIR SS	912	976	38.0259	-82.968	Mississippian	Active
LAWRENCE	WEIR SD	1102	1164	38.0248	-82.966	Mississippian	Active
LAWRENCE	LEE SANDSTONE	780	798	37.9724	-82.554	Pennsylvanian	Active
LAWRENCE	WEIR SD	881	953	38.0409	-82.948	Mississippian	Active
LAWRENCE	1ST WEIR	665	705	37.9939	-82.922	Mississippian	Active
MAGOFFIN	WEIR SS	1110	1204	37.6962	-83.004	Mississippian	Active
MAGOFFIN	WEIR SD	1178	1206	37.7363	-83.016	Mississippian	Pending
MAGOFFIN	WEIR SS	1275	1317	37.7158	-83.027	Mississippian	Active
MAGOFFIN	WEIR SS	1194	1442	37.7173	-83.031	Mississippian	Active

Table A. 1 continued

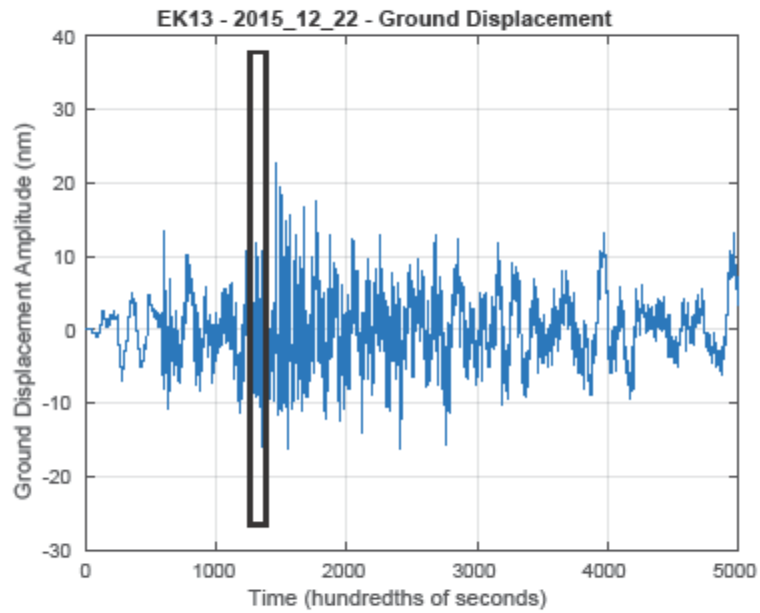
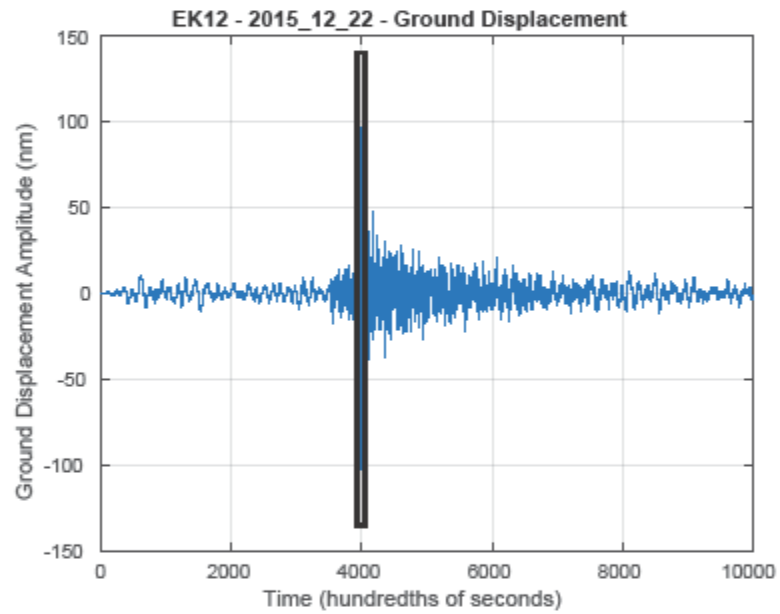
COUNTY	Injection Formation	Top (ft)	Bottom (ft)	Well Latitude	Well Longitude	Formation Age	Status
ESTILL	CORNIFEROUS	753	786	37.7179	-83.7367	Silurian	Inactive
ESTILL	KNOX GP	1500	2600	37.7327	-83.9104	Ordovician	Active
ESTILL	KNOX GP	1515	2632	37.7344	-83.8922	Ordovician	Active
ESTILL	KNOX GP	964	3163	37.5739	-83.8961	Ordovician	Active
LEE	CORNIFEROUS	1206	1236	37.6725	-83.6771	Silurian	Inactive
LEE	CORNIFEROUS	1114	1122	37.6054	-83.7878	Silurian	Active
LEE	LOCKPORT DOL	980	1000	37.6430	-83.6151	Silurian	Active
LEE	LOCKPORT DOL	847	873	37.7083	-83.7193	Silurian	Active
LEE	1ST CORNIFEROUS	1090	1100	37.6063	-83.7538	Silurian	Active
LEE	ROSE RUN SD, UPPER PART KNOX	4345	4395	37.6154	-83.6198	Ordovician	Active
LEE	BEEKMANTOWN DOL, UPPER PART KNOX	3826	3954	37.6490	-83.6338	Ordovician	Active
LEE	BEEKMANTOWN DOL, UPPER PART KNOX	3187	3282	37.6736	-83.7617	Ordovician	Active
POWELL	LOCKPORT DOL	1116	1134	37.7309	-83.7282	Silurian	Inactive
WOLFE	LOCKPORT DOL	1160	1246	37.7385	-83.6891	Silurian	Inactive
WOLFE	LOCKPORT DOL	1180	1211	37.7135	-83.6983	Silurian	Active
LEE	CORNIFEROUS	1100	1240	37.6371	-83.7322	Silurian	Inactive
ESTILL	CORNIFEROUS	765	787	37.7372	-83.8323	Silurian	Inactive
POWELL	LOCKPORT DOL	890	937	37.7280	-83.7128	Silurian	Active
LEE	LOCKPORT DOL	1100	1120	37.6038	-83.7550	Silurian	Other
LEE	CORNIFEROUS	1230	1274	37.6794	-83.6333	Silurian	Inactive
LEE	LOCKPORT DOL	1280	1306	37.6332	-83.6063	Silurian	Active

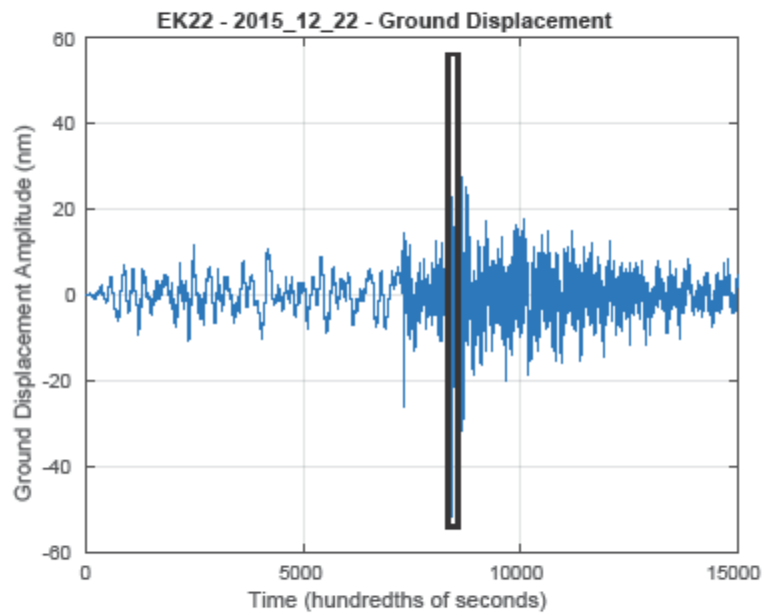
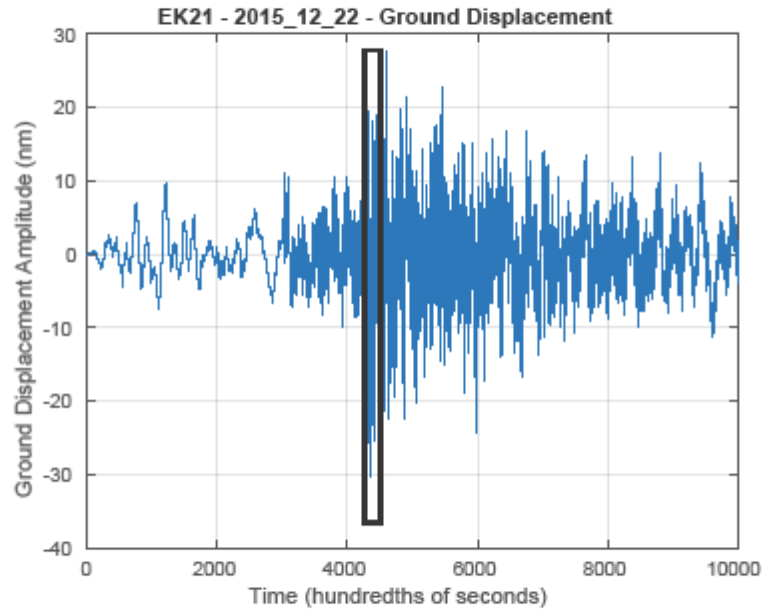
Appendix B - Moment Magnitude Calculations

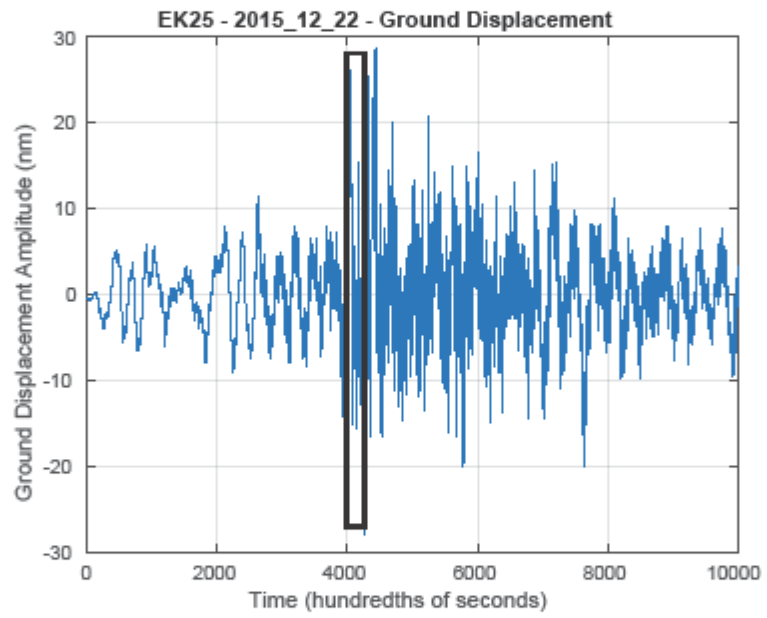
B.1 - High-pass filtered ground displacement waveforms of earthquakes

Vertical component ground displacement waveforms of earthquakes high-pass filtered above 0.8 Hz. The black rectangle outlines the 1 second of data around the S-wave onset that was Fourier transformed to be analyzed for the moment magnitude calculations.

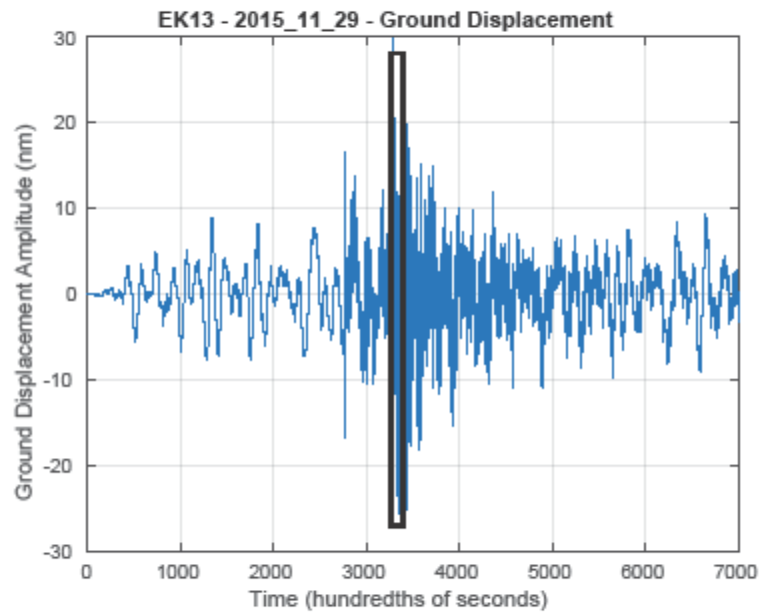
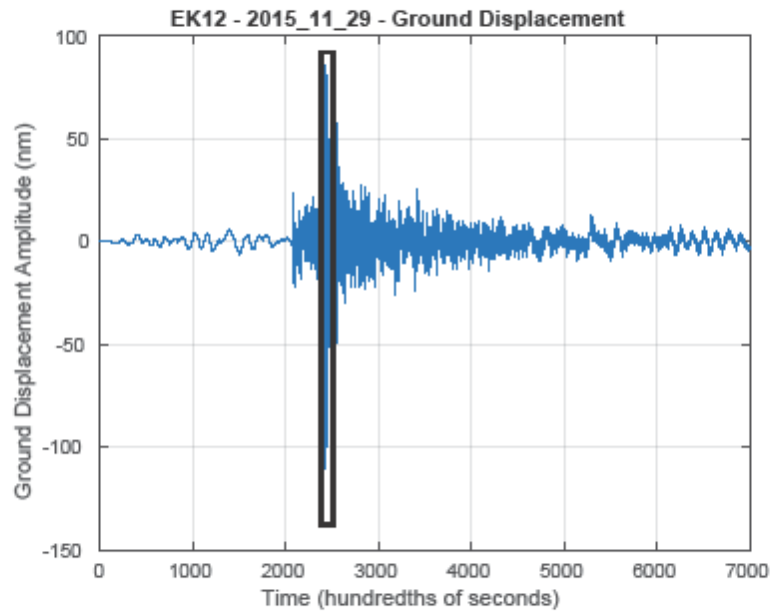
B.1.1 - December 22, 2015 Event

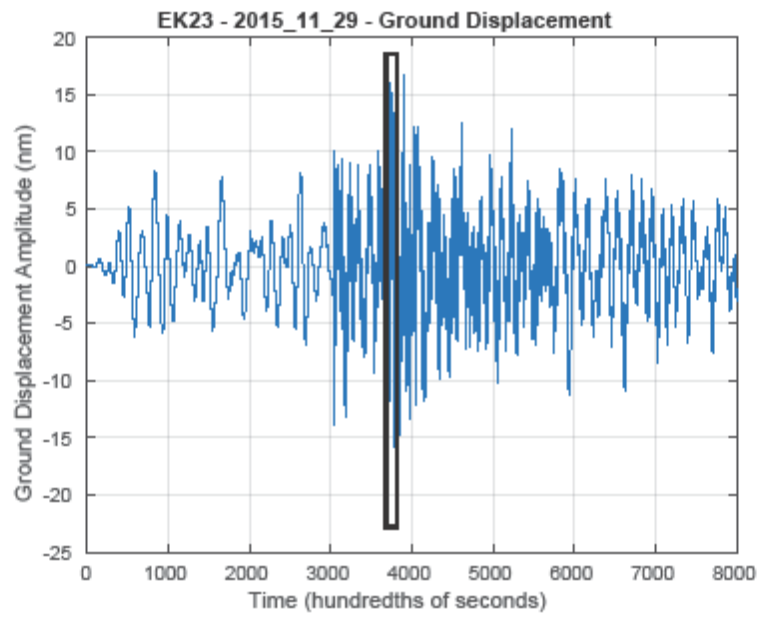
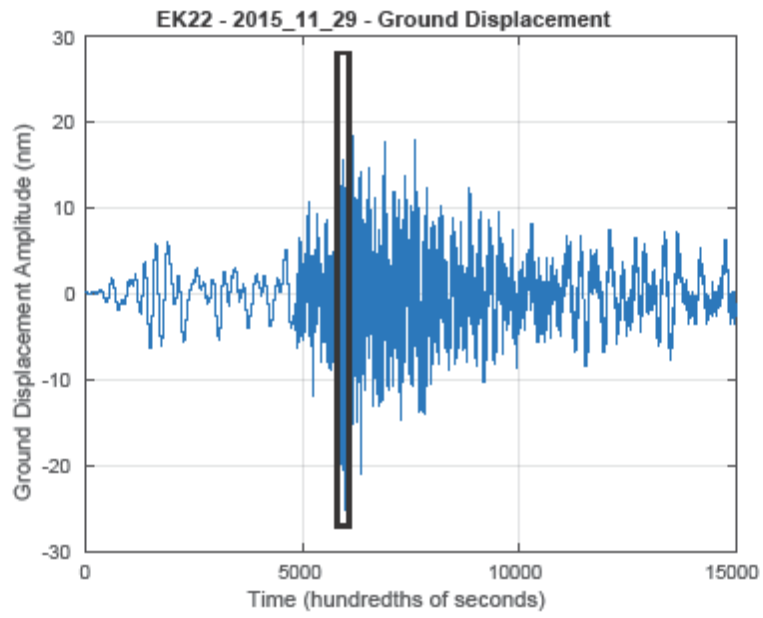


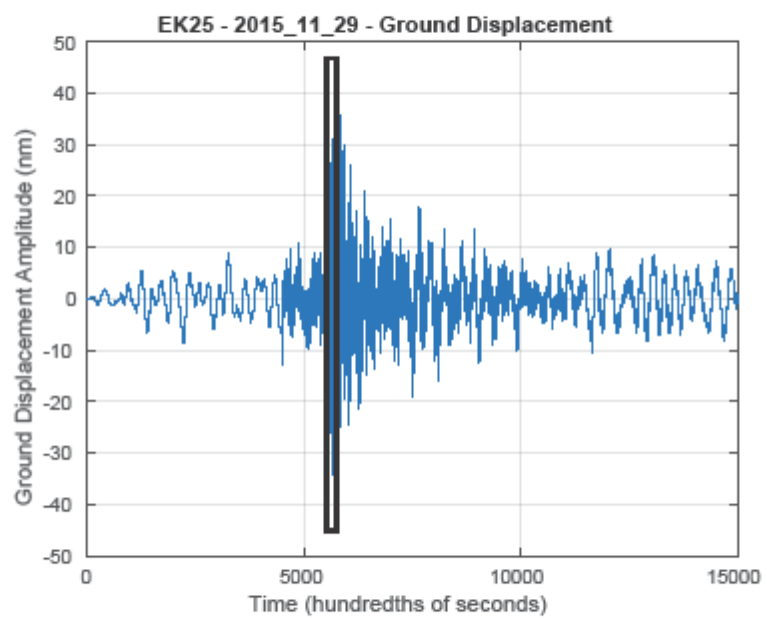




B.1.2 – November 29, 2015 Event





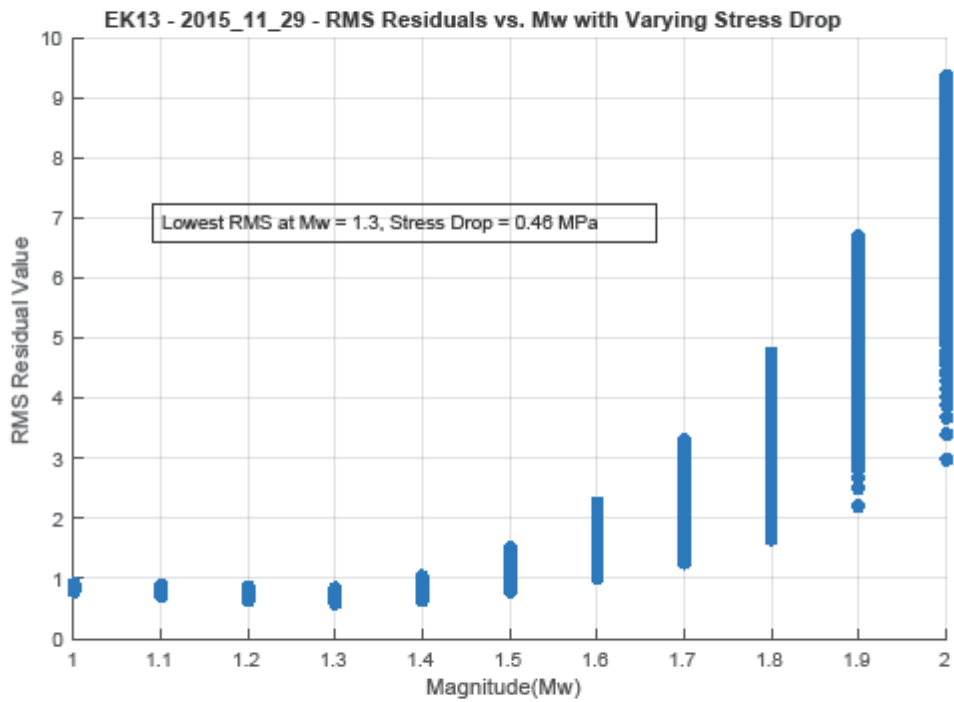
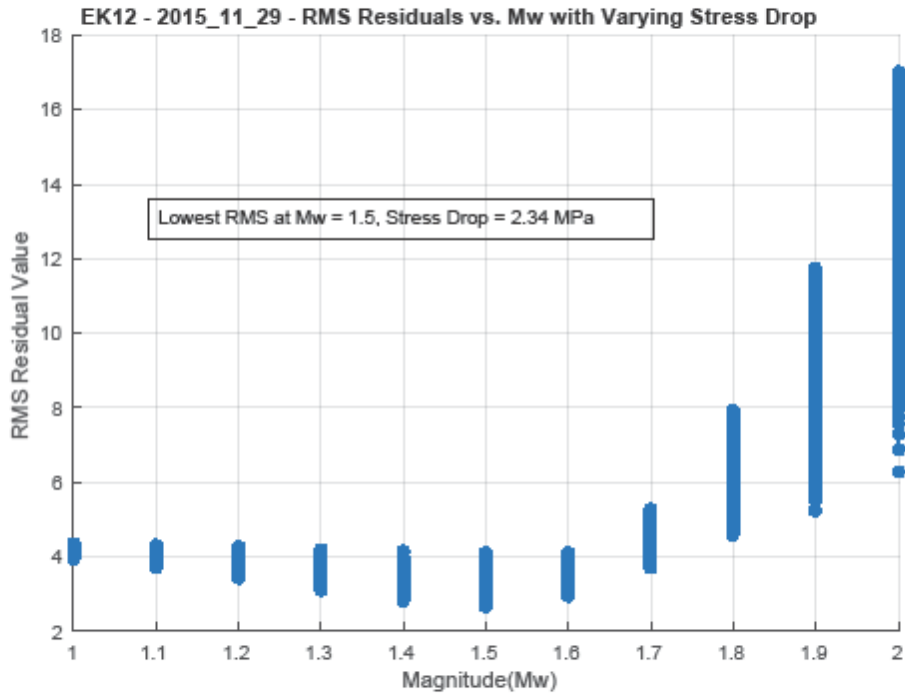


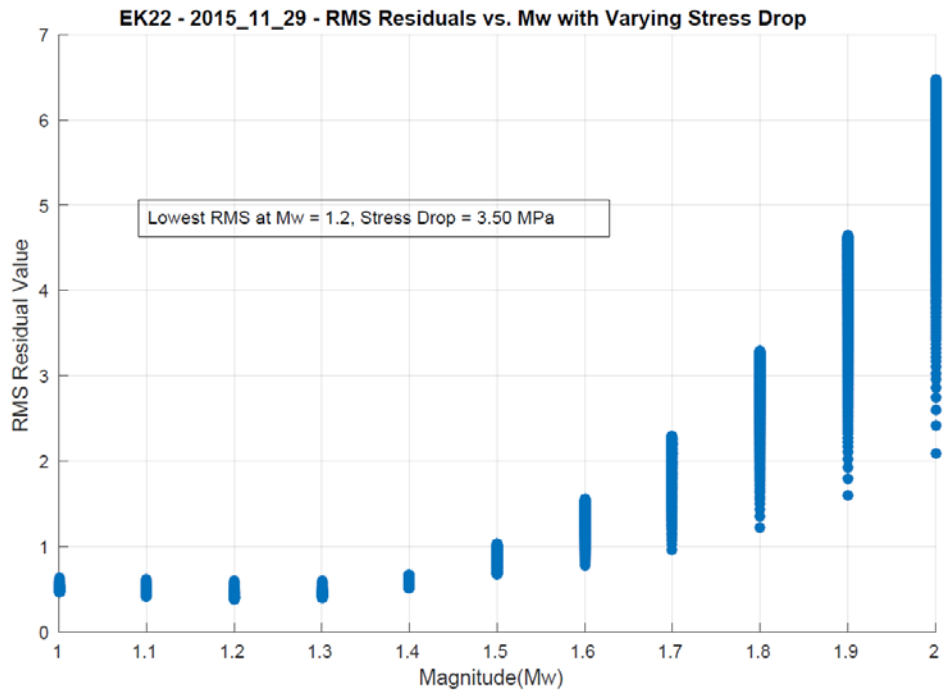
B.2 – Variation of Moment Magnitude and Stress Drop for Model of Best fit

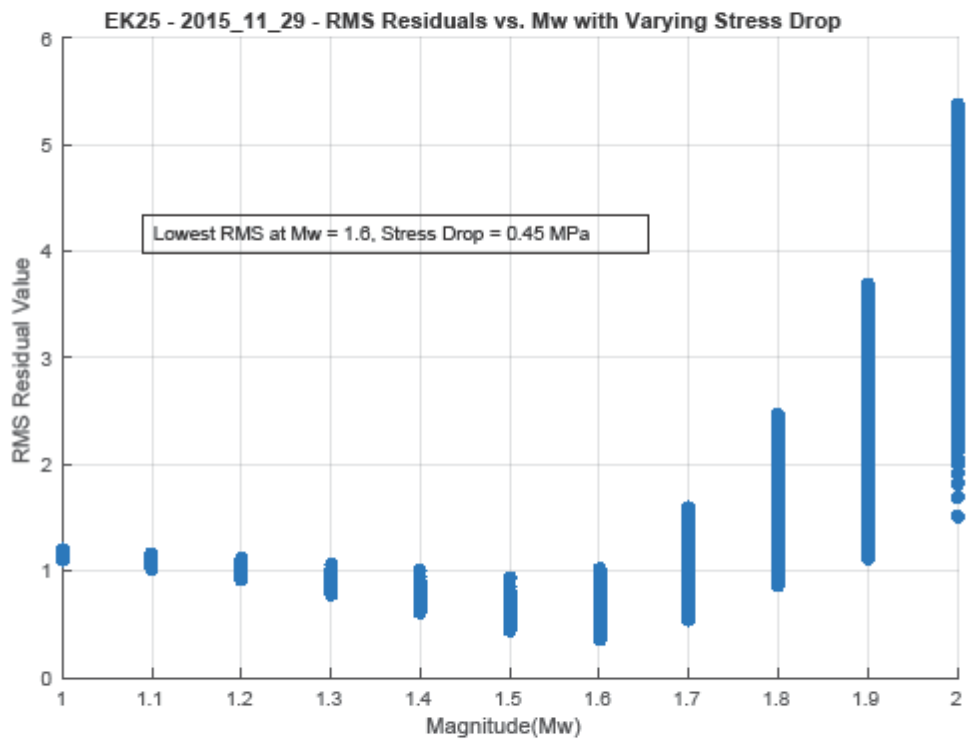
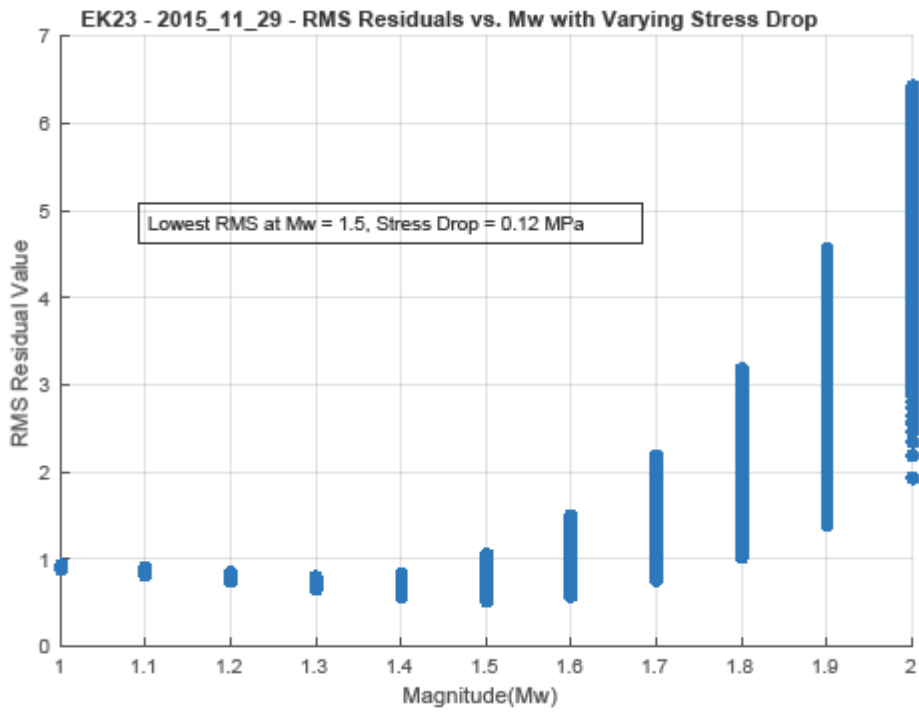
Graphs of root mean square residual while varying moment magnitude and stress drop to find the lowest root mean square residual. (Appendix D). Brune and Boatwright Models were tested to determine which model would produce the lowest residuals. Stress drops were varied from 0.001 to 10 MPa and moment magnitudes were varied from Mw1 to 2.

B.2.1 – Brune (1970) Model – November 29, 2015 Event

Station Name	Residual	Mw	Stress Drop (Pascals)	Energy Release (N-m)	Fault Radius (m)	Corner Frequency (Hz)
EK12	2.6739	1.5	2.34E+06	2.19E+11	34.46	21.94
EK13	0.59225	1.3	4.60E+05	1.10E+11	47.07	16.06
EK22	0.37914	1.2	3.50E+06	7.76E+10	21.33	35.44
EK23	0.52447	1.5	1.20E+05	2.19E+11	92.74	8.15
EK25	0.36481	1.6	4.50E+05	3.09E+11	66.98	11.29
Median	0.52447	1.5	4.60E+05	2.19E+11	47.07	16.06

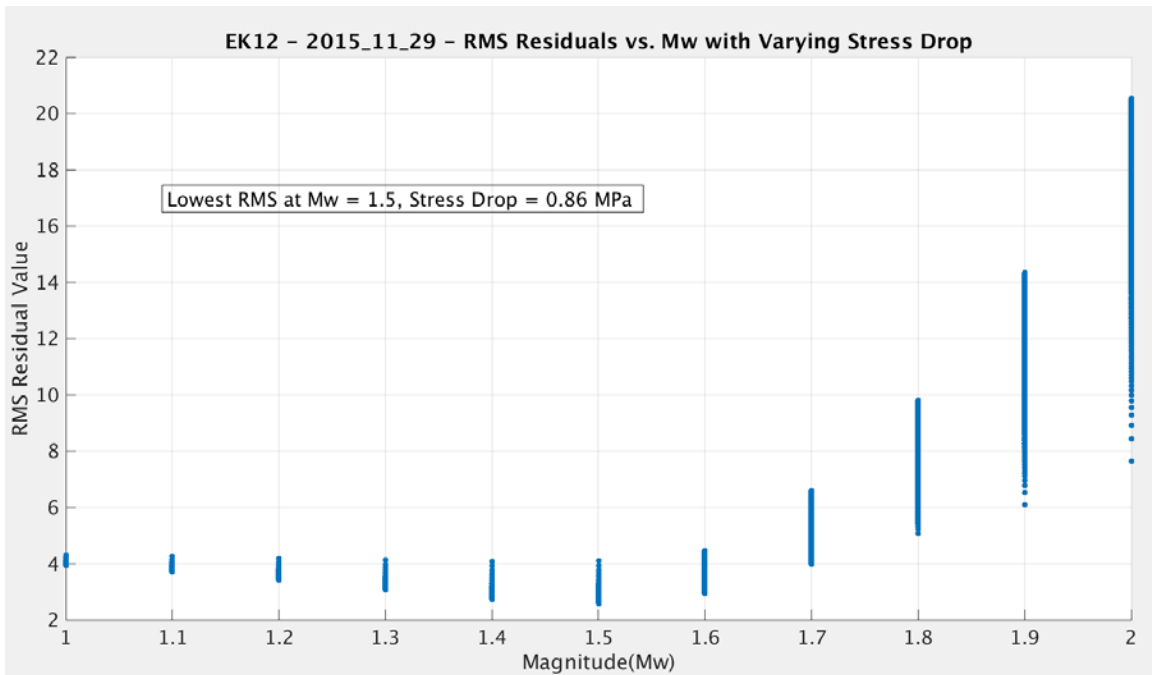


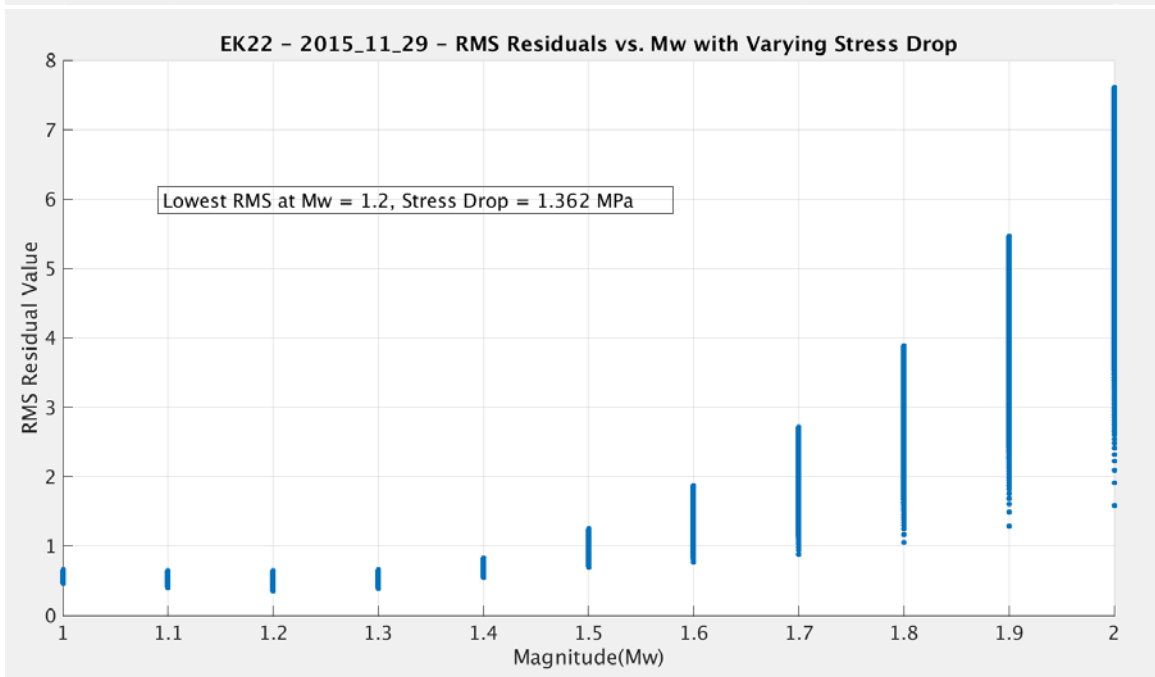
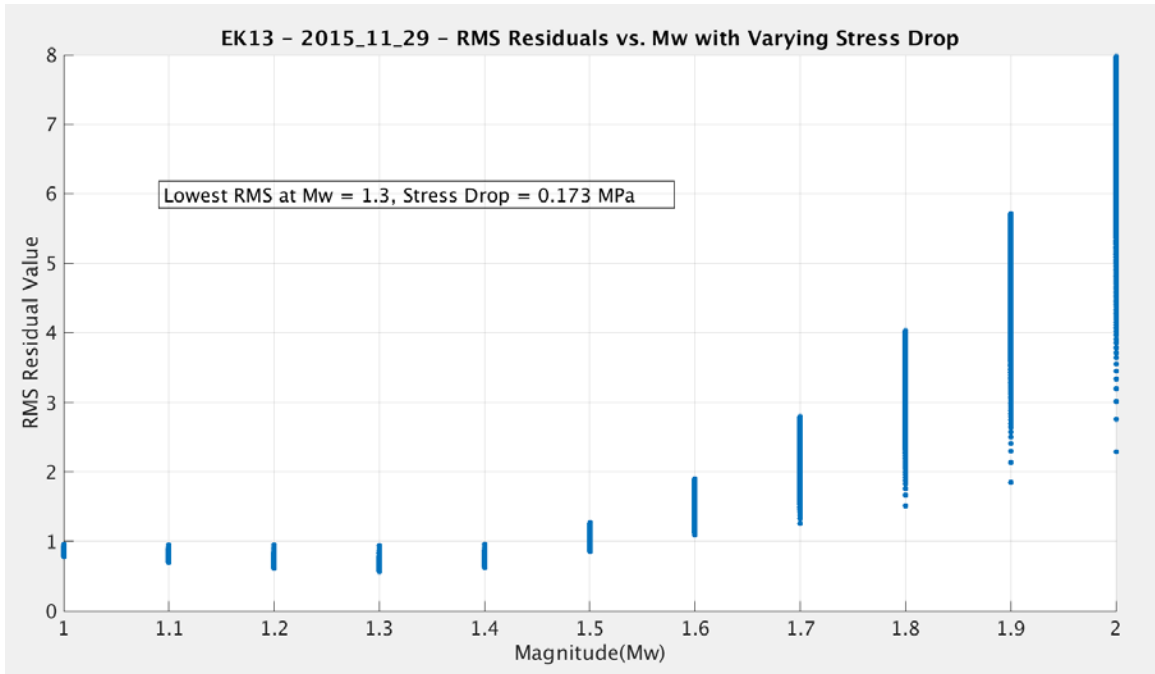


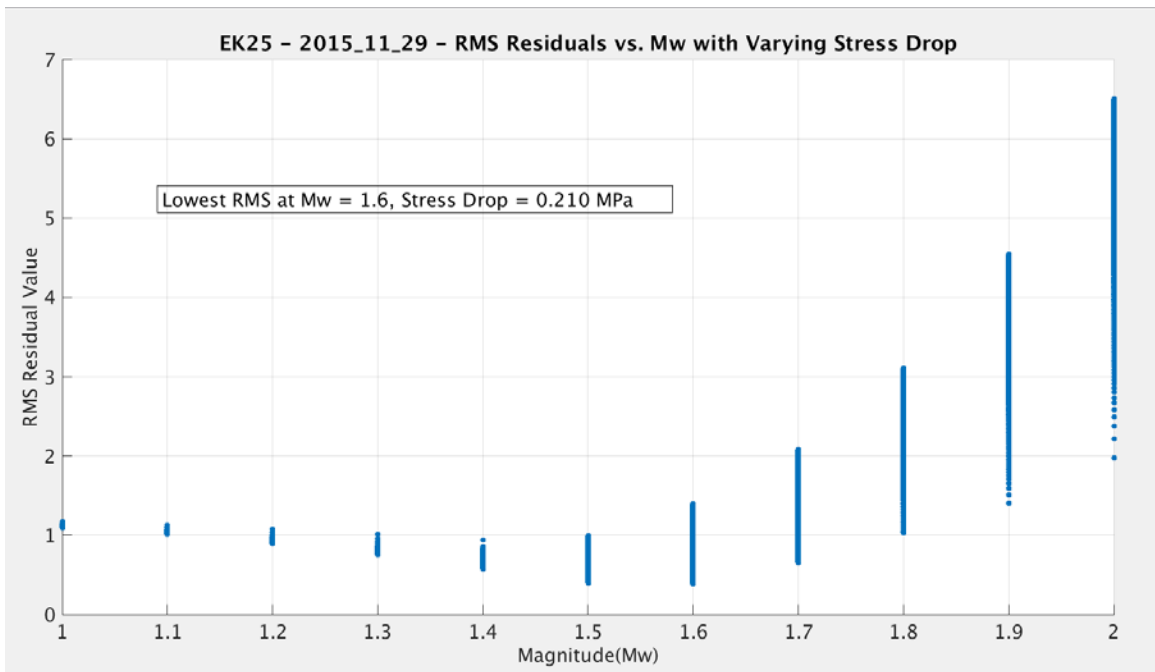
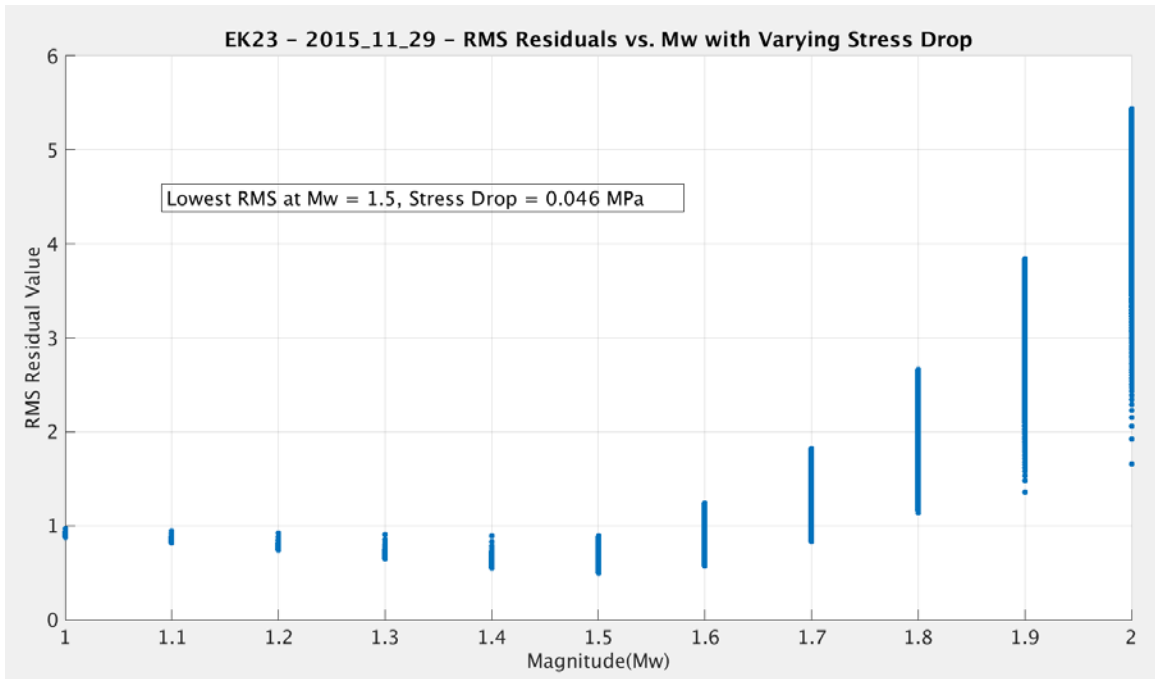


B.2.2 – Boatwright (1980) Model – November 29, 2015 Event

Station Name	Residual	Mw	Stress Drop (Pascals)	Energy Release (N-m)	Fault Radius (m)	Corner Frequency (Hz)
EK12	2.5634	1.5	8.60E+05	2.19E+11	48.10	15.72
EK13	0.56791	1.3	1.70E+05	1.10E+11	65.59	11.53
EK22	0.35646	1.2	1.36E+06	7.76E+10	29.23	25.86
EK23	0.49503	1.5	4.60E+04	2.19E+11	127.67	5.92
EK25	0.38355	1.6	2.10E+05	3.09E+11	86.35	8.76
Median	0.49503	1.5	2.10E+05	2.19E+11	65.59	11.53

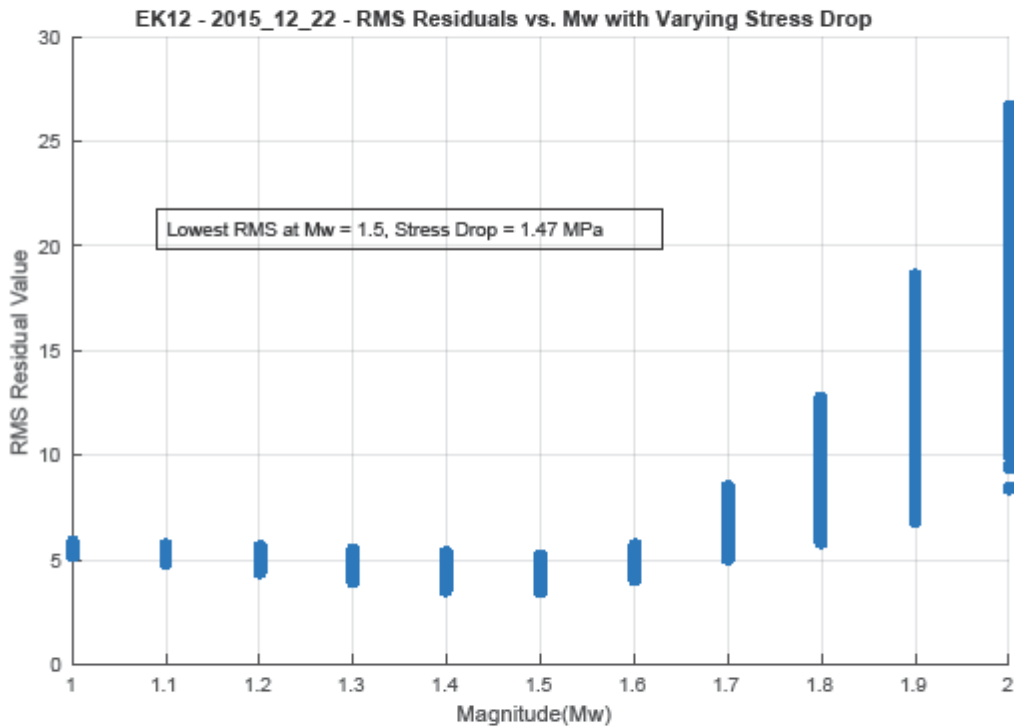


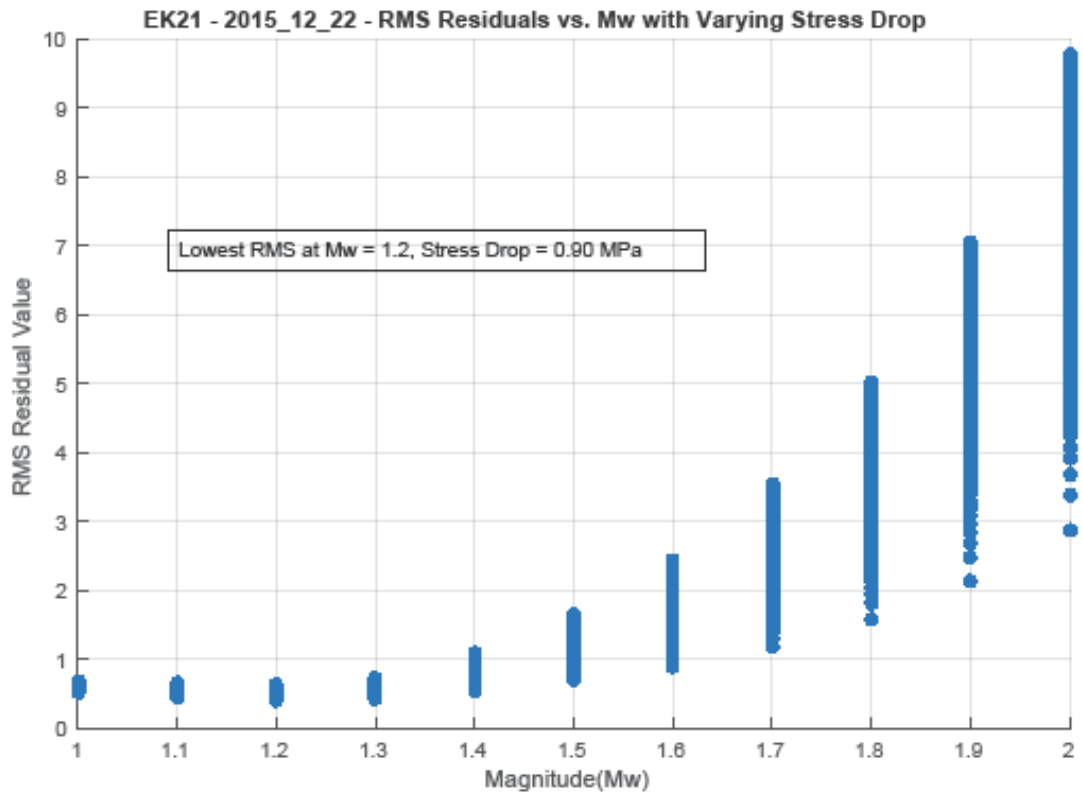
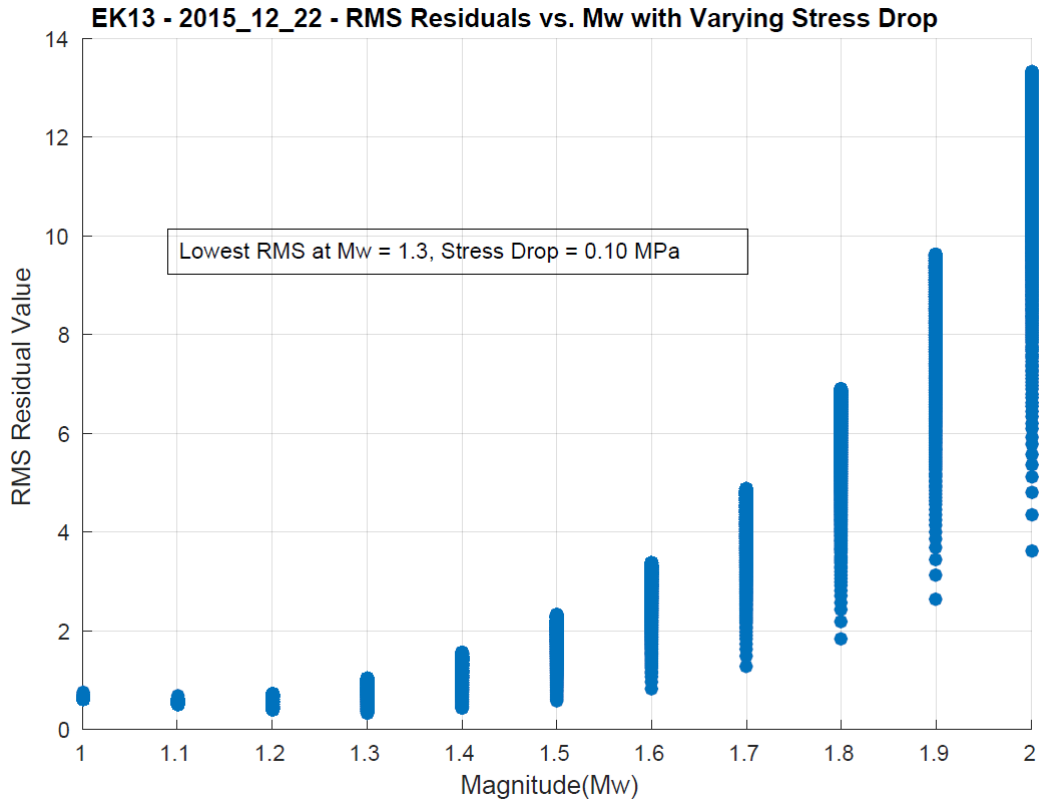


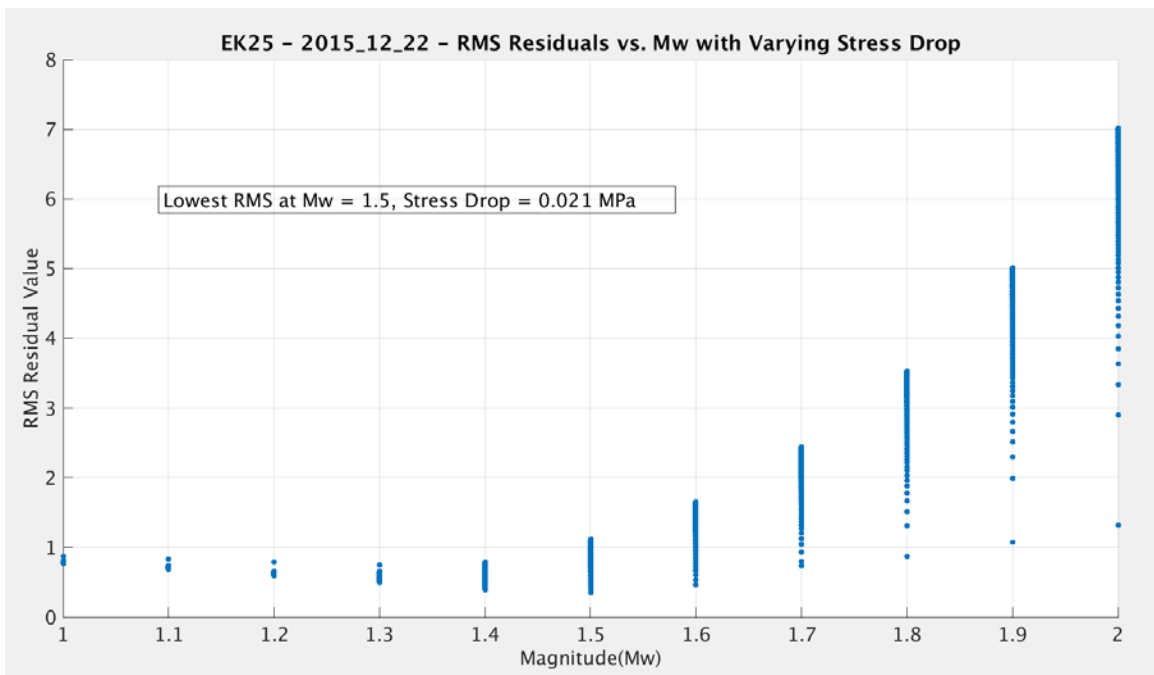
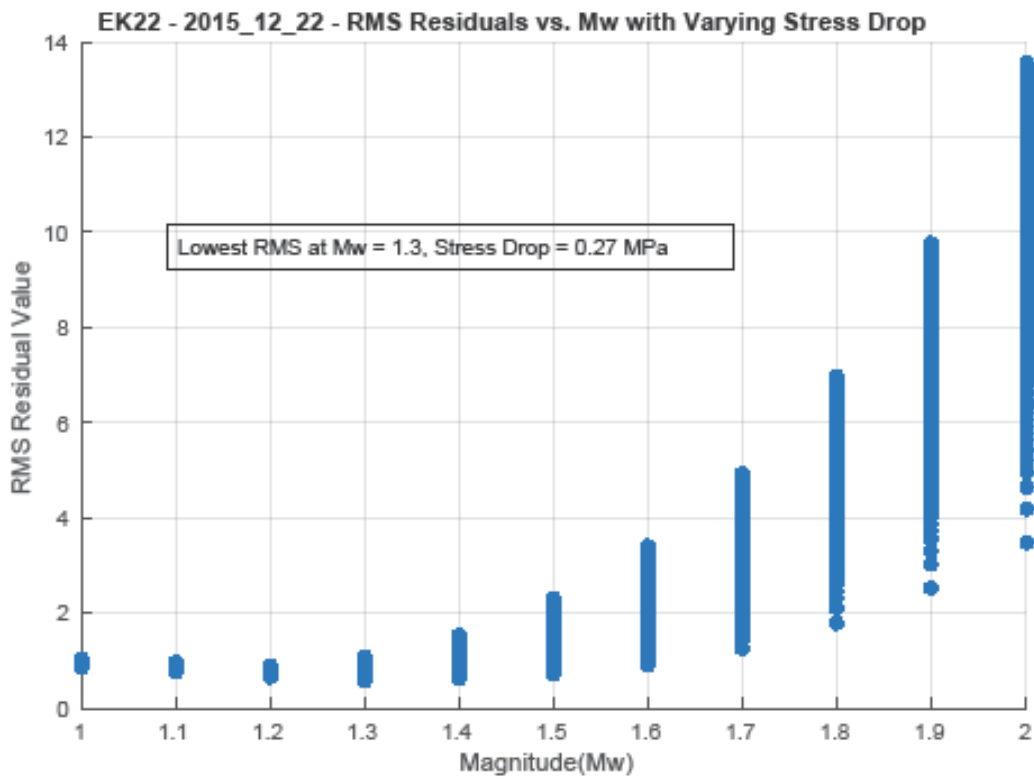


B.2.3 – Brune (1970) Model – December 22, 2015 Event

Station Name	Residual	Mw	Stress Drop (Pascals)	Energy Release (N-m)	Fault Radius (m)	Corner Frequency (Hz)
EK12	3.48210	1.5	1.47E+06	2.19E+11	40.23	18.79
EK13	0.34705	1.3	1.00E+05	1.10E+11	78.28	9.66
EK21	0.39580	1.2	9.00E+05	7.76E+10	33.54	22.54
EK22	0.58124	1.3	2.70E+05	1.10E+11	56.22	13.45
EK25	0.34157	1.5	2.10E+04	2.19E+11	165.80	4.56
Median	0.39580	1.3	2.70E+05	1.10E+11	56.22	13.45

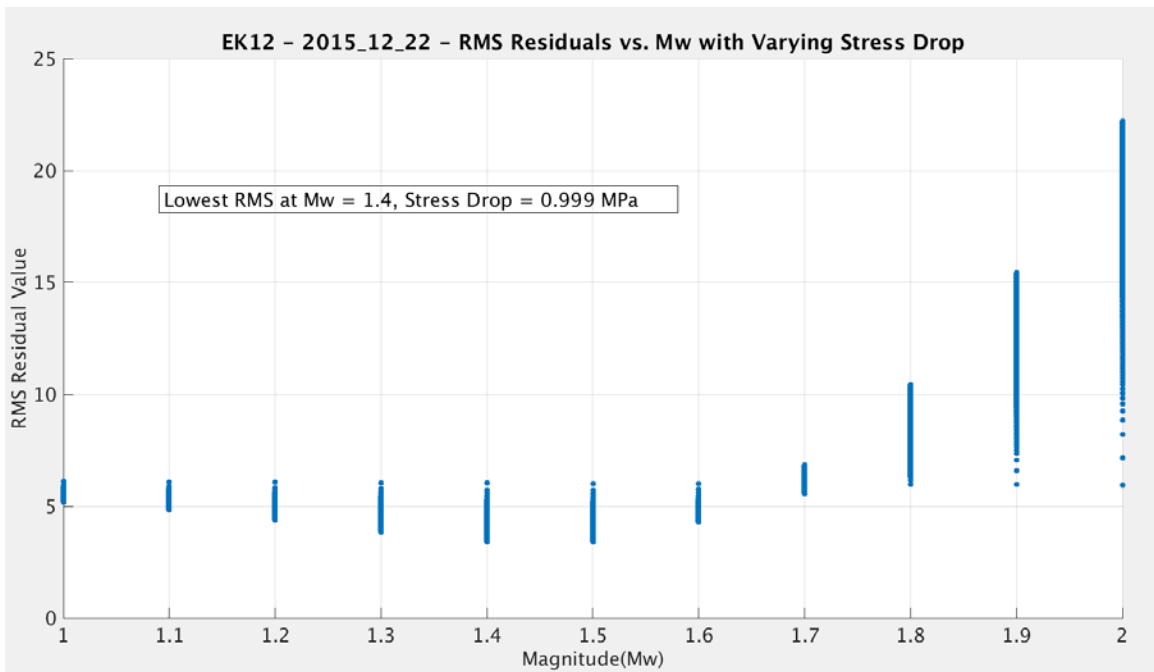


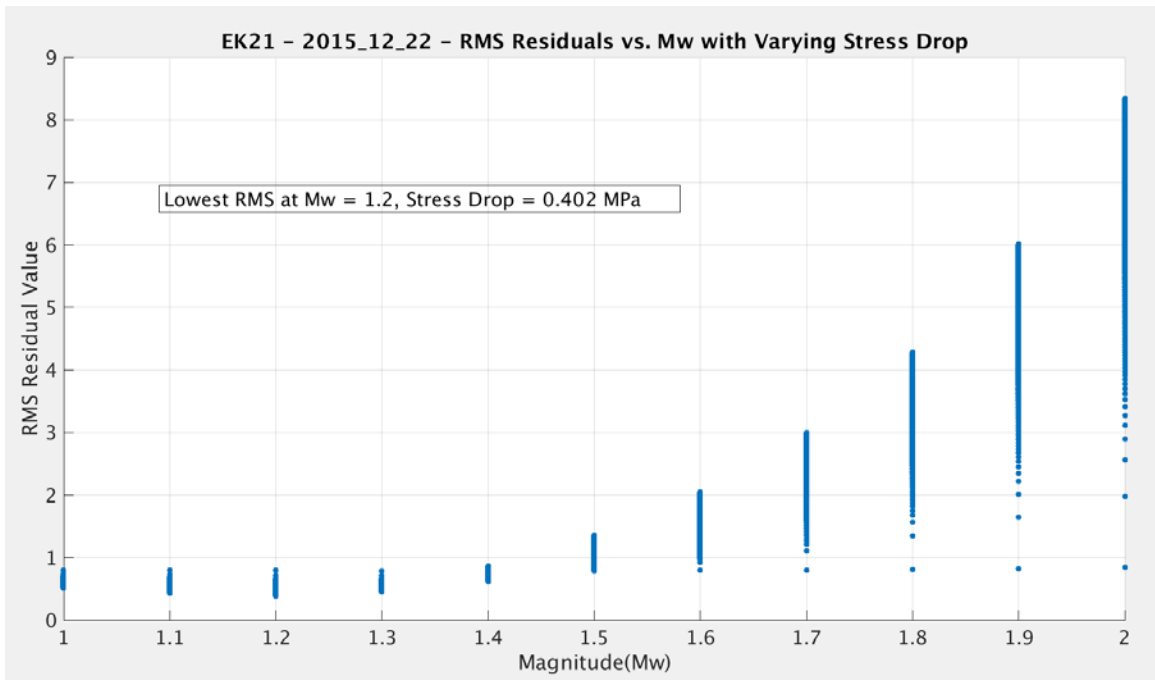
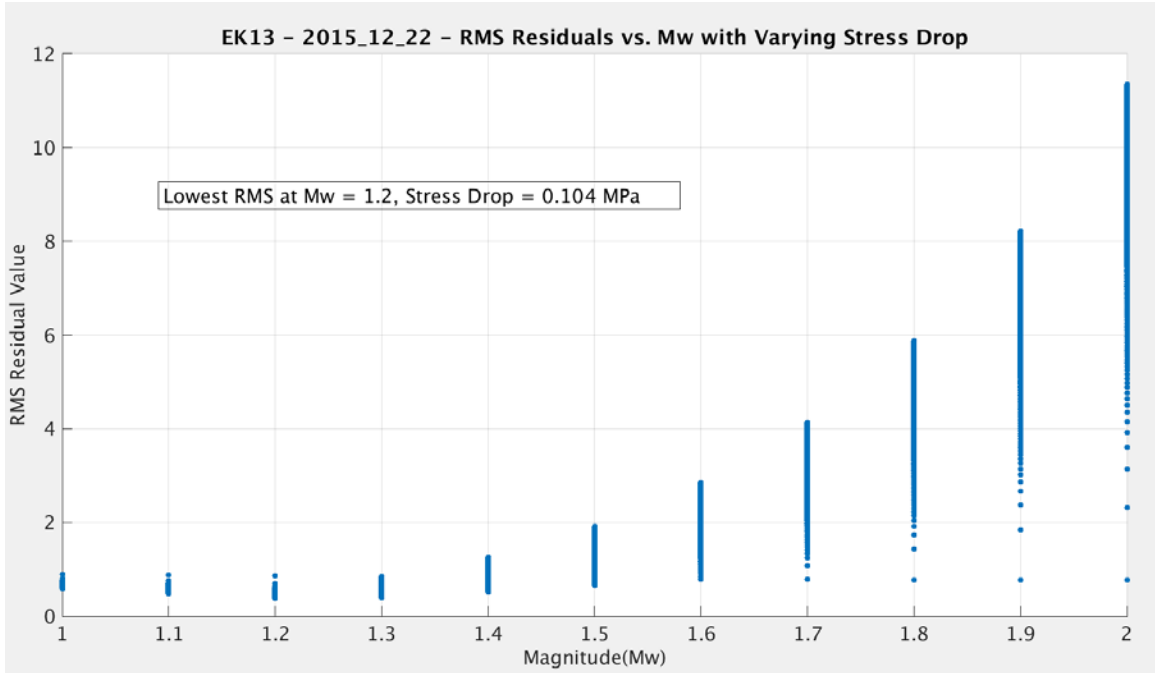


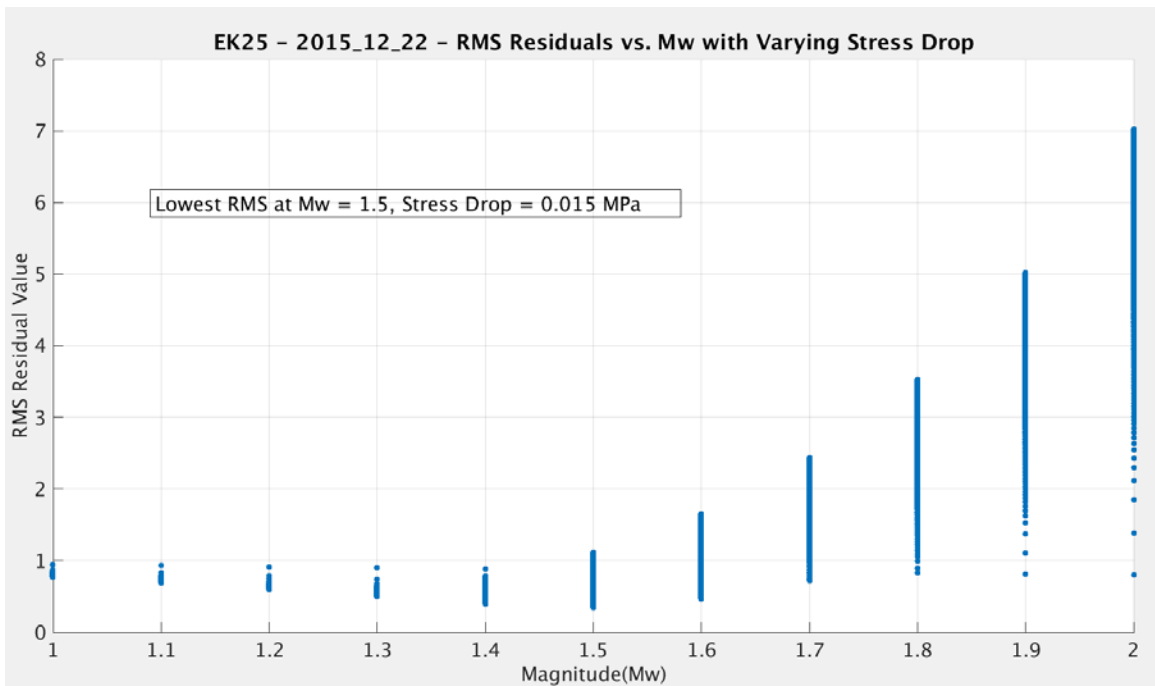
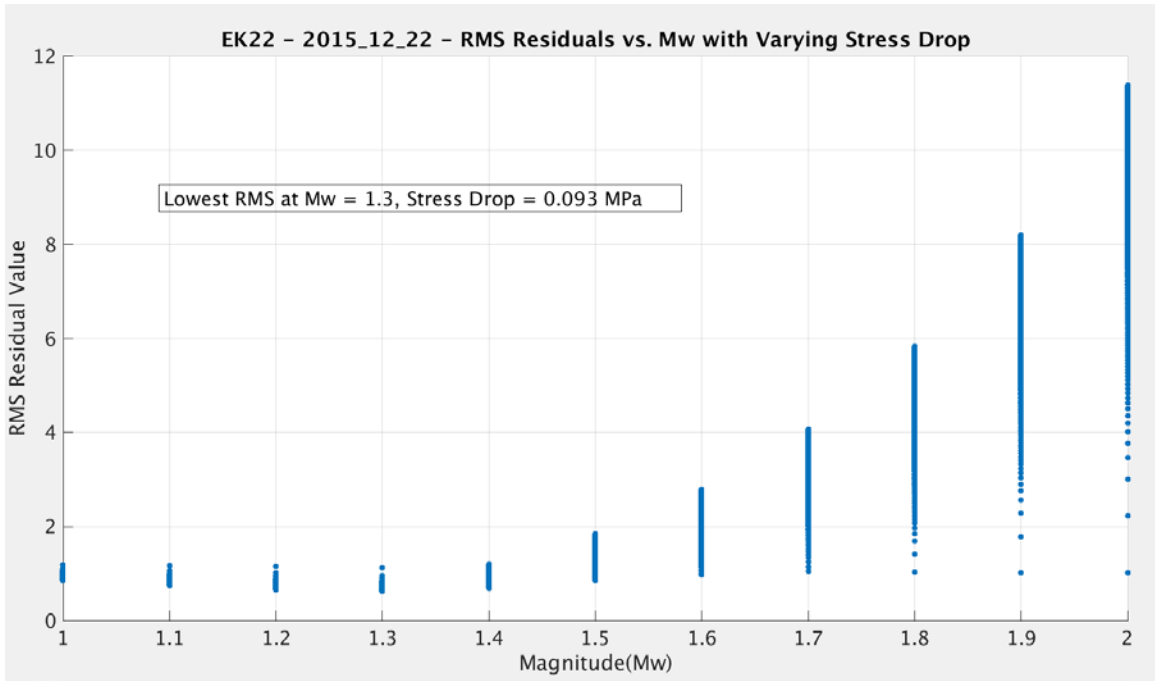


B.2.4 – Boatwright (1980) Model – December 22, 2015 Event

Station Name	Residual	Mw	Stress Drop (Pascals)	Energy Release (N-m)	Fault Radius (m)	Corner Frequency (Hz)
EK12	3.39990	1.4	9.99E+05	1.55E+11	40.78	18.54
EK13	0.38035	1.2	1.04E+05	7.76E+10	68.84	10.98
EK21	0.38962	1.2	4.02E+05	7.76E+10	43.87	17.23
EK22	0.61871	1.3	9.31E+04	1.10E+11	80.17	9.43
EK25	0.34114	1.5	1.51E+04	2.19E+11	185.07	4.08
Median	0.38962	1.3	1.04E+05	1.10E+11	68.84	10.98



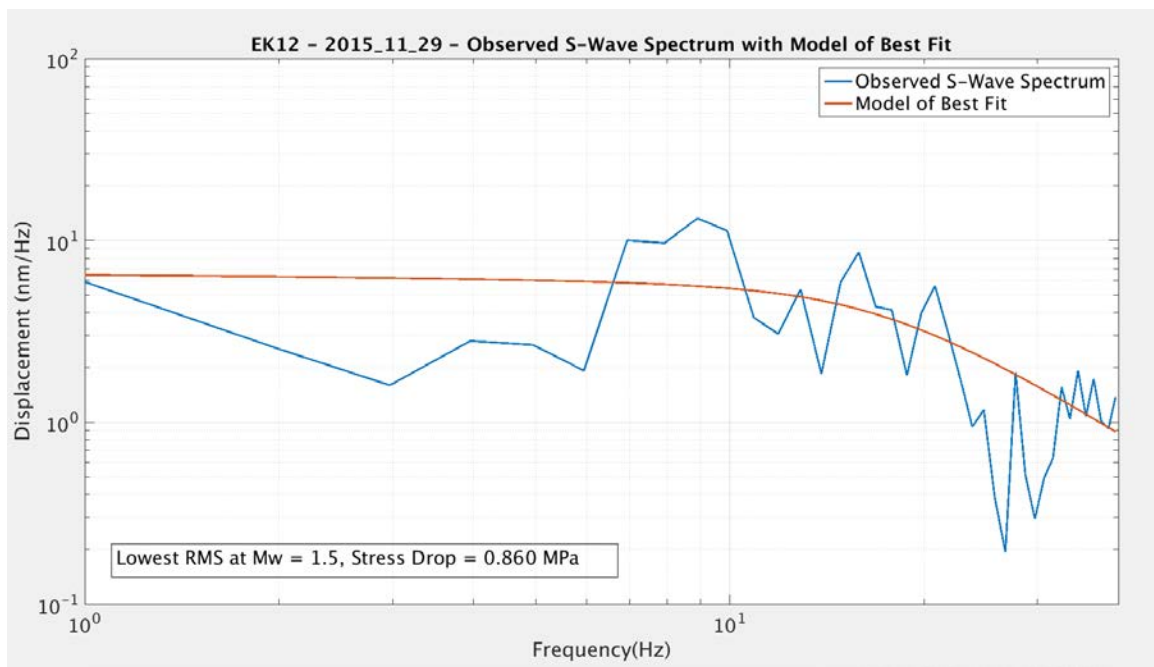


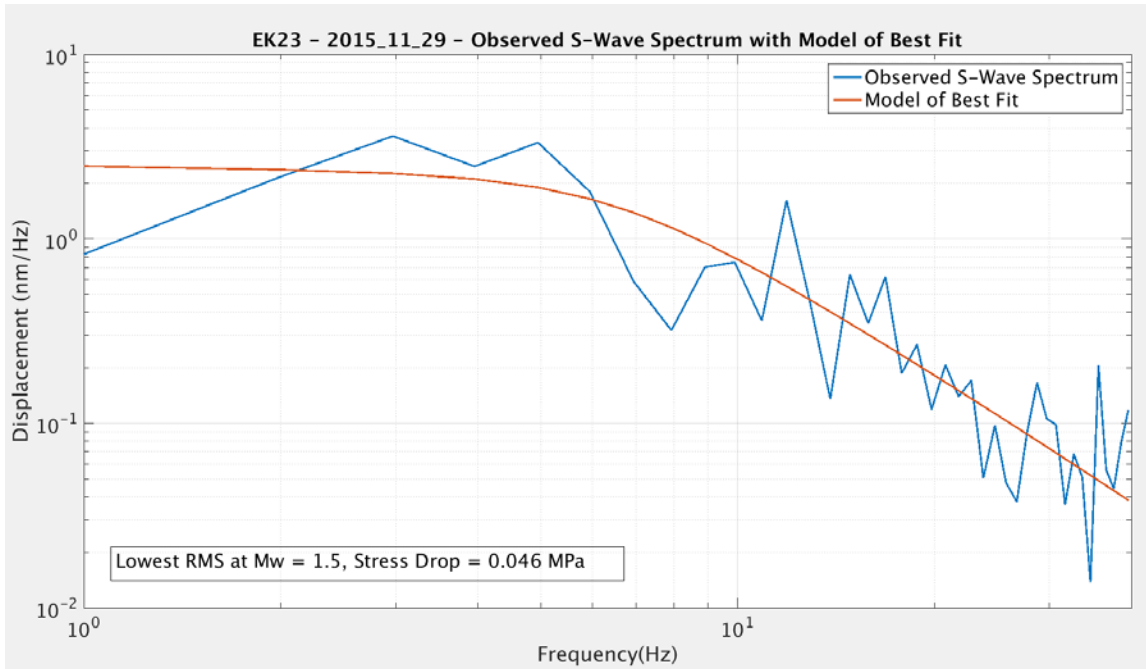
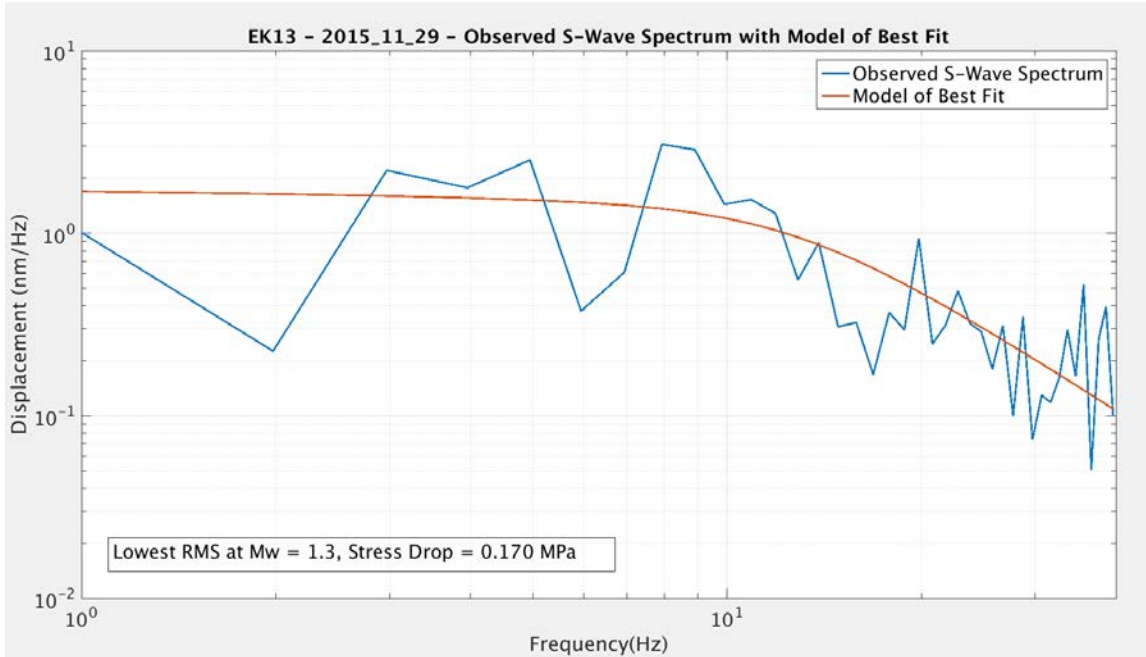


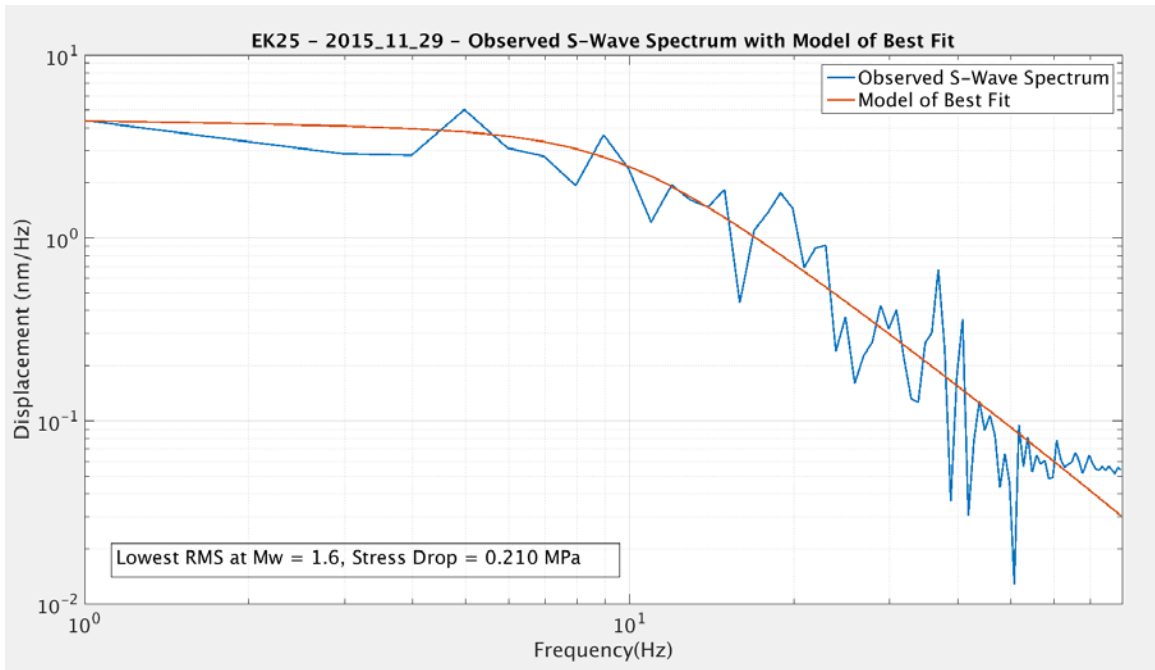
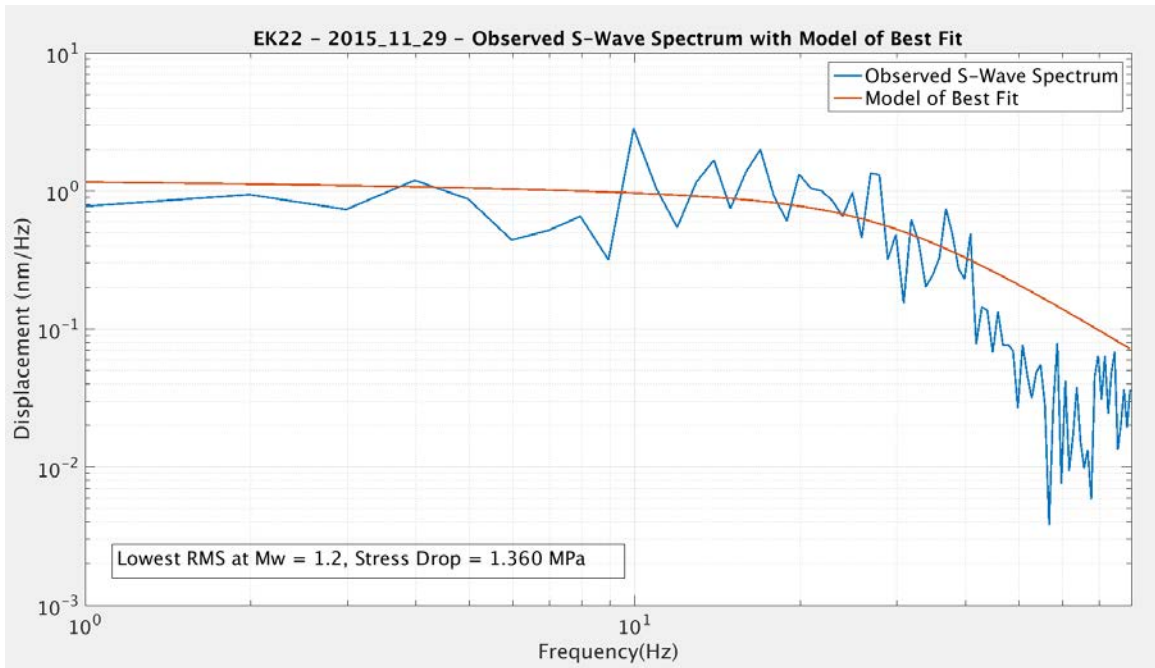
B.3 – Observed S-wave Spectrum vs. Source Spectrum Model of Best Fit

Lines of best fit were created from the point with the lowest residual value by varying moment magnitude (related to the low-frequency plateau) and stress drop (related to the corner frequency) as seen above. The lowest value was overlain on top of the first second of the S-wave onset, high-pass filtered, ground displacement data from both Brune (1970) and Boatwright (1980) source models.

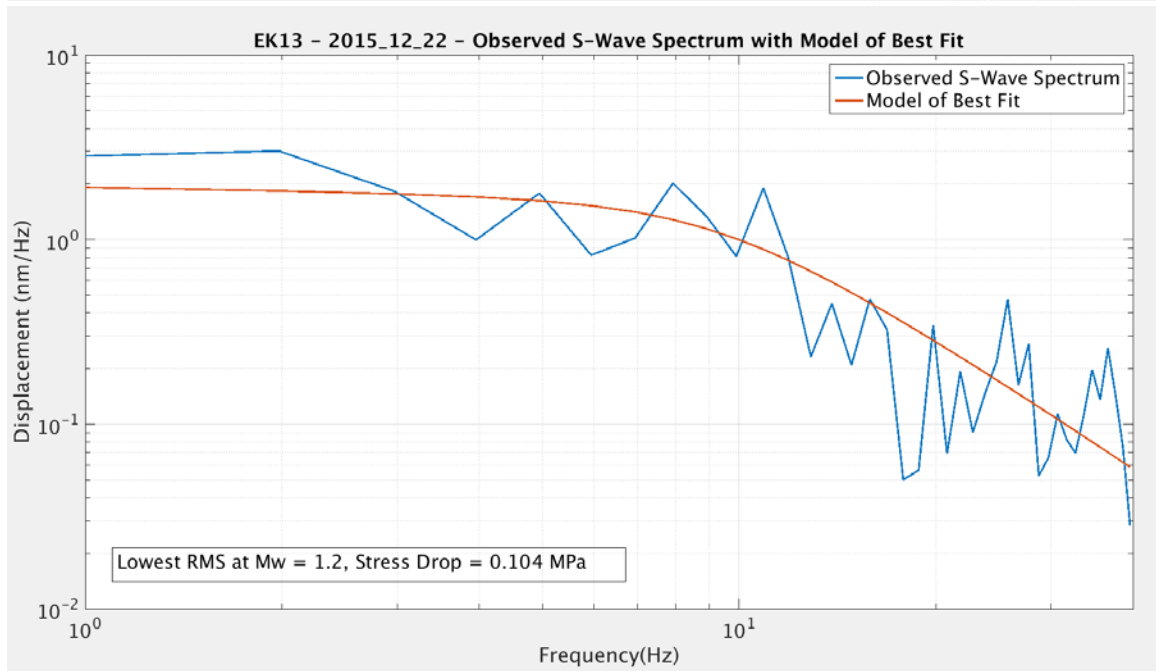
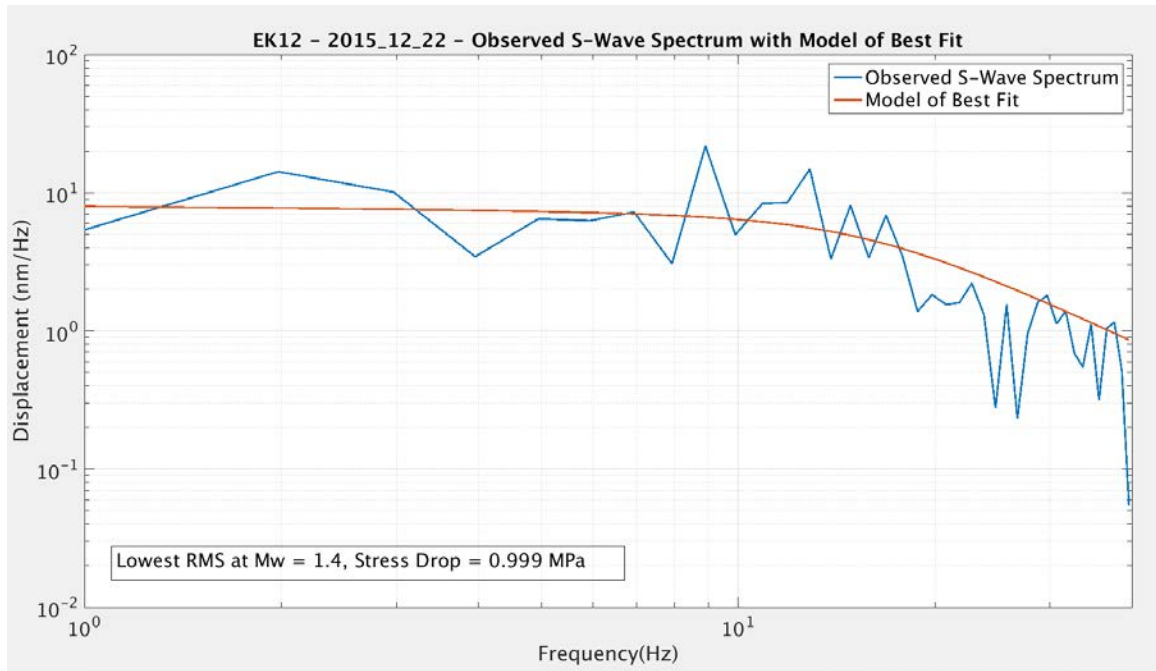
B.3.1 - November 29, 2015 event with Boatwright (1980) Model of Best Fit

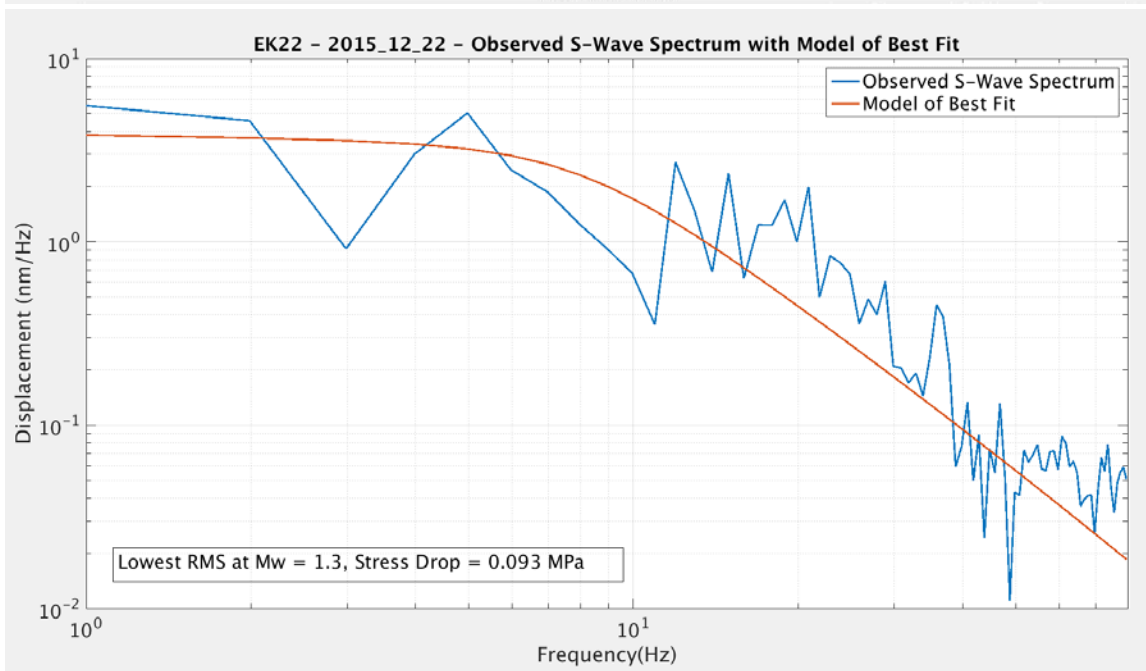
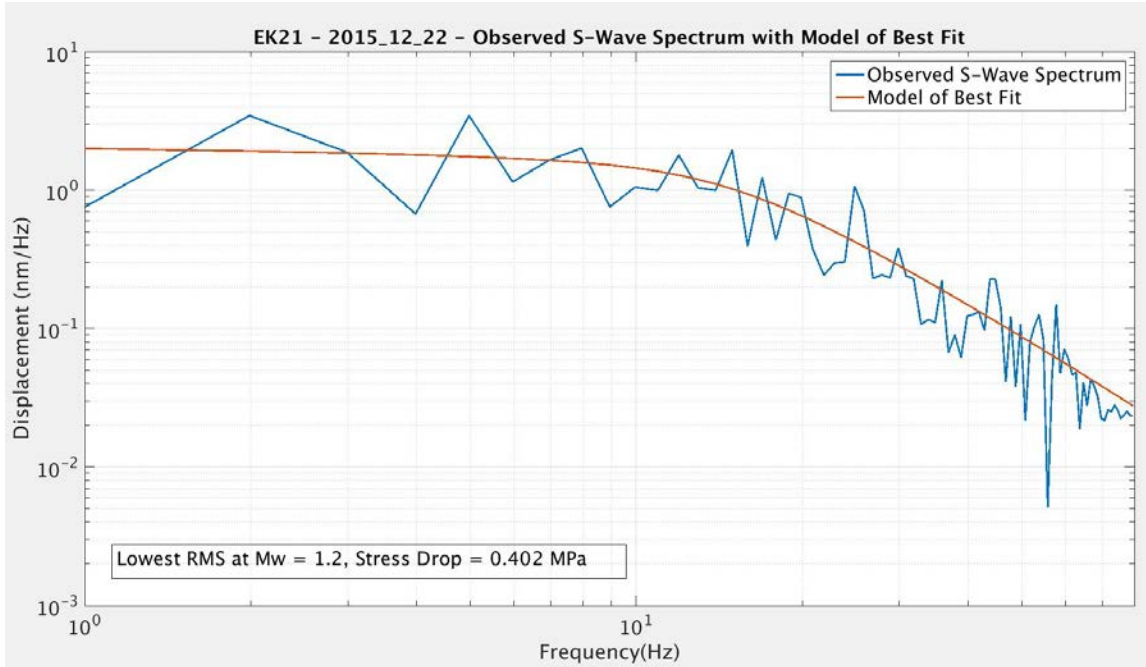


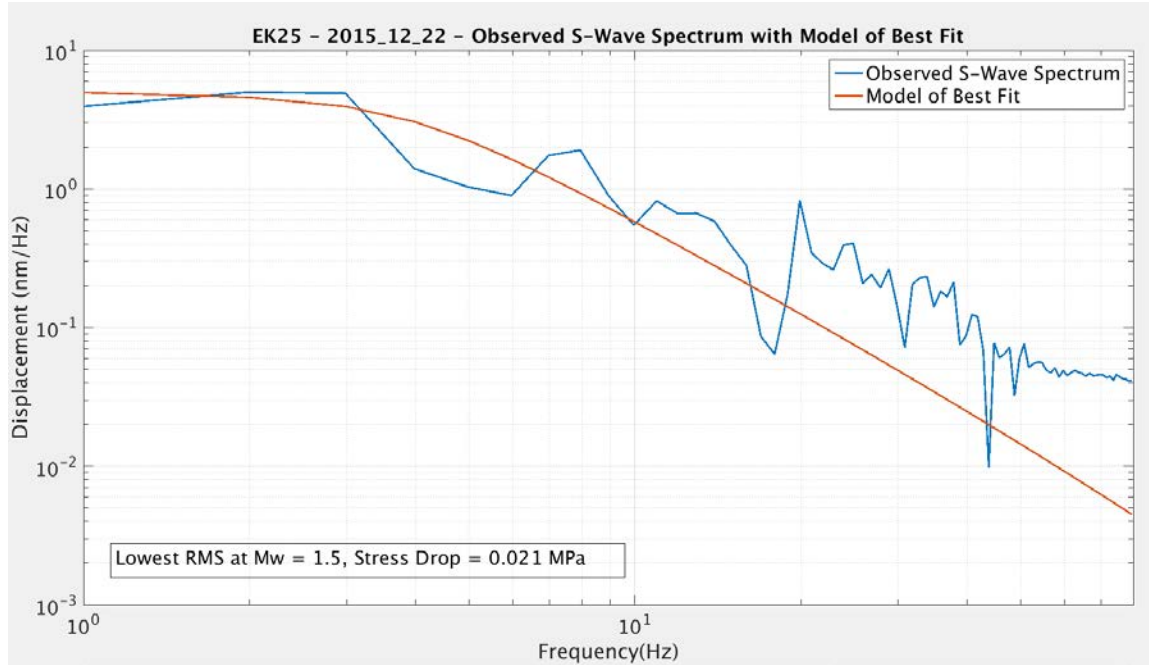




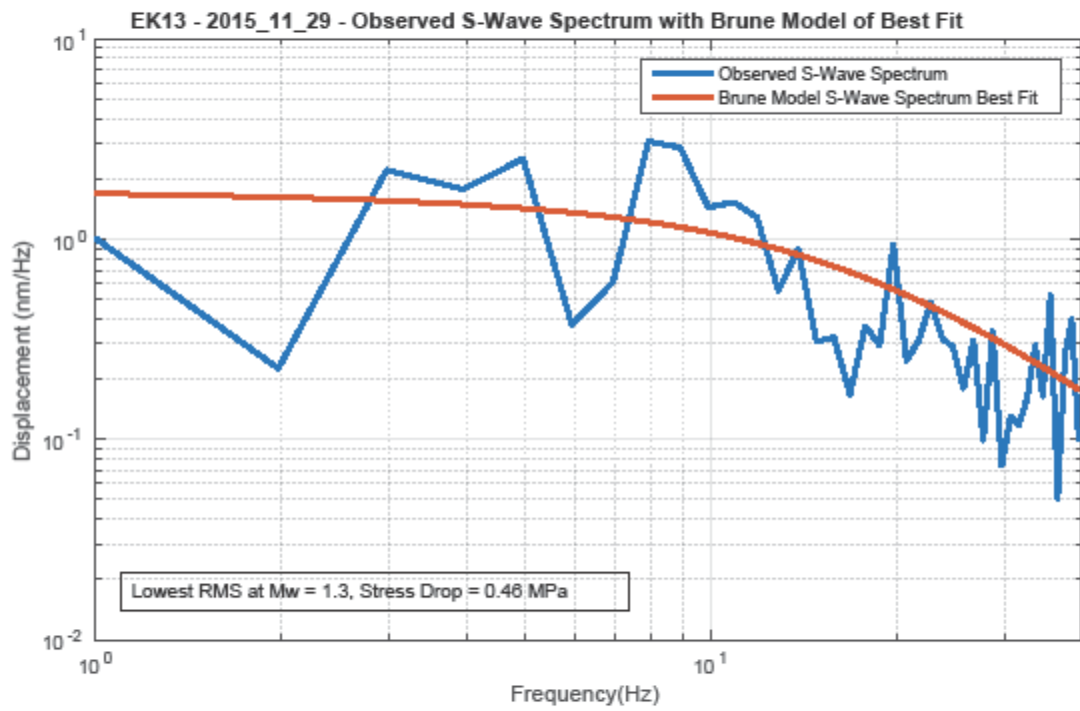
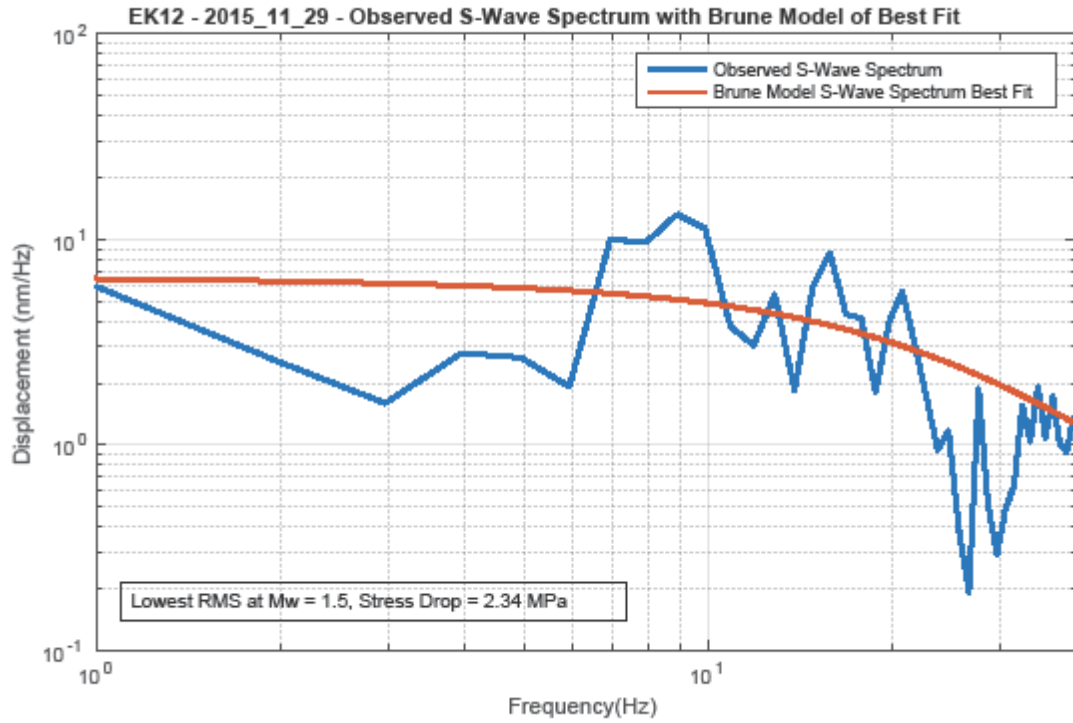
B.3.2 – December 22, 2015 Event with Boatwright(1980) Model of Best Fit

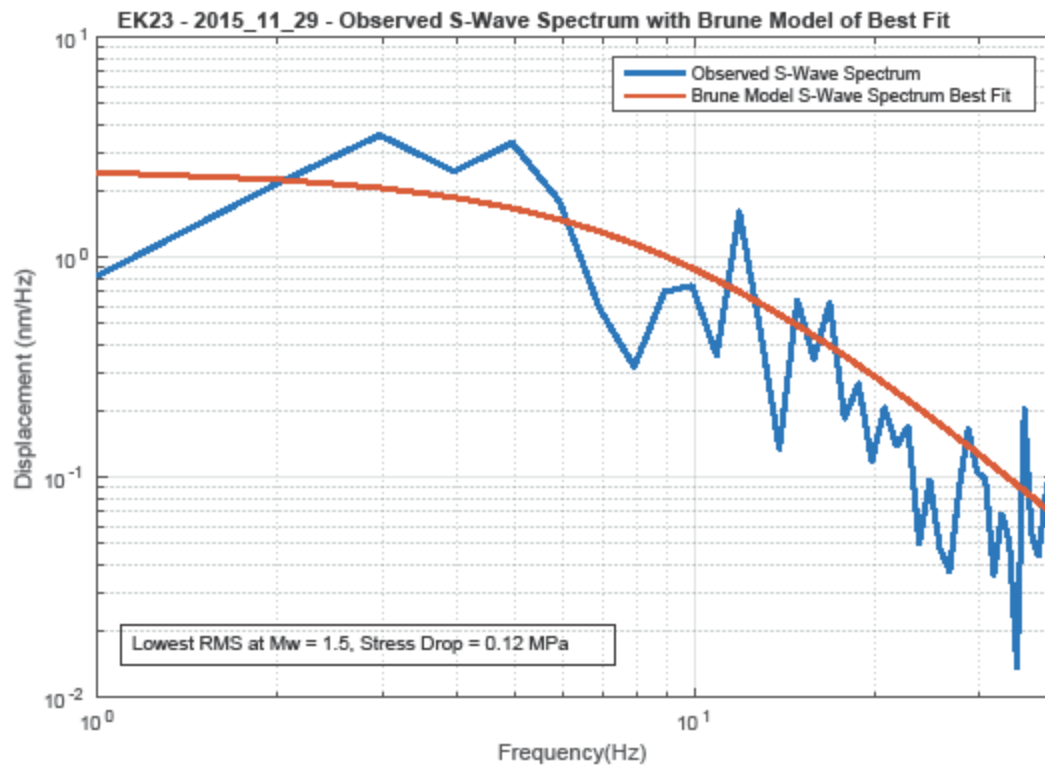
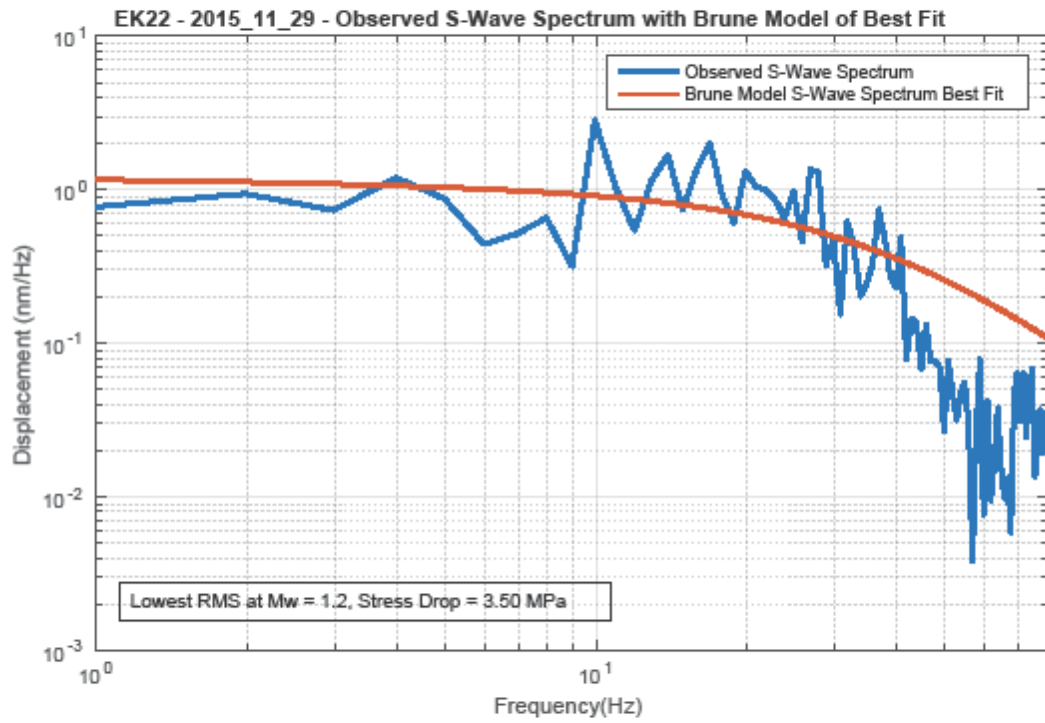


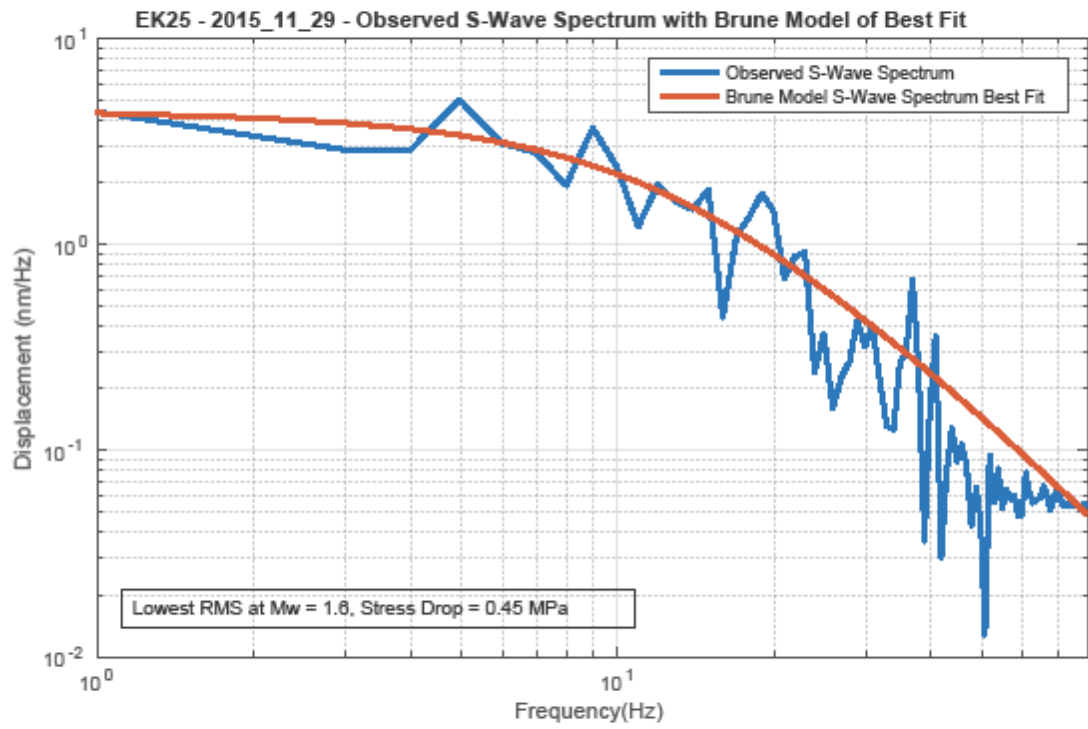




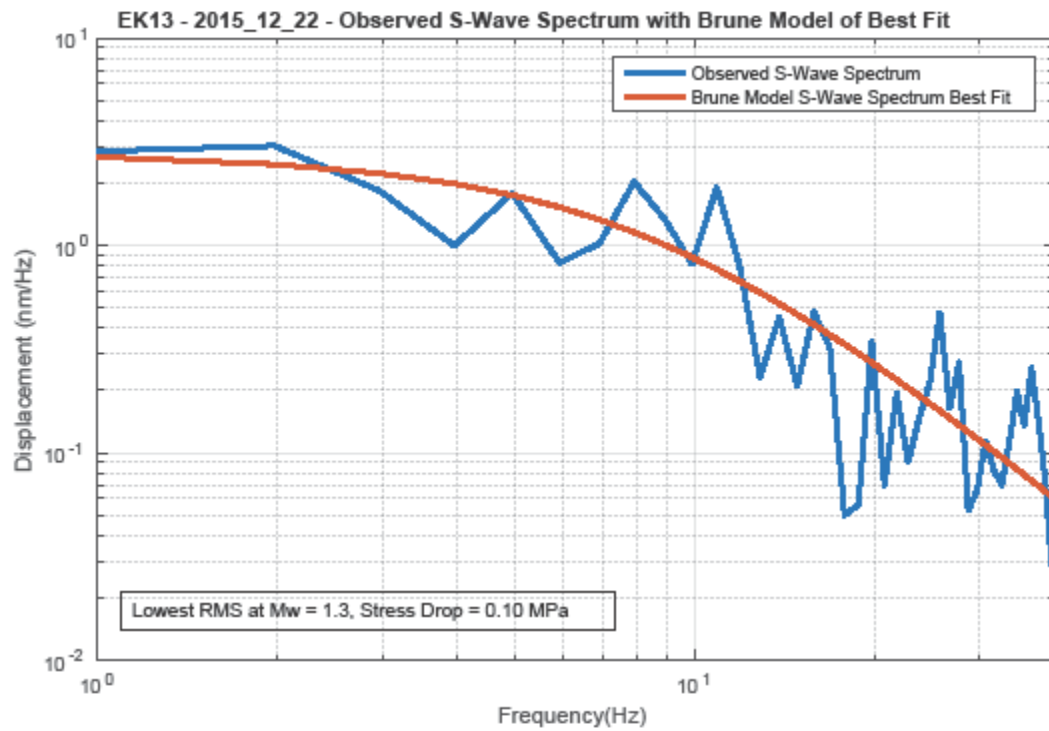
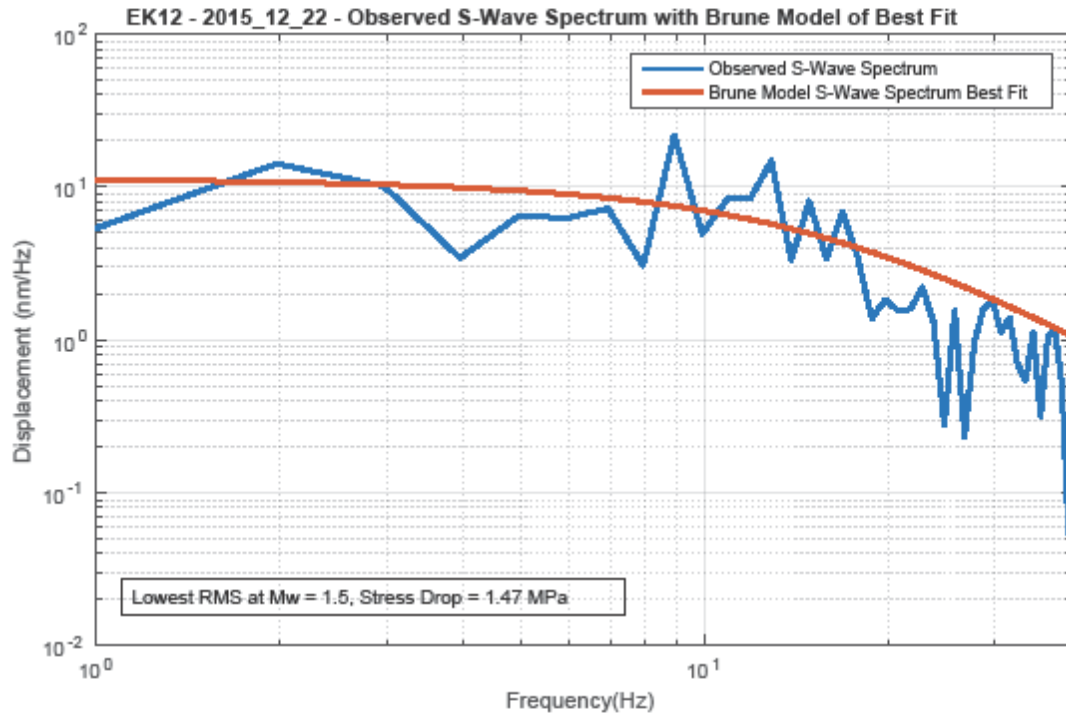
B.3.3 – November 29, 2015 Event with Brune (1970) Model of Best Fit

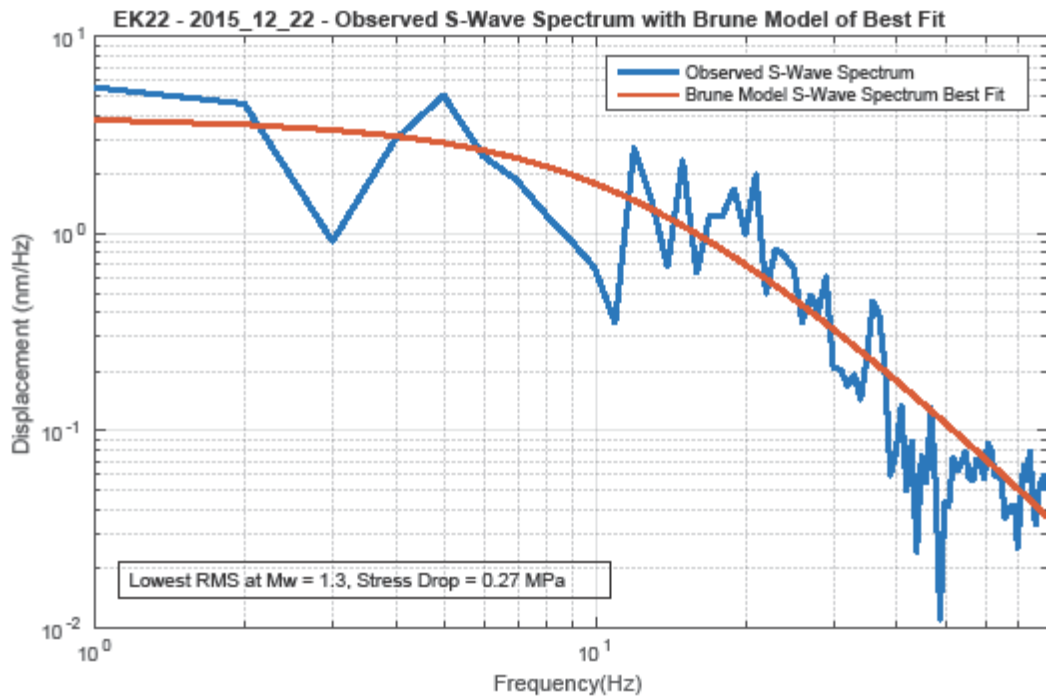
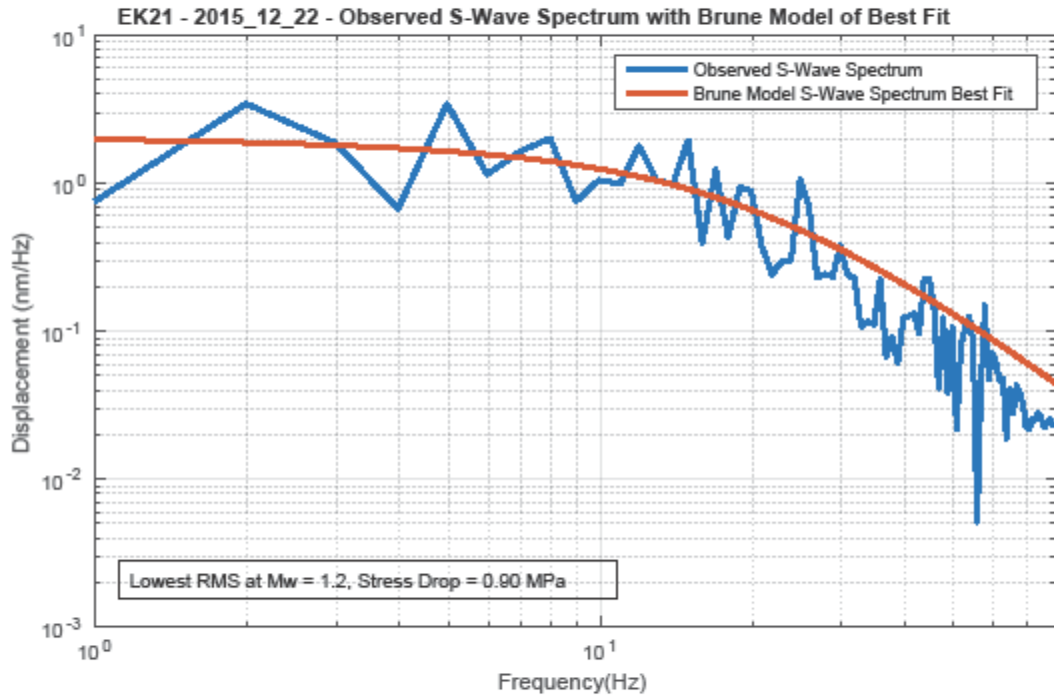


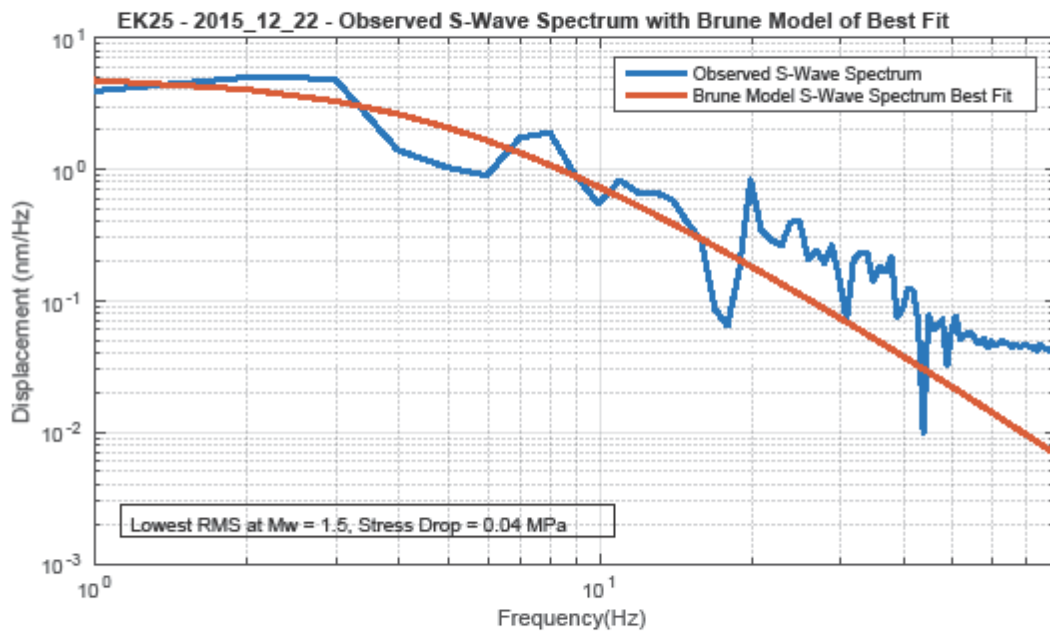




B.3.4 – December 22, 2015 Event with Brune (1970) Model of Best Fit



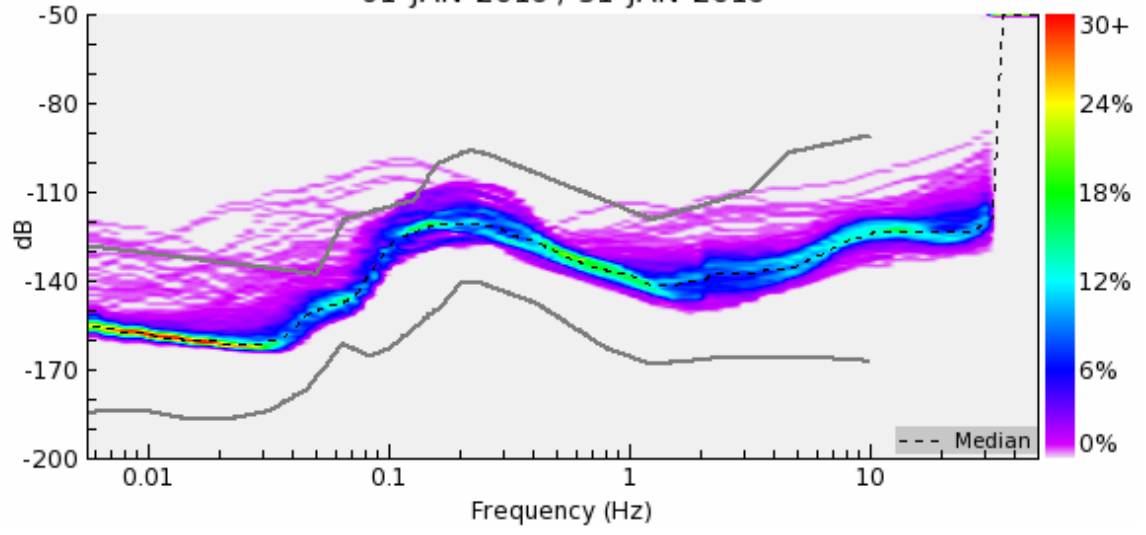




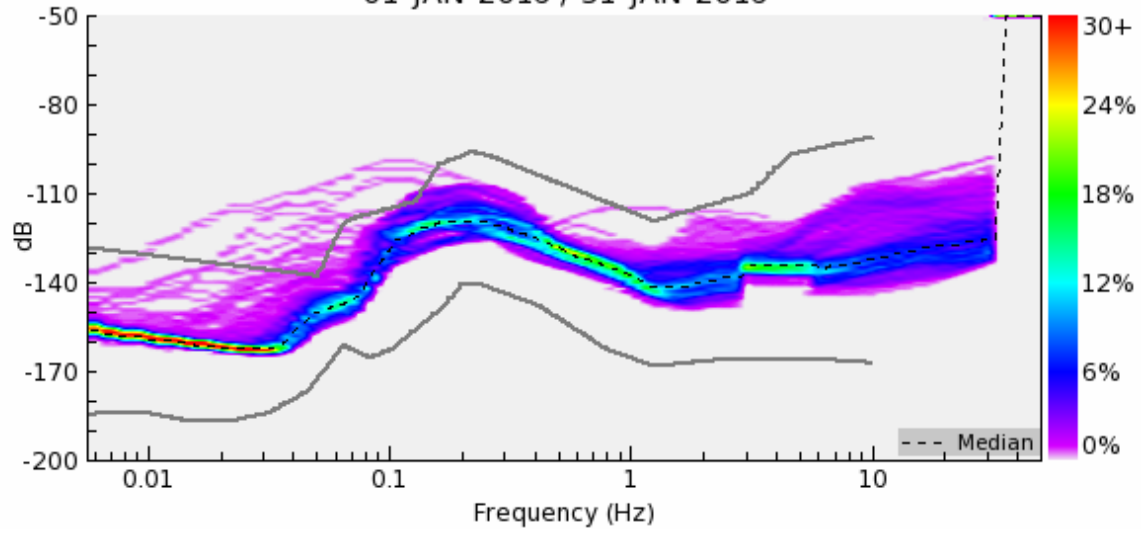
Appendix C: Power Spectral Density Probability Density Function Noise Plots

Y axis is in units of dB with respect to acceleration squared per Hz ($(\text{m/s}^2)^2/\text{Hz}$). Date ranges of PDFs and number of PSDs used are listed at top of graph. The New Low Noise Model (NLNM) and the New High Noise Model (NHNM) (McNamara, Buland, 2004) are shown in gray. Median noise data is shown as dashed line over plot. The following noise plots from PQLX for the Daytime hours(1100-2300 UTC).

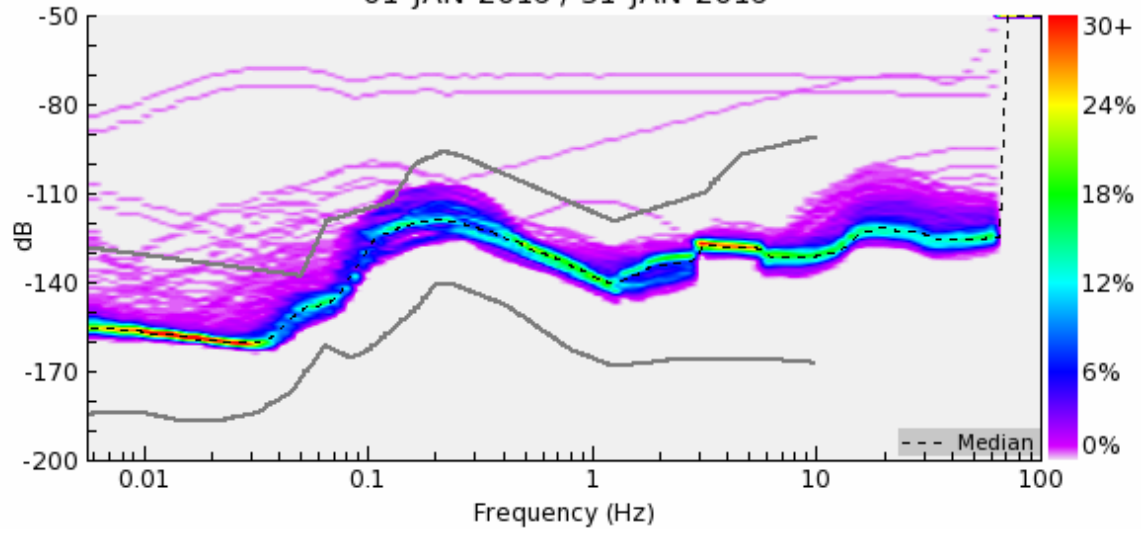
KY.EK12.00.HHZ : 775 PSDs
01-JAN-2016 / 31-JAN-2016



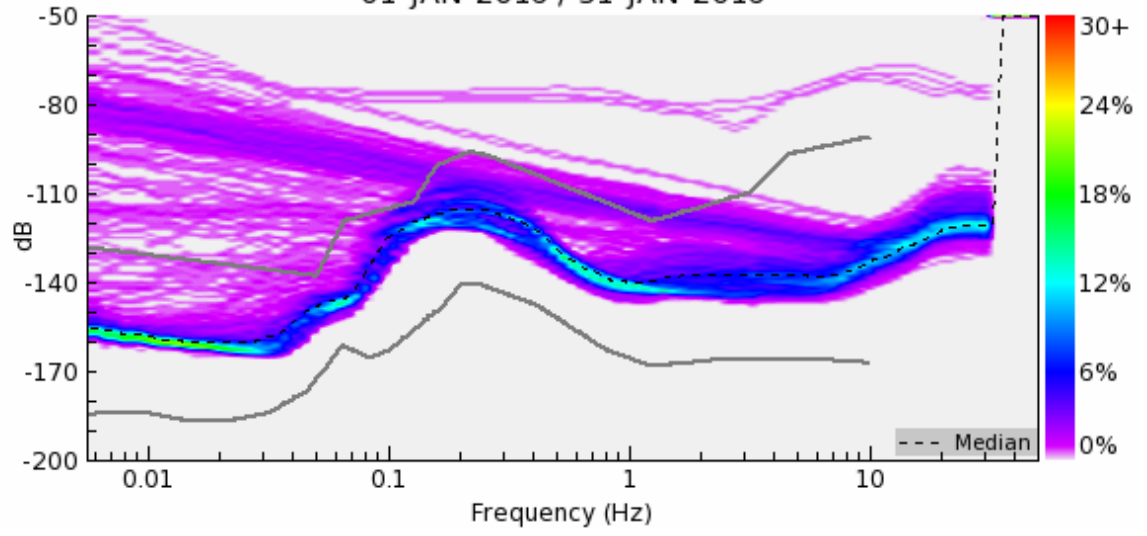
KY.EK13.00.HHZ : 763 PSDs
01-JAN-2016 / 31-JAN-2016



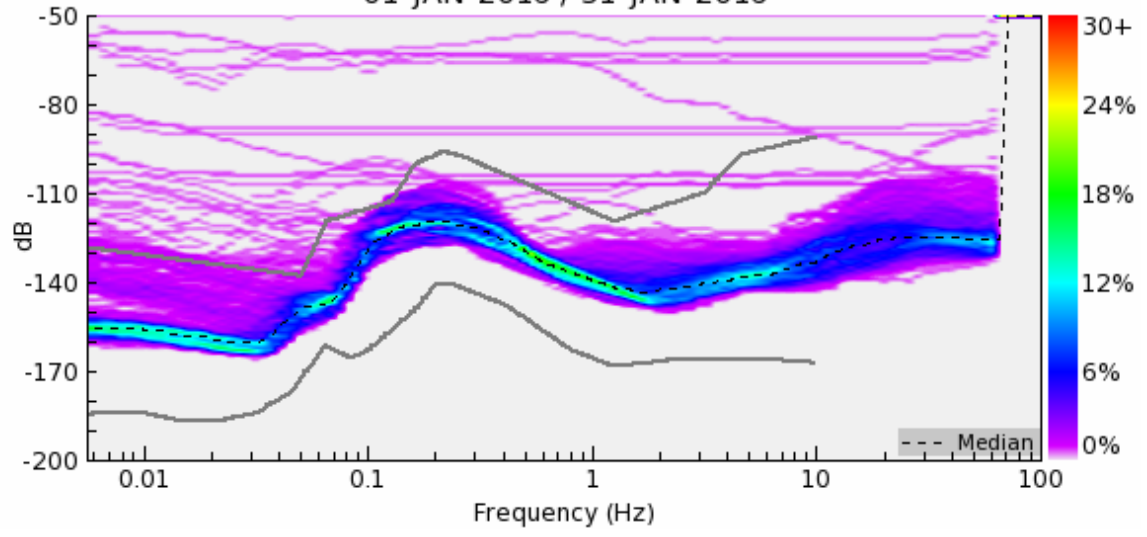
KY.EK14.00.HHZ : 773 PSDs
01-JAN-2016 / 31-JAN-2016



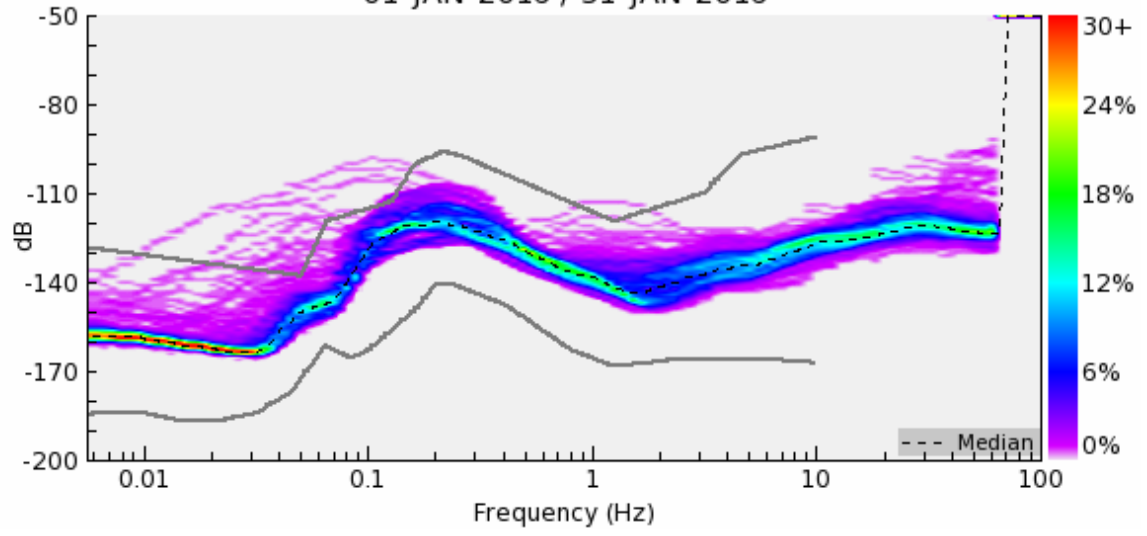
KY.EK20.00.HHZ : 775 PSDs
01-JAN-2016 / 31-JAN-2016



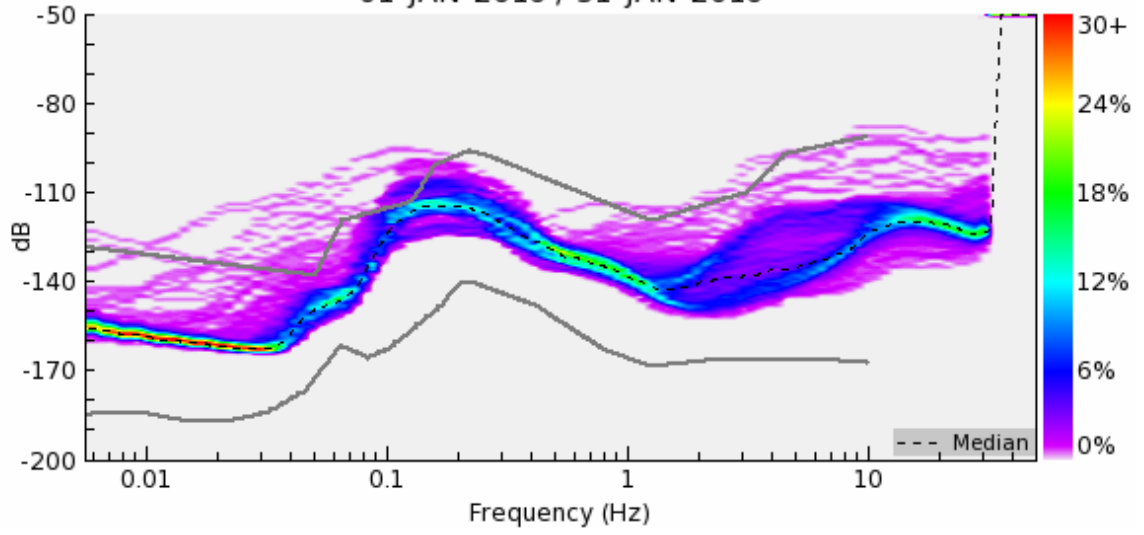
KY.EK21.00.HHZ : 773 PSDs
01-JAN-2016 / 31-JAN-2016



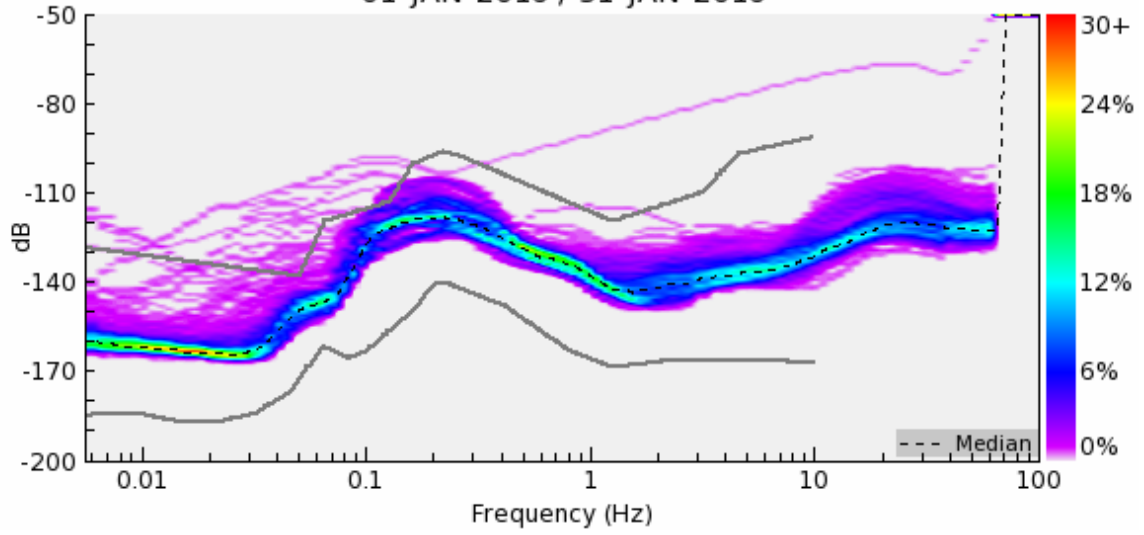
KY.EK22.00.HHZ : 775 PSDs
01-JAN-2016 / 31-JAN-2016



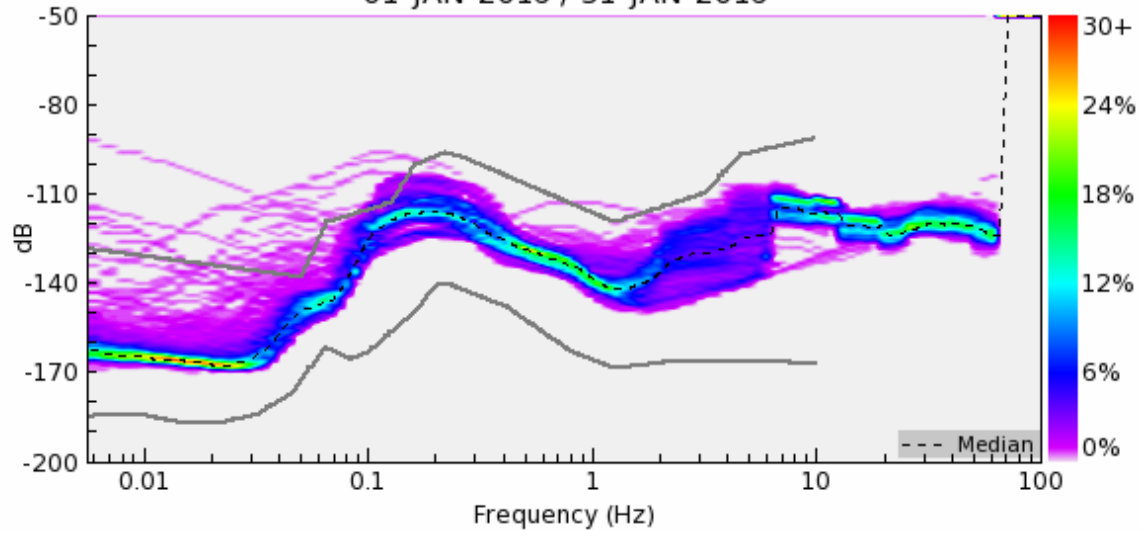
KY.EK23.00.HHZ : 768 PSDs
01-JAN-2016 / 31-JAN-2016



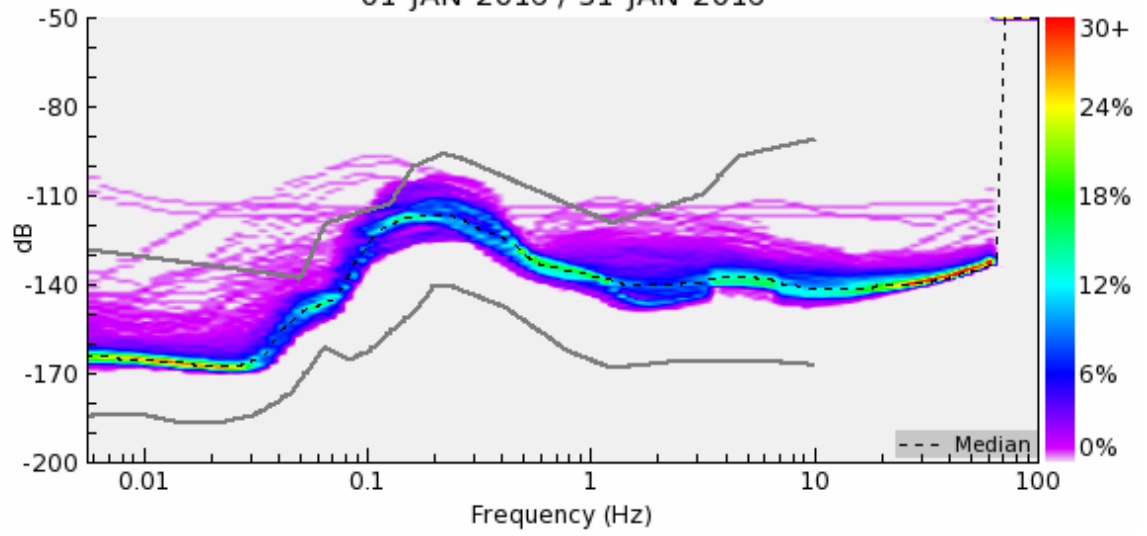
KY.EK25.00.HHZ : 773 PSDs
01-JAN-2016 / 31-JAN-2016



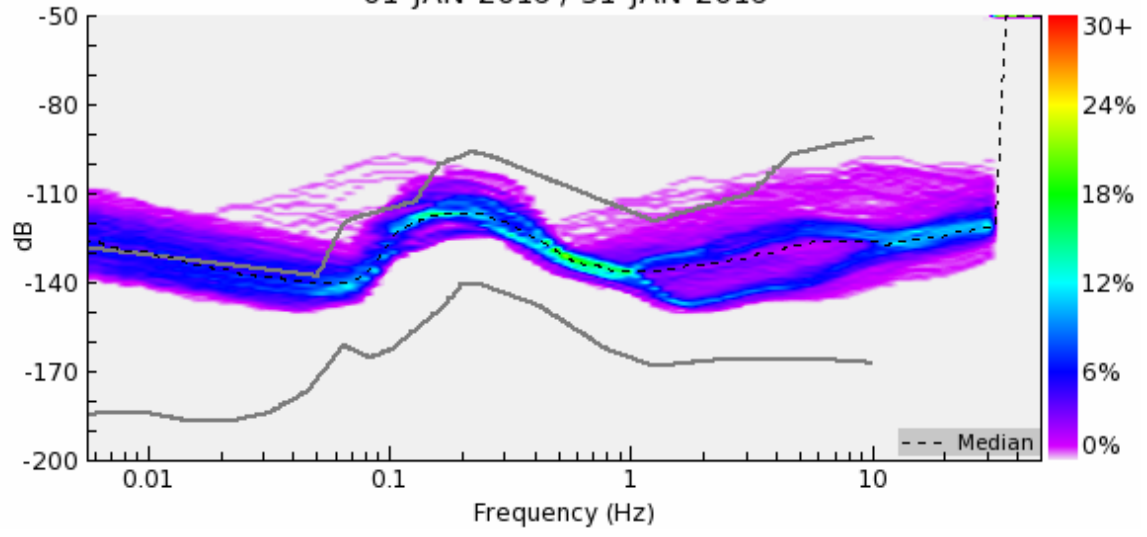
KY.EK26.00.HHZ : 774 PSDs
01-JAN-2016 / 31-JAN-2016



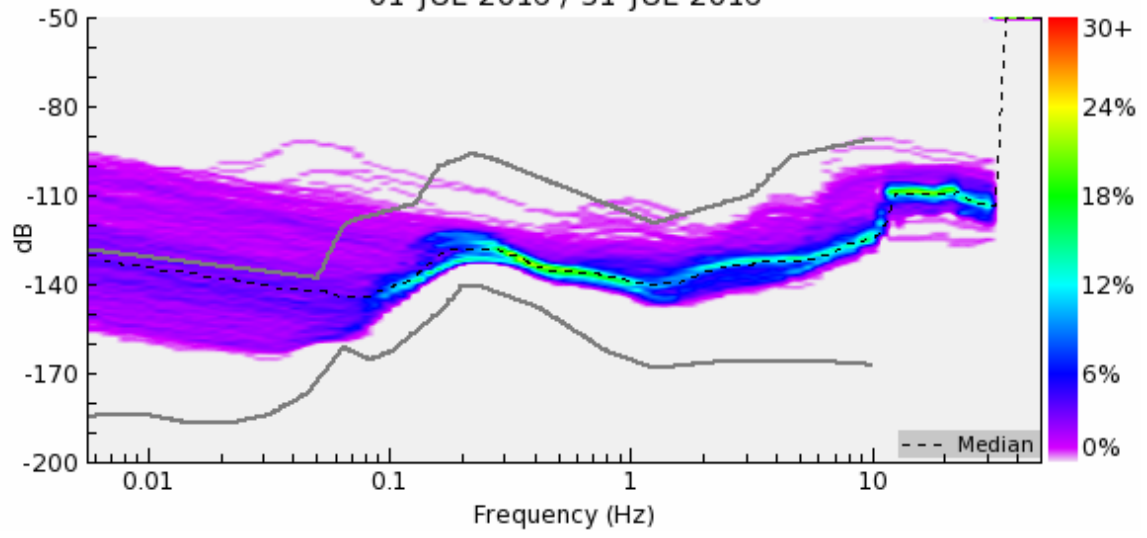
KY.EK32.00.HHZ : 775 PSDs
01-JAN-2016 / 31-JAN-2016



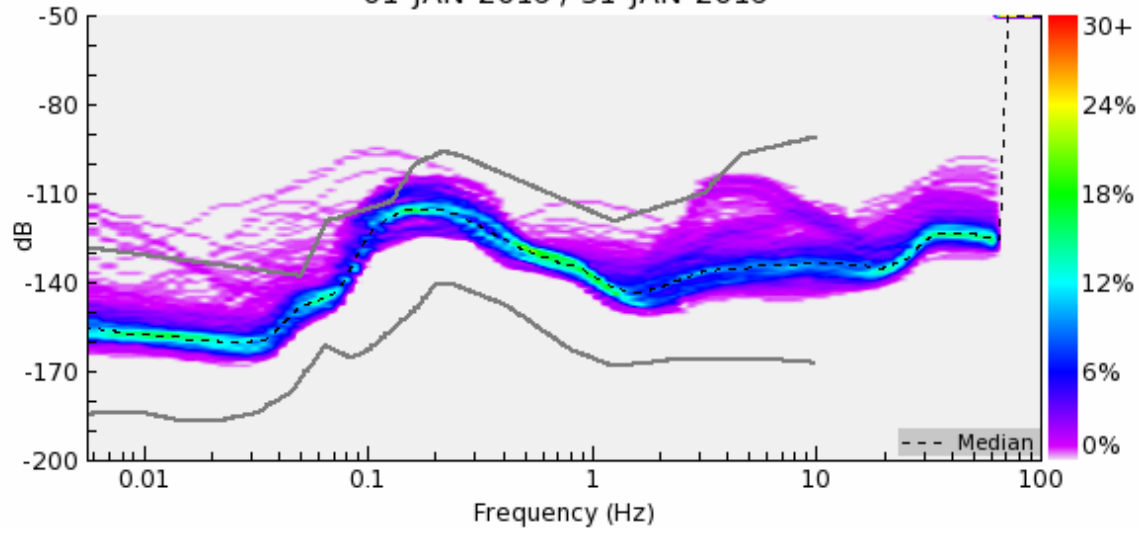
KY.EK33.00.HHZ : 767 PSDs
01-JAN-2016 / 31-JAN-2016



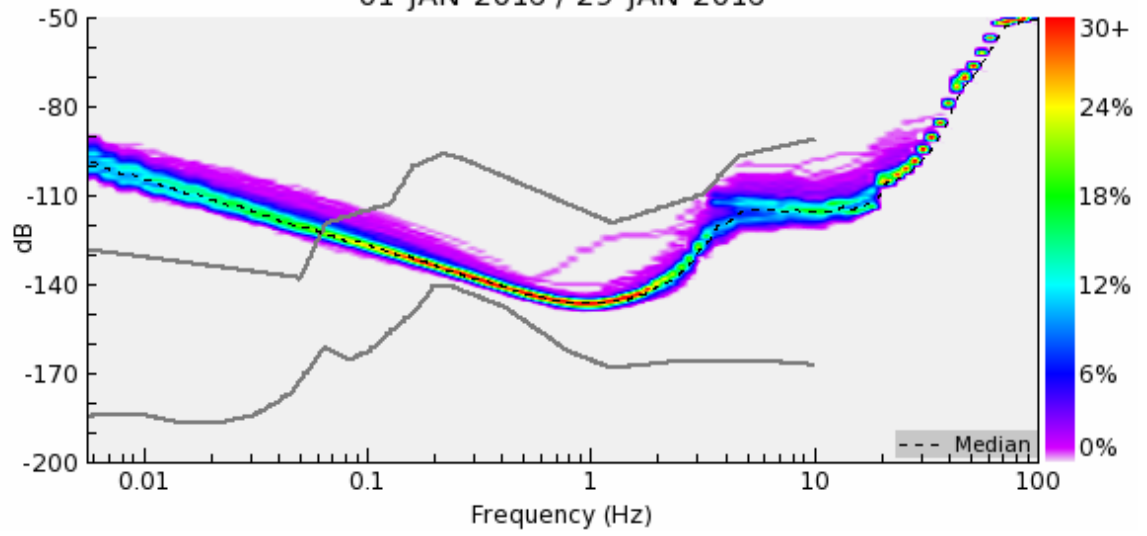
KY.EK34.00.HHZ : 775 PSDs
01-JUL-2016 / 31-JUL-2016



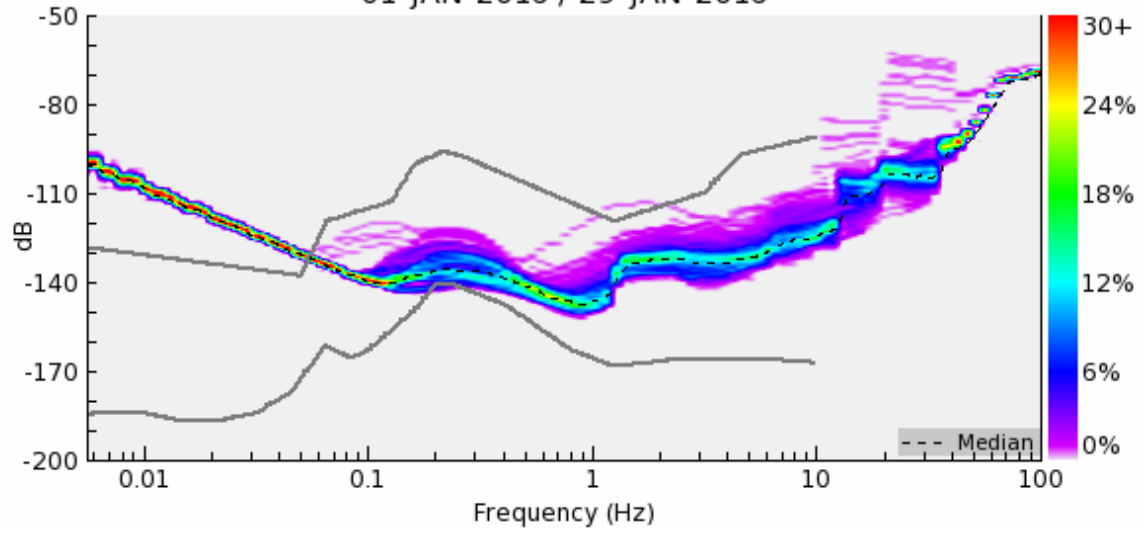
KY.EK35.00.HHZ : 771 PSDs
01-JAN-2016 / 31-JAN-2016



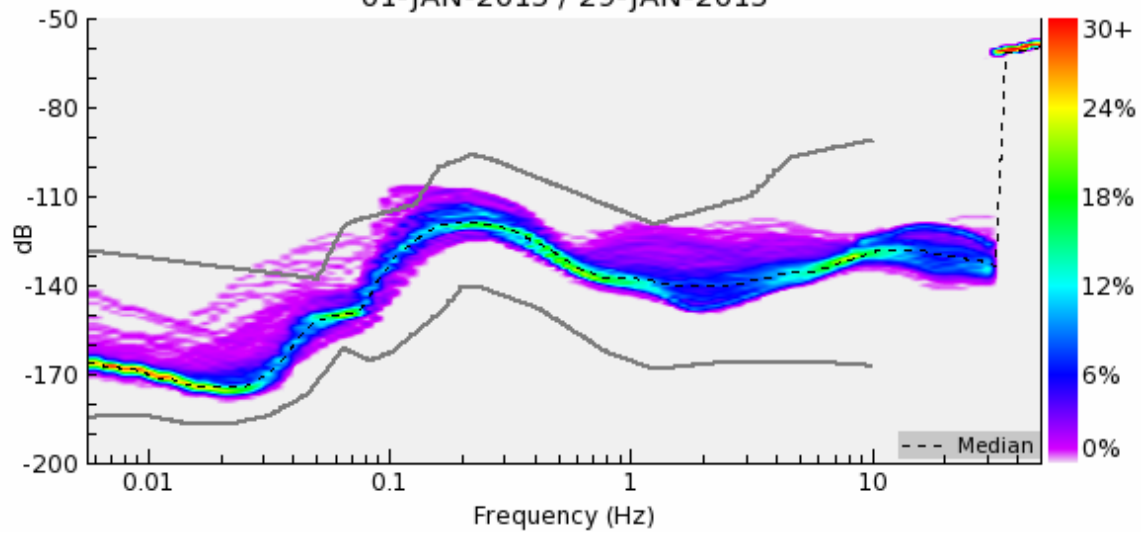
KY.PKKY.10.EHZ : 673 PSDs
01-JAN-2016 / 29-JAN-2016



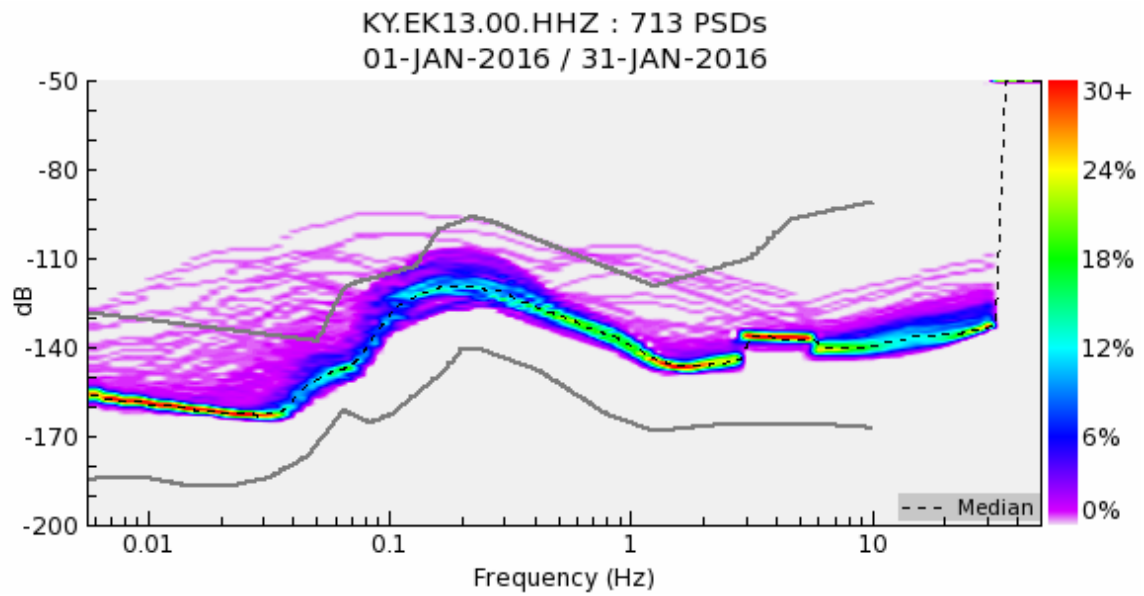
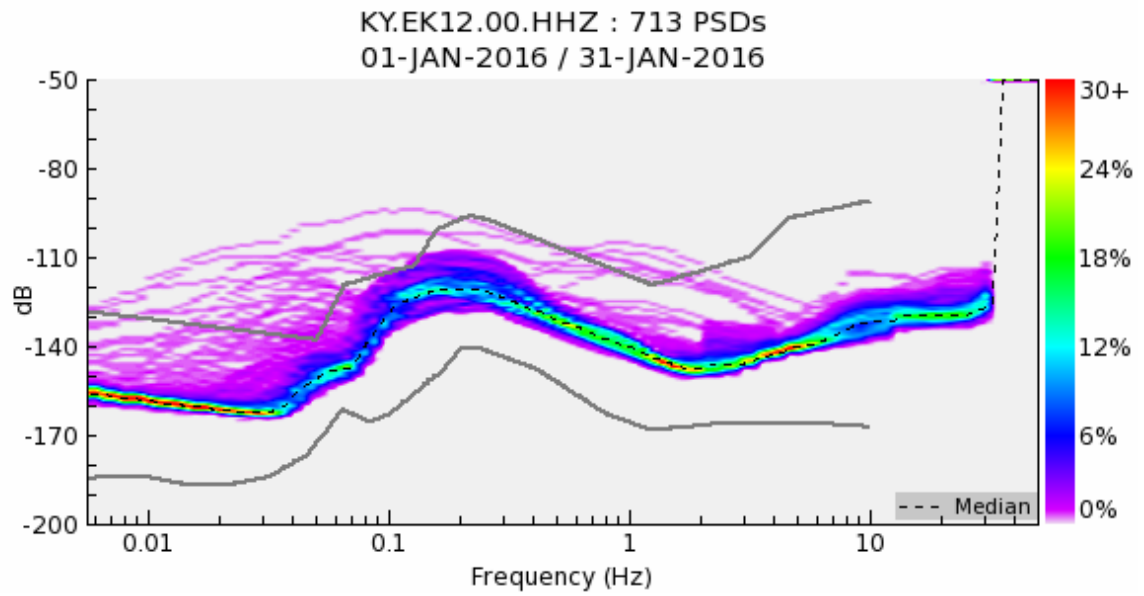
KY.ROKY.10.EHZ : 676 PSDs
01-JAN-2016 / 29-JAN-2016



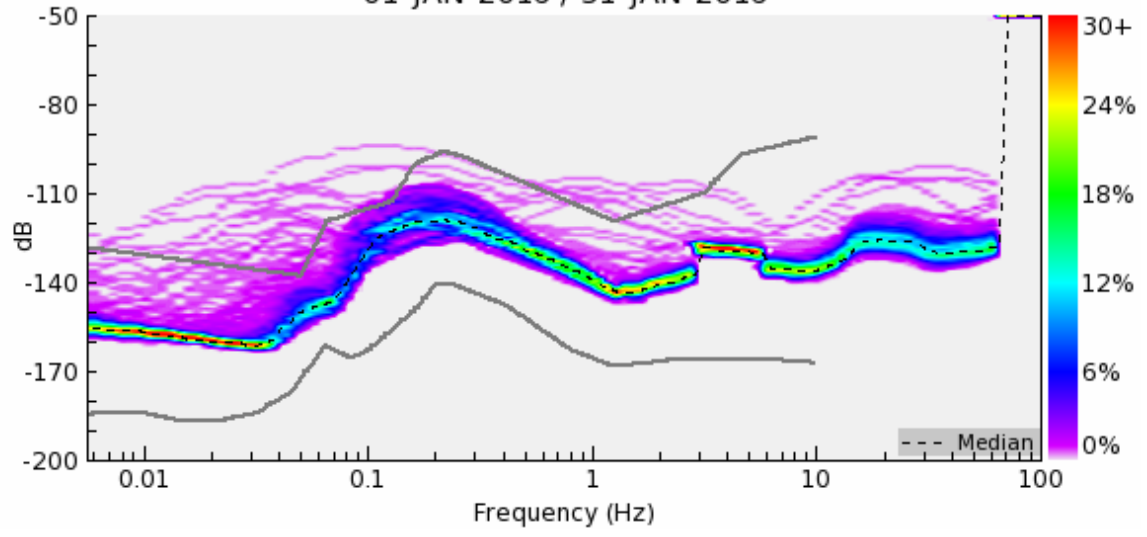
N4.S51A.--.HHZ : 696 PSDs
01-JAN-2015 / 29-JAN-2015



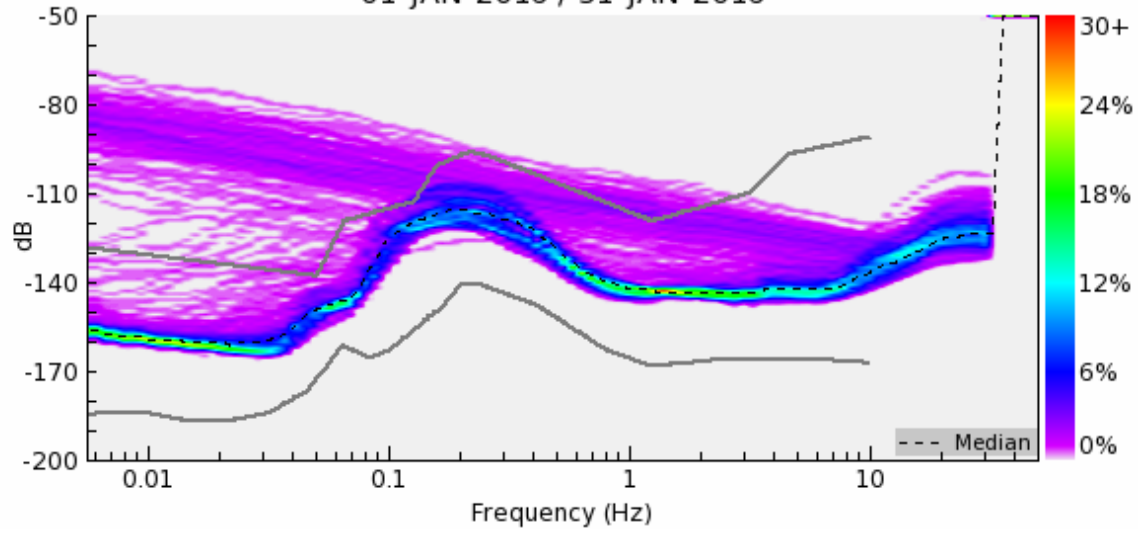
The following noise plots are for the nighttime hours from 0000-1100 UTC.



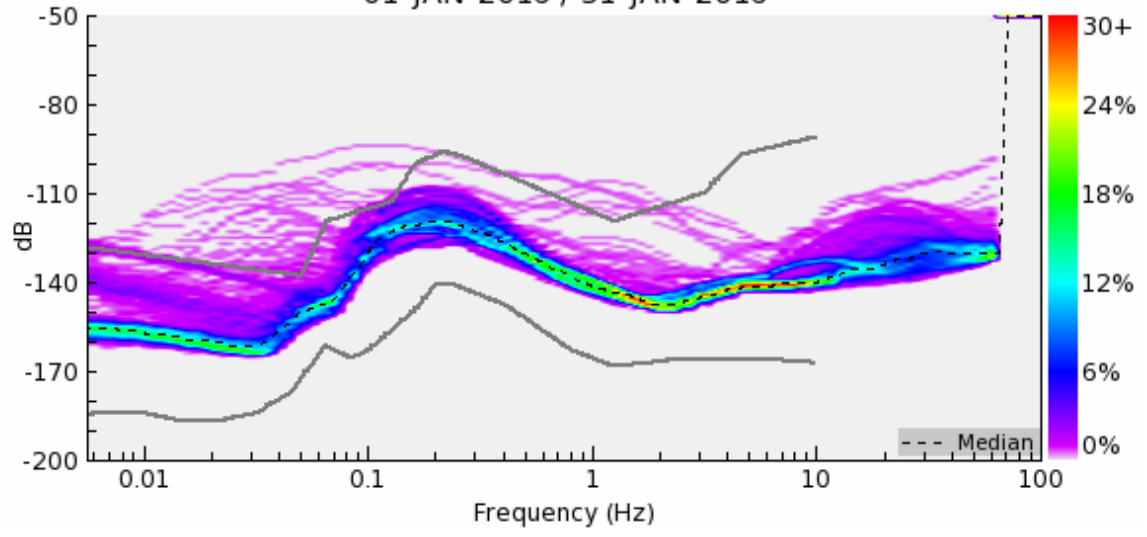
KY.EK14.00.HHZ : 713 PSDs
01-JAN-2016 / 31-JAN-2016



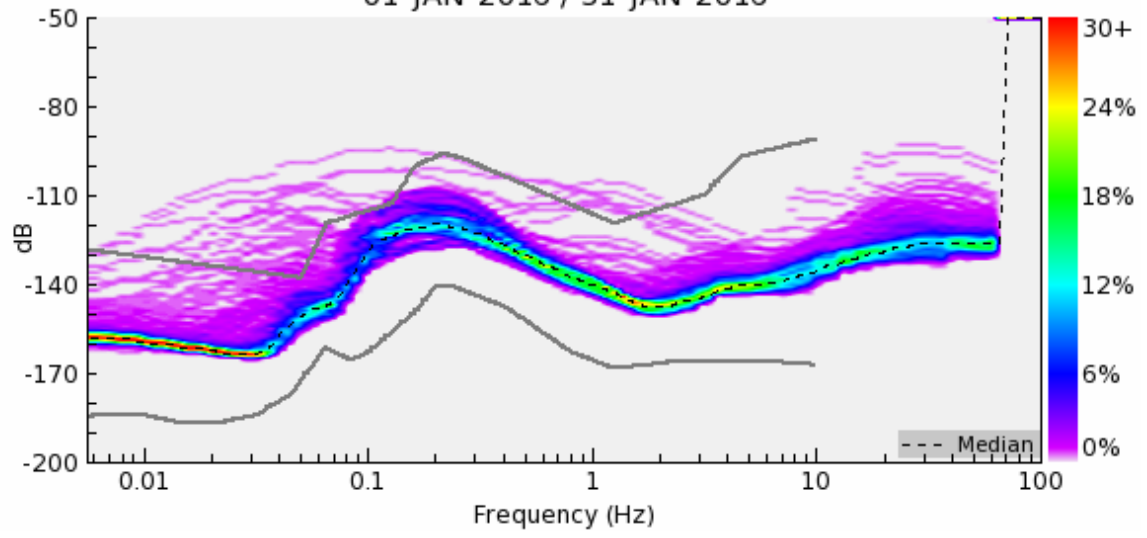
KY.EK20.00.HHZ : 713 PSDs
01-JAN-2016 / 31-JAN-2016



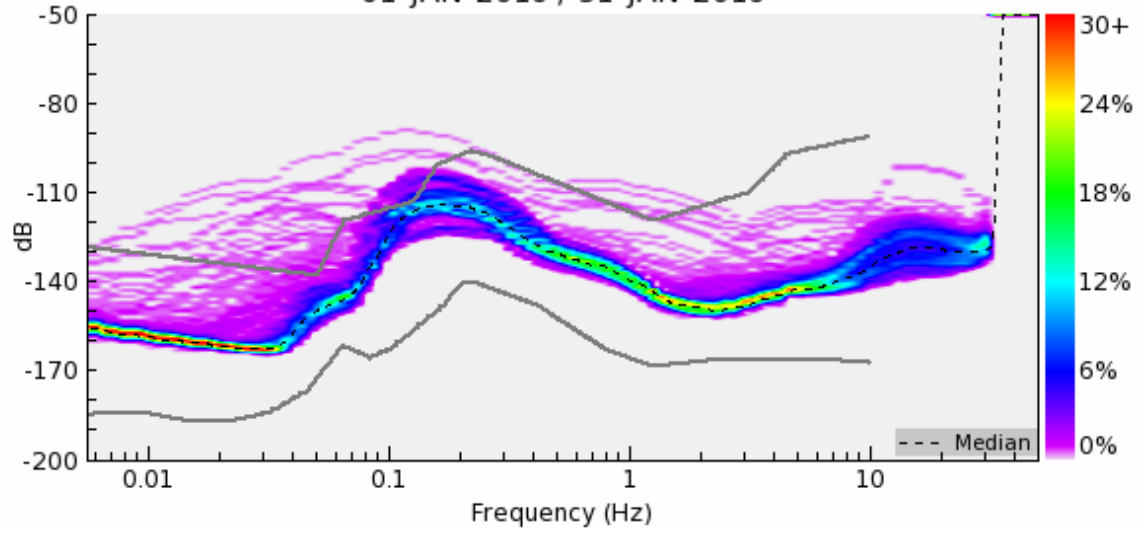
KY.EK21.00.HHZ : 713 PSDs
01-JAN-2016 / 31-JAN-2016



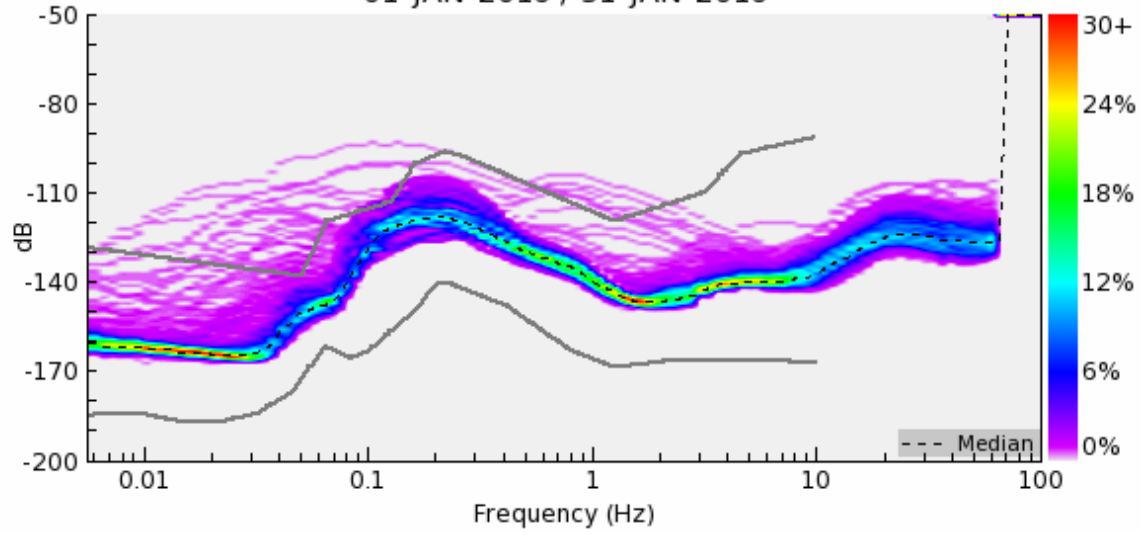
KY.EK22.00.HHZ : 712 PSDs
01-JAN-2016 / 31-JAN-2016



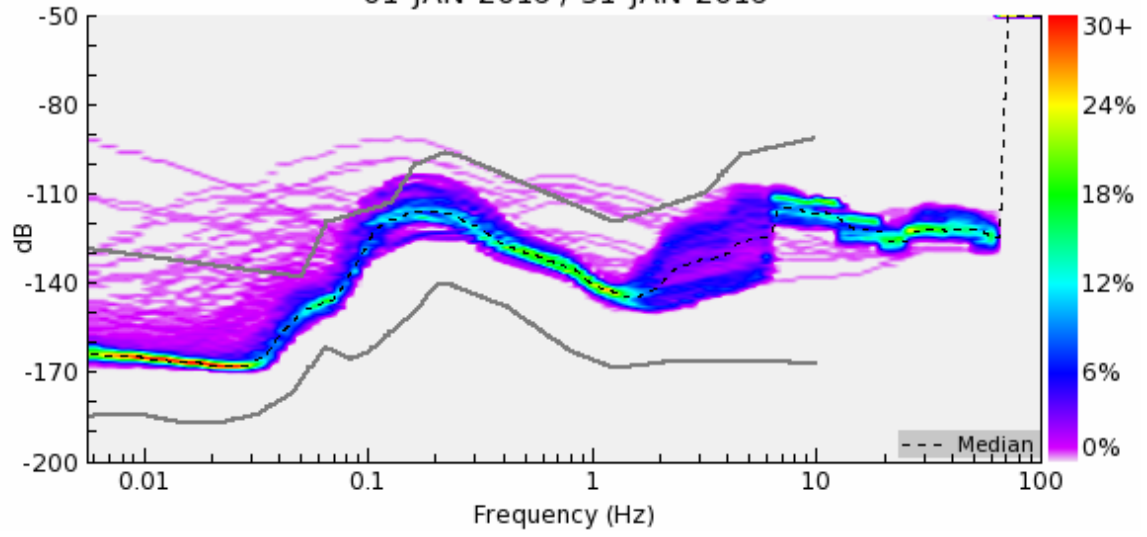
KY.EK23.00.HHZ : 713 PSDs
01-JAN-2016 / 31-JAN-2016



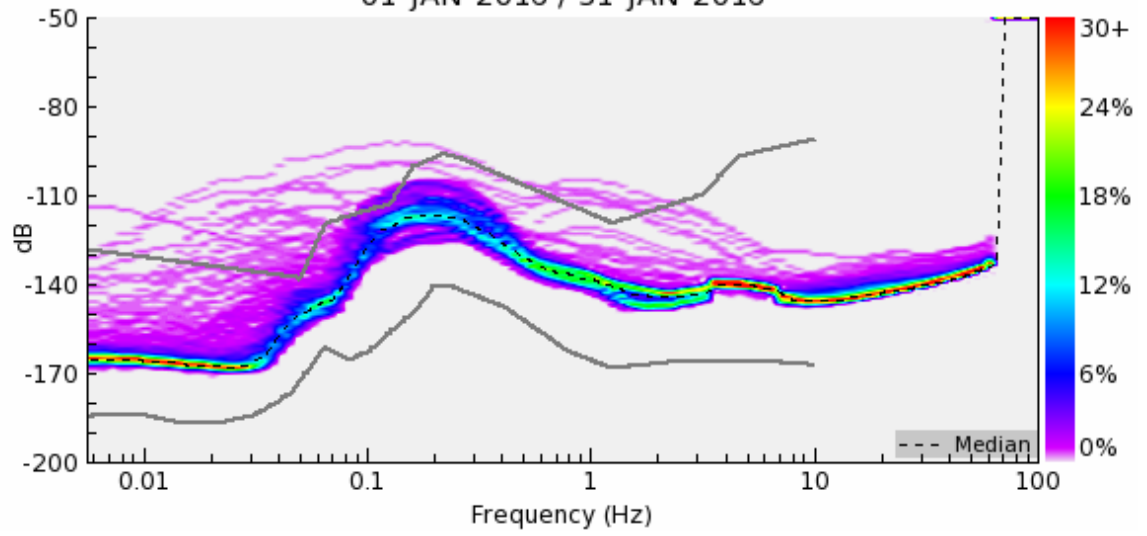
KY.EK25.00.HHZ : 713 PSDs
01-JAN-2016 / 31-JAN-2016



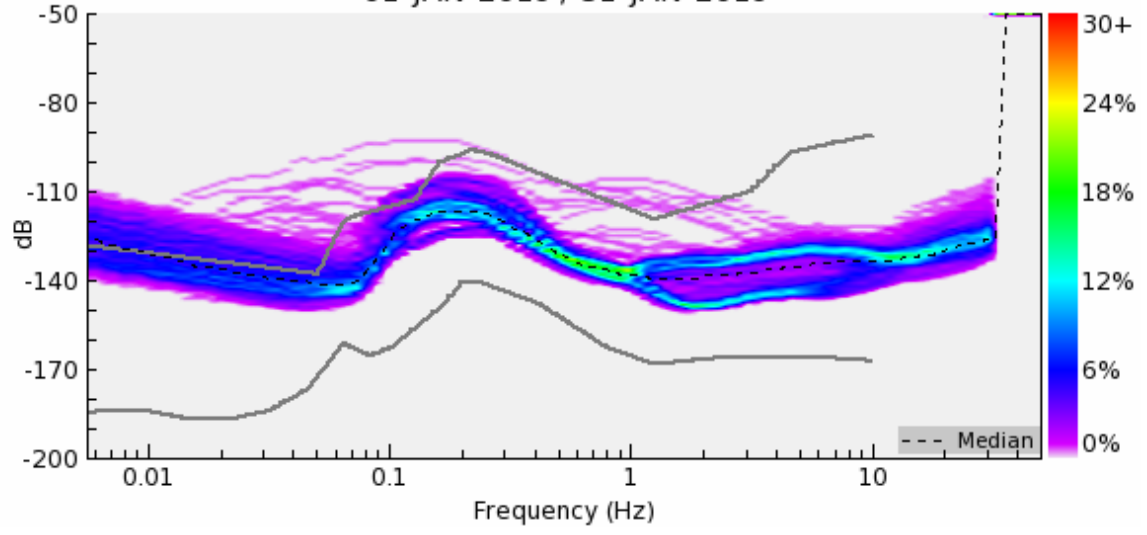
KY.EK26.00.HHZ : 713 PSDs
01-JAN-2016 / 31-JAN-2016



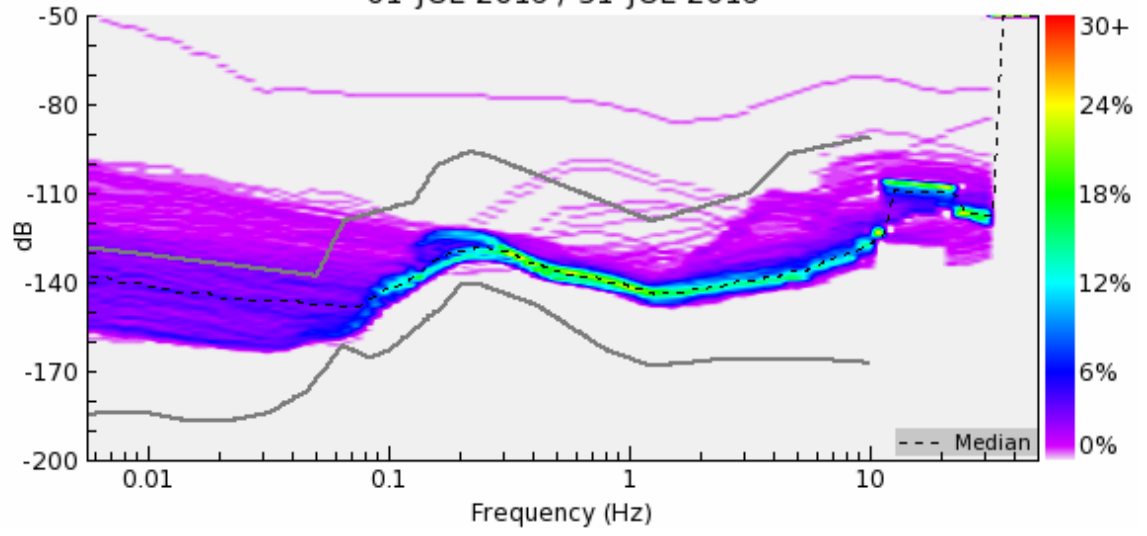
KY.EK32.00.HHZ : 713 PSDs
01-JAN-2016 / 31-JAN-2016



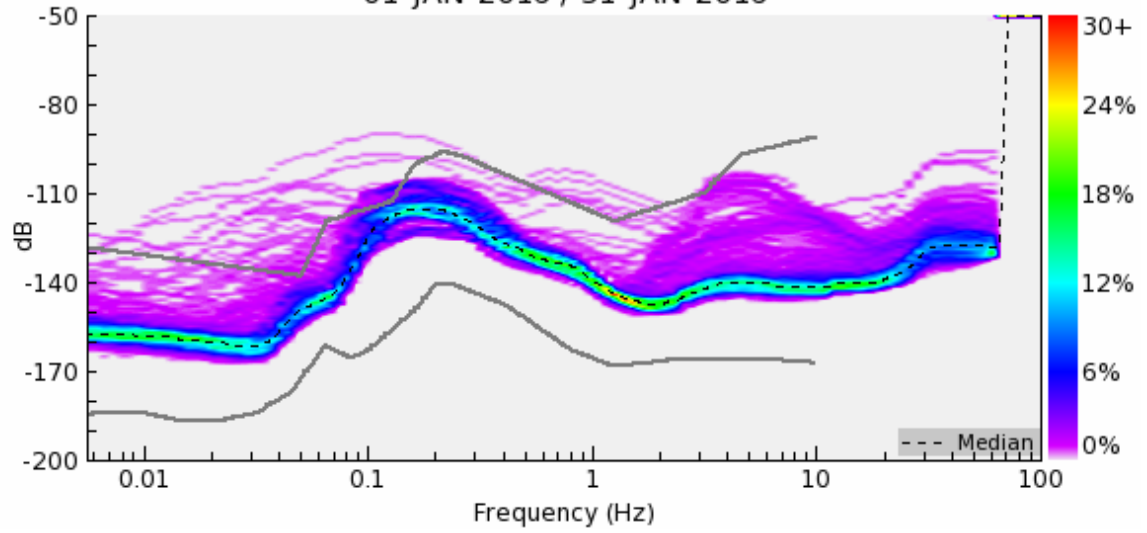
KY.EK33.00.HHZ : 713 PSDs
01-JAN-2016 / 31-JAN-2016



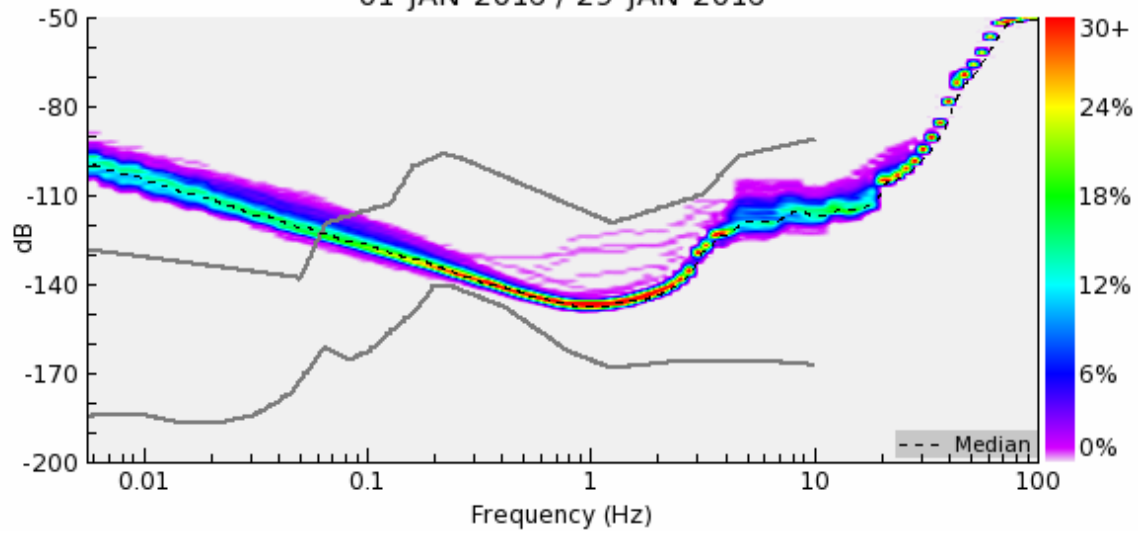
KY.EK34.00.HHZ : 713 PSDs
01-JUL-2016 / 31-JUL-2016



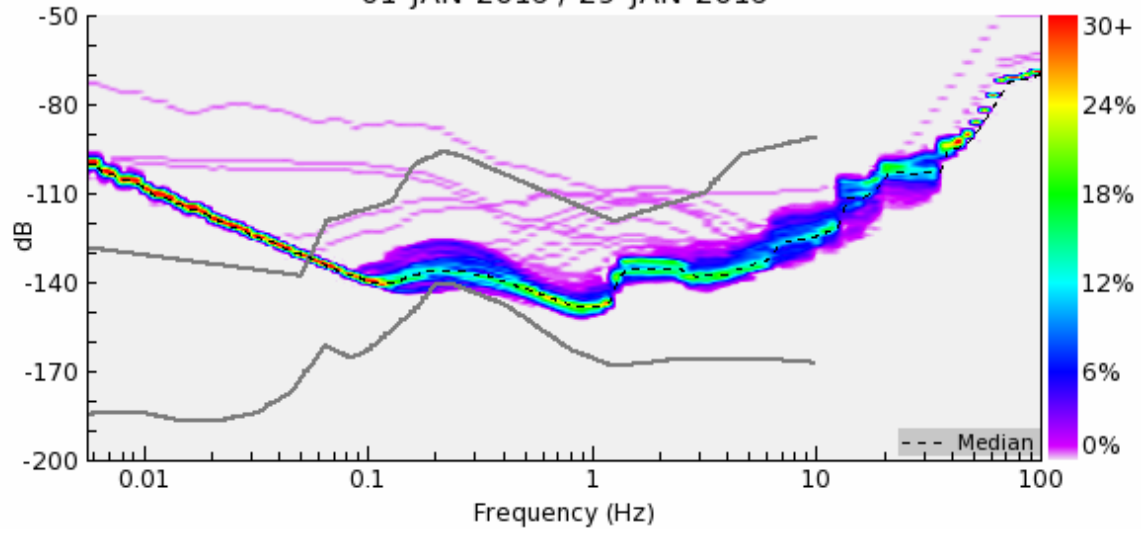
KY.EK35.00.HHZ : 713 PSDs
01-JAN-2016 / 31-JAN-2016



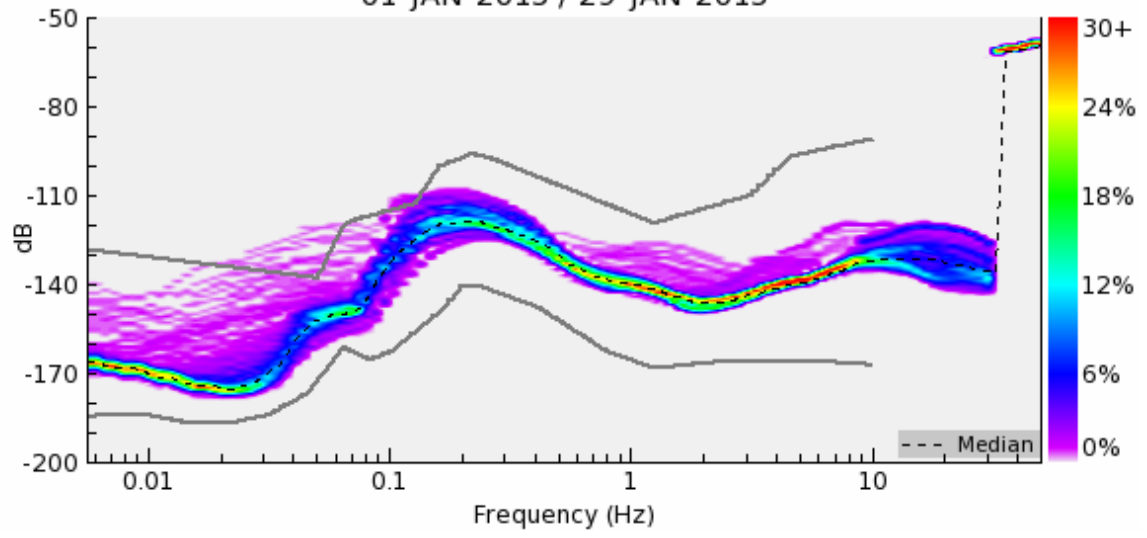
KY.PKKY.10.EHZ : 616 PSDs
01-JAN-2016 / 29-JAN-2016



KY.ROKY.10.EHZ : 622 PSDs
01-JAN-2016 / 29-JAN-2016



N4.S51A.--.HHZ : 639 PSDs
01-JAN-2015 / 29-JAN-2015



Appendix D: Local Magnitude Calculations

Local magnitudes were determined using the zero-to-peak amplitude measurements from the horizontal channels of each seismometer that was triggered for each event. The median of all local magnitude values listed below was used as a final local magnitude. MAD is an abbreviation for median absolute deviation and is used throughout this appendix.

D. 1 – Event Table for Local Magnitudes

Event	Date (mm/dd/yyyy)	Origin Time (UTC)	Latitude (Decimal Degrees)	Longitude (Decimal Degrees)	Depth (km)	M _L	M _L MAD
1	6/27/2015	7:16:25	38.634	-82.917	3.5	1.2	0.161
2	7/3/2015	5:20:53	36.867	-83.729	22.5	1.1	0.117
3	8/20/2015	2:45:41	37.999	-84.836	34.6	2.3	0.248
4	10/18/2015	7:24:11	38.725	-82.555	0.1	1.2	0.124
5	11/29/2015	1:27:30	38.235	-83.223	21.8	1.9	0.153
6	12/13/2015	0:41:18	38.674	-83.990	4.8	1.1	0.103
7	12/22/2015	15:20:33	38.260	-83.417	0.8	1.9	0.210
8	2/2/2016	8:09:03	38.335	-84.392	34.0	1.3	0.191
9	2/24/2016	3:30:05	38.535	-83.840	4.8	1.6	0.185
10	3/8/2016	14:25:29	38.911	-82.443	18.4	1.8	0.112
11	4/26/2016	19:24:04	38.123	-83.510	3.5	1.8	0.177
12	5/27/2016	6:04:18	38.789	-82.426	12.3	1.1	0.062

D. 2 – Event 1

Station Name	Station Channel	Amplitude (nm)	Distance (km)	M_L	MAD
EK14	N	30.3	41.5	1.7	0.5077
EK14	E	33.1	41.5	1.7	0.5461
EK25	N	12.4	56	1.4	0.1861
EK25	E	10.5	56	1.3	0.1138
EK35	N	4.7	88.1	1.0	0.1375
EK35	E	4.3	88.1	1.0	0.1761
S51A	N	4.2	125	1.1	0.1138
S51A	E	3.9	125	1.0	0.1460

D. 3 – Event 2

Station Name	Station Channel	Amplitude (nm)	Distance (km)	M_L	MAD
S51A	N	7.2	86.5	1.2	0.117
S51A	E	4.2	86.5	1.0	0.117

D. 4 – Event 3

Station Name	Station Channel	Amplitude (nm)	Distance (km)	M_L	MAD
EK14	N	106.2	190	2.5	0.294
EK14	E	72.6	190	2.4	0.129
EK25	N	73	178	2.4	0.119
EK25	E	95.9	178	2.5	0.238
EK26	N	26.4	198	1.9	0.303
EK26	E	29.2	198	2.0	0.259
EK35	N	41.3	187	2.1	0.119
EK35	E	23.7	187	1.9	0.360

D. 5 – Event 4

Station Name	Station Channel	Amplitude (nm)	Distance (km)	M_L	MAD
EK14	N	52.6	48.9	2.0	0.734
EK14	E	67.8	48.9	2.1	0.844
EK21	N	5.9	132	1.2	0.005
EK21	E	6.3	132	1.2	0.023
EK22	N	3.7	109	1.0	0.247
EK22	E	4.8	109	1.1	0.134
EK25	N	24.8	69.2	1.7	0.483
EK25	E	27.2	69.2	1.7	0.523
EK26	N	5.1	72.7	1.0	0.193
EK26	E	6.1	72.7	1.1	0.115
EK32	N	5.9	139	1.2	0.005
EK32	E	5.3	139	1.2	0.041
EK35	N	8.3	97.3	1.3	0.081
EK35	E	8.7	97.3	1.3	0.101
S51A	N	4.4	150	1.1	0.107
S51A	E	4.1	150	1.1	0.138

D. 6 – Event 5

Station Name	Station Channel	Amplitude (nm)	Distance (km)	M_L	MAD
EK21	N	80	53.8	2.2	0.242
EK21	E	95.7	53.8	2.2	0.320
EK23	N	46.5	44.8	1.9	0.034
EK23	E	62.3	44.8	2.0	0.093
EK25	N	90.7	37.4	2.1	0.215
EK25	E	125.9	37.4	2.3	0.358
EK26	N	46.8	59.1	2.0	0.029
EK26	E	41	59.1	1.9	0.027
EK32	N	31.3	68.6	1.8	0.112
EK32	E	19.6	68.6	1.6	0.315
EK33	N	48.9	53.6	1.9	0.027
EK33	E	57.4	53.6	2.0	0.097
EK35	N	21.4	61.2	1.6	0.302
EK35	E	18.6	61.2	1.6	0.363
EK22	E	48.9	35.6	1.9	0.063
EK22	N	36.2	35.6	1.7	0.194

D. 7 – Event 6

Station Name	Station Channel	Amplitude (nm)	Distance (km)	M_L	MAD
EK12	N	5.6	98.2	1.1	0.008
EK12	E	4.9	98.2	1.1	0.050
EK13	N	6	113	1.2	0.067
EK13	E	5.7	113	1.2	0.045
EK14	N	7.9	7.9	0.7	0.409
EK20	N	4.2	105	1.0	0.103
EK21	N	8.5	103	1.3	0.199
EK21	E	8.2	103	1.3	0.184
EK22	N	5.3	106	1.1	0.000
EK22	E	4.4	106	1.0	0.081
EK23	N	3.4	127	1.0	0.156
EK32	N	2.5	132	0.8	0.282
EK32	E	2.6	132	0.9	0.265
S51A	N	6.6	120	1.3	0.121
S51A	E	5.2	120	1.1	0.017

D. 8 – Event 7

Station Name	Station Channel	Amplitude (nm)	Distance (km)	M_L	MAD
EK25	N	47.1	54.5	1.9	0.0346
EK25	E	55.1	54.5	2.0	0.1027
EK26	N	28	76.2	1.8	0.1185
EK26	E	24.2	76.2	1.7	0.1818
EK32	N	23.5	71.8	1.7	0.2073
EK32	E	20.4	71.8	1.6	0.2688
EK35	N	28.6	76.2	1.8	0.1092
EK35	E	16.5	76.2	1.6	0.3481
FLKY	E	121.2	34.5	2.2	0.3432
R50A	N	15.4	79.7	1.5	0.3685
R50A	E	5.111	79.7	1.1	0.8475
S51A	N	31.4	70.7	1.8	0.0848
S51A	E	32.4	70.7	1.8	0.0712
EK12	N	396.2	31	2.7	0.8335
EK12	E	331.6	31	2.7	0.7562
EK13	N	98.9	51.6	2.2	0.3447
EK13	E	58.5	51.6	2.0	0.1166
EK14	N	47.2	62.5	2.0	0.0655
EK14	E	52	62.5	2.0	0.1075
EK20	N	2.34	70.6	0.7	1.2128
EK20	E	42.4	70.6	1.9	0.0453
EK21	N	105.3	50.3	2.3	0.3663
EK21	E	73.5	50.3	2.1	0.2101
EK22	N	83.5	41	2.1	0.2201
EK22	E	50.3	41	1.9	0.0000
EK23	N	17.2	58.9	1.5	0.3859
EK23	E	16.2	58.9	1.5	0.4119

D. 9 – Event 8

Station Name	Station Channel	Amplitude (nm)	Distance (km)	M_L	MAD
EK12	N	18.3	115	1.7	0.3520
EK12	E	17.1	115	1.7	0.3226
EK13	N	11	137	1.5	0.1663
EK13	E	7.5	137	1.3	0.0000
EK14	N	21	148	1.8	0.4624
EK20	E	8.7	81.1	1.3	0.0440
EK23	N	4.8	139	1.1	0.1909
EK23	E	3.5	139	1.0	0.3281
EK25	N	15.5	140	1.7	0.3196
EK25	E	8	140	1.4	0.0323
EK26	N	8.8	161	1.4	0.1011
EK26	E	5.4	161	1.2	0.1110
EK32	E	5.1	124	1.1	0.1875
S51A	N	5.2	104	1.1	0.2151
S51A	E	4.6	104	1.1	0.2684

D. 10 – Event 9

Station Name	Station Channel	Amplitude (nm)	Distance (km)	M_L	MAD
EK13	N	20.9	94.6	1.7	0.113
EK13	E	18.9	94.6	1.7	0.069
EK14	N	25.7	103	1.8	0.220
EK20	N	9.1	89	1.3	0.261
EK20	E	12.6	89	1.5	0.120
EK22	N	31.4	86	1.9	0.269
EK22	E	14.4	86	1.5	0.069
EK25	N	20.3	100	1.7	0.112
EK25	E	22.2	100	1.7	0.151
EK26	N	6.1	122	1.2	0.369
S51A	N	6.5	102	1.2	0.379
S51A	E	5.2	102	1.1	0.476

D. 11 – Event 10

Station Name	Station Channel	Amplitude (nm)	Distance (km)	M_L	MAD
EK13	N	44.1	82.7	2.0	0.215
EK13	E	37.2	82.7	1.9	0.141
EK14	N	106.8	71.5	2.4	0.568
EK14	E	187.8	71.5	2.6	0.813
EK20	N	16.1	180	1.7	0.066
EK20	E	17.2	180	1.7	0.037
EK22	N	24.9	131	1.8	0.062
EK22	E	24.7	131	1.8	0.058
EK25	N	164.1	91.9	2.6	0.808
EK25	E	200.5	91.9	2.7	0.895
EK26	N	10.1	94	1.4	0.398
EK26	E	13.6	94	1.5	0.269
EK32	N	16.2	162	1.7	0.083
EK32	E	14.1	162	1.6	0.143
EK33	N	20.4	141	1.8	0.010
EK33	E	22.1	141	1.8	0.025
EK35	N	17.5	119	1.7	0.111
EK35	E	23.1	119	1.8	0.010
S51A	N	15.5	173	1.7	0.090
S51A	E	14.7	173	1.7	0.113

D. 12 – Event 11

Station Name	Station Channel	Amplitude (nm)	Distance (km)	M_L	MAD
EK22	HE	134.6	32.4	2.3	0.474
EK22	HN	70.3	32.4	2.0	0.191
EK21	HE	201.9	34.2	2.5	0.662
EK21	HN	130.7	34.2	2.3	0.473
FLKY	E2	50.9	39.7	1.9	0.097
FLKY	E1	31.9	39.7	1.7	0.106
EK33	HE	29.8	52.8	1.7	0.072
EK33	HN	23.3	52.8	1.6	0.179
EK20	HN	34	53.4	1.8	0.013
EK20	HE	35	53.4	1.8	0.000
S51A	HE	39.9	54.2	1.9	0.060
S51A	HN	35.2	54.2	1.8	0.006
EK32	HE	26.8	58.8	1.7	0.095
EK32	HN	22.2	58.8	1.6	0.177
EK25	HE	23.9	60.9	1.7	0.137
EK25	HN	23	60.9	1.6	0.154
R50A	HE	21.4	73.8	1.7	0.143
R50A	HN	43.5	73.8	2.0	0.165
EK26	HE	16.9	81.6	1.6	0.224
EK26	HN	16.2	81.6	1.6	0.243
Q51A	HE	30.1	101	1.9	0.071
Q51A	HN	26.5	101	1.8	0.016
T50A	HN	18.7	170	1.8	0.031
T50A	HE	13.2	170	1.6	0.182
TZTN	B2	7.4	175	1.4	0.428
TZTN	B1	8.9	175	1.5	0.348
HZKY	EZ	12.2	100	1.5	0.323
EK12	HN	409	35.5	2.8	0.977
EK12	HE	243.7	35.5	2.6	0.752
EK13	HN	45.9	60.8	1.9	0.146
EK13	HE	95.3	60.8	2.3	0.463
EK14	HN	81	73.2	2.2	0.433
EK14	HE	50.4	73.2	2.0	0.227

D. 13 – Event 12

Station Name	Station Channel	Amplitude (nm)	Distance (km)	M_L	MAD
EK12	N	4.3	94.2	1.0	0.113
EK12	E	5.3	94.2	1.1	0.022
EK13	N	6.7	71.3	1.1	0.020
EK13	E	6.5	71.3	1.1	0.007
EK14	E	15.9	59.5	1.5	0.356
EK23	N	3.9	105	1.0	0.133
EK23	E	4.4	105	1.0	0.080
EK26	E	3.7	80.9	0.9	0.211
EK32	E	4.4	151	1.1	0.007
EK33	N	5.3	130	1.2	0.044
EK33	E	7.5	130	1.3	0.195
EK35	E	5.7	107	1.2	0.036

Appendix E: MATLAB Code for Methodology Analysis

Ground motion waveform is brought into MATLAB from SEISAN in units of nanometers and is high-pass filtered above 0.8 Hz.

Spectral_window.m

```

% Import the data that has already been high-pass filtered (e.g. 0.8 Hz)

% and corrected for the instrument response (i.e. output of mulplt in SEISAN)

% In SEISAN, start with highpass filter, then 'g' before windowing or 'r'. The output

% of mulplt is in the file signal.out:

% Save fileunder

% '/hd2/work/andrew/Important/Observed_Quake_Noise/' date '/' sta;

%This will allow proper call to file below

set(0, 'DefaulttextInterpreter', 'none')

prompt = 'Enter Event Date (yyyy_mm_dd) ';

date = input(prompt, 's');

brompt = 'Enter Station Network/Number (XXxx) ';

sta = input(brompt, 's');

% sample rate depends on station

% fs = 100; % 12,13,20,23,33,34

% fs = 200 % 14,21,22,25,26,32,35

if strcmp(sta,'EK12') || strcmp(sta,'EK13') || strcmp(sta,'EK20') || strcmp(sta,'EK23') ||
strcmp(sta,'EK34') || strcmp(sta,'EK33')

    fs = 100;

```

```

elseif strcmp(sta,'EK14') || strcmp(sta,'EK21') || strcmp(sta,'EK22') || strcmp(sta,'EK25') ||
strcmp(sta,'EK26') || strcmp(sta,'EK32') || strcmp(sta,'EK35')

    fs = 200;

else

    error(['sta ' sta ' does not exist'])

end

%Open ground motion waveform

fid = fopen(['hd2/work/andrew/Important/Observed_Quake_Noise/' date '/' sta] , 'r');

data = textscan(fid,'%f','HeaderLines',2);

fclose(fid);

% Find P-Wave onset and add the P-S time in seconds*100 to get S-wave onset

%Change Ss1 timeto S-wave onset and add the sample rate for 1 second

%depending on what station is being used here. Move rectangle until it

%marks 1 second window around S-wave

% 1s window data:

sS1 = 1;

sS2 = 7000;

```

```
%sS2 = sS1 + fs;  
  
data = data{1};  
  
data = data(sS1:sS2);  
  
plot(data)  
  
dim = [0.395 0.15 (fs/sS2) .75];  
  
annotation('rectangle', dim,'Linewidth', 2)  
  
str = sprintf('%s - %s - Ground Displacement',sta,date);  
  
title(str)  
  
grid on;  
  
xlabel('Time (hundredths of seconds)')  
  
ylabel('Ground Displacement Amplitude (nm)')
```


Code to find the lowest residual between the 1 second window around the S-wave onset high-pass filtered ground motion waveform of a real event and the modeled event. Found by varying moment magnitude and corner frequency

```
function RMS_residuals_better(Latd,Longd,z,sS1) % ,t1,t2)[RMS,M,sig] =
```

```
% Minimize misfit based on varying fc and Mw
```

```
% AND, this will give you the values for the best-fitting M and sig:
```

```
% indx = find(RMS == min(RMS));
```

```
% M(indx)
```

```
% sig(indx)
```

```
% smoothing-frequency for displacement spectra. If smooth_f = 0, no
```

```
% smoothing is done.
```

```
set(0, 'DefaulttextInterpreter', 'none')
```

```
prompt = 'Enter Event Date (yyyy_mm_dd) ';
```

```
date = input(prompt, 's');
```

```
brompt = 'Enter Station Network/Number (XXxx) ';
```

```
sta = input(brompt, 's');
```

```
mags = 1.5;
```

```

sigmas = 0.0151;

% RMS = zeros(length(mags)*length(sigmas),1);

RMS = [];

M = RMS;

sig = RMS;

%Defines sample rate for each station

if strcmp(sta,'EK12') || strcmp(sta,'EK13') || strcmp(sta,'EK20') || strcmp(sta,'EK23') ||
strcmp(sta,'EK34') || strcmp(sta,'EK33')

    fs = 100;

elseif strcmp(sta,'EK14') || strcmp(sta,'EK21') || strcmp(sta,'EK22') || strcmp(sta,'EK25') ||
strcmp(sta,'EK26') || strcmp(sta,'EK32') || strcmp(sta,'EK35')

    fs = 200;

else

    error(['sta ' sta ' does not exist'])

end

% Set station coords:

if strcmp(sta,'EK12')

    Lat_sta = 38.1287;

    Long_sta = -83.1042;

```

end

if strcmp(sta,'EK13')

Lat_sta = 38.2301;

Long_sta = -82.8286;

end

if strcmp(sta,'EK14')

Lat_sta = 38.29963;

Long_sta = -82.7037;

end

if strcmp(sta,'EK20')

Lat_sta = 37.7332;

Long_sta = -83.8661;

end

if strcmp(sta,'EK21')

Lat_sta = 37.81595;

Long_sta = -83.5315;

end

```
if strcmp(sta,'EK22')  
  
    Lat_sta = 37.91525;  
  
    Long_sta = -83.2507;  
  
end
```

```
if strcmp(sta,'EK23')  
  
    Lat_sta = 37.92127;  
  
    Long_sta = -82.9004;  
  
end
```

```
if strcmp(sta,'EK25')  
  
    Lat_sta = 38.13583;  
  
    Long_sta = -82.8145;  
  
end
```

```
if strcmp(sta,'EK26')  
  
    Lat_sta = 38.07035;  
  
    Long_sta = -82.581;  
  
end
```

```
if strcmp(sta,'EK32')  
  
    Lat_sta = 37.61982;  
  
    Long_sta = -83.3024;  
  
end
```

```
if strcmp(sta,'EK33')  
  
    Lat_sta = 37.75818;  
  
    Long_sta = -83.1249;  
  
end
```

```
if strcmp(sta,'EK34')  
  
    Lat_sta = 37.70558;  
  
    Long_sta = -82.7147;  
  
end
```

```
if strcmp(sta,'EK35')  
  
    Lat_sta = 37.85687;  
  
    Long_sta = -82.7147;  
  
end
```

```

% Import the data that has already been high-pass filtered (e.g. 0.8 Hz)

% and corrected for the instrument response (i.e. output of mulplt)

% so do highpass filter, then 'g' before windowing or 'r'. The output

% of mulplt is in the file signal.out:

%fid = fopen('/home/asholc2/work/Observed_Quake_Noise/EK13_12-22-
2015_grnddisp','r');

fid = fopen(['/hd2/work/andrew/Important/Observed_Quake_Noise/' date '/' sta] , 'r'); %in
displacement(nm)

data = textscan(fid,'%f','HeaderLines',2);

fclose(fid);

% convert data from nm/s to whatever you want:

%data = data./10^9;

% 1s(?) window data:

% sS1 = t1*fs;

% sS2 = t2*fs;

sS1 = sS1;

sS2 = sS1 + fs;

```

```

data = data{ 1 };

%data = data(sS1:sS2);

data = data(sS1:sS2);

%data = smooth(data,4);

% Calculate the FFT

DATA = fft(data);

DATA = abs(DATA)./fs;

% These are the frequency vectors for each FFT calculation:

fN = fs/2;

fmax = fN*0.8;

Nf = length(data); % This is the number of freq.s calculated

df = fs/Nf;

f = (0:Nf-1)*df;

indxf = f > 0 & f <= fmax;

f = f(indxf);

DATA = DATA(indxf);

%DATA = DATA(indxf)/1e3;

```

```

% if smooth_f ~= 0

%   hannum = floor(smooth_f/df);

%   if ~mod(hannum,2) %% Make sure it's odd:

%       hannum = hannum + 1;

%   end

%   [~,DATA] = hansmooth(f, DATA,hannum);

%   DATA = DATA';

% end

figure (1);

a1 = loglog(f,DATA,'Linewidth',2); M1 = 'Observed S-Wave Spectrum';

hold on

% Declare and initialize some variables:

C = 0.55*2*0.71;      %Radiation Pattern * Free Surface Amplification * Reduction
factor partitioning energy into 2 horizontal components (Boore,1983)

[vS, rho] = get_earthstr(z); % call to other program to define hamburg density model

```



```

Vs = vS;

Vsm = Vs*1e3; %Shear wave Velocity near the source (m/s)

DE = rho*1000; % density converted from (g/(cm^3)) to (kg/m^3)

q0 = 525; %Quality Factor Constant

qalpha = 0.45; %Quality Factor Exponent Constant

n=2; % Brune Value

gamma=2; % Boatwright Value

%Determines distance from station to event after converting to UTM via
%deg2utm(Palacios, 2006)

[Long,Lat, ~] = deg2utm(Latd, Longd);

[Long13,Lat13, ~] = deg2utm( Lat_sta,Long_sta);

d13 = (sqrt((Lat13-Lat)^2+(Long13-Long)^2))/1000;

[~,ttS, ~] = do_tlayer(d13,0.1,z);

trtime13 = ttS;

rh13 = ((d13^2+(z^2))^(1/2));

% call to function that determines incidence angle

[IA] = Inc_angle(d13,z);

```

```
IA13 = IA;
```

```
%Determines geometrial cpreading term
```

```
if (rh13 < 100);
```

```
    G = 1/rh13;
```

```
elseif (rh13 > 100);
```

```
    G = 1/sqrt(100*rh13);
```

```
end
```

```
% Varies magnitude and stress drop while determining residual upon each
```

```
% iteration
```

```
for k = 1:length(mags)
```

```
    for l = 1:length(sigmas)
```

```
        Mw = mags(k);
```

```
        sigma = sigmas(l) * 1e6;
```

```
%    d = srcspec(Mw,sigma,ttS,rh13,z,IA13,f);
```

```

Mo = 10.^((1.5*Mw)+9) ; %Seismic Moment: Energy released in N*m

Ro = ((7/16)*Mo/sigma).^1/3; %in meters

fc = 0.21*(Vsm)/Ro; %Use 0.21 for constant because it's for S-waves
accding to Madariaga(1977)

%

Q = q0.*f.^qalpha;

P = exp(-pi*f*trtime13./Q);

S =
(C*Mo./((4*pi)*DE*(Vsm^3)))/((ones(size(f)))+(f/fc).^(n*gamma)).^(1/gamma);

d = (1/sin(IA13)).*S.*P*(G/1000);

d = d.*1e9;

r = d' - DATA;

RMS = [RMS; sqrt(nansum(r.^2)/length(d))]; % ; rms(r)

M = [M; Mw];

sig = [sig; sigma];

a2 = loglog(f,d, 'Linewidth',2); M2 = 'Brune Model S-Wave Spectrum Best Fit';

end

end

```

```
T = table(M, sig, RMS);  
  
Low = min(RMS(:));  
  
[row, ~] = find(RMS == Low);  
  
RC = T(row,:);  
  
Mrow = T{row,'M'};  
  
sigrow = T{row,'sig'};  
  
sigrow = sigrow/1e6;
```

To plot the observed S-wave spectrum with the Brune Model of Best Fit, append the following code to the end of the RMS_residuals_better code.

```
figure(1);

fig=gcf;

set(findall(fig,'-property','FontSize'),'FontSize',20)

grid on;

% dim = [.2 .5 .3 .3];

legend([a1;a2], M1, M2)

str = sprintf('%s - %s - Observed S-Wave Spectrum with Brune Model of Best
Fit',sta,date);

title(str)

box = sprintf('Lowest RMS at Mw = %.1f, Stress Drop = %.3f MPa',Mrow,sigrow);

dim = [.15 .15 .38 0.05];

fig=gcf;

set(findall(fig,'-property','FontSize'),'FontSize',20)

annotation('textbox',dim,'String',box,'FontSize',20);

xlim([1 fmax])

% xlim([0.5 100])

xlabel('Frequency(Hz)')

ylabel('Displacement (nm/Hz)')
```

To plot the Residuals against the Moment Magnitude while varying the stress drop
append the following code onto the end of the RMS_residuals_better code

```
figure(3);

scatter(M, RMS, 'filled');

fig=gcf;

set(findall(fig,'-property','FontSize'),'FontSize',20);

str = sprintf('%s - %s - RMS Residuals vs. Mw with Varying Stress Drop',sta,date);

title(str);

dim = [.2 .7 .38 .04];

str = sprintf('Lowest RMS at Mw = %.1f, Stress Drop = %.3f MPa',Mrow,sigrow);

annotation('textbox',dim,'String',str,'FontSize',20);

% xlim([1.6 2.5])

grid on;

% ylim([1e3 1.5e5])

xlabel('Magnitude(Mw)','FontSize',20);

ylabel('RMS Residual Value','FontSize',20);
```

To plot the Stress drop of the lowest magnitude event over a range of stress drops append the following code to the end of the rms_residuals_better.m code above. This plot repeats information that the other two already show and was determined not to be as useful, although it does show a distinct valley of lowest residual values that the other plots do not show.

```
figure (4);

fig=gcf;

set(findall(fig,'-property','FontSize'),'FontSize',12)

scatter(sig/1e6, RMS, 'filled')

grid on;

dim = [.2 .5 .3 .3];

str = sprintf('Lowest RMS Residual at Stress Drop = %.2f MPa',sigrow);

annotation('textbox',dim,'String',str,'FitBoxToText','on');

str = sprintf('%s - %s - RMS Residuals vs. Stress Drop',sta,date);

title(str)

xlabel('Stress Drop (MPa)')

ylabel('RMS Residual Value')
```

Code to convert decimal degrees to Universal Transverse Mercator(UTM) coordinates (WGS84). Code was created by Rafael Palacios in 2006 and can be found open-source on MATLAB Central. (<https://www.mathworks.com/matlabcentral/fileexchange/10915-deg2utm?focused=5073379&tab=function>)

```
function [x,y,utmzone] = deg2utm(Lat,Lon)
% -----
% [x,y,utmzone] = deg2utm(Lat,Lon)
%
% Description: Function to convert lat/lon vectors into UTM coordinates (WGS84).
% Some code has been extracted from UTM.m function by Gabriel Ruiz Martinez.
%
% Inputs:
% Lat: Latitude vector. Degrees. +ddd.ddddd WGS84
% Lon: Longitude vector. Degrees. +ddd.ddddd WGS84
%
% Outputs:
% x, y , utmzone. See example
%
% Example 1:
% Lat=[40.3154333; 46.283900; 37.577833; 28.645650; 38.855550; 25.061783];
% Lon=[-3.4857166; 7.8012333; -119.95525; -17.759533; -94.7990166; 121.640266];
% [x,y,utmzone] = deg2utm(Lat,Lon);
% fprintf('%7.0f ',x)
% 458731 407653 239027 230253 343898 362850
% fprintf('%7.0f ',y)
% 4462881 5126290 4163083 3171843 4302285 2772478
% utmzone =
% 30 T
% 32 T
% 11 S
% 28 R
```



```

%    15 S
%    51 R
%
% Example 2: If you have Lat/Lon coordinates in Degrees, Minutes and Seconds
%   LatDMS=[40 18 55.56; 46 17 2.04];
%   LonDMS=[-3 29 8.58; 7 48 4.44];
%   Lat=dms2deg(mat2dms(LatDMS)); %convert into degrees
%   Lon=dms2deg(mat2dms(LonDMS)); %convert into degrees
%   [x,y,utmzone] = deg2utm(Lat,Lon)
%
% Author:
%   Rafael Palacios
%   Universidad Pontificia Comillas
%   Madrid, Spain
% Version: Apr/06, Jun/06, Aug/06, Aug/06
% Aug/06: fixed a problem (found by Rodolphe Dewarrat) related to southern
%   hemisphere coordinates.
% Aug/06: corrected m-Lint warnings
%-----

% Argument checking
%
error(nargchk(2, 2, nargin)); %2 arguments required
n1=length(Lat);
n2=length(Lon);
if (n1~=n2)
    error('Lat and Lon vectors should have the same length');
end

% Memory pre-allocation

```

```

%
x=zeros(n1,1);
y=zeros(n1,1);
utmzone(n1,:)= '60 X';

% Main Loop
%
for i=1:n1
    la=Lat(i);
    lo=Lon(i);

    sa = 6378137.000000 ; sb = 6356752.314245;

    %e = ( ( ( sa ^ 2 ) - ( sb ^ 2 ) ) ^ 0.5 ) / sa;
    e2 = ( ( ( sa ^ 2 ) - ( sb ^ 2 ) ) ^ 0.5 ) / sb;
    e2cuadrada = e2 ^ 2;
    c = ( sa ^ 2 ) / sb;
    %alpha = ( sa - sb ) / sa;          %f
    %ablandamiento = 1 / alpha;      % 1/f

    lat = la * ( pi / 180 );
    lon = lo * ( pi / 180 );

    Huso = fix( ( lo / 6 ) + 31);
    S = ( ( Huso * 6 ) - 183 );
    deltaS = lon - ( S * ( pi / 180 ) );

    if (la<-72), Letra='C';
    elseif (la<-64), Letra='D';
    elseif (la<-56), Letra='E';
    elseif (la<-48), Letra='F';

```

```

elseif (la<-40), Letra='G';
elseif (la<-32), Letra='H';
elseif (la<-24), Letra='J';
elseif (la<-16), Letra='K';
elseif (la<-8), Letra='L';
elseif (la<0), Letra='M';
elseif (la<8), Letra='N';
elseif (la<16), Letra='P';
elseif (la<24), Letra='Q';
elseif (la<32), Letra='R';
elseif (la<40), Letra='S';
elseif (la<48), Letra='T';
elseif (la<56), Letra='U';
elseif (la<64), Letra='V';
elseif (la<72), Letra='W';
else Letra='X';
end

```

```

a = cos(lat) * sin(deltaS);
epsilon = 0.5 * log( ( 1 + a) / ( 1 - a ) );
nu = atan( tan(lat) / cos(deltaS) ) - lat;
v = ( c / ( ( 1 + ( e2cuadrada * ( cos(lat) ) ^ 2 ) ) ) ^ 0.5 ) * 0.9996;
ta = ( e2cuadrada / 2 ) * epsilon ^ 2 * ( cos(lat) ) ^ 2;
a1 = sin( 2 * lat );
a2 = a1 * ( cos(lat) ) ^ 2;
j2 = lat + ( a1 / 2 );
j4 = ( ( 3 * j2 ) + a2 ) / 4;
j6 = ( ( 5 * j4 ) + ( a2 * ( cos(lat) ) ^ 2 ) ) / 3;
alfa = ( 3 / 4 ) * e2cuadrada;
beta = ( 5 / 3 ) * alfa ^ 2;
gama = ( 35 / 27 ) * alfa ^ 3;

```

```
Bm = 0.9996 * c * ( lat - alfa * j2 + beta * j4 - gama * j6 );  
xx = epsilon * v * ( 1 + ( ta / 3 ) ) + 500000;  
yy = nu * v * ( 1 + ta ) + Bm;  
  
if (yy<0)  
    yy=9999999+yy;  
end  
  
x(i)=xx;  
y(i)=yy;  
utmzone(i,:)=sprintf('%02d %c',Huso,Letra);  
end
```

This function defines the incidence angle of the incoming S-wave and corrects it to the vertical component as it is the only one being triggered in the triggering algorithm.

```
function [ IA ] = Inc_angle( km,Z )

% %Defines incidence angle

% Calls the function from SEISAN called tlayer to determine the traveltime
% at each layer based on the HGamburg velocity model. This code determines the
% slope of the line to determine the ray parameter which is then used to
% calculate incidence angle

fid = fopen('/mnt/seisdrobo1/work/andrew/Important/tlayer.out','rt');

data = textscan(fid, '%f %f %f %f %f', 'HeaderLines',11);

fclose(fid);

x = data{1};

tS = data{4};

zz = polyfit(x, tS, 2);

Z = polyder(zz);

p = polyval(Z,km);    %ray parameter, p

Vmax = 1/p;          %Maximum velocity sampled (In km/s)

Vmax = Vmax*1000;    %Maximum velocity in m/s

IA = asin(2850/Vmax);
```

Calls the dottlayer function in SEISAN that determines the travel time based on the Hmaburg Velocity Model.

```
function [ttP,ttS, km] = do_tlayer(km,delta,Z)

% km = the distance for which the travel time is desired

% delta = the distance increment (km)

% Z = source depth (km)

%

% USAGE: do_tlayer(dmax,delta,Z)

%fid = fopen('tlayer.inp','w+');

%fprintf(fid,'\n %f\n %f\n %f\n \n',[num2str(dist) num2str(delta) num2str(Z)]);

%fclose(fid);

[~,tt] = system(['do_tlayer.csh ' num2str(km) ' ' num2str(delta) ' ' num2str(Z)]);

tt = str2num(tt);

ttP = tt(1);

ttS = tt(2);

km = tt(3);
```

Function to determine the density of the earth at the earthquake source based on the Hmaburg Velocity Model

```
function [vS,rho] = get_earthstr(z)

fid = fopen('/hd2/work/andrew/Important/HAMBURG.txt','r');

earthstr = textscan(fid,'%f %f %f %f %*f %*f\n','Headerlines',1);

thickness = earthstr{1};

depth = zeros(18,1);

depth(1) = 0;

for k = 2:18

depth(k) = depth(k-1)+thickness(k);

end

indx = find(depth < z);

vS = earthstr{3}(indx(end));

rho = earthstr{4}(indx(end));
```

The function used to create the Minimum Detection Threshold Map for the daytime (1100-2300 UTC) is called SNM_Jan_Days_map.m as it creates a model for the station noise. Function currently tests Moment Magnitudes from 0 to 2.5 and is set to test 5 km grid spacing between UTM coordinates seen under East and Northin lines 15 and 16 of the code.

```
function SNM_Jan_Days_map(z,sigma)

% Mw is the input magnitude

% d is the epicentral distance (km)

% z is the focal depth (km)

j=0;

for Mw = 0.0:0.1:2.5

j=j+1;

i = 0;

for East = 230000:5000:400000 %;l = 1:length(Long);

    for North = 4130000:5000:4270000 %;k = 1:length(Lat);10
```



```

ratio = 3;

% h = (4/pi)/(4*pi);

C = 0.55*2*0.71;      %Radiation Pattern * Free Surface Amplification * Reduction
factor partitioning energy into 2 horizontal components (Boore,1983)

Mo = 10.^(1.5*Mw+9);   %Energy released in Nm

sigma = sigma * 1e6;   %STRESS Drop converted to Pascals

% KK = 0.91;          % 1/sqrt(2*0.6)

[vS, rho] = get_earthstr(z);

Vs = vS;

Vsm = Vs*1e3; %Shear wave Velocity near the source (m/s)

DE = rho*1000;      % density converted from (g/(cm^3)) to (kg/m^3)

q0 = 525;

qalpha = 0.45;

Ro = ((7/16)*Mo/sigma).^(1/3);

fc = 0.21*(Vsm)/Ro;    % 18; %corner frequency. K-value = 0.32 [Huang et al 2016]

%DE = (0.23*(Vsft^0.25))*1000 % density converted from (g/(cm^3)) to (kg/m^3)

n=2;

gamma=2;

```

```
%%%%%%%%%% Reading and overlaying a pqlx file
```

```
psd_file12 = 'EK12_HHZ_0101-0131_1100-2300';
```

```
matrix12 = dlmread(['/hd2/work/andrew/Important/Jan_Days/' psd_file12]);
```

```
psd_file13 = 'EK13_HHZ_0101-0131_1100-2300';
```

```
matrix13 = dlmread(['/hd2/work/andrew/Important/Jan_Days/' psd_file13]);
```

```
psd_file14 = 'EK14_HHZ_0101-0131_1100-2300';
```

```
matrix14 = dlmread(['/hd2/work/andrew/Important/Jan_Days/' psd_file14]);
```

```
psd_file20 = 'EK20_HHZ_0101-0131_1100-2300';
```

```
matrix20 = dlmread(['/hd2/work/andrew/Important/Jan_Days/' psd_file20]);
```

```
psd_file21 = 'EK21_HHZ_0101-0131_1100-2300';
```

```
matrix21 = dlmread(['/hd2/work/andrew/Important/Jan_Days/' psd_file21]);
```

```
psd_file22 = 'EK22_HHZ_0101-0131_1100-2300';
```

```
matrix22 = dlmread(['/hd2/work/andrew/Important/Jan_Days/' psd_file22]);
```

```
psd_file23 = 'EK23_HHZ_0101-0131_1100-2300';  
matrix23 = dlmread(['/hd2/work/andrew/Important/Jan_Days/' psd_file23]);  
  
psd_file25 = 'EK25_HHZ_0101-0131_1100-2300';  
matrix25 = dlmread(['/hd2/work/andrew/Important/Jan_Days/' psd_file25]);  
  
psd_file26 = 'EK26_HHZ_0101-0131_1100-2300';  
matrix26 = dlmread(['/hd2/work/andrew/Important/Jan_Days/' psd_file26]);  
  
psd_file32 = 'EK32_HHZ_0101-0131_1100-2300';  
matrix32 = dlmread(['/hd2/work/andrew/Important/Jan_Days/' psd_file32]);  
  
psd_file33 = 'EK33_HHZ_0101-0131_1100-2300';  
matrix33 = dlmread(['/hd2/work/andrew/Important/Jan_Days/' psd_file33]);  
  
psd_file34 = 'EK34_HHZ_0701-0731_1100-2300';  
matrix34 = dlmread(['/hd2/work/andrew/Important/Jan_Days/' psd_file34]);  
  
psd_file35 = 'EK35_HHZ_0101-0131_1100-2300';  
matrix35 = dlmread(['/hd2/work/andrew/Important/Jan_Days/' psd_file35]);
```

```

psd_fileS51A = 'S51A_HHZ_0101-0131_1100-2300';

matrixS51A = dlmread(['/hd2/work/andrew/Important/Jan_Days/' psd_fileS51A]);

psd_filePKKY = 'PKKY_HHZ_0101-0131_1100-2300';

matrixPKKY = dlmread(['/hd2/work/andrew/Important/Jan_Days/' psd_filePKKY]);

psd_fileROKY = 'ROKY_HHZ_0101-0131_1100-2300';

matrixROKY = dlmread(['/hd2/work/andrew/Important/Jan_Days/' psd_fileROKY]);

%matrix = dlmread(psd_file);

%Changes units from dB wrt (acceleration)^squared per Hz to
%dB wrt velocity^squared per Hz to Velocity^squared per Hz to Velocity per
%Hz

t12 = matrix12(:,1);           % Period (in sec)

```

```

x12 = 1./(matrix12(:,1));           % Convert to frequency (in Hz)

y12 = matrix12(:,2);               % Noise Measurement (dB wrt
(acceleration)^squared per Hz) - conversions done per Boormann(2013, Chapter 4)

y12 = y12 + 20*log10(t12/(2*pi));   % Noise Conversion to dB wrt
(velocity)^squared per Hz

y12 = (10.^(0.1*y12));              % Conversion to (Velocity)^Squared per Hz

y12 = sqrt(pi/2).*sqrt(2*y12.*x12/sqrt(2)); % Conversion to Velocity per Hz

```

```

t13 = matrix13(:,1);

x13 = 1./(matrix13(:,1));

y13 = matrix13(:,2);

y13 = y13 + 20*log10(t13/(2*pi));

y13 = 10.^(0.1*y13);

y13 = sqrt(pi/2).*sqrt(2*y13.*x13/sqrt(2));

```

```

t14 = matrix14(:,1);

x14 = 1./(matrix14(:,1));

y14 = matrix14(:,2);

y14 = y14 + 20*log10(t14/(2*pi));

y14 = 10.^(0.1*y14);

```

```
y14 = sqrt(pi/2).*sqrt(2*y14.*x14/sqrt(2));
```

```
t20 = matrix20(:,1);
```

```
x20 = 1./(matrix20(:,1));
```

```
y20 = matrix20(:,2);
```

```
y20 = y20 + 20*log10(t20/(2*pi));
```

```
y20 = 10.^(0.1*y20);
```

```
y20 = sqrt(pi/2).*sqrt(2*y20.*x20/sqrt(2));
```

```
t21 = matrix21(:,1);
```

```
x21 = 1./(matrix21(:,1));
```

```
y21 = matrix21(:,2);
```

```
y21 = y21 + 20*log10(t21/(2*pi));
```

```
y21 = 10.^(0.1*y21);
```

```
y21 = sqrt(pi/2).*sqrt(2*y21.*x21/sqrt(2));
```

```
t22 = matrix22(:,1);
```

```
x22 = 1./(matrix22(:,1));
```

```
y22 = matrix22(:,2);
```

```
y22 = y22 + 20*log10(t22/(2*pi));
```

```

y22 = 10.^(0.1*y22);

y22 = sqrt(pi/2).*sqrt(2*y22.*x22/sqrt(2));

t23 = matrix23(:,1);

x23 = 1./(matrix23(:,1));

y23 = matrix23(:,2);

y23 = y23 + 20*log10(t23/(2*pi));

y23 = 10.^(0.1*y23);

y23 = sqrt(pi/2).*sqrt(2*y23.*x23/sqrt(2));

t25 = matrix25(:,1);

x25 = 1./(matrix25(:,1));

y25 = matrix25(:,2);

y25 = y25 + 20*log10(t25/(2*pi));

y25 = 10.^(0.1*y25);

y25 = sqrt(pi/2).*sqrt(2*y25.*x25/sqrt(2));

t26 = matrix26(:,1);

x26 = 1./(matrix26(:,1));

y26 = matrix26(:,2);

y26 = y26 + 20*log10(t26/(2*pi));

```

$y_{26} = 10.^{(0.1*y_{26})}$;

$y_{26} = \sqrt{\pi/2}.*\sqrt{2*y_{26}.*x_{26}/\sqrt{2}}$;

$t_{32} = \text{matrix32}(:,1)$;

$x_{32} = 1./(\text{matrix32}(:,1))$;

$y_{32} = \text{matrix32}(:,2)$;

$y_{32} = y_{32} + 20*\log_{10}(t_{32}/(2*\pi))$;

$y_{32} = 10.^{(0.1*y_{32})}$;

$y_{32} = \sqrt{\pi/2}.*\sqrt{2*y_{32}.*x_{32}/\sqrt{2}}$;

$t_{33} = \text{matrix33}(:,1)$;

$x_{33} = 1./(\text{matrix33}(:,1))$;

$y_{33} = \text{matrix33}(:,2)$;

$y_{33} = y_{33} + 20*\log_{10}(t_{33}/(2*\pi))$;

$y_{33} = 10.^{(0.1*y_{33})}$;

$y_{33} = \sqrt{\pi/2}.*\sqrt{2*y_{33}.*x_{33}/\sqrt{2}}$;

$t_{34} = \text{matrix34}(:,1)$;

$x_{34} = 1./(\text{matrix34}(:,1))$;

$y_{34} = \text{matrix34}(:,2)$;

$y_{34} = y_{34} + 20*\log_{10}(t_{34}/(2*\pi))$;

y34 = 10.^(0.1*y34);

y34 = sqrt(pi/2).*sqrt(2*y34.*x34/sqrt(2));

t35 = matrix35(:,1);

x35 = 1./(matrix35(:,1));

y35 = matrix35(:,2);

y35 = y35 + 20*log10(t35/(2*pi));

y35 = 10.^(0.1*y35);

y35 = sqrt(pi/2).*sqrt(2*y35.*x35/sqrt(2));

tS51A = matrixS51A(:,1);

xS51A = 1./(matrixS51A(:,1));

yS51A = matrixS51A(:,2);

yS51A = yS51A + 20*log10(tS51A/(2*pi));

yS51A = 10.^(0.1*yS51A);

yS51A = sqrt(pi/2).*sqrt(2*yS51A.*xS51A/sqrt(2));

tPKKY = matrixPKKY(:,1);

xPKKY = 1./(matrixPKKY(:,1));

yPKKY = matrixPKKY(:,2);

yPKKY = yPKKY + 20*log10(tPKKY/(2*pi));

```

yPKKY = 10.^(0.1*yPKKY);

yPKKY = sqrt(pi/2).*sqrt(2*yPKKY.*xPKKY/sqrt(2));

tROKY = matrixS51A(:,1);

xROKY = 1./(matrixROKY(:,1));

yROKY = matrixROKY(:,2);

yROKY = yROKY + 20*log10(tROKY/(2*pi));

yROKY = 10.^(0.1*yROKY);

yROKY = sqrt(pi/2).*sqrt(2*yROKY.*xROKY/sqrt(2));

```

```

Q12 = q0.*x12.^qalpha;

Q13 = q0.*x13.^qalpha;

Q14 = q0.*x14.^qalpha;

Q20 = q0.*x20.^qalpha;

Q21 = q0.*x21.^qalpha;

Q22 = q0.*x22.^qalpha;

Q23 = q0.*x23.^qalpha;

Q25 = q0.*x25.^qalpha;

Q26 = q0.*x26.^qalpha;

```

Q32 = q0.*x32.^qalpha;
Q33 = q0.*x33.^qalpha;
Q34 = q0.*x34.^qalpha;
Q35 = q0.*x35.^qalpha;
QS51A = q0.*xS51A.^qalpha;
QPKKY = q0.*xPKKY.^qalpha;
QROKY = q0.*xROKY.^qalpha;

%Hypocentral Distance to EK13 3813806N 08249714W 0301 (No ELEVATION

%CORRECTION. ASSUMING ELEV = 0; Haversine Epicentral Distance

LatEK12d = 38.1287;

LongEK12d = -83.1042;

[LongEK12, LatEK12, ~] = deg2utm(LatEK12d, LongEK12d);

d12 = (sqrt((LatEK12-North)^2+(LongEK12-East)^2))/1000;

[~,ttS] = do_tlayer(d12,0.1,z);

trtime12 = ttS;

rh12 = (d12^2+(z^2))^(1/2);

LatEK13d = 38.2301;

```

LongEK13d = -82.8286;

[LongEK13,LatEK13, ~] = deg2utm(LatEK13d, LongEK13d);

d13 = (sqrt((LatEK13-North)^2+(LongEK13-East)^2))/1000;

[~,ttS] = do_tlayer(d13,0.1,z);

trtime13 = ttS;

rh13 = (d13^2+(z^2))^(1/2);

LatEK14d = 38.29963;

LongEK14d = -82.7037;

[LongEK14,LatEK14, ~] = deg2utm(LatEK14d, LongEK14d);

d14 = (sqrt((LatEK14-North)^2+(LongEK14-East)^2))/1000;

[~,ttS] = do_tlayer(d14,0.1,z);

trtime14 = ttS;

rh14 = (d14^2+(z^2))^(1/2);

LatEK20d = 37.7332;

LongEK20d = -83.8661;

[LongEK20,LatEK20, ~] = deg2utm(LatEK20d, LongEK20d);

d20 = (sqrt((LatEK20-North)^2+(LongEK20-East)^2))/1000;

[~,ttS] = do_tlayer(d20,0.1,z);

```

trtime20 = ttS;

rh20 = (d20^2+(z^2))^(1/2);

LatEK21d = 37.81595;

LongEK21d = -83.5315;

[LongEK21,LatEK21, ~] = deg2utm(LatEK21d, LongEK21d);

d21 = (sqrt((LatEK21-North)^2+(LongEK21-East)^2))/1000;

[~,ttS] = do_tlayer(d21,0.1,z);

trtime21 = ttS;

rh21 = (d21^2+(z^2))^(1/2);

LatEK22d = 37.91525;

LongEK22d = -83.2507;

[LongEK22,LatEK22, ~] = deg2utm(LatEK22d, LongEK22d);

d22 = (sqrt((LatEK22-North)^2+(LongEK22-East)^2))/1000;

[~,ttS] = do_tlayer(d22,0.1,z);

trtime22 = ttS;

rh22 = (d22^2+(z^2))^(1/2);

LatEK23d = 37.92127;

LongEK23d = -82.9004;

[LongEK23,LatEK23, ~] = deg2utm(LatEK23d, LongEK23d);

d23 = (sqrt((LatEK23-North)^2+(LongEK23-East)^2))/1000;

[~,ttS] = do_tlayer(d23,0.1,z);

trtime23 = ttS;

rh23 = (d23^2+(z^2))^(1/2);

LatEK25d = 38.13583;

LongEK25d = -82.8145;

[LongEK25,LatEK25, ~] = deg2utm(LatEK25d, LongEK25d);

d25 = (sqrt((LatEK25-North)^2+(LongEK25-East)^2))/1000;

[~,ttS] = do_tlayer(d25,0.1,z);

trtime25 = ttS;

rh25 = (d25^2+(z^2))^(1/2);

LatEK26d = 38.07035;

LongEK26d = -82.581;

[LongEK26,LatEK26, ~] = deg2utm(LatEK26d, LongEK26d);

d26 = (sqrt((LatEK26-North)^2+(LongEK26-East)^2))/1000;

[~,ttS] = do_tlayer(d26,0.1,z);

trtime26 = ttS;

rh26 = (d26^2+(z^2))^(1/2);

```

LatEK32d = 37.61982;

LongEK32d = -83.3024;

[LongEK32,LatEK32, ~] = deg2utm(LatEK32d, LongEK32d);

d32 = (sqrt((LatEK32-North)^2+(LongEK32-East)^2))/1000;

[~,ttS] = do_tlayer(d32,0.1,z);

trtime32 = ttS;

rh32 = (d32^2+(z^2))^(1/2);

LatEK33d = 37.75818;

LongEK33d = -83.1249;

[LongEK33,LatEK33, ~] = deg2utm(LatEK33d, LongEK33d);

d33 = (sqrt((LatEK33-North)^2+(LongEK33-East)^2))/1000;

[~,ttS] = do_tlayer(d33,0.1,z);

trtime33 = ttS;

rh33 = (d33^2+(z^2))^(1/2);

LatEK34d = 37.70558;

LongEK34d = -82.7147;

[LongEK34,LatEK34, ~] = deg2utm(LatEK34d, LongEK34d);

d34 = (sqrt((LatEK34-North)^2+(LongEK34-East)^2))/1000;

```

[~,ttS] = do_tlayer(d34,0.1,z);

trtime34 = ttS;

rh34 = (d34^2+(z^2))^(1/2);

LatEK35d = 37.85687;

LongEK35d = -82.7147;

[LongEK35,LatEK35, ~] = deg2utm(LatEK35d, LongEK35d);

d35 = (sqrt((LatEK35-North)^2+(LongEK35-East)^2))/1000;

[~,ttS] = do_tlayer(d35,0.1,z);

trtime35 = ttS;

rh35 = (d35^2+(z^2))^(1/2);

LatS51Ad = 37.6392;

LongS51Ad = -83.5935;

[LongS51A,LatS51A, ~] = deg2utm(LatS51Ad, LongS51Ad);

dS51A = (sqrt((LatS51A-North)^2+(LongS51A-East)^2))/1000;

[~,ttS] = do_tlayer(dS51A,0.1,z);

trtimeS51A = ttS;

rhS51A = (dS51A^2+(z^2))^(1/2);

LatPKKYd = 38.383;


```

LongPKKYd = -83.034;

[LongPKKY,LatPKKY, ~] = deg2utm(LatPKKYd, LongPKKYd);

dPKKY = (sqrt((LatPKKY-North)^2+(LongPKKY-East)^2))/1000;

[~,ttS] = do_tlayer(dPKKY,0.1,z);

trtimePKKY = ttS;

rhPKKY = (dPKKY^2+(z^2))^(1/2);

LatROKYd = 37.909;

LongROKYd = -83.926;

[LongROKY,LatROKY, ~] = deg2utm(LatROKYd, LongROKYd);

dROKY = (sqrt((LatROKY-North)^2+(LongROKY-East)^2))/1000;

[~,ttS] = do_tlayer(dROKY,0.1,z);

trtimeROKY = ttS;

rhROKY = (dROKY^2+(z^2))^(1/2);

```

```

% Incidence Angle

```

```

[~,ttS] = do_tlayer(500,0.1,z);

```

```

[IA] = Inc_angle(d12,z);

```

IA12 = IA;

[IA] = Inc_angle(d13,z);

IA13 = IA;

[IA] = Inc_angle(d14,z);

IA14 = IA;

[IA] = Inc_angle(d20,z);

IA20 = IA;

[IA] = Inc_angle(d21,z);

IA21 = IA;

[IA] = Inc_angle(d22,z);

IA22 = IA;

[IA] = Inc_angle(d23,z);

IA23 = IA;

[IA] = Inc_angle(d25,z);

IA25 = IA;

[IA] = Inc_angle(d26,z);

IA26 = IA;

[IA] = Inc_angle(d32,z);

IA32 = IA;

[IA] = Inc_angle(d33,z);

IA33 = IA;

[IA] = Inc_angle(d34,z);

IA34 = IA;

[IA] = Inc_angle(d35,z);

IA35 = IA;

[IA] = Inc_angle(dS51A,z);

IAS51A = IA;

[IA] = Inc_angle(dPKKY,z);

```
IAPKKY = IA;
```

```
[IA] = Inc_angle(dROKY,z);
```

```
IAROKY = IA;
```

```
%Diminution Function (Distance parameter)
```

```
if (rh12 < 100);
```

```
    G12 = 1/rh12;
```

```
elseif (rh12 > 100);
```

```
    G12 = 1/sqrt(100*rh12);
```

```
end
```

```
if (rh13 < 100);
```

```
    G13 = 1/rh13;
```

```
elseif (rh13 > 100);
```

```
    G13 = 1/sqrt(100*rh13);
```

```
end
```

```
if (rh14 < 100);
```

```
    G14 = 1/rh14;  
elseif (rh14 > 100);  
    G14 = 1/sqrt(100*rh14);  
end
```

```
if (rh20 < 100);  
    G20 = 1/rh20;  
elseif (rh20 > 100);  
    G20 = 1/sqrt(100*rh20);  
end
```

```
if (rh21 < 100);  
    G21 = 1/rh21;  
elseif (rh21 > 100);  
    G21 = 1/sqrt(100*rh21);  
end
```

```
if (rh22 < 100);  
    G22 = 1/rh22;  
elseif (rh22 > 100);  
    G22 = 1/sqrt(100*rh22);
```

end

if (rh23 < 100);

 G23 = 1/rh23;

elseif (rh23 > 100);

 G23 = 1/sqrt(100*rh23);

end

if (rh25 < 100);

 G25 = 1/rh25;

elseif (rh25 > 100);

 G25 = 1/sqrt(100*rh25);

end

if (rh26 < 100);

 G26 = 1/rh26;

elseif (rh26 > 100);

 G26 = 1/sqrt(100*rh26);

end

if (rh32 < 100);

```
    G32 = 1/rh32;  
elseif (rh32 > 100);  
    G32 = 1/sqrt(100*rh32);  
end
```

```
if (rh33 < 100);  
    G33 = 1/rh33;  
elseif (rh33 > 100);  
    G33 = 1/sqrt(100*rh33);  
end
```

```
if (rh34 < 100);  
    G34 = 1/rh34;  
elseif (rh34 > 100);  
    G34 = 1/sqrt(100*rh34);  
end
```

```
if (rh35 < 100);  
    G35 = 1/rh35;  
elseif (rh35 > 100);  
    G35 = 1/sqrt(100*rh35);
```

end

if (rhS51A < 100);

GS51A = 1/rhS51A;

elseif (rhS51A > 100);

GS51A = 1/sqrt(100*rhS51A);

end

if (rhPKKY < 100);

GPKKY = 1/rhPKKY;

elseif (rhPKKY > 100);

GPKKY = 1/sqrt(100*rhPKKY);

end

if (rhROKY < 100);

GROKY = 1/rhROKY;

elseif (rhROKY > 100);

GROKY = 1/sqrt(100*rhROKY);

end

%Brune Displacement Spectra

$$P12 = \exp(-\pi * x12 * \text{trtime}12 ./ Q12);$$

$$S12 =$$

$$(C * Mo ./ ((4 * \pi) * DE * (Vsm^3))) ./ ((\text{ones}(\text{size}(x12))) + ((x12 / fc).^n * \text{gamma})).^(1 / \text{gamma});$$

$$O12 = (1 / \sin(IA12)) * S12 * P12 * G12 / 1000;$$

$$P13 = \exp(-\pi * x13 * \text{trtime}13 ./ Q13);$$

$$S13 =$$

$$(C * Mo ./ ((4 * \pi) * DE * (Vsm^3))) ./ ((\text{ones}(\text{size}(x13))) + ((x13 / fc).^n * \text{gamma})).^(1 / \text{gamma});$$

$$O13 = (1 / \sin(IA13)) * S13 * P13 * G13 / 1000;$$

$$P14 = \exp(-\pi * x14 * \text{trtime}14 ./ Q14);$$

$$S14 =$$

$$(C * Mo ./ ((4 * \pi) * DE * (Vsm^3))) ./ ((\text{ones}(\text{size}(x14))) + ((x14 / fc).^n * \text{gamma})).^(1 / \text{gamma});$$

$$O14 = (1 / \sin(IA14)) * S14 * P14 * G14 / 1000;$$

$$P20 = \exp(-\pi * x20 * \text{trtime}20 ./ Q20);$$

$$S20 =$$

$$(C * Mo ./ ((4 * \pi) * DE * (Vsm^3))) ./ ((\text{ones}(\text{size}(x20))) + ((x20 / fc).^n * \text{gamma})).^(1 / \text{gamma});$$

$$O20 = (1 / \sin(IA20)) * S20 * P20 * G20 / 1000;$$

$$P21 = \exp(-\pi * x21 * trtime21 ./ Q21);$$

$$S21 =$$

$$(C * Mo ./ ((4 * \pi) * DE * (Vsm^3))) ./ ((\text{ones}(\text{size}(x21))) + ((x21 / fc).^ (n * \gamma))). ^ (1 / \gamma);$$

$$O21 = (1 / \sin(IA21)) * S21 * P21 * G21 / 1000;$$

$$P22 = \exp(-\pi * x22 * trtime22 ./ Q22);$$

$$S22 =$$

$$(C * Mo ./ ((4 * \pi) * DE * (Vsm^3))) ./ ((\text{ones}(\text{size}(x22))) + ((x22 / fc).^ (n * \gamma))). ^ (1 / \gamma);$$

$$O22 = (1 / \sin(IA22)) * S22 * P22 * G22 / 1000;$$

$$P23 = \exp(-\pi * x23 * trtime23 ./ Q23);$$

$$S23 =$$

$$(C * Mo ./ ((4 * \pi) * DE * (Vsm^3))) ./ ((\text{ones}(\text{size}(x23))) + ((x23 / fc).^ (n * \gamma))). ^ (1 / \gamma);$$

$$O23 = (1 / \sin(IA23)) * S23 * P23 * G23 / 1000;$$

$$P25 = \exp(-\pi * x25 * trtime25 ./ Q25);$$

$$S25 =$$

$$(C * Mo ./ ((4 * \pi) * DE * (Vsm^3))) ./ ((\text{ones}(\text{size}(x25))) + ((x25 / fc).^ (n * \gamma))). ^ (1 / \gamma);$$

$$O25 = (1 / \sin(IA25)) * S25 * P25 * G25 / 1000;$$

$$P26 = \exp(-\pi * x26 * trtime26 ./ Q26);$$

$$S26 = (C * Mo ./ ((4 * pi) * DE * (Vsm^3))) ./ ((ones(size(x26))) + ((x26/fc).^ (n * gamma))). ^ (1/gamma);$$

$$O26 = (1/\sin(IA26)) * S26 * P26 * G26/1000;$$

$$P32 = \exp(-pi * x32 * trtime32./Q32);$$

$$S32 = (C * Mo ./ ((4 * pi) * DE * (Vsm^3))) ./ ((ones(size(x32))) + ((x32/fc).^ (n * gamma))). ^ (1/gamma);$$

$$O32 = (1/\sin(IA32)) * S32 * P32 * G32/1000;$$

$$P33 = \exp(-pi * x33 * trtime33./Q33);$$

$$S33 = (C * Mo ./ ((4 * pi) * DE * (Vsm^3))) ./ ((ones(size(x33))) + ((x33/fc).^ (n * gamma))). ^ (1/gamma);$$

$$O33 = (1/\sin(IA33)) * S33 * P33 * G33/1000;$$

$$P34 = \exp(-pi * x34 * trtime34./Q34);$$

$$S34 = (C * Mo ./ ((4 * pi) * DE * (Vsm^3))) ./ ((ones(size(x34))) + ((x34/fc).^ (n * gamma))). ^ (1/gamma);$$

$$O34 = (1/\sin(IA34)) * S34 * P34 * G34/1000;$$

$$P35 = \exp(-pi * x35 * trtime35./Q35);$$

$$S35 = (C * Mo ./ ((4 * pi) * DE * (Vsm^3))) ./ ((ones(size(x35))) + ((x35/fc).^ (n * gamma))). ^ (1/gamma);$$

$$O35 = (1/\sin(IA35)) * S35 * P35 * G35/1000;$$

$$PS51A = \exp(-\pi * xS51A * trtimeS51A ./ QS51A);$$

$$SS51A = (C * Mo ./ ((4 * \pi) * DE * (Vsm^3))) ./ ((ones(size(xS51A))) + ((xS51A / fc) .^ (n * gamma))) .^ (1 / gamma);$$

$$OS51A = (1 / \sin(IAS51A)) * SS51A * PS51A * GS51A / 1000;$$

$$PPKKY = \exp(-\pi * xPKKY * trtimePKKY ./ QPKKY);$$

$$SPKKY = (C * Mo ./ ((4 * \pi) * DE * (Vsm^3))) ./ ((ones(size(xPKKY))) + ((xPKKY / fc) .^ (n * gamma))) .^ (1 / gamma);$$

$$OPKKY = (1 / \sin(IAPKKY)) * SPKKY * PPKKY * GPKKY / 1000;$$

$$PROKY = \exp(-\pi * xROKY * trtimeROKY ./ QROKY);$$

$$SROKY = (C * Mo ./ ((4 * \pi) * DE * (Vsm^3))) ./ ((ones(size(xROKY))) + ((xROKY / fc) .^ (n * gamma))) .^ (1 / gamma);$$

$$OROKY = (1 / \sin(IAROKY)) * SROKY * PROKY * GROKY / 1000;$$

$$O12 = O12 * (2 * \pi * x12);$$

```

O13 = O13.*(2*pi*x13);
% 10*log10(((2*abs(O13)).*x13/sqrt(2)).*(2*pi*x13)).*x13*(2*sqrt(2)/pi));

O14 = O14.*(2*pi*x14);

O20 = O20.*(2*pi*x20);

O21 = O21.*(2*pi*x21);

O22 = O22.*(2*pi*x22);

O23 = O23.*(2*pi*x23);

O25 = O25.*(2*pi*x25);

O26 = O26.*(2*pi*x26);

O32 = O32.*(2*pi*x32);

O33 = O33.*(2*pi*x33);

O34 = O34.*(2*pi*x34);

O35 = O35.*(2*pi*x35);

OS51A = OS51A.*(2*pi*xS51A);

OPKKY = OPKKY.*(2*pi*xPKKY);

OROKY = OROKY.*(2*pi*xROKY);

```

```

%Signal to Noise Ratio

```

```

SNR12 = (O12./y12);

```

```
A12 = 0;  
  
SNR12 = SNR12 > ratio;  
  
if sum(SNR12) > 0  
  
    A12 = 1;  
  
end
```

```
SNR13 = (O13./y13);  
  
A13 = 0;  
  
SNR13 = SNR13 > ratio;  
  
if sum(SNR13) > 0  
  
    A13 = 1;  
  
end
```

```
SNR14 = (O14./y14);  
  
A14 = 0;  
  
SNR14 = SNR14 > ratio;  
  
if sum(SNR14) > 0  
  
    A14 = 1;  
  
end
```

```
SNR20 = (O20./y20);  
  
A20 = 0;  
  
SNR20 = SNR20 > ratio;  
  
if sum(SNR20) > 0  
    A20 = 1;  
  
end
```

```
SNR21 = (O21./y21);  
  
A21 = 0;  
  
SNR21 = SNR21 > ratio;  
  
if sum(SNR21) > 0  
    A21 = 1;  
  
end
```

```
SNR22 = (O22./y22);  
  
A22 = 0;  
  
SNR22 = SNR22 > ratio;  
  
if sum(SNR22) > 0  
    A22 = 1;
```

end

SNR23 = (O23./y23);

A23 = 0;

SNR23 = SNR23 > ratio;

if sum(SNR23) > 0

 A23 = 1;

end

SNR25 = (O25./y25);

A25 = 0;

SNR25 = SNR25 > ratio;

if sum(SNR25) > 0

 A25 = 1;

end

SNR26 = (O26./y26);

A26 = 0;

SNR26 = SNR26 > ratio;

if sum(SNR26) > 0

 A26 = 1;

end

SNR32 = (O32./y32);

A32 = 0;

SNR32 = SNR32 > ratio;

if sum(SNR32) > 0

 A32 = 1;

end

SNR33 = (O33./y33);

A33 = 0;

SNR33 = SNR33 > ratio;

if sum(SNR33) > 0

 A33 = 1;

end

SNR34 = (O34./y34);

A34 = 0;

SNR34 = SNR34 > ratio;

if sum(SNR34) > 0

 A34 = 1;

end

SNR35 = (O35./y35);

A35 = 0;

SNR35 = SNR35 > ratio;

if sum(SNR35) > 0

 A35 = 1;

end

SNRS51A = (OS51A./yS51A);

AS51A = 0;

SNRS51A = SNRS51A > ratio;

if sum(SNRS51A) > 0

 AS51A = 1;

end

SNRPKKY = (OPKKY./yPKKY);

APKKY = 0;

SNRPKKY = SNRPKKY > ratio;

if sum(SNRPKKY) > 0

 APKKY = 1;

end

SNRROKY = (OROKY./yROKY);

AROKY = 0;

SNRROKY = SNRROKY > ratio;

if sum(SNRROKY) > 0

 AROKY = 1;

end

A = A12 + A13 + A14 + A20 + A21 + A22 + A23 + A25 + A26 + A32 + A33 + A34 +
A35 + AS51A + APKKY + AROKY;

i = i + 1;

% for j = 1:1:Mw

 if A > 3

 B(i,j) = 1;

 else

 B(i,j) = 0;

end

LatB(i,1) = North;

LongB(i,1) = East;

if B(i,j) > 0

 Magn(i,j) = Mw;

else

 Magn(i,j) = 2.5;

end

MagMat = horzcat(Magn);

```
M = (min(MagMat,[],2))
```

```
fclose('all');
```

```
end
```

```
end
```

```
end
```

```
X = reshape(LongB, 29, 35)
```

```
Y = reshape(LatB, 29, 35)
```

```
Z0 = reshape(M, 29, 35)
```

```
Station_y = [LatEK12; LatEK13; LatEK14; LatEK20; LatEK21; LatEK22; LatEK23;  
LatEK25; LatEK26; LatEK32; LatEK33; LatEK34; LatEK35; LatS51A; LatPKKY;  
LatROKY];
```

```
Station_x = [LongEK12; LongEK13; LongEK14; LongEK20; LongEK21; LongEK22;  
LongEK23; LongEK25; LongEK26; LongEK32; LongEK33; LongEK34; LongEK35;  
LongS51A; LongPKKY; LongROKY];
```

```
Station_Locations = [ Station_x, Station_y];
```

```
for pp=1:length(Station_y)
```

```
    BB(pp,:) = 1;
```

```
end
```

```
fid = fopen('5km01MwDays.out','w+');
```

```
fprintf(fid,'%s\n','Easting (km) Northing (km) Mmin');
```

```
fprintf(fid,'%f %f %f\n',X,Y,ZO);
```

```
fclose(fid)
```

```
scatter3(Station_x,Station_y,BB,100,'filled','^')
```

```
hold on;
```

```
contourf(X,Y,ZO);
```

```
axis([230000 400000 4130000 4270000 0 1])
```

```
title('Magnitude of Completeness for 4 station location at 4 km depth - Daytime(1100-  
2300 UTC)')
```

```
xlabel('Easting(m)')
```

```
ylabel('Northing(m)')
```

```
colorbar
```

To determine the Minimum detection threshold at night the code called SNM_Jan_Nights_map.m can be used. One need only to use different PQLX noise files that are taken from (0000-1100 UTC) to determine the detection threshold at night. PQLX median noise files are called from lines 42-88 with the following code.

```
psd_file12 = 'EK12_HHZ_0101-0131_0000-1100';
```

```
matrix12 = dlmread(['/hd2/work/andrew/Important/Jan_Nights/' psd_file12]);
```

```
psd_file13 = 'EK13_HHZ_0101-0131_0000-1100';
```

```
matrix13 = dlmread(['/hd2/work/andrew/Important/Jan_Nights/' psd_file13]);
```

```
psd_file14 = 'EK14_HHZ_0101-0131_0000-1100';
```

```
matrix14 = dlmread(['/hd2/work/andrew/Important/Jan_Nights/' psd_file14]);
```

```
psd_file20 = 'EK20_HHZ_0101-0131_0000-1100';
```

```
matrix20 = dlmread(['/hd2/work/andrew/Important/Jan_Nights/' psd_file20]);
```

```
psd_file21 = 'EK21_HHZ_0101-0131_0000-1100';
```

```
matrix21 = dlmread(['/hd2/work/andrew/Important/Jan_Nights/' psd_file21]);
```

```
psd_file22 = 'EK22_HHZ_0101-0131_0000-1100';
```

```
matrix22 = dlmread(['/hd2/work/andrew/Important/Jan_Nights/' psd_file22]);
```

```
psd_file23 = 'EK23_HHZ_0101-0131_0000-1100';
```

```
matrix23 = dlmread(['/hd2/work/andrew/Important/Jan_Nights/' psd_file23]);
```

```
psd_file25 = 'EK25_HHZ_0101-0131_0000-1100';
```

```
matrix25 = dlmread(['/hd2/work/andrew/Important/Jan_Nights/' psd_file25]);
```

```
psd_file26 = 'EK26_HHZ_0101-0131_0000-1100';
```

```
matrix26 = dlmread(['/hd2/work/andrew/Important/Jan_Nights/' psd_file26]);
```

```
psd_file32 = 'EK32_HHZ_0101-0131_0000-1100';
```

```
matrix32 = dlmread(['/hd2/work/andrew/Important/Jan_Nights/' psd_file32]);
```

```
psd_file33 = 'EK33_HHZ_0101-0131_0000-1100';
```



```
matrix33 = dlmread(['/hd2/work/andrew/Important/Jan_Nights/' psd_file33]);

psd_file34 = 'EK34_HHZ_0701-0731_0000-1100';

matrix34 = dlmread(['/hd2/work/andrew/Important/Jan_Nights/' psd_file34]);

psd_file35 = 'EK35_HHZ_0101-0131_0000-1100';

matrix35 = dlmread(['/hd2/work/andrew/Important/Jan_Nights/' psd_file35]);

psd_fileS51A = 'S51A_HHZ_0101-0131_0000-1100';

matrixS51A = dlmread(['/hd2/work/andrew/Important/Jan_Nights/' psd_fileS51A]);

psd_filePKKY = 'PKKY_HHZ_0101-0131_0000-1100';

matrixPKKY = dlmread(['/hd2/work/andrew/Important/Jan_Nights/' psd_filePKKY]);

psd_fileROKY = 'ROKY_HHZ_0101-0131_0000-1100';

matrixROKY = dlmread(['/hd2/work/andrew/Important/Jan_Nights/' psd_fileROKY]);
```

Appendix F: All stations Used for the EKMMP

Station Name	Latitude	Longitude	Network Code	Project Utilization Code
EK12	38.1287	-83.10416667	EK	1, 2, 3, 4
EK13	38.2301	-82.82856667	EK	1, 2, 3, 4
EK14	38.29963333	-82.70368333	EK	1, 2, 3, 4
EK20	37.7332	-83.86605	EK	1, 2, 3, 4
EK21	37.81595	-83.53151667	EK	1, 2, 3, 4
EK22	37.91525	-83.25071667	EK	1, 2, 3, 4
EK23	37.92126667	-82.90043333	EK	1, 2, 3, 4
EK25	38.13583333	-82.81446667	EK	1, 2, 3, 4
EK26	38.07035	-82.58103333	EK	1, 2, 3, 4
EK32	37.61981667	-83.3024	EK	1, 2, 3, 4
EK33	37.75818333	-83.12488333	EK	1, 2, 3, 4
EK34	37.70558333	-82.74953333	EK	1, 2, 3, 4
EK35	37.85686667	-82.7147	EK	1, 2, 3, 4
FLKY	38.426	-83.751	KY	1, 2
HZKY	37.251083	-83.2067	KY	1, 2
PKKY	38.383	-83.034	KY	1, 2, 3, 4
Q51A	39.026	-83.3456	N4	1, 2
Q52A	38.9622	-82.2669	N4	1, 2
R50A	38.2816	-84.3274	N4	1, 2
R53A	38.3307	-81.9513	N4	1, 2
ROKY	37.909	-83.926	KY	1, 2, 3, 4
S51A	37.6392	-83.5935	N4	1, 2, 3, 4
S54A	37.7997	-81.3114	N4	1, 2
T50A	37.0204	-84.8384	N4	1, 2
TZTN	36.54389	-83.54897	US	1, 2
U54A	36.5209	-81.8204	N4	1, 2
ASTN	36.327	-83.476	ET	2
BCRT	35.766	-84.576	ET	2
BHKY	38.035	-84.505	KY	2
BLA	37.2113	-80.42049	US	2
CCNC	36.02364	-82.71475	ET	2
CCRT	35.466	-84.054	ET	2
CPCT	35.44975	-84.52181	ET	2
CPRT	36.1567	-83.8807	ET	2
DYTN	35.491	-85.092	ET	2
ETT	35.326	-84.455	ET	2
GRBT	35.674	-84.197	ET	2
KH50	37.42	-84.46	XO	2

KH54	37.41	-84.16	XO	2
KI51	37.19	-84.51	XO	2
KI53	37.18	-84.21	XO	2
KJ50	37.05	-84.58	XO	2
KJ52	36.92	-84.25	XO	2
KK50	36.87	-84.801	XO	2
LRVA	36.788	-82.786	ET	2
MCWV	39.6581	-79.8456	US	2
N51A	40.9183	-82.3748	N4	2
N53A	40.8065	-80.8377	N4	2
O52A	40.1158	-81.8361	N4	2
O54A	40.1821	-80.3778	N4	2
P48A	39.4605	-85.4258	N4	2
P51A	39.4818	-83.0601	N4	2
P53A	39.4868	-81.3896	N4	2
Q54A	38.9836	-80.8338	N4	2
Q56A	39.041	-79.1871	N4	2
R49A	38.2916	-85.1714	N4	2
R55A	38.2825	-80.1195	N4	2
SOKY	37.526	-85.965	KY	2
T57A	36.9983	-79.2538	N4	2
U56A	36.3472	-80.3829	N4	2
V51A	35.8033	-84.3511	N4	2
V52A	35.8417	-83.5959	N4	2
V53A	35.6694	-82.8124	N4	2
W52A	35.0935	-83.9277	N4	2
WMTN	35.248	-84.9732	ET	2
WSNC	35.1725	-83.58064	ET	2

Network Code	Name of Network
ET	CERI Southern Appalachian Seismic Network
KY	Kentucky Seismic and Strong Motion Network
N4	Central and Eastern US Network
US	United States National Seismic Network
XO	Ozark Illinois Indiana Kentucky (OIINK) Flexible Array Experiment (Stations active 3/15/2015 - 10/17/2015)

Project Utilization Code	Station Utility Within Project
1	Stations Used for Network Detection
2	Stations Used for Location
3	Stations Used for Estimating Local Magnitude
4	Station Used for Detection Threshold

REFERENCES

- Aki, K. (1980). Scattering and attenuation of shear waves in the lithosphere. *Journal of Geophysical Research: Solid Earth*, 85(B11), 6496-6504.
- Aki, K. R. (1980). *Quantitative Seismology: Theory and Methods*, 1.
- Atkinson, G. M. (2014). The attenuation of Fourier amplitudes for rock sites in eastern North America. *Bulletin of the Seismological Society of America*, 104(1), 513-528.
- Bendat, J. S. (1971). *Random data: analysis and measurement procedures Fourth Edition*. New York: Wiley.
- Boatwright, J. (1980). A spectral theory for circular seismic sources; simple estimates of source dimension, dynamic stress drop, and radiated seismic energy. *Bulletin of the Seismological Society of America* 70(1), 1-27.
- Bockholt, B. M. (2015). Local magnitude and anomalous amplitude distance decay in the eastern Tennessee seismic zone. *Seismological Research Letters*.
- Boore, D. M. (1983). Stochastic simulation of high-frequency ground motions based on seismological models of the radiated spectra. *Bulletin of the Seismological Society of America* 73 (6A), 1865-1894.
- Bormann, P. &. (2013). Seismic signals and noise. New manual of seismological observatory practice (NMSOP-2), IASPEI, GFZ German Research Centre for Geosciences, Potsdam, Chapter 4.

- Brune, J. N. (1970). Tectonic stress and the spectra of seismic shear waves from earthquakes. *Journal of geophysical research* 75(26), 4997-5009.
- Chapman, M. E. (2002). *Southeastern United States Seismic Network Bulletin, Number 36*. Retrieved from www.geol.vt.edu/outreach/vtso/anonftp/catalog/bul36.pdf
- Cooley, J. W. (1965). An algorithm for the machine calculation of complex Fourier series. *Mathematics of computation* 19(90), 297-301.
- D. Harris, J. D. (1996). Exploration Cambrian potential indicated in Kentucky Rome trough. *Oil and Gas Journal*.
- Davis, S. D. (1993). Did (or will) fluid injection cause earthquakes?-criteria for a rational assessment. *Seismological Research Letters*, 64(3-4), 207-224.
- Ellsworth, W. L. (2013). Injection-induced earthquakes. *Science*, 341(6142), 1225942.
- Eshelby, J. D. (1957). The determination of the elastic field of an ellipsoidal inclusion, and related problems. *Proceedings of the Royal Society of London A: Mathematical, Physical and Engineering Sciences (Vol. 241, No. 1226)*, 376-396.
- Evans, D. (1966). Evans, D. M. (1966). The Denver area earthquakes and the Rocky Mountain Arsenal disposal well. *The Mountain Geologist* v. 3.
- Frohlich, C. H. (2011). The Dallas–Fort Worth earthquake sequence: October 2008 through May 2009. . *Bulletin of the Seismological Society of America*, 101(1), 327-340.

- Gao D., S. R. (2000). Along-Axis Segmentation and Growth History of the Rome Trough in the Central Appalachian Basin. *AAPG Bulletin. Volume 84, No. 1*, 75-99.
- Harris, D. C. (2004). Rome Trough Consortium final report and data distribution: Lexington, Kentucky, Kentucky Geological Survey, Series 12, Open File Report OF-04-06 (CD-ROM).
- Harris, D. C. (2015). Cambrian Rogersville Shale in the Rome Trough, Kentucky and West Virginia: A Potential New Unconventional Reservoir in the Appalachian Basin. *Oral session presented at 2016 AAPG Annual Convention and Exhibition, Lexington, KY.*
- Herrmann, R. B. (1983). Short-period Lg magnitudes: Instrument, attenuation, and source effects. *Bulletin of the Seismological Society of America*, 73(6A), 1835-1850.
- Herrmann, R. B. (1997). Faulting parameters of earthquakes in the New Madrid, Missouri, region. *Engineering geology*, 46(3-4), 299-311.
- Hickman Jr, J. B. (2011). Structural evolution of an intracratonic rift system; Mississippi Valley graben, Rough Creek graben, and Rome trough of Kentucky, USA.
- Horton, S. (2012). Disposal of hydrofracking waste fluid by injection into subsurface aquifers triggers earthquake swarm in central Arkansas with potential for damaging earthquake. *Seismological Research Letters* 83(2), 250-260.
- Incorporated Research Institutions for Seismology, Retrieved 2017, from https://www.iris.edu/hq/inclass/interactive/usarray_station_how_it_works

- Johnson, C. B. (1995). Earthworm: A Flexible Approach to Seismic Network Processing. *IRIS Newsletter 14(2)*, pp. 1-4.
- K. M. Keranen, M. W. (2014). Keranen, K. M., Weingarten, M., Abers, G. A., Bekins, B. A., & Ge, S. (2014). Sharp increase in central Oklahoma seismicity since 2008 induced by massive wastewater injection. *Science*, *345(6195)*, 448-451.
- Kanamori, H. (1977). The energy release in great earthquakes. *Journal of geophysical research* *82(20)*, 2981-2987.
- Keranen, K. M. (2013). Potentially induced earthquakes in Oklahoma, USA: Links between wastewater injection and the 2011 Mw 5.7 earthquake sequence. *Geology*, *41(6)*, 699-702.
- Keranen, K. M. (2014). Sharp increase in central Oklahoma Seismicity since 2008 Induced by Massive Wastewater Injection.
- Kim, W. Y. (2013). Induced seismicity associated with fluid injection into a deep well in Youngstown, Ohio. *Journal of Geophysical Research: Solid Earth* *118 (7)*, 3506-3518.
- Madariaga, R. (1976). Dynamics of an expanding circular fault. *Bulletin of the Seismological Society of America*, *66(3)*, 639-666.
- McNamara, D. E. (2004). Ambient noise levels in the continental United States. *Bulletin of the seismological society of America*, *94(4)*, 1517-1527.
- Nanometrics, Inc., Retrieved 2015, from www.nanometrics.ca

- National Research Council. (2013). *Induced seismicity potential in energy technologies*. National Academies Press.
- Ottmöller L, H. J. (1999, Sep). SeisAn Earthquake Analysis Software. *Seismological Research Letters*, pp. 532-534.
- Ottmöller, L. a. (2003). Moment magnitude determination for local and regional earthquakes based on source spectra. *Bulletin of the Seismological Society of America*, 93(1), 203-214.
- Patchen, D. G. (2006). A Geologic Play Book for Trenton-Black River Appalachian Basin Exploration: Pittsburgh, PA. 601.
- Peterson, J. (1993). *Observations and modeling of seismic background noise*.
- Richter, C. F. (1935). Richter, C. F. (1935). An instrumental earthquake magnitude scale. *Bulletin of the Seismological Society of America* 28, no. 1, 1-32.
- Rubinstein, J. L. (2014). The 2001–present induced earthquake sequence in the Raton Basin of northern New Mexico and southern Colorado. *Bulletin of the Seismological Society of America*.
- Rubinstein, J. L., & Mahani, A. B. (July/August 2015). Myths and facts on Wastewater Injection, Hydraulic Fracturing, Enhanced Oil Recovery, and Induced Seismicity. *Seismological Research Letters*. Volume 86. Number 4.
- Ryder, H. G. (2003). *Evidence for Cambrian Petroleum Source Rocks in the Rome Trough of West Virginia and Kentucky, Appalachian Basin*. Open-File Report 05-1443.

- Skoumal, R. J. (2015). Earthquakes induced by hydraulic fracturing in Poland Township, Ohio. *Bulletin of the Seismological Society of America*, 105(1), pp. 189-197.
- Sloss, L. L. (1988). Sequences in the cratonic Interior of North America: Geological Society of America Bulletin. v. 74, no. 2, p. 93-114.
- T. White, J. D. (2001). Fault Kinematics in the Rome Trough. *Geological Society of America, Abstracts with Programs*. , Vol. 33, No. 4. A-42.
- Thomas, W. A. (1991). The Appalachian-Ouachita Rifted Margin of Southeastern North-America: Geological Society of America Bulletin. v. 103, no. 3, p. 415-431.
- Wallace E. Pratt, D. W. (1926). Local Subsidence of the Goose Creek Oil Field. *The Journal of Geology* 34, no. 7, Part 1, 577-590.
- Wang, R. G. (2016). Source analysis of a potential hydraulic-fracturing-induced earthquake near Fox Creek, Alberta. *Geophysical Research Letters*.
- Weingarten, M. G. (2015). Weingarten, M., Ge, S., Godt, J. W., Bekins, B. A., & Rubinstein, J. L. (2015). High-rate injection is associated with the increase in US mid-continent seismicity. *Science*, 348(6241), 1336-1340.
- Yeck, W. L. (2017). Oklahoma experiences largest earthquake during ongoing regional wastewater injection hazard mitigation efforts. *Geophys. Res. Lett.*, 44, 711–717.
- Zoback, M. L. (1989). Tectonic stress field of the continental United States. *Geological Society of America Memoirs*, 172, 523-540.

VITA

Andrew S. Holcomb

Education

2013: Bachelor of Science Geology, University of Kentucky

Professional Experience

2015-2017: Teaching Assistant, University of Kentucky

2015-2016: Research Assistant, University of Kentucky

2015-2015: Student Employee, Kentucky Geological Survey

2013-2014: Engineering Technician/ Laboratory Supervisor, GEM Engineering

2012-2013: Student Employee, Kentucky Geological Survey

Abstracts

Holcomb, A. S., Carpenter, N. S., Woolery, E. W., & Wang, Z. Monitoring Baseline Microseismicity in the Rome Trough, Eastern Kentucky: Year One Observations and Network Performance. In *2017 SSA Meeting*

Holcomb, A. S., Carpenter, N. S., Woolery, E. W., & Wang, Z. Monitoring Induced Microseismicity in the Rome Trough, Eastern Kentucky USA. In *2016 AAPG Eastern Section Meeting*.

Holcomb, A. S., Carpenter, N. S., Woolery, E. W., & Wang, Z. Monitoring Induced Microseismicity in the Rome Trough, Eastern Kentucky, USA. In *2015 Eastern Section SSA Meeting*

